USING PARTICLE IMAGE VELOCIMETRY (PIV) TO INVESTIGATE THE EFFECTS OF ROUGHNESS ON CONFINED FLOW AROUND A HYDROFOIL

by

Chad Kirk Nielson

A thesis submitted to the faculty of
The University of Utah
in partial fulfillment of the requirements for the degree of

Master of Science

Department of Mechanical Engineering

The University of Utah

May 2013

The University of Utah Graduate School

STATEMENT OF THESIS APPROVAL

The thesis of **Chad Kirk Nielson**

has been approved by the following supervisory committee members:

Eric R. Pardyjak	, Chair	**01-05-2013** Date Approved
Meredith M. Metzger	, Member	**01-05-2013** Date Approved
Rob Stoll	, Member	**01-09-2013** Date Approved

and by **Timothy A. Ameel** , Chair of

the Department of **Mechanical Engineering**

and by Donna M. White, Interim Dean of The Graduate School.

ABSTRACT

There are numerous applications in engineering in which the effects of roughness on fluid flow efficiency are important. This work is focused on better understanding the effects of roughness on the flow field downstream of a cambered (nonsymmetric) hydrofoil in a confined channel. Experiments were conducted using three different hydrofoils each having different levels of roughness and tested at three different angles of attack (0°, 10°, and 17°). Particle Image Velocimetry (PIV) was used to capture two-dimensional vector fields. These data were used to estimate mean vorticity, terms of the Reynolds stress tensor, and terms of the Reynolds Averaged Navier-Stokes (RANS) equations. The work was exploratory in nature and did not give definitive answers to the questions posed. The results suggested that findings from experiments involving airfoils in unconfined environments and those involving hydrofoils near an air/water surface should not be generally applied to a confined environment. The experiments indicate that the effects of roughness are highly dependent on angle of attack. For the 0° experiments, roughness delayed separation and dampened turbulence intensity observed outside of the boundary layer. However, for the 10° and 17° experiments, flow over rougher hydrofoils separated earlier, while the effects on turbulence intensity were mixed—there was not any discernible monotonic pattern from the smoothest to roughest cases, with the middle roughness often being higher or lower than either of the other two. However, these findings are inconclusive due to the fact that the roughness profile was somewhat

different, even though the equivalent sand grain roughness value was appropriate. All of the flow quantities calculated are shown graphically in the thesis and the appendices, and many additional observations were made beyond the scope of this abstract. The results of this work make a strong argument for further investigation of the effects of roughness on many flow quantities in confined flow, suggesting that the vast research done on hydrofoils in open flow—or potentially any objects—is not necessarily applicable.

This thesis is dedicated first and foremost to my lovely wife, Keira Marie Nielson. Without your support throughout this process, this work would simply not exist. You sacrificed selflessly of your time and energy so that I could achieve my dreams. While I may get the credit, you were the one with all the strength.

I cannot find the words to express my gratitude for my mom, Michelle Kaye Cat. Every redeeming quality of character I possess is because of you. You taught me to be the man I am today, a man I can be proud of. You are my hero.

With my deepest love and gratitude, I give thanks to my late father, Chad Howard Nielson. Though you passed away when I was young, you taught me that I had it in me to be anything, and I could never settle for anything less than greatness.

Finally, I must give thanks to my Godfather, Thomas Bachtell. You may never know the true magnitude of the influence you have had over my life, but I absolutely would not be here today, on this path of success, or maybe even alive on this Earth, without your benevolent influence in my life. Thank God for you.

TABLE OF CONTENTS

ACKNOWLEDGEMENTS

First, I must acknowledge Keira Nielson, who besides years of emotional support, put in over thirty hours of work in editing the figures I produced so they were presentable. Thank you!

I also acknowledge and thank Dr. Eric R. Pardyjak for all of the time and effort he put in to helping me to achieve my goals. He is a great professor, a great scientist, and a great human being. The Mechanical Engineering Department at the University of Utah and the students who come through it are blessed to have such a committed and hardworking individual in their ranks. God bless you sir. I would also like to thank the other members of my committee, Dr. Meredith M. Metzger and Dr. Rob Stoll. My life is better for having had the opportunity to work with all of them.

I would be remiss if I did not acknowledge the tremendous amount of time and energy put in by Nipun Gunawardena in performing the actual experiments with me. I would not have been able to solve all the practical experimental problems that I ran into without his knowledge and labor. He is a tremendous man who will undoubtedly go on to do great things.

I would also like to give thanks to a few people who took the time to share with me their expertise along the way: Tom Slowik is the ultimate problem solver, and he never balked when I came to him and said “so I really need this random, odd-shaped device.

How can we make it?" Holly Jayne Oldroyd and Bhagirath Addepalli taught me how to use and understand Insight and Particle Image Velocimetry.

Thank you God for all the loving family and friends that you put into my life who, for reasons far beyond my comprehension, put up with me for all these years. Being in graduate school is infinitely easier than being in a relationship with someone in graduate school. Thanks especially to Kim K. for his unique role in keeping me sane, not an easy task I can assure you. Thank you to my best friend Kip, a special man who I am so fortunate to have in my life.

Finally, I cannot go without mentioning the teaching faculty in the Department of Mechanical Engineering. This thesis is not just the culmination of three years of planning, testing, writing, and lots of hair pulling. If not for the great teachers I had in getting my undergraduate degree, I would have never been able to even begin. I would especially like to thank some of the more memorable teachers I had, professors who left an impression on me that will last a lifetime (in no particular order): Dr. Timothy A. Ameel, Dr. Daniel O. Adams, Dr. Meredith M. Metzger, Dr. Eric Pardyjack, Dr. K. Larry DeVries, Dr. Mark Minor, Dr. Kent Udell, Dr. William Provancer, Dr. Patrick McMurtry, and Dr. Kuan Chen.

CHAPTER 1

INTRODUCTION

1.1 Motivation and Background

There are numerous applications in engineering in which the effects of roughness on flow efficiency are important. One particular case is that of deep-sea mineral mining, where large pumps sit on or near the sea floor and pump water and minerals up long shafts to ships on the surface for processing (Park, Yoon, & Kang, 2009). These pumps are energy intensive, and due to the nature of the sediment-rich water they are pumping, the internal components of the pumps are exposed to great amounts of pitting, scratching, and other various forms of surface degradation. Because of the high costs associated with powering the pump and replacing pump blades in deep-water applications, it becomes very important to quantify the effects that roughness has on head loss accurately.

Unfortunately, previous work in this area is quite limited for this specific application. Researchers that have studied the effects of roughness on hydrofoils have mainly focused on sea vessel equipment. Therefore, laboratory models have involved open-channels with an air-water interface, usually submerging the hydrofoil completely, but close enough to the surface such that the effects of the surface are dominating (Chen & Chwang, 2002). A large body of research exists involving flow around unconfined airfoils, and as long as dynamic similitude can be achieved, these experiments may be applicable. However, the internal elements of turbomachinery exist in a confined environment. The effects of the

bounding surfaces enclosing hydrofoils inside a pump are so significant that it is difficult to apply the results of open-flow research to the internal flow problem.

The experiments conducted in the present research required the ability to capture fluid velocity vector fields in the downstream wake of the flow as opposed to single point measurements (e.g., hot-film anemometry, laser Doppler anemometry, etc.). There are several experimental methods available for capturing whole field velocity vectors. Two examples are Particle Image Velocimetry (PIV) and Molecular Tagging Velocimetry (MTV) (Tropea, Yarin, & Foss, 2007). For this research, PIV was chosen because it provided the necessary resolution and accuracy at a much lower cost.

According to Tropea et al. (2007, p. 309):

> …One of the most successful measurement methods that has emerged in the past two decades [for whole field vectors] is *particle image velocimetry* (PIV)… The principal of PIV is based on the measurement of the displacement of small tracer particles that are carried by the fluid during a short time interval.

A common two-dimension implementation of PIV involves illuminated tracer particles with a thin laser sheet, and a high-speed camera is used perpendicular to the plane of the laser sheet to capture image pairs of the illuminated particles. By correlating the location of the particles in each image of a pair, a vector field is formed (TSI Inc., 2011).

1.2 Approach

For this work, an experiment was performed to measure the effects of surface roughness on various quantities of flow downstream of an asymmetric hydrofoil. The hydrofoil used was a NACA 5512, using 1000 points generated from http://www.ppart.de/aerodynamics/profiles/NACA4.html. The scope of this experiment was restricted by the flow facility, which permitted moderate Reynolds number turbulent flow over a hydrofoil, designed to simulate the flow inside of turbomachinery. Velocity

vector fields were measured using PIV, and these vector fields were used to calculate various statistical quantities of flow. This work, unlike many previous to it, did not focus on the boundary layer. In fact, no data were taken very close to the surface of the hydrofoil, and instead, the entire flow field in the confined space was considered.

The experiments performed for this project were done with a Reynolds number ($^{uc}/_{\nu}$) of $5.4 \cdot 10^4$—, where u is the characteristic velocity in ms^{-1}, c is the chord length in m, and ν is the kinematic viscosity in m^2s^{-1}. Three angles of attack were considered: 0°, 10°, and 17.5°. Three relative roughness (RR_s) values—defined as (k_s/c), where k_s is the equivalent sand grain roughness height in m and c is the chord length measured in m—were compared: $1.26 \cdot 10^{-3}$, $1.85 \cdot 10^{-3}$, and $2.12 \cdot 10^{-3}$. While roughness was the primary independent variable considered, different angles of attack were used to better understand how the *effects of roughness differed across different geometries.*

The objective of this thesis is to build a foundation for future research in this area. The complicated geometry inside turbomachinery makes it impossible to represent it in a general matter in the same way that axial turbines can be generalized with turbine cascades. The scope of this research is not to model the *actual* geometry inside of turbomachinery, but rather to model some of the physical conditions *that are common within* turbomachinery. In this case, the hydrofoil was placed in a converging-diverging channel in order to generate repeatable pressure gradients around the hydrofoil (in addition to any gradients created by the hydrofoil itself). The differing angles of attack allow for comparisons of flow with little to no angle, as well as sharp angles that may involve complete separation. Both of these characteristics can be found inside of turbomachinery devices.

The range of angles of attack was determined experimentally to include a standard zero degree angle of attack as well as an angle of attack that included strong separation and a downstream wake. Preliminary experiments were performed using 2.5° angle of attack increments from 0° until clear separation was observed, which happened at 17.5°. The final choices of 0°, 10°, and 17.5° were based on having an approximately even spread between 0° and the separation angle, 17.5°. The value of k_s was determined using nominal grain sizes and the work of Zhang (2006).

1.3 Current Study Approach

This confined flow hydrofoil modeling study is relatively unique in its approach to measuring the effects of roughness on turbulence field variables using PIV. This type of work is relatively new to our laboratory and aims to lay the foundation for future research in this area. Since no generic shape or orientation can be made for flow inside of complex 3D turbomachinery, the challenge is to discover the basic turbulent characteristics of the flow around a simplified model of the problem and to investigate the impacts of roughness. The basic methodology is to use PIV to directly measure as many terms in the governing dynamic equations as possible, in order to provide a mechanistic understanding of the flow.

Chapter 2 will focus on the background research upon which this thesis is built, including previous PIV experiments, various hydrofoil experiments, derivation of the fundamental equations used, and the history of research on roughness and its relation to fluid dynamics. Chapter 3 outlines the experimental setup used, as well as the equations considered and how results were computed from discrete data points. Chapter 4 gives a detailed description of the results, including many of the plots that make up the bulk of

quantifiable results of the experiment, and discusses what they might mean. Chapter 5 presents the final conclusions reached from the results of the experiment, and recommends additional future work. Because of the large amount of flow quantities calculated and plotted, not all of them are found in the main body of work. The Appendix contains all of the results that are not in the body of the thesis.

CHAPTER 2

BACKGROUND

2.1 Motivation for Research—Description of Turbine Problem

Hydraulic turbines are particularly susceptible to performance degradation from surface roughness. The turbines used in underwater mineral mining are extreme examples of this. These turbines require consistent high flow rates even with high loads (Park, Yoon, & Kang, 2009). By their very nature, these pumps experience high rates of surface degradation due to pitting from the minerals harvested. They also operate at depths upwards of 1000 m, making routine maintenance and part replacement costly and difficult. Quantifying performance losses for these turbines related to surface degradation is vital in understanding the cost-benefit analysis of using strong and more expensive materials, as well as the point at which part replacement becomes necessary and cost-effective.

2.2 Equations of Motion

Analyzing turbulent flows can be difficult, hence choosing useful tools to aid in this process is important. In the present analysis, the Reynolds Averaged Navier-Stokes (RANS) equation, the vorticity equation, and the Reynolds stress tensor are used to better understand the flow physics being studied. The RANS equations is a fundamental

governing equation for the ensemble average behavior of turbulent flows. The vorticity equation allows for the quantification of the rotational aspects of flow and the development of structures in the flow that are important to transport processes (e.g., vortices). The terms of the Reynolds stress tensor are really part of the RANS equations, but are often considered separately to quantify turbulence in a flow field.

2.2.1 The Reynolds Averaged Navier-Stokes Equations

This chapter presents the RANS equations that will be used in the analysis of the acquired data following Tennekes and Lumley (1972, pp. 27-31). In order to derive the RANS equations, it is necessary to begin with two fundamental equations of turbulent flow, the continuity equation for incompressible flow

$$\frac{\partial u_i}{\partial x_i} = 0, \tag{2.1}$$

where u_i is the component of velocity in the x_i direction, and the Navier-Stokes equations (if the assumption is made that there are no body forces acting on the element)

$$\frac{\partial u_i}{\partial t} + u_j \frac{\partial u_i}{\partial x_j} = -\frac{1}{\rho}\frac{\partial p}{\partial x_i} + \nu \frac{\partial^2 u_i}{\partial x_j \partial x_i}, \tag{2.2}$$

where ρ is the density of the fluid (kgm^{-3}), p is the pressure (Nm^{-2}), and ν is the kinematic viscosity (m^2s^{-1}).

While Equation 2.2 accurately describes the instantaneous behavior of turbulent flow, it is not very practical to use in this form. Reynolds decomposition is used to change each variable into its mean and fluctuating components. For example, the instantaneous value of velocity can be defined as

$$u_i = \overline{u_i} + u_i', \tag{2.3}$$

where $\overline{u_i}$ is the mean (ensemble averaged) velocity and u_i' is the fluctuation of the instantaneous value from the mean. If the flow is ergodic (see e.g., Pope 2001), the ensemble average and time averages are the same and the mean time averaged velocity can be defined as

$$\overline{u_i} = \lim_{T\to\infty} \frac{1}{T} \int_{t_0}^{t_0+T} u_i dt. \tag{2.4}$$

The fluctuating component is simply the difference between the instantaneous value and the mean, as can be shown by rearranging Equation 2.3

$$u_i' = u_i - \overline{u_i}. \tag{2.5}$$

After decomposing each variable in Equations 2.1 and 2.2 into their mean and fluctuating components, the entire equations can be averaged. The result leads to Equation 2.6 and 2.7. Equation 2.7 is a special set of equations known as the Reynolds Averaged Navier-Stokes (RANS) equations

$$\frac{\partial \overline{u_i}}{\partial x_i} = 0, \tag{2.6}$$

$$\frac{\partial \overline{u_i}}{\partial t} + \overline{u_i}\frac{\partial \overline{u_i}}{\partial x_j} + \frac{\partial}{\partial x_j}\left(\overline{u_i' u_j'}\right) = -\frac{1}{\rho}\frac{\partial \overline{p}}{\partial x_i} + \nu \frac{\partial^2 \overline{u_i}}{\partial x_j \partial x_i}. \tag{2.7}$$

2.2.2 The Mean Vorticity Equation

A simple definition for vorticity comes from Kundu and Cohen (Kundu & Cohen, 2004, p. 59): "…it is generally customary to deal with twice the angular velocity, which

is called the vorticity of the element." Mathematically, vorticity is defined as the curl of the velocity vector

$$\boldsymbol{\omega} = \nabla \times \boldsymbol{u}. \tag{2.8}$$

In Equation 27, the bold font indicates a vector quantity. Breaking Equation 2.7 into its vector components yields

$$\omega_1 = \frac{\partial u_3}{\partial x_2} - \frac{\partial u_2}{\partial x_3}, \omega_2 = \frac{\partial u_1}{\partial x_3} - \frac{\partial u_3}{\partial x_1}, \omega_3 = \frac{\partial u_2}{\partial x_1} - \frac{\partial u_1}{\partial x_2}. \tag{2.9}$$

For two-dimensional analysis, with $x_1 = x$ and $x_2 = y$, the equation for vorticity simplifies to

$$\omega_z = \frac{\partial v}{\partial x} - \frac{\partial u}{\partial y}. \tag{2.10}$$

Written in the right-handed coordinate system, ω_z will be negative for a clockwise rotation and positive for a counterclockwise rotation. For these experiments, we are particularly interested in statistically steady flow. For this case, the vorticity can simply be averaged at each point to produce the desired statistics, as long as considerations of convergence are taken into account

$$\overline{\omega_z} = \frac{\partial \bar{v}}{\partial x} - \frac{\partial \bar{u}}{\partial y}. \tag{2.11}$$

2.3 Particle Image Velocimetry (PIV)

The approach of this research involves the analysis of flow quantities that can be derived from direct measurements of instantaneous velocity vectors in a vector field. For this reason, typical popular measurement techniques, such as hot-wire anemometry and

laser-Doppler anemometry (LDA) could not be used, because they "…provide a quantitative and accurate sample of the flow at a given point… [but they] are unable to capture the instantaneous flow organization, also known as coherent flow structures, observed in turbulent flows" (Tropea, Yarin, & Foss, 2007, p. 309). What is needed for the present experiments is what Raffel et al. (1998, p. 5) refer to as a "whole field technique."

Because of its ability to measure entire flow fields, PIV can partially determine elements of the instantaneous velocity gradient tensor du_i/dx_j within a plane (Tropea, Yarin, & Foss, 2007, p. 311). The quantity of interest for this work, the vorticity, can be obtained accurately from a PIV velocity field if "…the PIV measurement data is accurate, does not contain spurious data, and that the spatial resolution is adequate to perform a differentiation of the data" (Tropea, Yarin, & Foss, 2007, p. 340). Various measures were taken to ensure all three of these criteria were met satisfactorily and are outlined in the methods and procedures section.

Having satisfied the above conditions, the mean vorticity can then be calculated for each element using a finite difference formulation for Equation 2.11 (Tropea, Yarin, & Foss, 2007, p. 340)

$$\omega_z(i,j) \cong \frac{\bar{v}(i+1,j)-\bar{v}(i-1,j)}{2\Delta x} - \frac{\bar{u}(i,j+1)-\bar{u}(i,j-1)}{2\Delta y}. \tag{2.12}$$

where $\omega_z(i,j)$ is the vorticity in the z direction, v is the velocity in the y direction, u is the velocity in the x direction, and (i,j) are indices in the x- and y-directions, respectively. Because of the overlap in the data, it is important that all four points

surrounding (i, j) are "good" (not spurious) data points as well, or the vorticity at that point cannot be computed.

In the analysis that follows, similar differencing is used to compute all of the values in the RANS equations (see e.g., Oldroyd (2010, pp. 69,82) and Bourgoyne et al. (2005)). The same considerations apply that would apply to the vorticity data and other applications of the RANS equations, including those outlined above for vorticity, as well as the importance that the value of $\overline{u'^2}$ and $\overline{v'^2}$ converge satisfactorily. This simple differencing technique is quite sensitive, and can lead to poor derivative estimates as a result of noise in the data.

2.4 Hyrdofoil Theory

It is helpful to briefly review some of what is known about classical flow around a hydrofoil in order to motivate the assumptions and terminology used in this work. Fox, Mcdonald, and Pritchard (2004, pp. 409-412) do a good job of reviewing this in their development of the boundary layer concept (although their analysis is actually for an airfoil, the same concepts apply). Figure 2.1 is adapted from this work (2004, p. 410) and shows a generalized view of viscous flow around an airfoil. There is a stagnation point at the leading edge. A laminar boundary layer begins, moving away from the stagnation point on the top (suction side) and bottom (pressure side) of the foil. On each side, there is a transition point at which the boundary layer becomes turbulent. There is also a distinct point on each side called the "separation point," and after this point is a viscous wake region.

The separation point is of particular interest for this work. It is important to note that the separation point can be (and often is) at a different location on the suction side as well

as the pressure side of the foil. The separation is caused by an adverse pressure gradient (Fox, McDonald, & Pritchard, 2004, p. 409), and because the pressure gradient is designed to be more adverse on the suction side, the flow will usually separate on the suction side farther upstream of the trailing edge than it will the pressure side. In fact, it could separate only from the suction side and not separate from the pressure side at all. Separation is defined mathematically as the point at which the wall-normal velocity gradient at the surface is zero (Fox, McDonald, & Pritchard, 2004, p. 430)

$$\frac{\partial u}{\partial y}\Big)_{y=0} = 0. \tag{2.13}$$

Unfortunately, this type of exact data is not available for this research. However, a best estimate of the separation point was made using visual clues from the streamline plots for the instances where it appeared to have occurred.

Another important phenomenon of relevance is the Kutta condition, and a brief review of it is done here from "Fundamentals of Aerodynamics" (Anderson J. D., 2007, pp. 313-315). This phenomenon was first discovered by M. Wilhelm Kutta. Flow over an airfoil (or in this case, a hydrofoil) behaves differently than over most objects. The stagnation point might initially begin on the upper surface of the foil, but this "…is not tolerated very long by nature" (Anderson, 2007, p. 314). The stagnation point moves towards the tip until it reaches there, and eventually at steady state the flow comes smoothly off the trailing edge, the top and bottom flows meeting in parallel flow. This only occurs if the tip of the foil is sufficiently sharp that when flow attempts to curl around the trailing edge and form a stagnation point that is exactly opposite the leading edge stagnation point, the very small radius of the trailing edge causes the fluid to try to

move 'infinitely fast.' Figure 2.2, adapted from Anderson (2007, p. 313), illustrates how the flow initially "tries" to go on the left, and how it eventually ends up flowing on the right because of the Kutta condition. The condition on the right is the steady state condition of flow over an airfoil. In this way, nature forces the flow to adopt the value of circulation that results in the flow leaving smoothly. It is because of the Kutta condition that this value of circulation ends up being high enough to generate the lift required to lift an object.

2.5 Relevant Previous Research

While no specific previous research could be found in which the effects of roughness inside of turbomachinery are considered in the same manner that is proposed in this thesis, a multitude of previous similar experiments provide Insight into some of the results that can be expected, as well as guidance in the best methods of the experiment.

2.5.1 Roughness Characterization Methods

Some of the earliest experiments involving the effects that roughness has on wall-bounded flows were those performed by Nikuradse (1933) and Schlichting (1936), and much of the research reviewed here follows from their seminal work. Long before the invention of advanced surface analytical technology such as those existing today, Nikuradse and Schlichting used sand grains of known diameter to simulate roughness by gluing them to test-specimen surfaces. Schlichting went on to test a number of other roughness types by using shapes other than spheres, such as spherical segments, and introduced the concept of "equivalent sand grain roughness": *the size of sand grains that would give the same resistance as the surface in question.*

Eventually, computers allowed researchers to analyze large data sets and consider more options that were previously unreasonable to calculate by hand. For example, Coleman (1984) re-evaluated the validity of the assumptions made by Schlichting. He found that "…Schlichting made several assumptions which had significant effects on the final values which he reported." According to Coleman, Schlichting neglected the shear on the two smooth side walls and made assumptions about the value that he used for the wall shift that have shown to be highly inaccurate with various geometries. As Coleman points out, "…work reported in the years since 1936 has made the use of these assumptions unnecessary…" (Coleman, Hodge, & Taylor, 1984)

Eventually, three-dimensional optical profilometry technology made it possible to evaluate any kind of surface and compare it to the equivalent sand grain roughness. This technology uses high-powered microscopes and reflective surfaces to develop three-dimensional profiles of rough surfaces. Van Rij et al. (2002) used this technology to further expand on the roughness parameter developed by Sigal and Danberg (1988), (1990). Van Rij et al. were able to use optical profilometry to develop correlations that are appropriate for any surface roughness, and thus modified the roughness parameter (Λ_s) developed by Sigal and Danberg to yield

$$\Lambda_s = \left(\frac{S}{S_f}\right)\left(\frac{S_f}{S_s}\right)^{-1.6}, \tag{2.14}$$

where S is the reference area, or the area of the smooth surface before adding on the roughness, S_f is the total frontal area over the rough surface, and S_s is the total frontal wetted surface area. Using this value, the relation of equivalent sand grain roughness k_s to roughness height k is given by

$$\frac{k_s}{k} = \begin{cases} 1.583 \times 10^{-5}\Lambda_s^{5.683} & \Lambda_s \leq 7.842 \\ 1.802\Lambda_s^{0.03038} & 7.842 \leq \Lambda_s \leq 28.12. \\ 255.5\Lambda_s^{-1.454} & 28.12 \leq \Lambda_s \end{cases} \quad (2.15)$$

Zhang et al. (2006) used this roughness parameter characterization technique to measure the effects of roughness on aerodynamic losses on a turbine vane. They produced roughness elements using nickel-based particles and an aluminum filled epoxy to create a surface with known grain sizes—similar to sand paper—that was reflective enough for accurate profilometry measurements. They used particles of size 52.59 μm and 125.19 μm, with k_s/k values of 1.889 and 1.959, respectively. Similar to the research in the present work, they used a cambered foil in confined flow. However, their research involved air flow at high enough velocities that the Mach number was significant. It also involved a confined flow that curved with the camber of the foil. They found a definite positive correlation between roughness and loss:

> Total pressure losses, Mach number deficits, and deficits of kinetic energy all increase at each y/cx location within the wake as k_s/cx increases, regardless of the level, uniformity, or variability of the roughness along the surfaces of the vanes.

Unfortunately, due to the need for a nonreflective surface in the present experiment as well as limitations on funding, it was not possible to obtain optical profilometry measurements using the technique described by Van Rij et al. (2002) and Zhang et al. (2006) because the commercial sand paper used was not reflective. Hopkins (2010) was able to make accurate profilometry measurement of commercial sand paper using a Nanovea 3-D Profilometer (p. 41). Hopkins used *very* similar "sand paper grits" as those used in the present research. He reported average grain sizes of 92 μm, 140 μm, and 425 μm (as compared to the average grain sizes in this research of 82 μm, 140 μm, and 348 μm). Hopkins even used the same brand of Gator Grit ® sand paper (p. 40).

Unfortunately, he did not specify the exact type of sand paper used, and since Gator Grit ® has many different types of sand paper for each grit—with large variations in the grain density between some of them—the resulting values of k from his research could not be used for this work. However, they do give an additional opportunity for comparison, which is extremely important considering the lack of consistent methodology for classifying roughness amongst different researchers. Hopkins also found that the nominal values given for average grain size correlated extremely well with profilometry measurements (p. 53), providing confidence in the accuracy of using commercial sand-paper and assuming nominal grain sizes for correlating grit values.

After considering all of the previous approaches to quantifying roughness, and considering the facilities and technologies available, the method of approximating k_s by using the Van Rij modification of the Sigal roughness parameter (Λ_s) was chosen for the present work. Rather than using optical profilometry to determine the values of S_f and S_s as Van Rij did, the values were estimated by assuming the sand paper surface was similar to the sand paper used by Hopkins (2010) and using a visual approximation to determine the spacing.

2.5.2 Using PIV to Quantify Vorticity

While PIV is relatively new, flow visualization has been used for a long time to characterize vortex shedding. Barnes and Corlett (1993) were one of the first to compare the correlation between a PIV-measured velocity field and the associated flow structures visualized using traditional die injection techniques. Their results found that the two were very well correlated despite the low resolution of the early PIV technology used. While

they did not actually calculate the quantity vorticity, they were able to demonstrate the ability of PIV to measured velocities associated with coherent structures in the flow.

Although it involved Reynolds numbers around an order of magnitude bigger than those in the present work, Zobeiri et al. (2010) computed vorticity in the near wake of a hydrofoil using PIV. Their experiment involved a noncambered hydrofoil at 0°, comparing a truncated edge with complete symmetry and an asymmetric oblique edge.

2.5.3 Using PIV to Quantify Terms of the Reynolds Stress Tensor and Terms of the RANS Equation

Bourgoyne et al. (2005) used PIV and LDV (Laser-Doppler Velocimetry) to look at vortex shedding from a hydrofoil. They compare the results of the Reynolds stress tensor terms computed using each method. Specifically, using single point LDV measurements, a profile was created approximately one chord length downstream of the hydrofoil. Their results showed a tendency for the PIV values of Reynolds normal stress in both the streamwise and crossflow directions to have smaller magnitudes than LDV. They noted, "…both revealed similar trends and profile shapes (p. 297)." However, they felt that "…In general, the larger PIV sampling volume suppressed $\overline{u'^2}$, $\overline{v'^2}$ and $\overline{u'v'}$ compared to equivalent LDV measurements (p. 297)." However, the Reynolds sheer stress term appears to be almost identical at all locations shown. Their results indicate a region of positive Reynolds sheer stress below the hydrofoil (downstream of the pressure side) and negative Reynolds sheer stress above the hydrofoil (downstream of the suction side).

Oldroyd (2010, pp. 53-54,69) used PIV to measure the Reynolds shear stress term ($\overline{u'v'}$) in fully developed pipe flow and compared her results to previous research. Her experiment was conducted at Re=12,700, and she compared her results to an experiment

using DNS data conducted at Re=5,300 and another experiment conducted at Re=24,600 using LDV. Her results compared relatively well, "…[exhibiting] the expected trends and relative magnitudes when compared to experimental and computational results found in the literature" (p. 88). These findings are important because they verify the ability of PIV to accurately calculate turbulent quantities at least as well as other widely used methods. Oldroyd (2010) also showed that her statistics converged somewhat after 500 images, and the results showed very little change between 1500 images and the 3062 images that she took for the experiment (it is important to remember, however, that her geometry is much simpler than the one in this experiment).

2.5.4 The Effects of Surface Roughness on Head Loss

In general, roughness increases loss in flow, although there are some exceptions to this such as the case of 'riblets,' which have been shown to decrease skin friction in certain instances (for example, Walsh 1990), these exceptions are not discussed in this thesis. Many of the articles already referenced previously in this chapter show the correlation between increased roughness and head loss, such as Nikuradse (1933), Schlichting (1936), Sigal and Danberg (1990), Van Rij et al. (2002), Yun et al. (2005), and Varghese et al. (1978). This section also includes a few examples of pertinent experiments and their findings.

Ida (1965) studied the effects of impeller vane roughness on the characteristics of a mixed flow propeller pump. His findings indicated that "…total efficiency decreases with increasing roughness." He also found that "…vane roughness has a harmful influence…at the best efficiency point and in the higher capacity range, but has little effect at low capacity where the backflow arises."

Varghese et al. (1978) studied the influence of volute surface roughness (as opposed to the impeller vane considered by Ida) on the performance of a centrifugal pump. Their findings also showed considerable decrease in performance with increased roughness: "In the case of the experimental pump, the maximum overall efficiency is decreased by about 7.5 percent when the volute surface roughness is increased from 0.08 mm to 1.2 mm (p. 475)." They did, however, note that there was no noticeable effect on the impeller flow, indicating that "…mere increase in the roughness of the volute surface cannot result in overloading the driving motor or engine (p. 475)." In their conclusions, they also went on to suggest that "…it is necessary to study the mechanism of turbulent mixing within the volute (p. 476)."

Yun et al. (2005) studied the effects of blade surface roughness in a single-stage axial turbine, with consideration given to the shape of the roughness elements as well as the height. As noted in the beginning of this chapter, simple roughness height is not enough to characterize the aerodynamic characteristics of fluid flow, thus leading to the methodology of using equivalent sand grain roughness height to compare the aerodynamic effects of two separate roughness profiles. Their results showed that there was significant loss of turbine efficiency with increasing roughness, and that this "…efficiency penalty [itself also] increases with increasing roughness" (p. 142). They also found that "…as in cascades, a rotating turbine's performance is more sensitive to roughness on the suction side of stator vanes than on the pressure side" (p. 142).

Keirsbulck et al. (2002) used PIV to study the turbulent boundary layer and see how it differed over a *k*-type rough wall as opposed to a smooth surface. "k-type" roughness refers to "two-dimensional bars of square cross-section normally placed in the flow

direction" (pp. 127-8). They used a hot-wire probe to measure the mean and fluctuating components of velocity and derived their turbulence quantities from these data. PIV was used to capture the flow field near both the smooth and rough surface; however, only "…qualitative measurements have been achieved using the PIV technique" (p. 133). They found that "…the PIV velocity fields confirm the behavior of the structures predicted by the [hot-wire probe] quadrant analysis in the wall regions" (p. 134).

2.5.5 Unconfined Flow over Hydrofoils and Considerations of Surface Effects (Froude Number)

Chen and Chwang (2002) investigated the free-surface influence on the wake of a fully submerged hydrofoil using a numerical simulation, and found it to be significant. They found that in particular, the Froude number—a nondimensional number characterizing the ratio of inertial forces and gravitational forces to achieve dynamic similitude whenever waves are considered—had an effect on the relationship between the Strouhal number and the Reynolds number. The Strouhal number characterizes the frequency of vortex shedding off an object and thus plays a vital role in characterizing turbulence. They showed that not only does the surface affect the frequency of vortex shedding, but the vortex patterns are different as well. The energy transfer between kinetic and potential energy is responsible for interesting vortex behaviors. Even more so than with a free-stream airfoil, a fully submerged hydrofoil that is anywhere near an air-water surface experiences different flow physics than confined, wall-bounded flow.

2.5.6 Effects of Cavitation

For this thesis, effects of cavitation have been ignored. However, it is important to discuss the effects of cavitation briefly and to discuss the effects cavitation can create when they occur.

In his work "Cavitation in Fluid Machinery and Hydraulic Structures," Arndt (1981) gives a broad discussion about cavitation. Among other things, he notes that it can "affect performance… through increased drag… limitations on the thrust produced… decreased power output and efficiency… and a drop in head and efficiency produced by pumps (p. 273)." In addition, it can affect the accuracy of flow meters, as well as create noise and vibration. He defines cavitation thus:

> Cavitation is normally defined as the formation of the vapor phase in a liquid. The term cavitation (originally coined by R. E. Froude) can imply anything from the initial formation of bubbles (inception) to large-scale, attached cavities (supercavitation). The formation of individual bubbles and subsequent development of attached cavities, bubble clouds, etc., is directly related to reductions in pressure to some critical value, which in turn is associated with dynamical effects, either in a flowing liquid or in an acoustical field (p. 275).

In reality, "…often economic or other operational considerations necessitate operation with some cavitation (p. 275)." Cavitation is affected by roughness, and future work should absolutely consider it as a dependent variable of study. However, it is beyond the scope of this work.

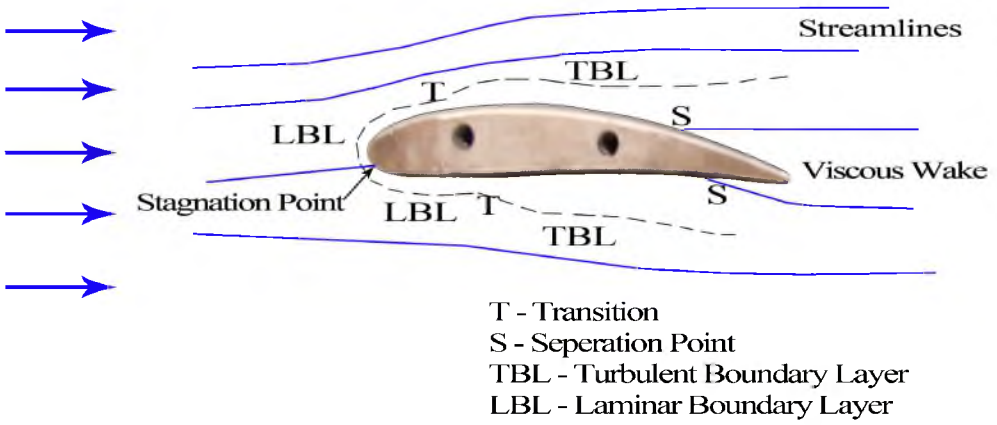

Figure 2.1. Graphical depiction of classic flow over an airfoil, adapted from Fox, McDonald, and Pritchard (2004, p. 410).

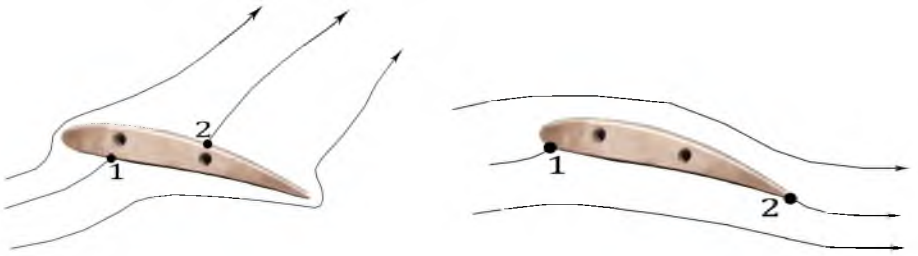

Figure 2.2. Illustration of the Kutta condition showing initial flow (left) and flow after steady state has been achieved. Adapted from Anderson (2007, p. 313).

CHAPTER 3

METHODS

This chapter details the setup and methodology for the experiments. First, a detailed description of the flow channel is given to describe the experimental environment. Next, a description of the hydrofoils and their fabrication is presented. Finally, details of the PIV methodology used to acquire and process the images is described.

The test section, the removable insert to the test section, and the hydrofoil parts were all designed in SolidWorks before they were manufactured. Nominal sizes are shown in this chapter, and may differ from the final dimensions, even with the CNC machined hydrofoils.

3.1 Flow Facility

The flow facility used for this experiment is a "6 inch flow visualization water tunnel" from Engineering Laboratory Design (ETL, 1999). The flow facility originally came with an open-channel type test section, but this was removed and replaced with a custom built channel designed for confined flow. A centrifugal pump (G&L Model No. 2x2-1/2x6 SST-C) capable of delivering 280 GPM using 1.5 BHP was used to move the fluid. It utilizes a variable speed drive assembly, capable of adjusting the pump frequency in increments of 0.1 Hz.

3.2 Test Section

The standard square test section for the water channel was replaced with a custom-designed section fabricated from polycarbonate material for the main structure, with glass windows on the bottom and one of the sides, and a removable piece composed of acrylic. When fully assembled, the internal geometry of the test section would be that of a single piece that was 99 cm long and had a square cross-section with a nominal measurement of 15.2 cm per side on the inside. However, due to the imperfections at the borders of the insertable acrylic piece and the glass windows, there is some variation to this shape at the edges of the channel.

Figure 3.1-a shows a view of the SolidWorks model of the assembled test section. Figure 3.1-b is an exploded view of the same model so that some of the individual parts can be seen well.

3.2.1 Test Section Sides

The four main sides of the test section were made from single pieces of polycarbonate material, and machined manually on an end mill. Figure 3.2-a shows a drawing of the bottom piece. The seat for the window is located 40.6 cm from the upstream end of the test section. The window itself is 19.1 cm long by 7.6 cm wide. The opening for the camera viewing window is 17.8 cm long and 6.4 cm wide. Figure 3.2-b shows a drawing of the side piece that had a window for the laser sheet to pass through. The seat for the window is located 40.6 cm from the upstream end of the test section. The window itself is 19.1 cm long by 14.7 cm wide. The opening for the laser sheet to pass through is 17.8 cm long and 13.5 cm wide. The other side of the test section has no windows or other cutouts, and has the same external dimensions as the window side.

Figure 3.3-a shows the top of the test section. The cutout section designed for the removable piece is 58.4 cm long by 14.0 cm wide. The cutout begins only 4.5 cm from the upstream end of the test section. Threaded inserts on both sides and ends of the removable pieces were originally designed to hold the test section in place and apply enough pressure to form a seal. However, due to cracking in the polycarbonate material that developed from using the treaded inserts, they were abandoned in favor of clamps. There is a small channel, 0.26 cm wide and 0.20 cm deep, and approximately 0.64 cm from the edge. This channel is designed to contain a custom-cut O-ring with a 0.26 cm diameter, used to create a water-tight seal. Figure 3.3-b is a zoomed-in cutout of one of the corners of the opening to illustrate details.

3.2.2 Removable Piece and Components

A 2.5 cm thick piece of acrylic designed to fit into the test section can be seen in Figure 3.4. There is a circular hole with a diameter of 6.4 cm, located 43.8 cm downstream from the upstream end of the removable section. A cylindrical piece inserts into this hole and attaches to the hydrofoil (see Figure 3.5). A channel similar to the one described above was created to ensure a seal between the cylindrical piece and the removable acrylic piece. This circular piece allows the hydrofoil to be rotated to a specified angle. Notches were created using a CNC etching tool in the acrylic piece at 2.5° increments. A corresponding notch was created on the side of the cylinder in the same plane as the bolt holes used to attach the hydrofoil, providing a method of aligning the cylinder with the direction of flow. All of these elements were designed to ensure consistent location of each hydrofoil after they are removed and re-inserted and rotated.

A bleed-hole (not shown) was drilled into the acrylic piece approximately 11 cm downstream of the large circular hole to allow air to escape.

3.2.3 The Hydrofoils

A view of the hydrofoil showing its profile is shown in Figure 3.6. The foils have a nominal chord length of 11.3 cm, a span of 15.2 cm, and a maximum height of 1.22 cm. The hydrofoil profile is a NACA5512 that was generated using an algorithm found at http://www.ppart.de/aerodynamics/profiles/NACA4.html using 100 data points. The points were input into SolidWorks and a curve was fit to them to create the profile. The hydrofoils were manufactured using a CNC machine from this profile, and while it is impossible to eliminate all sources of error, this method kept the nonuniformity between them to a minimum.

Despite the steps taken to ensure uniformity, manufacturing limitations resulted in slight differences in the hydrofoils' shape on the ends. While these imperfections were extremely small, they resulted in slightly different angles of attack at different spanwise locations, leading to larger errors at the plane of the laser sheet. To accommodate for this, masks were created in the T.S.I.'s PIV processing software Insight to record the approximate location of the suction-side surface of the hydrofoil in the laser sheet plane during the first set of experiments (the smoothest case), and subsequent experiments were visually adjusted to match this line. By visual inspection, the largest magnitude of error of the physical location of each hydrofoil relative to the others is between 1 and 2 mm.

3.3 Characteristic Reynolds Number

A brief description of the methodology used to determine Reynolds number is given. Because of the nature of the geometry, it was not possible to get a true value of upstream velocity. Figure 3.7-a shows a simplified top-view of the flow channel setup, with the hydrofoil inserted at the plane of the laser sheet (not to scale). As can be seen, the location of the airfoil is at the apex of the diffuser. Any value of velocity taken upstream or downstream would not relate effectively to the point where the hydrofoil was placed because the cross-sectional area is significantly different. However, it is not possible to measure the velocity at this point when the airfoil is placed inside the test section. Therefore, an average velocity was measured at the point of the apex of the diffuser while the hydrofoil was removed from the flow channel (as can be seen in Figure 3.7-b). The reason this is referred to as a pseudo-upstream velocity is because if the cross-sectional area of the entire flow channel were constant, this would be the velocity upstream of the hydrofoil (as illustrated in Figure 3.7-c).

There are a number of errors involved with this methodology. The flow resistance is greater when the hydrofoils are inserted, resulting in a lower volumetric flow rate for the same pump frequency. The velocity described in this method would be the upstream velocity if the entire flow channel was of constant cross-section, but of course it is not. Therefore, the velocity indicated is representative and does not actually refer to the velocity at any point in the flow. Despite these limitations, this was considered the best method to describe the velocity (and therefore the Reynolds number) of the overall flow. This problem is indicative of the greater challenges associated with confined flow that are not encountered in open stream experiments.

3.4 Determination of Equivalent Sand Grain Roughness (k_s)

Recall Equation 2.2, restated here as Equation 3.1

$$\Lambda_S = \left(\frac{S}{S_f}\right)\left(\frac{S_f}{S_s}\right)^{-1.6}, \tag{3.1}$$

where S is the reference area, or the area of the smooth surface before adding on the roughness, S_f is the total frontal area over the rough surface, and S_s is the total frontal wetted surface area. Using this value, the relation of equivalent sand grain roughness (k_s) to roughness height (k) is given by

$$\frac{k_s}{k} = \begin{cases} 1.583 \times 10^{-5}\Lambda_S^{5.683} & \Lambda_S \leq 7.842 \\ 1.802\Lambda_S^{0.03038} & 7.842 \leq \Lambda_S \leq 28.12. \\ 255.5\Lambda_S^{-1.454} & 28.12 \leq \Lambda_S \end{cases} \tag{3.2}$$

The assumption was made that the sand paper surface (or at least the sand grain elements) would be similar to those used by Hopkins (2010). Based on his profilometry, they can be characterized as hemispheres on top of circular cylinders with the same diameter (d) as the hemisphere and a height equal to the hemispheres radius (r). The sample area considered was circular with a radius of r_a (which was 0.264 cm, leading to an area of $2.19 \cdot 10^{-5}$ m^2) and the amount of grains inside the sample area of n. Using these assumptions, the formulae for S, S_f, and S_s become

$$S = \pi r_a^2, \tag{3.3}$$

$$S_f = n\left(\frac{\pi r^2}{2} + rd\right), \tag{3.4}$$

$$S_s = n\left(\frac{4\pi r^2}{4} + r\frac{\pi d}{2}\right). \quad (3.5)$$

Table 3.1 summarizes these values for each of the three roughness values, including the resulting Λ_s and the final values of k_s, k, and $\frac{k_s}{k}$. The relative roughness values based off of equivalent sand grain roughness (RR_s) are also tabulated using the nominal chord length of 11.27 cm (defined as k_s/c).

3.5 Data Acquisition and Processing

Figure 3.8 shows a schematic of the data acquisition and processing setup relative to the test section.

3.5.1 PIV System and Parameters

The PIV system consists of a laser, camera, synchronizer, and frame grabber boards. The system used in this experiment is the same system that was used by Oldroyd (2010, pp. 24-34) and unless otherwise stated, technical specifications for the hardware are taken from this thesis. The system is operated by a computer using Insight 3G v 9.0 by TSI Inc. with a Dual 1.86GHz Processor, 2MB of Ram, and a Duel Input, 64 Bit frame grabber.

3.5.1.1 Laser System

The laser used was a pulsed New Wave Research Solo 120 ND:YAG 532nm. The laser is capable of delivery a maximum energy of 120 mJ per pulse. The beam was focused into a laser sheet using a two-lens combination. The first lens is a 25 mm focal length spherical lens. This lens focuses the beam first to a point, from which it then diverges outward, doubling in diameter every 25mm. The second lens is a 12.5 mm focal length cylindrical lens. By setting the cylindrical lens horizontally 37.5 mm away from

the spherical lens, the beam is refocused in the vertical direction but not the horizontal. This two-lens combination creates a laser sheet that will expand in the horizontal direction but stay roughly the same size in the vertical direction. See Figure 3.9 and Figure 3.10 for a descriptive drawing of this setup and a photograph, respectively.

In order to further refine the thickness of the laser sheet, a 0.165 cm wide slot was machined into a thin sheet of metal and attached to the test section where the laser sheet enters. Two small holes for dowel pins were also machined into the metal sheet on which a small bubble-level was set to ensure the sheet was level.

3.5.1.2 Camera Setup

Because this experiment used 2D PIV imaging, only one camera was required. The camera used for this experiment was a TSI PowerView Plus 4MP CCD camera. A 532 nm notch filter was used to isolate the wavelength of the laser system to filter out ambient light and any laser light that had reflected off a colored surface and changed wavelength.

3.5.1.3 Acquisition Parameters

For 2D PIV, a single instantaneous measurement of a velocity field requires two images taken sequentially from each other separated by a time of Δt. In this thesis, any reference to the amount of 'images' taken for an experiment *actually refers to an image pair.* Precise timing between the sequential firing of the two laser pulses and the exposure of each image is imperative, and the synchronizer ensures this timing.

Lacking any kind of precedent for PIV for this exact situation, the decision on how many images to take to reach convergence was based off of experimental equipment limitations. The assumption was made that the higher the angle of attack, the larger

potential for turbulence, and the higher convergence requirements. Keeping the system limitations in mind, the number of images taken for each angle of attack was 4500, 5500, and 7000 for 0°, 10°, and 17°, respectively (1000 images were taken for the test case with no hydrofoil in the flow). As is shown in Section 4.1, these amounts proved more than adequate for satisfactory convergence.

There are many important timing factors that affect the quality of vectors produced by PIV (see Figure 3.12 for a screen shot of the timing diagram). The most important is the amount of time between laser pulses for each image pair (Δt). If this value is too small, an insufficient amount of movement will have occurred for the algorithm to appropriately identify the vector. Conversely, if Δt is too large, the correlation between particles in image one and image two is not possible. A simple "rule-of-thumb" formula can be used to determine a useful maximum for this value (Equation 3.6)

$$\Delta t = \frac{0.25 \cdot D}{V}, \tag{3.6}$$

where Δt is the time between each laser pulse, D is the width of an interrogation region, and V is the velocity of the fluid. This formula is designed to ensure that no particle travels a distance more than one-quarter the size of the interrogation region. For a 16 x 16 pixel interrogation area and a calibration ratio of 70.42 µm/pixel, the value of D is equal to 1,127µm. Assuming a maximum velocity of 0.75 ms^{-1}, the value of the maximum Δt becomes 376 µs.

This is just a starting point, and trial and error was used to find an ideal value (one which maximized the number of acceptable velocity vectors). For this experiment, the final value of Δt was 350 µs. Other important factors include the laser pulse delay and the

PIV exposure, both of which were found through trial and error in order to have the proper amount of light and exposure in each frame.

3.5.2 Image Processing System

The images were processed using a newer version of Insight than the one used to acquire them. This was done because a newer version was available that could be installed on a much faster PC with more memory—thereby making it possible to process more images in a reasonable period of time—that was not compatible with the available image frame grabber. In total, 52,000 images were processed. This number was far more than the original system used by Oldroyd (2010, p. 37) was capable of processing.

3.5.2.1 Calibration

For 2D PIV imaging with one camera, calibration was only needed to convert the velocity field coordinates and vectors to mm and mms^{-1}, respectively (TSI Inc., 2011, pp. 9-1). This was done using a precision-machined calibration plate with colored points located in a grid pattern of 5mm square. The calibration plate is suspended with the grid pattern facing the camera, and the surface with the grid pattern at the plane of the laser sheet. For this experiment, because the camera was mounted from the bottom (vertically), a level was used to assure the calibration plate was normal to the camera. An image was taken of the calibration plate using Insight and two points on the grid were mapped between each other. The known distance between these points was entered depending on how many grid spaces apart they were (the farther apart the points are from each other, the more accurate the correlation will be), and Insight used this information to create a calibration factor. For this experiment, the calibration factor was found to be 70.42 μm/pixel.

3.5.2.2 Processing Mask

The processing mask is the area of the image in which vectors will be processed. For this experiment, a simple rectangular processing mask was chosen. Each image taken had an area of 2048 X 2048 pixels; however, only a 1768-width X 1320-height (pixels) area was selected for the processing mask. This resulted in a data area of approximately 125-width by 93-height (cm).

3.5.2.3 Background Subtraction

Background subtraction is a common image enhancement technique used to filter out the 'fixed' parts of the image in an effort to make the 'variable' parts of the image (the suspended particles) more apparent (TSI Inc., 2011, pp. 8-13). T.S.I.'s "…Background Image Subtraction is a two-step process: 1) generate the background image; 2) subtract the background image from each image. Insight is able to perform these two processing steps in one image" (TSI Inc., 2011, pp. 8-13) .

The background image was generated in this experiment using 'Minimum Intensity.' Minimum intensity does not typically have as good of a signal-to-noise ratio as average intensity, but it has the advantage of not reducing the intensity of any of the particles. In the case of this experiment, both methods of background subtraction were tested, and the minimum intensity setting was found to be the only setting that improved the results without reducing the intensity to insufficient levels on the margins of the processing area. By using the appropriate setting, Insight automatically subtracts this image from each image in the experiment set and creates a new set of images that can then be fed into the processor.

Unfortunately, because of the differing reflectivity of the 100 grit roughness hydrofoil, background subtraction could not be used without losing valuable areas of data on the margins. Because of this, there are a few areas near the hydrofoil in which insufficient data were taken. It is important to remember that background subtraction does not in any way alter the vector field, it merely reduces the amount of spurious vectors; therefore, there is no nonuniformity introduced by using background subtraction on some of the experiments but not others.

3.5.2.4 Image Processing

A complete description of how PIV works can be found in "Insight 3G/4G User's Guide" (2011, pp. 10-10 to 10-23) and is covered briefly here. A Recursive Nyquist Grid is used to obtain increased resolution. For the first pass, a 32 X 32 pixel sized interrogation area is used. For the second pass, a higher resolution 16 X 16 pixel size interrogation area is used, using the information from the initial pass as a starting point. This method results in more accuracy than would be achieved by simply starting with a 16 X 16 pixel sized interrogation area. A Gaussian Mask is used to weight the pixels in the center of the interrogation area more than those around the edges. A Fast Fourier Transform is used to generate a correlation map, and a Gaussian Peak Engine is used to locate the correlation peak and determine the most likely displacement for the fluid particles in that area. These displacements are then divided by the time between laser pulses (Δt) to calculate the velocity vector for that point.

3.6 Postprocessing/Data Reduction Using MATLAB

MATLAB was used to process all of the vector files produced by Insight, and to use them to calculate desired quantities of flow. Data from Insight were processed into Matlab data files (.mat files). All values for the "choice code" variable were converted to a 0 for spurious vectors and a 1 for "good" vectors. The "choice code" variable is a designation given to each vector processed by Insight indicating whether Insight considers it a good correlation or not. For each image, the data were further refined by removing any values outside of three standard deviations from the mean (both positive and negative) in an attempt to further remove any spurious vectors missed by Insight. The data sets were then averaged (mean) at each vector across all of the images in that experiment.

In order to further remove spurious vectors, the values of the fluctuating component's velocity (u' and v') were calculated twice. First, the mean at each vector location was calculated across all the images for each particular experiment, resulting in nine separate mean vector fields (values were calculated ignoring spurious vectors). The fluctuating components of velocity were then calculated at each instantaneous vector using this mean, and the Reynolds stress tensor terms were determined from these. Data were then further removed (and the corresponding "choice code" value set to zero) in which streamwise Reynolds normal stress ($\overline{u'^2}$) was outside of three standard deviations for that particular vector location. This process was different than the one used to originally refine the data because it compared each point to the same location in other images instead of comparing each point to other locations in the same image. This was done because convergence plots indicated that about 1 out of 100 or less random fluctuating

components of velocity at each location were of an order of magnitude greater than the rest of the data, preventing proper convergence. These spikes were considered highly likely to be spurious vectors that had slipped past Insights filtering or the first attempt to refine the data, and they had a large effect on the mean values. After these few points were determined, the refined "choice code" variable was used to further refine the original instantaneous vector field, and the process to find the mean and fluctuating components of velocity were repeated.

Vorticity was calculated from the mean velocity data using a central difference derivative method and Equation 3.7 (restated from Equation 2.9)

$$\overline{\omega_z} = \frac{\partial \bar{v}}{\partial x} - \frac{\partial \bar{u}}{\partial y}. \tag{3.7}$$

Note that the central difference method for derivative approximation reduced the size of each dimension by two data points.

Using the velocity vectors, the rest of the results were calculated. The Reynolds stress tensor values were averaged at each vector to produce the mean Reynolds normal stresses and the Reynolds shear stress (also reducing the size in each dimension by two data points). Finally, each directly calculable term from the RANS equations was computed using a central difference approximation (reducing the size of each dimension by two data points)—this is covered later in Chapter 4. Using appropriate values (see Chapter 4), each flow quantity was normalized. Finally, the RANS terms were smoothed using a 9-point median windowing method to reduce some of the noise in them (this process further reduced the size in each direction by an additional two data points).

Table 3.1. Summary of values from k_s calculations.

	180 Grit	100 Grit	50 Grit
d (μm)	82	140	348
d (m)	$8.20 \cdot 10^{-5}$	$1.40 \cdot 10^{-4}$	$3.48 \cdot 10^{-4}$
r (m)	$4.10 \cdot 10^{-5}$	$7.00 \cdot 10^{-5}$	$1.74 \cdot 10^{-4}$
n	255	47	40
S (m^2)	$2.19 \cdot 10^{-5}$	$2.19 \cdot 10^{-5}$	$2.19 \cdot 10^{-5}$
S_f (m^2)	$1.53 \cdot 10^{-6}$	$8.22 \cdot 10^{-7}$	$4.32 \cdot 10^{-6}$
S_s (m^2)	$1.80 \cdot 10^{-6}$	$9.65 \cdot 10^{-7}$	$5.07 \cdot 10^{-6}$
Λs	18.49	34.41	6.54
ks/k	1.73	1.49	0.69
ks (m)	$1.42 \cdot 10^{-4}$	$2.08 \cdot 10^{-4}$	$2.39 \cdot 10^{-4}$
c (m)	0.1127	0.1127	0.1127
RR_s	$\mathbf{1.26 \cdot 10^{-3}}$	$\mathbf{1.85 \cdot 10^{-3}}$	$\mathbf{2.12 \cdot 10^{-3}}$

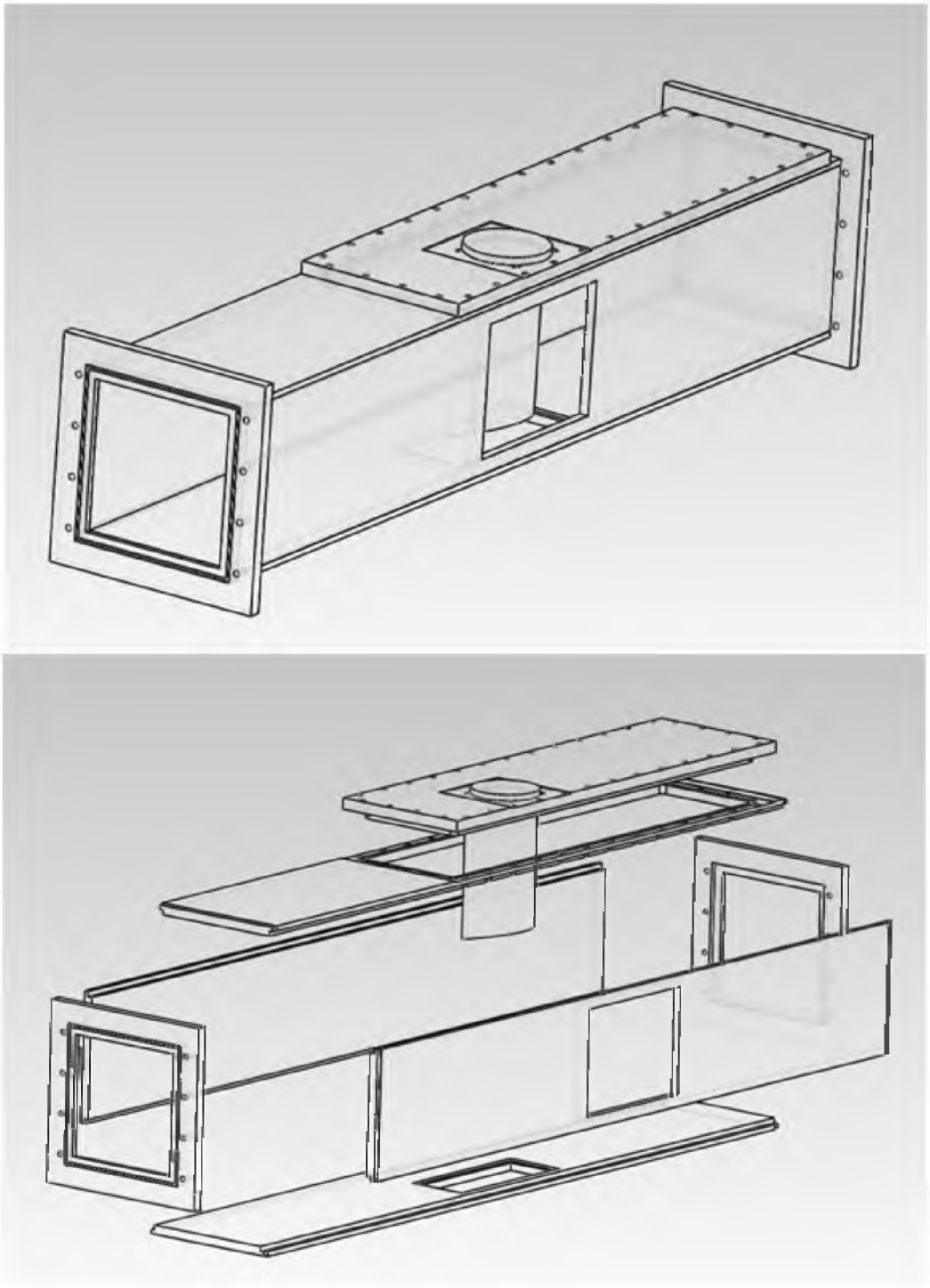

Figure 3.1 SolidWorks assembly of test section. a) (above) regular view. b) (below) Exploded to enhance detail.

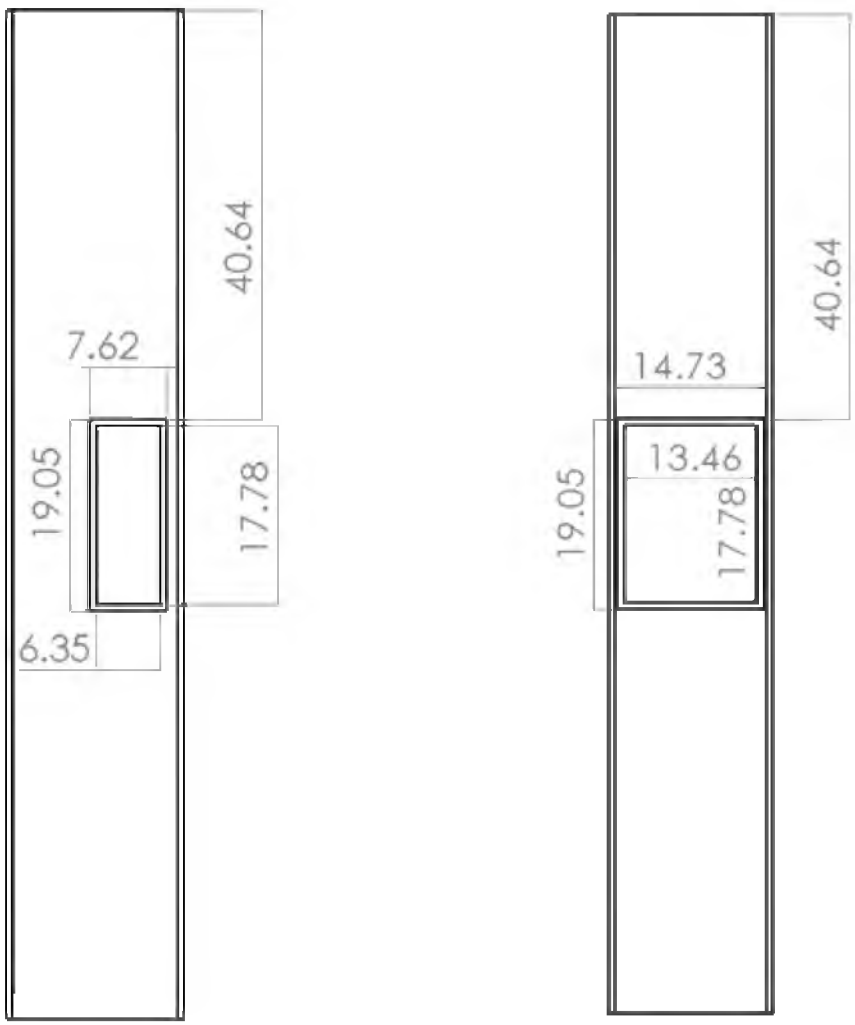

Figure 3.2. SolidWorks drawings of relevent test section sides. a) (left) Bottom side of the test section. b) (right) ”Window side” of the test section.

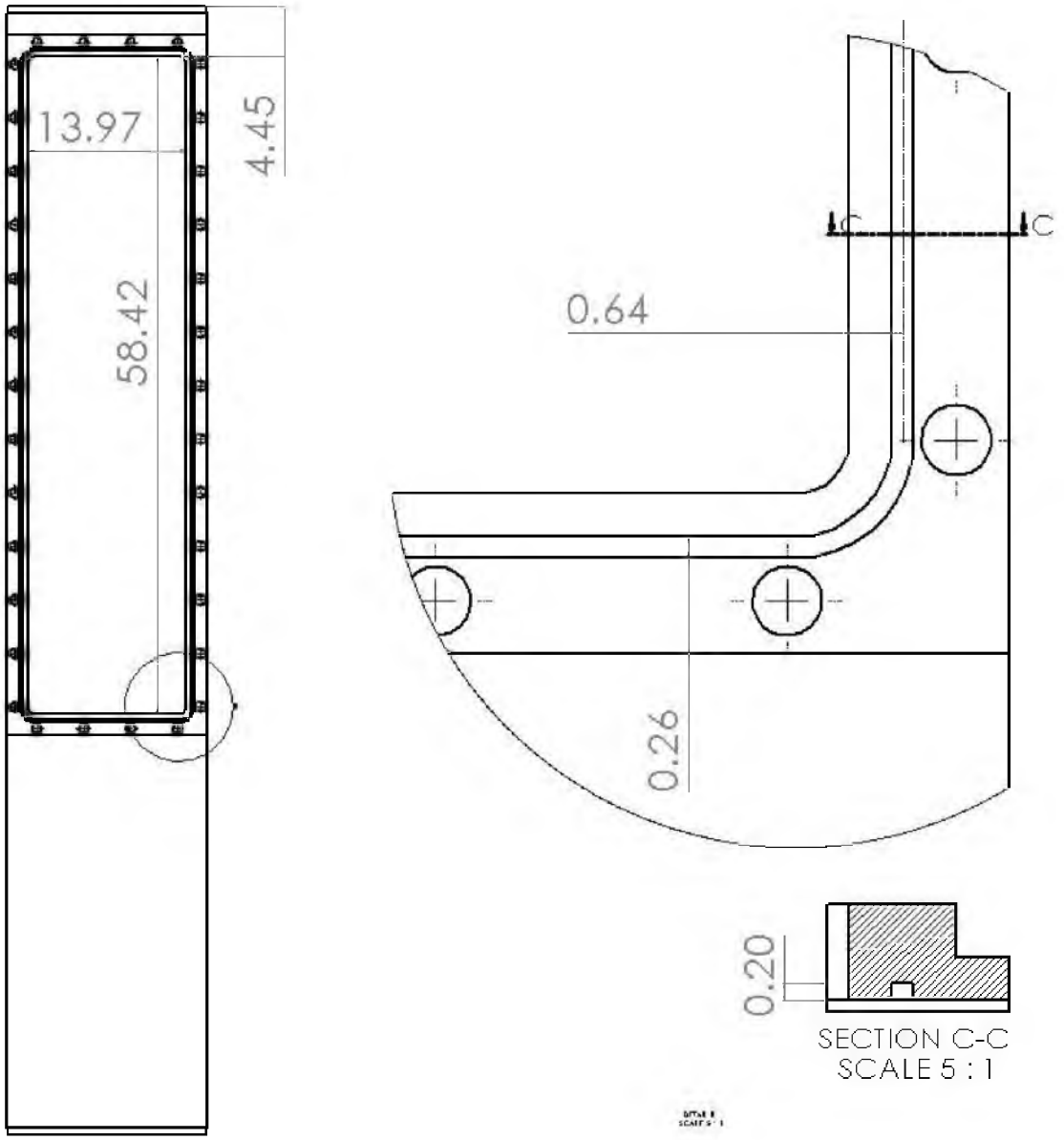

Figure 3.3. SolidWorks drawing of the top of the test section. a) (left) Full view. b) (right) Cutout view showing the dimensions of the O-ring chord channel.

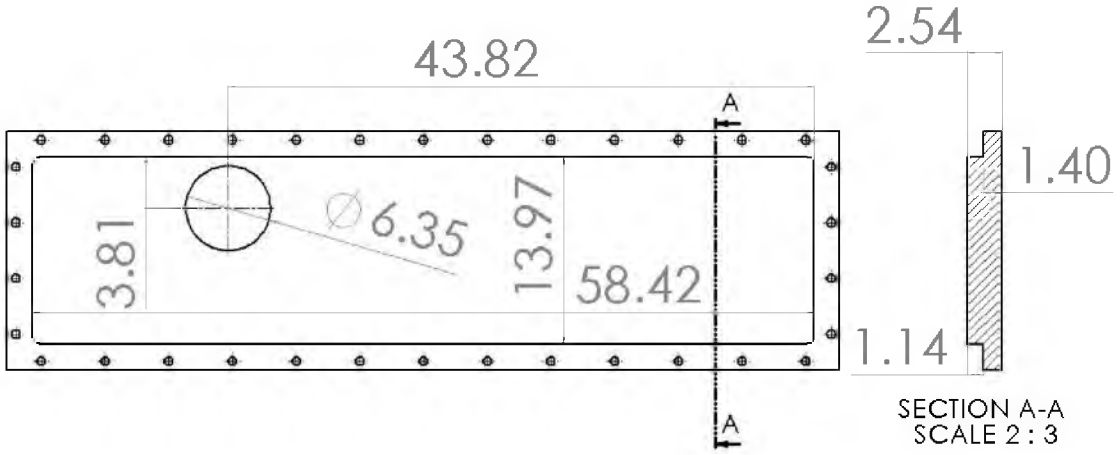

Figure 3.4. SolidWorks drawing of the removable piece designed to fit into the part of the test section depicted in Figure 3.3.

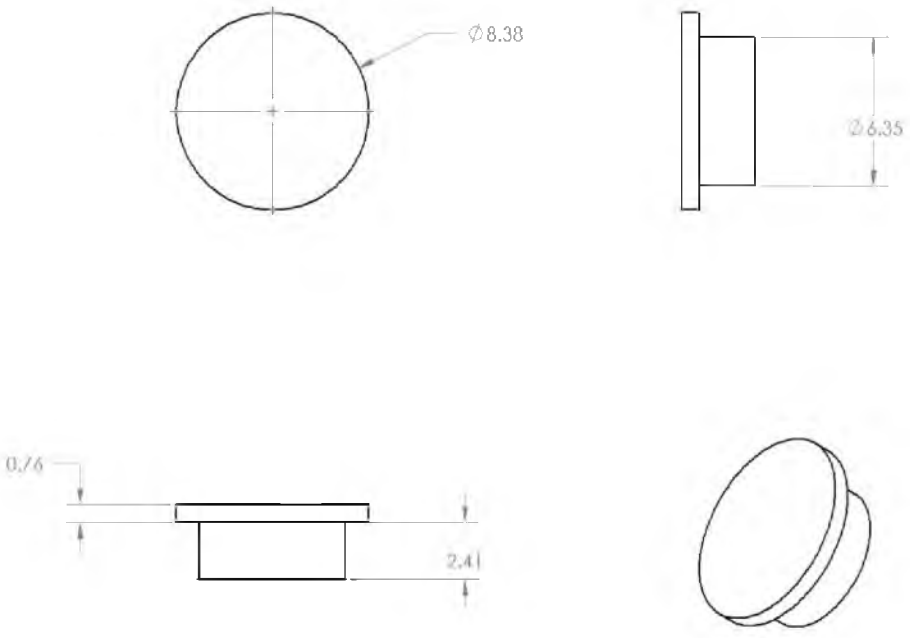

Figure 3.5. Cylindrical piece used to attach the hydrofoil to the test section and manipulate its location/orientation.

Figure 3.6. Image of hydrofoil profile with dimensions (in cm) shown.

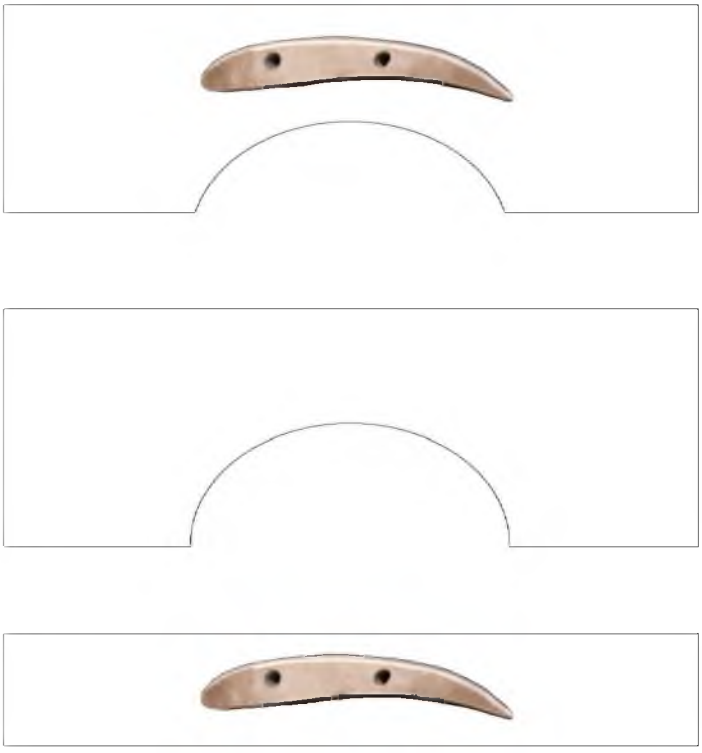

Figure 3.7. Three part schematic cross-sectional view to illustrate what the characterstic velocity represents. a) (top) Experimental set-up. b) (middle) Experimental set-up without hydrofoil in it, used to determine a characteristic velocity. c) (bottom) View if cross-sectional area was constant.

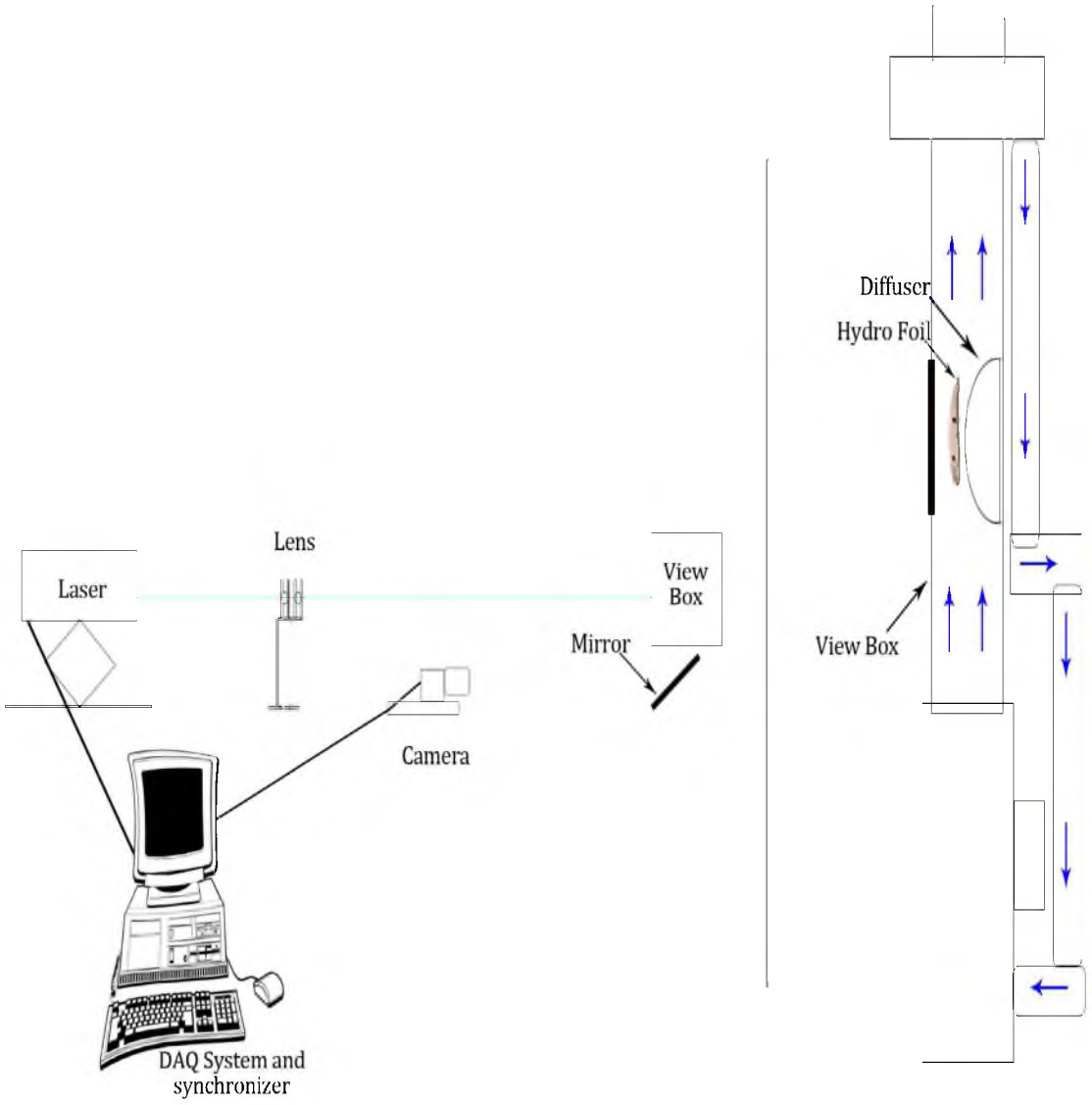

Figure 3.8. Schematic of the experiment and data acquisition system (computer image used from http://library.albany.edu/usered/webeval/images/computer.gif).

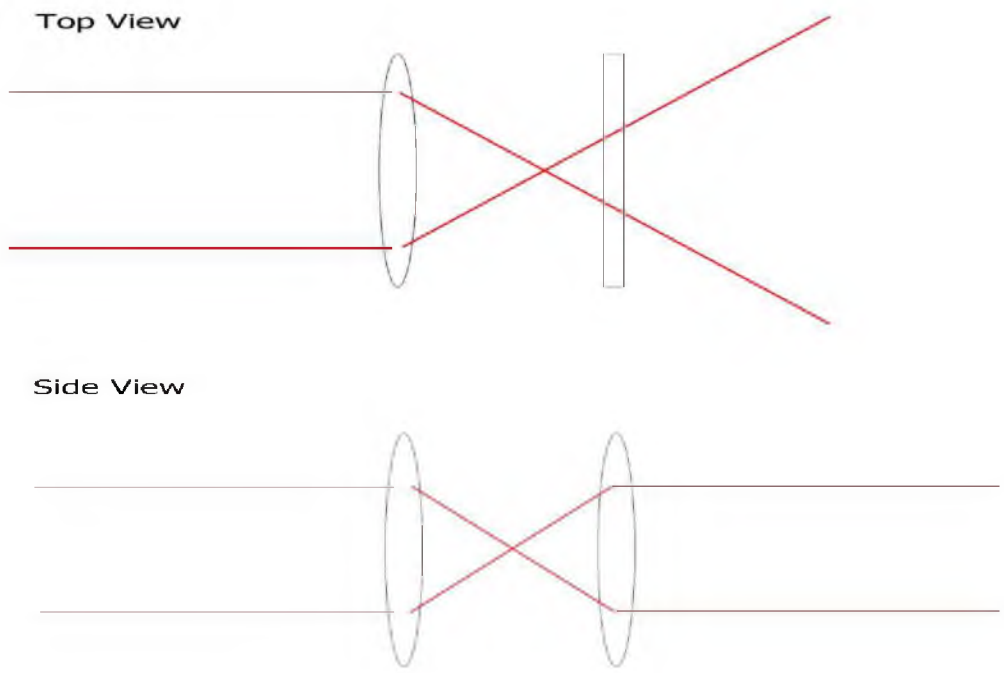

Figure 3.9. Simplified diagram of lens setup depicting how the laser beam was refocused into a sheet using two lenses.

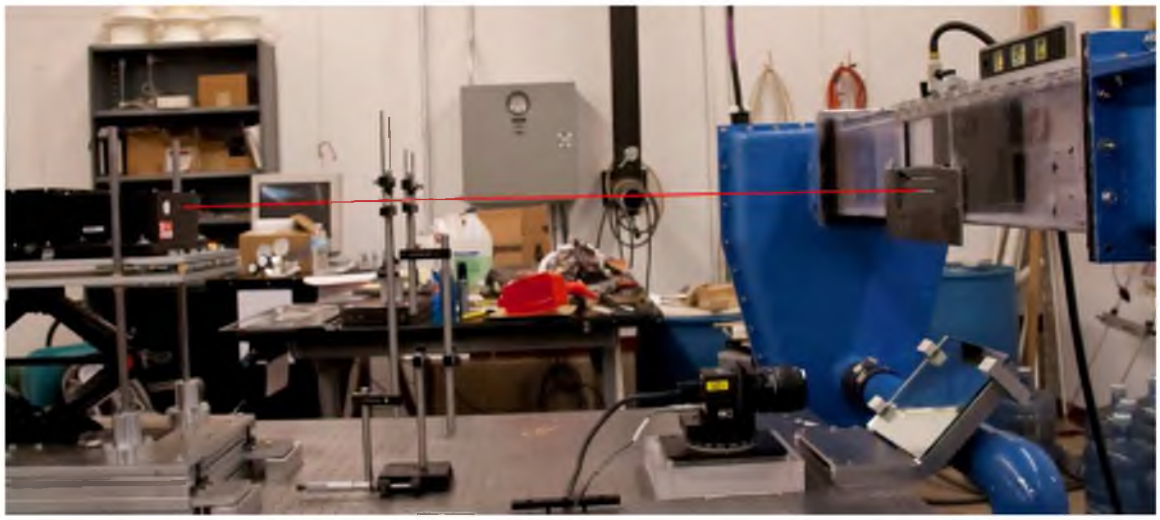

Figure 3.10. Side view of the experimental setup with an illustration of the laser beam/sheet.

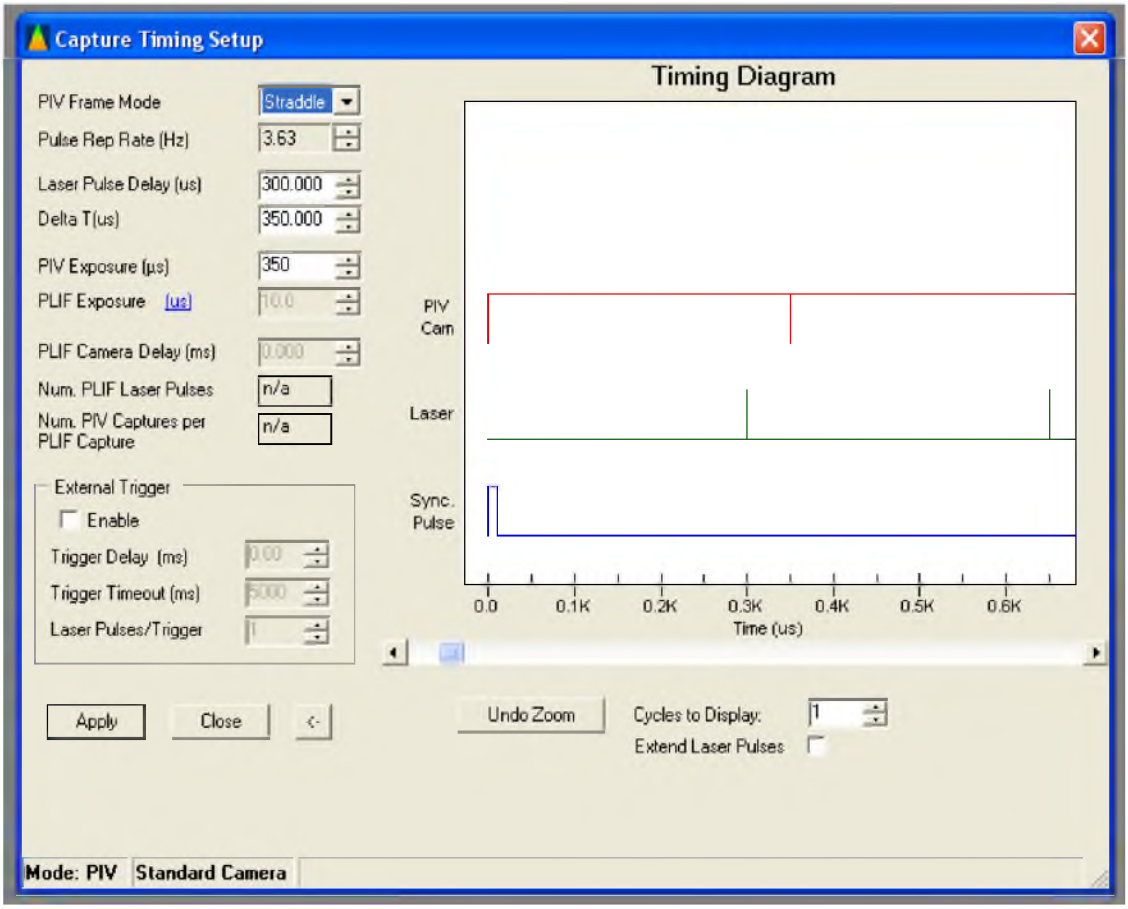

Figure 3.12. Screenshot of the timing setup window from T.S.I.'s Insight software for the experiment.

CHAPTER 4

RESULTS AND DISCUSSION

4.1 Preliminary Results

4.1.1. Results for Determination of Characteristic Velocity

The characteristic velocity used for the Reynolds number was determined by finding the maximum velocity at the apex of the diffuser without an airfoil in the test section. It was used, along with the nominal chord length and a standard value of the kinematic viscosity of water at room temperature, to determine a characteristic Reynolds number for this experiment. These data are summarized in Table 4.1 (note that the characteristic velocity shown here was only used to calculate a representative Reynolds number, it was not used to normalize any values).

4.1.2 Results for Normalizing Velocities

Before plotting, all data were normalized by the characteristic velocity specific to each experiment. The value was determined by finding the mean velocity (magnitude) over a certain length in the entrance area of each data set. The location of this line is shown in the choice code plots (the low roughness data set for these are plotted in Figure 4.1-3, and all of them can be found in the Appendix).

When rounding to two significant figures, no apparent pattern can be seen in characteristic velocity between the different roughnesses. There is an expected monotonic

increase in velocities from 0° to 17°, as the cross-sectional area through which the fluid is forced is smaller for larger angles of attack (even though the increase in head loss causes a lower pump head for the same pump frequency). All of the normalizing velocities have been summarized in Table 4.2. For the velocity contour from the data set taken with no hydrofoil, the normalizing velocity used was 0.42 ms^{-1}.

Depending on the units of the results presented, flow quantities in this work have been normalized by one of four values. The velocity results have been normalized by the values presented in Table 4.2. Other normalizing factors can be found in Tables 4.3 through 4.5. In each case, the appropriate normalizing values used are indicated. In the case of Tables 4.3 and 4.5, the nominal chord length is also used. Because Tables 4.4 and 4.5 contain the square of the normalizing velocity, the differences are greater between each experiment than those found in Table 4.2.

4.2 Relevant Equations and Terms

4.2.1 RANS Equations and Reynolds Stress Terms

This section presents the terms that were used to evaluate the results of the experiment, beginning with the basic equations of motion.

Recall from Section 2.2.1 the following Equations (2.6)

$$\frac{\partial \overline{u_i}}{\partial t} + \overline{u_i}\frac{\partial \overline{u_i}}{\partial x_j} + \frac{\partial}{\partial x_j}\left(\overline{u_i' u_j'}\right) = -\frac{1}{\rho}\frac{\partial \overline{p}}{\partial x_i} + \nu\frac{\partial^2 \overline{u_i}}{\partial x_j \partial x_i} \tag{4.1}$$

Written in index notation, Equation 4.1 represents a set of equations. For this experiment, it is assumed that the flow is statistically steady, and *only two dimensions are considered.* Using these assumptions, the *x* and *y* components of Equation 2.6 may be rewritten as Equations 4.2 and 4.3

$$\overline{u}\frac{\partial \overline{u}}{\partial x}+\overline{v}\frac{\partial \overline{u}}{\partial y}+\frac{\partial}{\partial x}\left(\overline{u'^2}\right)+\frac{\partial}{\partial y}\left(\overline{u'v'}\right)=-\frac{1}{\rho}\frac{\partial \overline{p}}{\partial x}+\nu\frac{\partial^2 \overline{u}}{\partial x\partial x}+\nu\frac{\partial^2 \overline{u}}{\partial y\partial y}, \tag{4.2}$$

$$\overline{u}\frac{\partial \overline{v}}{\partial x}+\overline{v}\frac{\partial \overline{v}}{\partial y}+\frac{\partial}{\partial y}\left(\overline{v'^2}\right)+\frac{\partial}{\partial x}\left(\overline{u'v'}\right)=-\frac{1}{\rho}\frac{\partial \overline{p}}{\partial y}+\nu\frac{\partial^2 \overline{v}}{\partial x\partial x}+\nu\frac{\partial^2 \overline{v}}{\partial y\partial y}. \tag{4.3}$$

The viscous terms on the right-hand side of the equation are generally considered to be negligible away from the wall and were dropped.

When experimentally computing terms in Equations 4.2 and 4.3, it is necessary to also include a term that accounts for the sum of all errors in the measurements, errors in computations, as well as the contributions from any neglected terms. Here, this term is defined as ϵ. All of the terms in Equations 4.2 and 4.3 can be calculated directly from the experimental data except for the pressure gradient terms. Equations 4.2 and 4.3 are rearranged to put the unknown values on the left-hand side and the values that are directly calculated from the data set on the right-hand side to form Equations 4.4 and 4.5

$$\underbrace{-\frac{1}{\rho}\frac{\partial \overline{p}}{\partial x}+\epsilon}_{I}=\underbrace{\overline{u}\frac{\partial \overline{u}}{\partial x}}_{II}+\underbrace{\overline{v}\frac{\partial \overline{u}}{\partial y}}_{III}+\underbrace{\frac{\partial}{\partial x}\left(\overline{u'^2}\right)}_{IV}+\underbrace{\frac{\partial}{\partial y}\left(\overline{u'v'}\right)}_{V}, \tag{4.4}$$

$$\underbrace{-\frac{1}{\rho}\frac{\partial \overline{p}}{\partial y}+\epsilon}_{VI}=\underbrace{\overline{u}\frac{\partial \overline{v}}{\partial x}}_{VII}+\underbrace{\overline{v}\frac{\partial \overline{v}}{\partial y}}_{VIII}+\underbrace{\frac{\partial}{\partial y}\left(\overline{v'^2}\right)}_{IX}+\underbrace{\frac{\partial}{\partial x}\left(\overline{u'v'}\right)}_{X}. \tag{4.5}$$

Terms I and VI are the pressure gradient terms, and represent a pressure gradient in each direction normalized by the fluid density (the accumulated sum of all errors are also in these terms). Terms II, III, VII, and VIII represent advection of mean momentum in the flow. Terms IV and IX represent the gradient of normal Reynolds stress in the flow, and terms V and X represent the gradient of Reynolds sheer stress in the flow.

The problem that becomes apparent when looking at the left-hand of Equation 4.4 and 4.5 is the fact that there are two terms for which no data directly exists, the pressure gradient terms and the cumulative error term. Without knowing the exact error for each measurement, it is not possible to quantify the error propagated into each term, and therefore, the relative magnitude of the error term compared to the pressure gradient term cannot be estimated. While this method is employed in this thesis to estimate the pressure gradients, this error must be kept in mind.

Note the terms inside the derivatives on the right-hand side of Equations 4.4 and 4.5. In terms II, III, VII, and VIII, the mean velocity in the streamwise and cross-flow direction are present. In terms IV, V, IX, and XI, the following three terms are present: $\overline{u'^2}$, $\overline{v'^2}$, and $\overline{u'v'}$. These three terms are the time-averaged elements of the Reynolds stress tensor, and represent the streamwise Reynolds normal stress, cross-flow Reynolds normal stress, and Reynolds sheer stress, respectively. In addition to the RANS terms themselves, all of these additional values are plotted and considered, with special attention given to the results of the Reynolds stress tensor values.

4.3 Final Results

In this chapter, we summarize typical results from the complete experimental matrix. Because of the nature of the nonsymmetrical geometry and the large quantity of data, the majority of the results are graphical. However, some direct quantification was done and is discussed more at the end of this section. All figures not in the main body of the thesis can be found in the Appendix. In each case, the x and y-axis are normalized by nominal chord length, and the origin of the x-y plane is set at the approximate location of the trailing edge of the hydrofoil. For the figures related to the data set with no hydrofoil

present, the origin is set at the bottom left corner. Each quantity is normalized by an appropriate value. We assume that in confined flow, the surrounding environment plays an important role in the governing physics, which is why a coordinate system relative to the direction of flow in the test section is used, not a coordinate system relative to the hydrofoil surface (tangential/normal).

In each contour plot, the range of values was manually set to find a meaningful range for the data, as well as to ensure that any plots being compared were on the same scale. Sometimes, because of either noise or small areas where values were much greater in magnitude than others, values in the plot are outside of the range of the scale of the figure. MATLAB's convention for this is to show empty (white) spots anywhere a value is *below* the *lowest* end of the range, and dark red anywhere a value is *above* the *highest* end of the range. The areas that fall below the range are much easier to identify, as the white color is of sharp contrast to dark blue values of the bottom end of the scale that surround it. The areas that fall above the range can be difficult to identify as the red is the same color as the high end of the range, and thus they are only identifiable if they are of a certain size.

An important limitation of this work is the lack of data taken within the boundary layer, since the boundary layer dynamics play an important role in separation and other statistics downstream. Assumptions are made about the behavior inside the boundary layer when possible based on the surrounding flow field, especially with regards to the point of separation.

For each angle of attack, three roughness values were used. Throughout this thesis, they will be referred to as 'low roughness,' 'medium roughness,' and 'high roughness.' These correspond to RR_s $1.26 \cdot 10^{-3}$, RR_s $1.85 \cdot 10^{-3}$, and RR_s $2.12 \cdot 10^{-3}$, respectively.

For this thesis, the terms 'delayed' and 'hastened' are used to describe the relative change in location of separation for different roughness values. They are *only* used to compare different roughnesses for the same geometry, never to compare between different geometries. The term 'delayed' separation will be used to mean the point of separation is *farther* down the surface of the hydrofoil, or closer to the trailing edge. The term 'hastened' separation will mean the opposite.

Because of the nature of the nonsymmetrical geometry and the two-dimensional vector fields that comprised the results of this experiment, it is not possible to quantify any one value that 'represents' or is 'characteristic' of a data set such as is typically done for direct comparison. For this type of experiment and the data taken, graphical results were much more informative. However, for each geometry, four unique points were chosen that characterize the experiment for directly comparable quantitative analysis. These values have been tabulated and are shown in this chapter to *supplement* the figures. Figures 4.1-3 show where these four points are for each geometry using the normalized velocity magnitude contour plots for the medium roughness experiments to give context (note that the points are the same for every quantity calculated). The coordinates of these points are found in Table 4.6.

It is important to keep in mind that while all of the flow quantities considered were tabulated in this manner, the values are not always instructive or meaningful. In many cases, for instance, changes in the flow pattern between different roughness values caused

the maximum or minimum to be in different areas. Some cases where they were meaningful are discussed here, but this discussion is not exhaustive.

4.3.1 "Choice Code" Contour Plots

Figures 4.4-6 contain contour plots that represent the 'quality' of data at each point for all of the low roughness values. There is very little difference amongst most of them, aside from a few more "no-data" regions in the medium roughness experiments. Hence, only one set is shown here (all can be found in the Appendix). These are referred to as "Choice Code" contour plots because they are primarily determined by what TSI's software Insight calls "choice codes," which is Insight's way of indicating whether or not a vector is spurious. Insight is able to filter out about 95% of spurious vectors during its initial processing phase (TSI Inc., 2011, pp. 10-30). Further vector field validation can filter out most of the remaining spurious vectors. Regardless of whether a vector was determined spurious by Insight or during postprocessing steps in MATLAB, the value of the choice code is set to zero for that instantaneous vector (and one if it is not spurious). This binary quality control system is used to filter out spurious vectors from the mean data sets. In addition, the mean of the choice code value at each point was determined, and this is what is plotted. Note that points below 75% 'good' vectors were considered bad points and filtered out of any mean data sets. These plots also indicate the location of the three points chosen to test convergence statistics, as well as the line from which the normalizing velocity for each data set was determined.

For the most part, data were either above 90% good or far below the 75% threshold. Most of the data inside the area considered resulted in good vectors, with a few exceptions. In every experiment, there were isolated pockets of bad data in the

downstream area adjacent to the diffuser. These were approximately in the same locations in all data sets, and it is likely they were a result of burnt pixels in the digital camera from previous use. For the medium roughness experiments, the higher reflectivity of the hydrofoil required the light intensity be turned lower. Because of this, background subtraction was not possible on these data sets, as it resulted in the loss of a large amount of good data. These data sets were just as good as the others except in the very small area right at the inlet of the camera view, and in the case of the 0° experiment, a small section right near the hydrofoil (both of these instances can be clearly seen on the choice code plots).

4.3.2 Convergence Plots

Convergence plots for each experiment (including the data set without a hydrofoil in it) can be found in the Appendix for $\overline{u'^2}$. A convergence plot for the high roughness experiment at 17° (chosen randomly) has also been included in this section (Figure 4.7) as an example. With very few exceptions, all of the plots looked very similar. Because there is no clear precedent on how many images to take for such an experiment of this nature to achieve satisfactory convergence, values were chosen with the intention of exceeding the amount needed. These values of 4500 images for the 0° experiments, 5500 images for the 10° experiments, and 7000 images for the 17° experiments (and 1000 images for the data set without an airfoil) were chosen based on the amount of available space while considering that the higher angles of attack would likely result in increased turbulence, and therefore require more images to converge.

The results shown in the Appendix for $\overline{u'^2}$ show excellent convergence, usually long before the last image. In the few examples where there continued to be 'creep', such as

point 1 of the medium roughness experiment at 0°, the scale is much smaller than the other points. In general, convergence at all points was satisfactory, and in most cases excellent.

4.3.3 Mean Velocity

For all instances, the mean velocity has been normalized by the value found in Table 4.2 for V_∞

$$\bar{V}^* = \frac{\bar{V}}{V_n}, \tag{4.6}$$

$$\bar{u}^* = \frac{\bar{u}}{V_n}, \tag{4.7}$$

$$\bar{v}^* = \frac{\bar{v}}{V_n}. \tag{4.8}$$

For this thesis, mean velocity results are shown three different ways: contour plots, velocity profiles, and streamlines. All three of these are plotted in this section. For the experiment in which no hydrofoil was present, all three contours provide an indication of the effect the diffuser has on the flow without a hydrofoil (see Figures 4.8-10). In most of the camera view, the flow is very steady above the diffuser, with a very noticeable boundary layer in the near wake of the diffuser (this can be seen most easily by looking at the magnitude contour plot, or Figure 4.10). The $\bar{v}^*$V-bar' contour plot (Figure 4.9) shows a steady negative velocity indicative of a negative pressure gradient in the area just downstream of the diffuser. The $\bar{u}^*$U-bar' contour in Figure 4.8 shows a generally steady flow other than near the diffuser.

4.3.3.1 0° Angle of Attack

For the experiments at an angle of attack of 0°, differences are minimal across the three roughnesses. The streamline plots (Figures 4.11-13) indicate that the flow does not separate from the airfoil for any of the roughness considered. Figures 4.14-16 show velocity profiles, separated into two images to emphasize the area above the hydrofoil and the area below the hydrofoil separately. The only distinguishable difference observed is that $\bar{u}^*$ is smaller in the area directly near the trailing edge above the air foil for higher roughnesses, perhaps indicative of an extended boundary layer that is smaller with higher roughnesses. The magnitude of the velocity deficit in the near wake of the foil also appears to be inversely related to the roughness. These observations are also apparent when looking at the contour plots for this experiment (Figures 4.17-4.19 for $\bar{u}^*$, Figures 4.20-4.22 for $\bar{v}^*$, and Figures 4.23-4.25 for $\bar{V}^*$)

Table 4.7 shows the selected values for normalized velocities at 0°. For these, all but point 2 suggest meaningful information. For instance, the values of $\bar{\boldsymbol{u}}^*$ in the exit area of the pressure side (point 1) are decreasing with increasing roughness, whereas 0.2 chord lengths downstream (point 3), they are increasing with increasing roughness. This confirms what was observed visually, that the roughness is decreasing the velocity deficit in the wake region. The value $\bar{u}^*$ right above the trailing edge (point 4) is 42% higher for the high roughness than the low, showing the effect roughness might have to reduce the size of the extended boundary layer here.

4.3.3.2 10° Angle of Attack

For the 10° degree experiments (Figure 4.26-28), the flow does not appear to separate for the lower or medium roughness, but does appear to *possibly* separate for the higher roughness, as there is a clear recirculation region near the trailing edge. The velocity profiles (Figures 4.29-31) suggest the opposite phenomenon is occurring in the area above and just upstream of the trailing edge, as the velocity deficit in this area increases with increasing roughness. This suggests that the higher roughness could be increasing the size of the extended boundary layer rather than decreasing it.

The $\bar{u}^*$ plots (Figures 4.32-34) show that at the highest roughness, there is actually an area of negative streamwise vorticity right above the tip of the trailing edge, indicating a complete wake region that might be indicative of separation near the edge (Figures 4.35-37). The $\bar{v}^*$ plots show a significant decrease of negative values for the highest roughness. The $\bar{V}^*$ plots show an increase in the velocity deficit region both downstream of and above the trailing edge with increasing roughness.

Table 4.8 shows the selected values for normalized velocities at 10°. Point 3 and point 4 show how much greater the velocity deficit downstream of and above the hydrofoil is for the high roughness than the low roughness—over 75% less velocity by magnitude downstream and over 78% less above the leading edge.

4.3.3.3 17° Angle of Attack

For the 17° angle of attack experiments, there is an inverse relationship between roughness and the length downstream along the hydrofoil that the boundary layer travels before separating, which can be observed and even somewhat quantified with the streamline plots (Figures 4.41-43). For the low roughness case, there is no clear evidence

of separation, although much like with the 10° high roughness case, there likely could be very close to the trailing edge. The medium roughness 17° experiment is the first one where clear evidence exists that separation has occurred upstream of the trailing edge. Unfortunately, because the leading edge is not in the field of data collection, these points cannot be quantified in the typical fashion of distance from the leading edge. Instead, their location in relation to the trailing edge can be estimated. This location is estimated on both the medium and high roughness plots (and marked with a green dot). For the medium roughness, the separation point is approximately 0.450 chord lengths from the trailing edge, while the high roughness separates approximately 0.589 chord lengths from the trailing edge. The velocity profiles (Figures 4.44-46) also suggest this separation by showing negative streamwise velocity that suggests a recirculation region (this can also be seen in the $\bar{u}^*$ plots in Figures 4.47-49).

The $\bar{v}^*$ contour plots (Figures 4.50-52) show that for the low roughness, all of the velocity movement was negative, or moving downward relative to the figure. For the other two roughnesses, there was actually more negative movement than positive, even a little bit above the hydrofoil. In both higher roughness plots there is a region of strong positive $\bar{v}^*$—it appears to be near max for the plot, or about 0.25. This suggests that there is a region of very low pressure advecting from the suction side surface of the hydrofoil, and as the flow exits from beneath the pressure side, it flows into this region. The magnitude contour plots ($\bar{V}^*$) are show in Figures 4.53-55.

Table 4.9 shows the selected values for normalized velocities at 17°. Because there was a completely different flow pattern observed for the low roughness and the other two, comparisons of some of these values between the low and medium or low and high

roughness should be done with care. It does show, however, that at every point, the values of $\bar{v}^*$ is higher for both medium and high roughness than it is for the low roughness. Also, the value of velocity magnitude ($\bar{V}^*$) is less at point 2 for both higher roughnesses, which supports the idea that this is a low-pressure recirculation region for the two higher roughness values.

4.3.4 Mean Vorticity Contours

Mean vorticity contours are plotted in Figures 4.56-64. In these two-dimensional vorticity plots, clockwise rotations are negative and counterclockwise rotations are positive. These values of normalized mean vorticity ($\overline{\omega_z}^*$) were calculated from the mean vector data and normalized by dividing by the values in Table 4.3 (see Equation 4.9)

$$\overline{\omega_z}^* = \frac{\overline{\omega_z} \cdot c}{V_{in}}. \tag{4.9}$$

Table 4.9 shows the selected values for normalized mean vorticity ($\overline{\omega_z}^*$) for all angles of attack.

The best evidence of the effects of roughness on vorticity is observed in the 0° experiment. There is a region of clockwise (negative) vorticity concentrated on the top (suction side) of the hydrofoil near the trailing edge, and a region of counterclockwise (positive) vorticity in the jet region below the hydrofoil (pressure side). The magnitude for both of these vorticity regions decreases monotonically with increasing roughness. Point 1 is near neutral when compared with the rest of the image as it is two orders of magnitude smaller, but it does indicate that the vorticity in this region went from clockwise to counterclockwise with increasing rotation. Point 4 is the best located to

accurately measure the change in vorticity (on the suction side)— $-1.86 \cdot 10^{-2}$ in the low roughness to $-0.69 \cdot 10^{-2}$ in the high roughness, for a decrease in magnitude of 63%.

For the 10° experiments (Figures 4.59-61), the opposite trend is observed. There is a region of negative vorticity observed on the suction side near the trailing edge, but its magnitude is relatively small and it is not easily discernible how much it changes from one roughness to another. The values for point 4 do not show a consistent trend and are a level of magnitude smaller than the scale of the graph. There is a concentrated area of positive vorticity observed on the pressure side jet, and it clearly increases in magnitude monotonically from the smoothest to the roughest case. The location of maximum vorticity in this area moves around, so the table does not give good information as to how much. However, based off of the colorbar, the low roughness does not exceed 0.03, whereas the high roughness has a small area that hits or even exceeds the maximum scale for these plots (0.045). Also, this jet appears to be curling upward toward the flow on the suction side for the high roughness experiment in a way that it is not doing for the other two, suggesting the possibility of a recirculation region here.

For the 17° case, separation definitely occurs for the higher roughnesses but not the low roughness. As a result, the low roughness case cannot be reasonably compared to the other two because the separation dominates the local vorticity However, the flow pattern for the two higher roughnesses is fairly consistent, so meaningful comparisons can be made between them. In this case, in contrast to the 10° experiments, the magnitude of the jet appears smaller for the high roughness than it does for the medium roughness. The location of these maxima in the jets was not consistent. The table values do not necessarily reflect these magnitudes; the value of the medium roughness is clearly above

the 0.045 max in the colorbar, whereas the high roughness case appears to max out at about 0.04.

4.3.5 Reynolds Stress Contours

The Reynolds stress tensor when broken down into its components in two-dimensions has three terms: Reynolds normal stress in the streamwise direction ($\overline{u'^2}$), Reynolds normal stress in the cross-flow direction ($\overline{v'^2}$), and Reynolds shear stress ($\overline{u'v'}$). Gradients of these terms are in the RANS equations, but there is also value in analyzing the terms themselves as they generally represent important characteristics of turbulence. For the analysis in this section, the Reynolds stresses have been averaged over all images at each vector location and normalized by dividing by the values in Table 4.4

$$\overline{u'^2}^* = \frac{\overline{u'^2}}{V_n{}^2}, \tag{4.10}$$

$$\overline{v'^2}^* = \frac{\overline{v'^2}}{V_n{}^2}, \tag{4.11}$$

$$\overline{u'v'}^* = \frac{\overline{u'v'}}{V_n{}^2}. \tag{4.12}$$

Figures 4.65-73 show $\overline{u'^2}^*$, Figures 4.74-82 show $\overline{v'^2}^*$, and $\overline{u'v'}^*$ are shown in Figures 4.83-4.91. Values at select points are tabulated in Tables 4.8, 4.9, and 4.10 for 0°, 10°, and 17° experiments, respectively.

The Reynolds stress contours for the 0° experiments demonstrate an apparent inverse relationship between roughness and turbulence. This pattern is evident when looking at all three of the Reynolds stress terms. Looking at the values in Table 4.11 for point 4

illustrates this best, as all three values decrease steadily in magnitude from low to high roughness: $\overline{u'^2}^*$ decreases from $5.50 \cdot 10^{-2}$, to $3.50 \cdot 10^{-2}$, to $1.52 \cdot 10^{-2}$ from highest to lowest roughness; $\overline{v'^2}^*$ decreases from $4.47 \cdot 10^{-2}$, to $3.07 \cdot 10^{-2}$, to $1.67 \cdot 10^{-2}$; and $\overline{u'v'}^*$ decreases (in magnitude) from $-2.54 \cdot 10^{-2}$, to $-1.44 \cdot 10^{-2}$, to $-0.57 \cdot 10^{-2}$ from highest to lowest roughness. The monotonic pattern from smooth to rough is not as clear in the 10° degree Reynolds stress contour plots, although there is some evidence of it. For instance, looking at Table 4.12, the value of $\overline{u'v'}^*$ at point 3 decreases (in magnitude) from $-1.11 \cdot 10^{-2}$, to $-0.65 \cdot 10^{-2}$, to $0.3 \cdot 10^{-2}$ from highest to lowest roughness, even becoming ever so slightly positive at the high roughness. The negative Reynolds shear stress emanating from the suction side has a smaller magnitude (point 4) for the high roughness experiment ($-4.20 \cdot 10^{-2}$) than it does for the low roughness experiment ($-4.20 \cdot 10^{-2}$), while the negative Reynolds shear stress in the pressure-side jet region (point 1) is much greater in magnitude at the high roughness ($-4.19 \cdot 10^{-2}$) compared to the low roughness ($-0.96 \cdot 10^{-2}$). This relationship is also observed in the $\overline{u'^2}^*$ and $\overline{v'^2}^*$ contours—in general, the early separation of the roughest case causes smaller turbulence on the suction side of the hydrofoil and immediately downstream.

As with other quantities, the Reynolds stresses for the 17° low roughness case cannot be compared to the other two roughnesses because the higher roughnesses separate and the low one does not. These values at specific points are tabulated in Table 4.13, although more can be learned from looking at the relative magnitudes of the plots in this case. Every value is higher in the rougher case both downstream in the wake region and above the hydrofoil on the pressure side nearer the leading edge.

4.3.6 RANS Terms Contours

The terms of the RANS equations in the *x* and *y* direction are plotted in the Appendix, as well as some conglomerate figures in this section. The values at specific points, although of lesser value than for the other terms because of the noise inherent, are plotted in Tables 4.14 through 4.19. Table 4.20 is a summary of their exact figure numbers for reference, and some of them have been shown in this section as well for discussion. The equations are restated in Equation 4.13 and Equation 4.14 (from Equation 3.3 and Equation 3.4)

$$\underbrace{-\frac{1}{\rho}\frac{\partial \overline{p}}{\partial x}}_{I} + \epsilon = \underbrace{\overline{u}\frac{\partial \overline{u}}{\partial x}}_{II} + \underbrace{\overline{v}\frac{\partial \overline{u}}{\partial y}}_{III} + \underbrace{\frac{\partial}{\partial x}\left(\overline{u'^2}\right)}_{IV} + \underbrace{\frac{\partial}{\partial y}\left(\overline{u'v'}\right)}_{V}, \tag{4.13}$$

$$\underbrace{-\frac{1}{\rho}\frac{\partial \overline{p}}{\partial y}}_{VI} + \epsilon = \underbrace{\overline{u}\frac{\partial \overline{v}}{\partial x}}_{VII} + \underbrace{\overline{v}\frac{\partial \overline{v}}{\partial y}}_{VIII} + \underbrace{\frac{\partial}{\partial y}\left(\overline{v'^2}\right)}_{IX} + \underbrace{\frac{\partial}{\partial x}\left(\overline{u'v'}\right)}_{X}. \tag{4.14}$$

The units for these terms are normalized by dividing each one by the values in Table 4.5, the results of which are shown in Equation 4.15 and Equation 4.16

$$\underbrace{-\frac{1}{\rho}\frac{\partial \overline{p}^*}{\partial x}}_{I} + \epsilon = \underbrace{\overline{u}\frac{\partial \overline{u}^*}{\partial x}}_{II} + \underbrace{\overline{v}\frac{\partial \overline{u}^*}{\partial y}}_{III} + \underbrace{\frac{\partial}{\partial x}\left(\overline{u'^2}\right)^*}_{IV} + \underbrace{\frac{\partial}{\partial y}\left(\overline{u'v'}\right)^*}_{V}, \tag{4.15}$$

$$\underbrace{-\frac{1}{\rho}\frac{\partial \overline{p}^*}{\partial y}}_{VI} + \epsilon = \underbrace{\overline{u}\frac{\partial \overline{v}^*}{\partial x}}_{VII} + \underbrace{\overline{v}\frac{\partial \overline{v}^*}{\partial y}}_{VIII} + \underbrace{\frac{\partial}{\partial y}\left(\overline{v'^2}\right)^*}_{IX} + \underbrace{\frac{\partial}{\partial x}\left(\overline{u'v'}\right)^*}_{X}. \tag{4.16}$$

In order to compare the contributions from each of the terms on the overall balance, each equation was plotted using the same color scale for a particular angle of attack, the results of which are summarized in Table 4.21. These values have been averaged over all images

at each vector location and normalized by dividing by the values in Table 4.5. Also, recall that these figures were smoothed using a 9-point median windowing method.

4.3.6.1 The RANS Equation in the x-Direction

For all angles of attack, the contours of Term I and Term II are extremely noisy, especially in the area "above" (suction side) the hydrofoil. Because Term I is a summation of the Terms II through V, the noise in Term I can be attributed mainly to Term II—the streamwise advection of mean streamwise velocity. An extreme example (which is plotted in Figure 4.92) shows Term II for low roughness at 0°. The cause of this noise is unknown, although it was thought that the large values of $\overline{u}$ in this area magnifying the noise inherently present in the finite difference derivative term for a value that is changing slowly. In general, Term II and Term III were the dominant terms. Term IV was negligible for most experiments, and Term V had a modest effect in the near wake region.

4.3.6.1.1 0° Angle of Attack

For these experiments, many areas of the contour plot for Term I (outside of the noise) are near zero, or at a smaller magnitude than other terms. The only exception is above the trailing edge, where there are significant negative values between $-1.5 \cdot 10^{-3}$ for the low roughness and $-2.0 \cdot 10^{-3}$ for the high roughness. For the other terms, most of the significant values are near (and downstream of) the trailing edge. The left portion of Figure 4.93 shows a cutout for each term of this area, using the high roughness experiment as an example. As with most of the RANS data, Term II and Term III are the dominant terms for the most part. Notice that the positive values of Term II are mostly

balanced by the negative values of Term III, with a similar relationship occurring between Term IV and Term V. These values balance out, resulting in the small magnitude of Term I. This is important for two reasons: the first being it shows that the pressure gradient term is not dominant; it also serves to further validate the reliability of the RANS data terms as calculated from PIV data.

As with most of the flow quantities from the 0° experiments, all of the RANS terms for the streamwise equation show a monotonic decrease in magnitude with increasing roughness. This phenomenon has been consistently observed in other quantities and shows up in all five terms of the RANS equations considered here. To illustrate the difference between the smoothest and the roughest case, the right side of Figure 4.93 shows the same area of interested mentioned above, but for the high roughness experiment. The negative region for Term III is below the range of the chart ($-2.5 \cdot 10^{-3}$) for the low roughness but between $-2.5 \cdot 10^{-3}$ and $-2.0 \cdot 10^{-3}$ for the high roughness. Likewise, there is a strong positive region for Term II in the low roughness that exceeds $2.0 \cdot 10^{-3}$, but this area is nearly zero (and even slightly negative) for the higher roughness.

4.3.6.1.2 10° Angle of Attack

As with the 0° experiments, the regions above (suction side) the hydrofoil are very noisy. Similarly, as in the 0° experiments, Term I is very small in most areas other than the noise introduced from Term II. Term III has significant values in a slightly larger area than with the 0° experiments, and a small positive jet coming from under (pressure side) the trailing edge of the hydrofoil. Term 4 and Term 5 are still very small compared to the other terms (even relatively smaller, in fact).

Other than the regularly observed pattern of higher roughness values having earlier separation (especially evident in Term II and Term III), there is no really easily defined pattern between the difference roughness values. As such, they have not been plotted in this section.

4.3.6.1.3 17° Angle of Attack

The 17° angle of attack experiments follow the pattern observed above of having the area above (suction side) the hydrofoil dominated by so much noise, no observations can really be made. Because (as was hypothesized above) the noise is mainly due to the large values of streamwise velocity magnifying the noisy derivatives in Term II, the area of noise is not actually the entire area above the hydrofoil, because of the low-velocity area in the wake region above it. As with all of the 17° data, good comparison between the three roughness values is not possible, due to the separation that occurs in the two higher roughness experiments that is not observed in the low roughness experiment.

Comparison amongst the five terms for just the two highest roughnesses does lead to some notable observations. Figures 4.94-96 show cutouts for each term in an area of interest around the near wake region, including near the trailing edge and the diffuser (this is a different, larger area than was investigated for the 0° experiments). In the two higher roughnesses, there are two notable regions where Term II and Term III are significant. Since Term II and Term III mostly balance, comparing just the values of Term III is informative. For the medium roughness, there is a negative stream in the $-1.5 \bullet 10^{-3}$ to $-2.0 \bullet 10^{-3}$ range, and a positive stream around $1.0 \bullet 10^{-3}$. However, in the higher roughness experiment, the negative stream has a maximum around $-1.0 \bullet 10^{-3}$ and the

positive stream below $0.5 \cdot 10^{-3}$. The roughness 'dampened out' the values for these experiments.

4.3.6.2 The RANS Equation in the y-Direction

The pressure gradient term (Term VI) in the y-direction was significant for most of the experiments. Similar to the *x*-direction equation, the term in the equation involving $\overline{u}$ (Term VII) was extremely noisy. In this equation, it was the term involving $\overline{u'v'}$ that was negligible (Term X). However, in both equations, it was the $\frac{\partial}{\partial x}$ of a turbulence quantity that was negligible, suggesting that this was more to do with the change in the *x*-direction being less than the actual turbulence quantities themselves.

4.3.6.2.1 0° Angle of Attack

All of the terms followed the pattern seen in other flow quantities of a monotonic decrease in magnitude with increasing vorticity with one exception: an area of positive values above the trailing edge of the hydrofoil seen in Term VII (and consequently, showing up in Term VI). Figure 4.97 shows a cutout of this area for both terms, with Term VII on the left and Term VI on the right. It is not clear exactly what physical phenomenon is causing this, but because of the sign associated with Term VI, positive values of Term VI indicate a negative vertical pressure gradient in this direction. This region is 'dampened out' by roughness, as the values for Term VI are nearly $-1.5 \cdot 10^{-3}$ for the low roughness but less than $-0.5 \cdot 10^{-3}$ for the high roughness.

4.3.6.2.2 10° Angle of Attack

For these experiments, there is both a strong area of positive and negative pressure gradient above the hydrofoil, similar to the 0° angle of attack but more pronounced. This

is one of the few situations where a term other than Term VII—in this case, term IX—has a meaningful impact on the overall pressure gradient. Figure 4.98 shows the near wake region for Term IX on the left and Term VI on the right to show the effect that term IX is having on the overall pressure gradient.

4.3.6.2.3 17° Angle of Attack

For these, the strong values (up to $1.5 \cdot 10^{-3}$) of Term VII in the jet emanating from the pressure side of the hydrofoil dominated the effect on the pressure gradient as well as everywhere else in the area of interest. Figure 4.99 shows a cutout of this area for both Term VII (left) and Term VI (right) to show that the pressure gradient term is almost entirely resulting from Term VII. As with other quantities, the separating that occurred for the low roughness but not the higher two makes comparison to it difficult. As with other RANS terms, the pressure gradient here (Term VI) is dampened out by the higher roughness, although the effect is less pronounced. Both appear to reach the $1.5 \cdot 10^{-3}$ maximum, but the higher roughness has a smaller area of higher values.

Table 4.1. Parameters used to determine the Reynolds number for the experiment.

Characteristic Velocity	0.486 ms^{-1}
Nominal Chord Length	11.3 cm
Kinematic Viscosity	$1.01 \cdot 10^{-6}$ m^2s^{-1}
Reynolds Number	$\mathbf{5.42 \cdot 10^4}$

Table 4.2. Normalizing velocities used for each of the different experiments. The data under the column labeled "Experiment" indicates the roughness and angle of attack for each case.

Experiment	Velocity (ms^{-1})
RR_s $1.26 \cdot 10^{-3}$ - 0°	0.55
RR_s $1.26 \cdot 10^{-3}$ - 10°	0.57
RR_s $1.26 \cdot 10^{-3}$ - 17°	0.57
RR_s $1.85 \cdot 10^{-3}$ - 0°	0.59
RR_s $1.85 \cdot 10^{-3}$ - 10°	0.61
RR_s $1.85 \cdot 10^{-3}$ - 17°	0.61
RR_s $2.12 \cdot 10^{-3}$ - 0°	0.75
RR_s $2.12 \cdot 10^{-3}$ - 10°	0.72
RR_s $2.12 \cdot 10^{-3}$ - 17°	0.72

Table 4.3. Normalizing values for vorticity, V_n/c.

Experiment	Velocity/Chord (s-1)
RR_s 1.26·10^{-3} - 0°	4.92
RR_s 1.26·10^{-3} - 10°	5.02
RR_s 1.26·10^{-3} - 17°	5.07
RR_s 1.85·10^{-3} - 0°	5.26
RR_s 1.85·10^{-3} - 10°	5.41
RR_s 1.85·10^{-3} - 17°	5.39
RR_s 2.12·10^{-3} - 0°	6.69
RR_s 2.12·10^{-3} - 10°	6.36
RR_s 2.12·10^{-3} - 17°	6.40

Table 4.4. Normalizing values for Reynolds Stresses, $V_n{}^2$.

Experiment	Velocity^2 (m^{2}s^{-2})
RR_s 1.26·10^{-3} - 0°	0.31
RR_s 1.26·10^{-3} - 10°	0.32
RR_s 1.26·10^{-3} - 17°	0.33
RR_s 1.85·10^{-3} - 0°	0.35
RR_s 1.85·10^{-3} - 10°	0.37
RR_s 1.85·10^{-3} - 17°	0.37
RR_s 2.12·10^{-3} - 0°	0.57
RR_s 2.12·10^{-3} - 10°	0.51
RR_s 2.12·10^{-3} - 17°	0.52

Table 4.5. Normalizing values for RANS terms, $V_n{}^2/c$.

Experiment	Velocity^2/Chord (m^{1}s^{-2})
RR_s 1.26·10^{-3} - 0°	2.73
RR_s 1.26·10^{-3} - 10°	2.84
RR_s 1.26·10^{-3} - 17°	2.90
RR_s 1.85·10^{-3} - 0°	3.12
RR_s 1.85·10^{-3} - 10°	3.30
RR_s 1.85·10^{-3} - 17°	3.28
RR_s 2.12·10^{-3} - 0°	5.04
RR_s 2.12·10^{-3} - 10°	4.56
RR_s 2.12·10^{-3} - 17°	4.62

Table 4.6. Locations of "selected" points in normalized Cartesian coordinates from the trailing edge.

			x^*	y^*
0°	Point 1	Exit area of pressure side	0.048	-0.160
	Point 2	Near wake of trailing edge	0.038	-0.030
	Point 3	0.2 x/c downstream of trailing edge	0.198	0.001
	Point 4	Immediately above trailing edge (suction side)	0.002	0.041
			x^*	y^*
10°	Point 1	Exit area of pressure side	0.060	-0.101
	Point 2	Near wake of trailing edge	0.060	-0.026
	Point 3	0.2 x/c downstream of trailing edge	0.201	-0.001
	Point 4	Immediately above trailing edge (suction side)	-0.016	0.060
			x^*	y^*
17°	Point 1	Exit area of pressure side	0.098	-0.080
	Point 2	0.2 x/c downstream and 0.1 y/c above trailing edge	0.199	0.076
	Point 3	Immediately above trailing edge (suction side)	0.053	0.061
	Point 4	Slightly upstream of trailing edge in possible wake region	-0.053	0.151

Table 4.7. Values at selected points for normalized velocities of 0° experiments.

	Roughness	$\bar{u}^*$	$\bar{v}^*$	$\bar{V}^*$
Point 1	Low	0.787	-0.056	0.789
	Medium	0.756	-0.069	0.759
	High	0.749	-0.072	0.752
	Roughness	$\bar{u}^*$	$\bar{v}^*$	$\bar{V}^*$
Point 2	Low	0.265	0.043	0.268
	Medium	0.078	0.003	0.078
	High	0.186	-0.018	0.186
	Roughness	$\bar{u}^*$	$\bar{v}^*$	$\bar{V}^*$
Point 3	Low	0.464	-0.057	0.467
	Medium	0.508	-0.091	0.516
	High	0.584	-0.094	0.592
	Roughness	$\bar{u}^*$	$\bar{v}^*$	$\bar{V}^*$
Point 4	Low	0.407	-0.138	0.430
	Medium	0.577	-0.176	0.604
	High	0.702	-0.172	0.723

Table 4.8. Values at selected points for normalized velocities of 10° experiments.

	Roughness	$\bar{u}^*$	$\bar{v}^*$	$\bar{V}^*$
Point 1	Low	0.756	-0.061	0.759
	Medium	0.701	-0.103	0.709
	High	0.766	-0.041	0.767
	Roughness	$\bar{u}^*$	$\bar{v}^*$	$\bar{V}^*$
Point 2	Low	0.265	-0.054	0.271
	Medium	0.111	-0.031	0.115
	High	0.248	-0.009	0.248
	Roughness	$\bar{u}^*$	$\bar{v}^*$	$\bar{V}^*$
Point 3	Low	0.534	-0.135	0.551
	Medium	0.463	-0.105	0.475
	High	0.133	-0.019	0.134
	Roughness	$\bar{u}^*$	$\bar{v}^*$	$\bar{V}^*$
Point 4	Low	0.665	-0.227	0.703
	Medium	0.551	-0.174	0.578
	High	0.150	-0.024	0.152

Table 4.9. Values at selected points for normalized velocities of 17° experiments.

	Roughness	$\bar{u}^*$	$\bar{v}^*$	$\bar{V}^*$
Point 1	Low	0.831	-0.210	0.857
	Medium	0.855	-0.051	0.857
	High	0.876	-0.065	0.879
	Roughness	$\bar{u}^*$	$\bar{v}^*$	$\bar{V}^*$
Point 2	Low	0.191	-0.103	0.216
	Medium	-0.131	-0.038	0.136
	High	-0.104	-0.037	0.110
	Roughness	$\bar{u}^*$	$\bar{v}^*$	$\bar{V}^*$
Point 3	Low	0.098	-0.055	0.112
	Medium	-0.079	0.016	0.080
	High	-0.133	0.001	0.133
	Roughness	$\bar{u}^*$	$\bar{v}^*$	$\bar{V}^*$
Point 4	Low	0.290	-0.093	0.304
	Medium	0.006	0.036	0.036
	High	-0.072	0.064	0.096

Table 4.10. Values at selected points for normalized vorticity ($\overline{\omega_z}^*$) for all experiments.

	Roughness	0°	10°	17°
Point 1	Low	$-7.02 \cdot 10^{-4}$	$4.52 \cdot 10^{-4}$	$3.42 \cdot 10^{-3}$
	Medium	$0.94 \cdot 10^{-4}$	$0.73 \cdot 10^{-4}$	$0.37 \cdot 10^{-3}$
	High	$2.57 \cdot 10^{-4}$	$2.21 \cdot 10^{-4}$	$1.05 \cdot 10^{-3}$
	Roughness	**0°**	**10°**	**17°**
Point 2	Low	$1.88 \cdot 10^{-2}$	$0.01 \cdot 10^{-2}$	$-3.06 \cdot 10^{-3}$
	Medium	$0.26 \cdot 10^{-2}$	$-0.08 \cdot 10^{-2}$	$-1.78 \cdot 10^{-3}$
	High	$-0.16 \cdot 10^{-2}$	$2.57 \cdot 10^{-2}$	$-0.62 \cdot 10^{-3}$
	Roughness	**0°**	**10°**	**17°**
Point 3	Low	$-2.24 \cdot 10^{-3}$	$-3.34 \cdot 10^{-3}$	$-2.86 \cdot 10^{-3}$
	Medium	$-4.04 \cdot 10^{-3}$	$-6.66 \cdot 10^{-3}$	$-1.37 \cdot 10^{-3}$
	High	$-3.57 \cdot 10^{-3}$	$0.20 \cdot 10^{-3}$	$-0.73 \cdot 10^{-3}$
	Roughness	**0°**	**10°**	**17°**
Point 4	Low	$-1.86 \cdot 10^{-2}$	$-5.56 \cdot 10^{-3}$	$-4.53 \cdot 10^{-3}$
	Medium	$-1.36 \cdot 10^{-2}$	$-8.78 \cdot 10^{-3}$	$-1.85 \cdot 10^{-3}$
	High	$-0.69 \cdot 10^{-2}$	$-7.12 \cdot 10^{-3}$	$-2.04 \cdot 10^{-3}$

Table 4.11. Values at selected points for normalized Reynolds stresses of 0° experiments.

	Roughness	$\overline{u'^2}^*$	$\overline{v'^2}^*$	$\overline{u'v'}^*$
Point 1	Low	$2.87 \cdot 10^{-3}$	$1.20 \cdot 10^{-3}$	$1.31 \cdot 10^{-4}$
	Medium	$3.65 \cdot 10^{-3}$	$1.10 \cdot 10^{-3}$	$-1.65 \cdot 10^{-4}$
	High	$2.97 \cdot 10^{-3}$	$1.06 \cdot 10^{-3}$	$-1.82 \cdot 10^{-4}$
	Roughness	$\overline{u'^2}^*$	$\overline{v'^2}^*$	$\overline{u'v'}^*$
Point 2	Low	$3.70 \cdot 10^{-2}$	$1.57 \cdot 10^{-2}$	$8.57 \cdot 10^{-3}$
	Medium	$1.79 \cdot 10^{-2}$	$1.61 \cdot 10^{-2}$	$1.78 \cdot 10^{-3}$
	High	$1.94 \cdot 10^{-2}$	$1.63 \cdot 10^{-2}$	$-1.42 \cdot 10^{-3}$
	Roughness	$\overline{u'^2}^*$	$\overline{v'^2}^*$	$\overline{u'v'}^*$
Point 3	Low	$2.43 \cdot 10^{-2}$	$3.55 \cdot 10^{-2}$	$-0.99 \cdot 10^{-2}$
	Medium	$2.50 \cdot 10^{-2}$	$2.48 \cdot 10^{-2}$	$-1.25 \cdot 10^{-2}$
	High	$1.83 \cdot 10^{-2}$	$1.51 \cdot 10^{-2}$	$-0.82 \cdot 10^{-2}$
	Roughness	$\overline{u'^2}^*$	$\overline{v'^2}^*$	$\overline{u'v'}^*$
Point 4	Low	$5.50 \cdot 10^{-2}$	$4.47 \cdot 10^{-2}$	$-2.54 \cdot 10^{-2}$
	Medium	$3.50 \cdot 10^{-2}$	$3.07 \cdot 10^{-2}$	$-1.44 \cdot 10^{-2}$
	High	$1.52 \cdot 10^{-2}$	$1.67 \cdot 10^{-2}$	$-0.57 \cdot 10^{-2}$

Table 4.12. Values at selected points for normalized Reynolds stresses of 10° experiments.

	Roughness	$\overline{u'^2}^*$	$\overline{v'^2}^*$	$\overline{u'v'}^*$
Point 1	Low	$2.00 \cdot 10^{-2}$	$1.52 \cdot 10^{-2}$	$-0.96 \cdot 10^{-4}$
	Medium	$1.80 \cdot 10^{-2}$	$1.38 \cdot 10^{-2}$	$0.48 \cdot 10^{-4}$
	High	$3.10 \cdot 10^{-2}$	$0.78 \cdot 10^{-2}$	$-4.19 \cdot 10^{-4}$
	Roughness	$\overline{u'^2}^*$	$\overline{v'^2}^*$	$\overline{u'v'}^*$
Point 2	Low	$1.44 \cdot 10^{-2}$	$1.03 \cdot 10^{-2}$	$-1.73 \cdot 10^{-3}$
	Medium	$0.92 \cdot 10^{-2}$	$0.52 \cdot 10^{-2}$	$0.01 \cdot 10^{-3}$
	High	$3.13 \cdot 10^{-2}$	$0.79 \cdot 10^{-2}$	$4.57 \cdot 10^{-3}$
	Roughness	$\overline{u'^2}^*$	$\overline{v'^2}^*$	$\overline{u'v'}^*$
Point 3	Low	$2.74 \cdot 10^{-2}$	$1.57 \cdot 10^{-2}$	$-1.11 \cdot 10^{-2}$
	Medium	$1.40 \cdot 10^{-2}$	$0.87 \cdot 10^{-2}$	$-0.65 \cdot 10^{-2}$
	High	$1.38 \cdot 10^{-2}$	$1.30 \cdot 10^{-2}$	$0.03 \cdot 10^{-2}$
	Roughness	$\overline{u'^2}^*$	$\overline{v'^2}^*$	$\overline{u'v'}^*$
Point 4	Low	$1.83 \cdot 10^{-2}$	$1.00 \cdot 10^{-2}$	$-7.57 \cdot 10^{-3}$
	Medium	$1.26 \cdot 10^{-2}$	$0.73 \cdot 10^{-2}$	$-6.05 \cdot 10^{-3}$
	High	$1.24 \cdot 10^{-2}$	$0.64 \cdot 10^{-2}$	$-4.20 \cdot 10^{-3}$

Table 4.13. Values at selected points for normalized Reynolds stresses of 17° experiments.

	Roughness	$\overline{u'^2}^*$	$\overline{v'^2}^*$	$\overline{u'v'}^*$
Point 1	Low	$6.65 \cdot 10^{-3}$	$9.89 \cdot 10^{-3}$	$-1.46 \cdot 10^{-4}$
	Medium	$3.18 \cdot 10^{-3}$	$1.97 \cdot 10^{-3}$	$1.54 \cdot 10^{-4}$
	High	$4.87 \cdot 10^{-3}$	$5.29 \cdot 10^{-3}$	$5.13 \cdot 10^{-4}$
	Roughness	$\overline{u'^2}^*$	$\overline{v'^2}^*$	$\overline{u'v'}^*$
Point 2	Low	$5.60 \cdot 10^{-2}$	$3.58 \cdot 10^{-2}$	$-2.22 \cdot 10^{-2}$
	Medium	$1.74 \cdot 10^{-2}$	$1.35 \cdot 10^{-2}$	$-0.25 \cdot 10^{-2}$
	High	$2.90 \cdot 10^{-2}$	$2.11 \cdot 10^{-2}$	$-0.45 \cdot 10^{-2}$
	Roughness	$\overline{u'^2}^*$	$\overline{v'^2}^*$	$\overline{u'v'}^*$
Point 3	Low	$4.07 \cdot 10^{-2}$	$2.57 \cdot 10^{-2}$	$-1.46 \cdot 10^{-2}$
	Medium	$1.07 \cdot 10^{-2}$	$0.56 \cdot 10^{-2}$	$0.05 \cdot 10^{-2}$
	High	$1.60 \cdot 10^{-2}$	$1.04 \cdot 10^{-2}$	$-0.06 \cdot 10^{-2}$
	Roughness	$\overline{u'^2}^*$	$\overline{v'^2}^*$	$\overline{u'v'}^*$
Point 4	Low	$5.83 \cdot 10^{-2}$	$3.73 \cdot 10^{-2}$	$-2.69 \cdot 10^{-2}$
	Medium	$0.73 \cdot 10^{-2}$	$0.58 \cdot 10^{-2}$	$-0.03 \cdot 10^{-2}$
	High	$1.97 \cdot 10^{-2}$	$1.68 \cdot 10^{-2}$	$-0.47 \cdot 10^{-2}$

Table 4.14. Values at selected points for normalized terms of the RANS equations in the *x*-direction of 0° experiments.

	Roughness	$\underbrace{-\frac{1}{\rho}\frac{\partial \overline{p}^*}{\partial x}+\epsilon}_{I}$	$\underbrace{\overline{u}\frac{\partial \overline{u}^*}{\partial x}}_{II}$	$\underbrace{\overline{v}\frac{\partial \overline{u}^*}{\partial y}}_{III}$	$\underbrace{\frac{\partial}{\partial x}\left(\overline{u'^2}\right)^*}_{IV}$	$\underbrace{\frac{\partial}{\partial y}\left(\overline{u'v'}\right)^*}_{V}$
Point 1	Low	$-0.97\cdot10^{-4}$	$-0.39\cdot10^{-4}$	$-3.35\cdot10^{-5}$	$-1.30\cdot10^{-5}$	$-1.09\cdot10^{-5}$
	Medium	$-5.20\cdot10^{-4}$	$-5.20\cdot10^{-4}$	$-0.12\cdot10^{-5}$	$-0.09\cdot10^{-5}$	$0.28\cdot10^{-5}$
	High	$-4.16\cdot10^{-4}$	$-4.13\cdot10^{-4}$	$1.61\cdot10^{-5}$	$-1.72\cdot10^{-5}$	$-0.19\cdot10^{-5}$
	Roughness	$\underbrace{-\frac{1}{\rho}\frac{\partial \overline{p}^*}{\partial x}+\epsilon}_{I}$	$\underbrace{\overline{u}\frac{\partial \overline{u}^*}{\partial x}}_{II}$	$\underbrace{\overline{v}\frac{\partial \overline{u}^*}{\partial y}}_{III}$	$\underbrace{\frac{\partial}{\partial x}\left(\overline{u'^2}\right)^*}_{IV}$	$\underbrace{\frac{\partial}{\partial y}\left(\overline{u'v'}\right)^*}_{V}$
Point 2	Low	$-6.81\cdot10^{-4}$	$3.01\cdot10^{-4}$	$-5.03\cdot10^{-4}$	$0.88\cdot10^{-4}$	$-5.67\cdot10^{-4}$
	Medium	$-1.14\cdot10^{-4}$	$1.22\cdot10^{-4}$	$0.11\cdot10^{-4}$	$2.67\cdot10^{-4}$	$-5.14\cdot10^{-4}$
	High	$0.67\cdot10^{-4}$	$4.91\cdot10^{-4}$	$-0.33\cdot10^{-4}$	$1.82\cdot10^{-4}$	$-5.73\cdot10^{-4}$
	Roughness	$\underbrace{-\frac{1}{\rho}\frac{\partial \overline{p}^*}{\partial x}+\epsilon}_{I}$	$\underbrace{\overline{u}\frac{\partial \overline{u}^*}{\partial x}}_{II}$	$\underbrace{\overline{v}\frac{\partial \overline{u}^*}{\partial y}}_{III}$	$\underbrace{\frac{\partial}{\partial x}\left(\overline{u'^2}\right)^*}_{IV}$	$\underbrace{\frac{\partial}{\partial y}\left(\overline{u'v'}\right)^*}_{V}$
Point 3	Low	$-1.45\cdot10^{-4}$	$5.69\cdot10^{-4}$	$-1.34\cdot10^{-4}$	$-1.56\cdot10^{-4}$	$-4.23\cdot10^{-4}$
	Medium	$0.14\cdot10^{-4}$	$4.81\cdot10^{-4}$	$-3.81\cdot10^{-4}$	$-1.33\cdot10^{-4}$	$0.47\cdot10^{-4}$
	High	$1.84\cdot10^{-4}$	$2.73\cdot10^{-4}$	$-3.52\cdot10^{-4}$	$0.36\cdot10^{-4}$	$2.27\cdot10^{-4}$
	Roughness	$\underbrace{-\frac{1}{\rho}\frac{\partial \overline{p}^*}{\partial x}+\epsilon}_{I}$	$\underbrace{\overline{u}\frac{\partial \overline{u}^*}{\partial x}}_{II}$	$\underbrace{\overline{v}\frac{\partial \overline{u}^*}{\partial y}}_{III}$	$\underbrace{\frac{\partial}{\partial x}\left(\overline{u'^2}\right)^*}_{IV}$	$\underbrace{\frac{\partial}{\partial y}\left(\overline{u'v'}\right)^*}_{V}$
Point 4	Low	$-1.01\cdot10^{-3}$	$1.19\cdot10^{-3}$	$-2.60\cdot10^{-3}$	$-3.12\cdot10^{-4}$	$7.09\cdot10^{-4}$
	Medium	$-1.57\cdot10^{-3}$	$0.38\cdot10^{-3}$	$-2.42\cdot10^{-3}$	$-2.55\cdot10^{-4}$	$7.15\cdot10^{-4}$
	High	$-1.08\cdot10^{-3}$	$0.08\cdot10^{-3}$	$-1.21\cdot10^{-3}$	$-1.10\cdot10^{-4}$	$1.69\cdot10^{-4}$

Table 4.15. Values at selected points for normalized terms of the RANS equations in the *x*-direction of 10° experiments.

	Roughness	$\underbrace{-\frac{1}{\rho}\frac{\partial \overline{p}^*}{\partial x}+\epsilon}_{I}$	$\underbrace{\overline{u}\frac{\partial \overline{u}^*}{\partial x}}_{II}$	$\underbrace{\overline{v}\frac{\partial \overline{u}^*}{\partial y}}_{III}$	$\underbrace{\frac{\partial}{\partial x}\left(\overline{u'^2}\right)^*}_{IV}$	$\underbrace{\frac{\partial}{\partial y}\left(\overline{u'v'}\right)^*}_{V}$
Point 1	Low	$-2.33\cdot10^{-4}$	$-2.3\cdot210^{-4}$	$0.64\cdot10^{-5}$	$-0.75\cdot10^{-5}$	$0.08\cdot10^{-5}$
	Medium	$1.53\cdot10^{-4}$	$1.61\cdot10^{-4}$	$-0.01\cdot10^{-5}$	$-0.58\cdot10^{-5}$	$-0.14\cdot10^{-5}$
	High	$2.05\cdot10^{-4}$	$2.35\cdot10^{-4}$	$-1.18\cdot10^{-5}$	$-1.04\cdot10^{-5}$	$-0.75\cdot10^{-5}$
	Roughness	$\underbrace{-\frac{1}{\rho}\frac{\partial \overline{p}^*}{\partial x}+\epsilon}_{I}$	$\underbrace{\overline{u}\frac{\partial \overline{u}^*}{\partial x}}_{II}$	$\underbrace{\overline{v}\frac{\partial \overline{u}^*}{\partial y}}_{III}$	$\underbrace{\frac{\partial}{\partial x}\left(\overline{u'^2}\right)^*}_{IV}$	$\underbrace{\frac{\partial}{\partial y}\left(\overline{u'v'}\right)^*}_{V}$
Point 2	Low	$1.14\cdot10^{-4}$	$6.35\cdot10^{-4}$	$0.33\cdot10^{-4}$	$-0.04\cdot10^{-4}$	$-5.50\cdot10^{-4}$
	Medium	$0.68\cdot10^{-4}$	$1.93\cdot10^{-4}$	$-0.04\cdot10^{-4}$	$1.26\cdot10^{-4}$	$-2.47\cdot10^{-4}$
	High	$2.98\cdot10^{-4}$	$0.78\cdot10^{-4}$	$2.68\cdot10^{-4}$	$1.93\cdot10^{-4}$	$-2.42\cdot10^{-4}$
	Roughness	$\underbrace{-\frac{1}{\rho}\frac{\partial \overline{p}^*}{\partial x}+\epsilon}_{I}$	$\underbrace{\overline{u}\frac{\partial \overline{u}^*}{\partial x}}_{II}$	$\underbrace{\overline{v}\frac{\partial \overline{u}^*}{\partial y}}_{III}$	$\underbrace{\frac{\partial}{\partial x}\left(\overline{u'^2}\right)^*}_{IV}$	$\underbrace{\frac{\partial}{\partial y}\left(\overline{u'v'}\right)^*}_{V}$
Point 3	Low	$-9.26\cdot10^{-4}$	$-8.62\cdot10^{-4}$	$-5.04\cdot10^{-4}$	$2.50\cdot10^{-4}$	$1.91\cdot10^{-4}$
	Medium	$-1.19\cdot10^{-4}$	$6.61\cdot10^{-4}$	$-7.67\cdot10^{-4}$	$-0.47\cdot10^{-4}$	$0.34\cdot10^{-4}$
	High	$-0.58\cdot10^{-4}$	$1.67\cdot10^{-4}$	$0.13\cdot10^{-4}$	$0.83\cdot10^{-4}$	$-3.21\cdot10^{-4}$
	Roughness	$\underbrace{-\frac{1}{\rho}\frac{\partial \overline{p}^*}{\partial x}+\epsilon}_{I}$	$\underbrace{\overline{u}\frac{\partial \overline{u}^*}{\partial x}}_{II}$	$\underbrace{\overline{v}\frac{\partial \overline{u}^*}{\partial y}}_{III}$	$\underbrace{\frac{\partial}{\partial x}\left(\overline{u'^2}\right)^*}_{IV}$	$\underbrace{\frac{\partial}{\partial y}\left(\overline{u'v'}\right)^*}_{V}$
Point 4	Low	$-1.27\cdot10^{-4}$	$1.10\cdot10^{-3}$	$-1.29\cdot10^{-3}$	$-1.17\cdot10^{-4}$	$1.80\cdot10^{-4}$
	Medium	$-2.00\cdot10^{-4}$	$1.15\cdot10^{-3}$	$-1.58\cdot10^{-3}$	$-0.07\cdot10^{-4}$	$2.33\cdot10^{-4}$
	High	$0.52\cdot10^{-4}$	$0.28\cdot10^{-3}$	$-0.20\cdot10^{-3}$	$0.45\cdot10^{-4}$	$-0.69\cdot10^{-4}$

Table 4.16. Values at selected points for normalized terms of the RANS equations in the *x*-direction of 17° experiments.

	Roughness	$\underbrace{-\frac{1}{\rho}\frac{\partial \overline{p}^*}{\partial x}+\epsilon}_{I}$	$\underbrace{\overline{u}\frac{\partial \overline{u}^*}{\partial x}}_{II}$	$\underbrace{\overline{v}\frac{\partial \overline{u}^*}{\partial y}}_{III}$	$\underbrace{\frac{\partial}{\partial x}\left(\overline{u'^2}\right)^*}_{IV}$	$\underbrace{\frac{\partial}{\partial y}\left(\overline{u'v'}\right)^*}_{V}$
Point 1	Low	$-5.88\cdot10^{-4}$	$-1.53\cdot10^{-3}$	$4.75\cdot10^{-4}$	$3.07\cdot10^{-4}$	$1.63\cdot10^{-4}$
	Medium	$6.04\cdot10^{-4}$	$0.62\cdot10^{-3}$	$-0.60\cdot10^{-4}$	$0.21\cdot10^{-4}$	$0.26\cdot10^{-4}$
	High	$-2.52\cdot10^{-4}$	$-0.19\cdot10^{-3}$	$-0.06\cdot10^{-4}$	$-0.42\cdot10^{-4}$	$-0.19\cdot10^{-4}$
	Roughness	$\underbrace{-\frac{1}{\rho}\frac{\partial \overline{p}^*}{\partial x}+\epsilon}_{I}$	$\underbrace{\overline{u}\frac{\partial \overline{u}^*}{\partial x}}_{II}$	$\underbrace{\overline{v}\frac{\partial \overline{u}^*}{\partial y}}_{III}$	$\underbrace{\frac{\partial}{\partial x}\left(\overline{u'^2}\right)^*}_{IV}$	$\underbrace{\frac{\partial}{\partial y}\left(\overline{u'v'}\right)^*}_{V}$
Point 2	Low	$-6.07\cdot10^{-4}$	$-2.08\cdot10^{-5}$	$-3.29\cdot10^{-4}$	$-0.75\cdot10^{-4}$	$-1.82\cdot10^{-4}$
	Medium	$-3.34\cdot10^{-4}$	$-0.69\cdot10^{-5}$	$-0.54\cdot10^{-4}$	$-1.57\cdot10^{-4}$	$-1.16\cdot10^{-4}$
	High	$-1.80\cdot10^{-4}$	$-5.92\cdot10^{-5}$	$-0.23\cdot10^{-4}$	$0.26\cdot10^{-4}$	$-1.24\cdot10^{-4}$
	Roughness	$\underbrace{-\frac{1}{\rho}\frac{\partial \overline{p}^*}{\partial x}+\epsilon}_{I}$	$\underbrace{\overline{u}\frac{\partial \overline{u}^*}{\partial x}}_{II}$	$\underbrace{\overline{v}\frac{\partial \overline{u}^*}{\partial y}}_{III}$	$\underbrace{\frac{\partial}{\partial x}\left(\overline{u'^2}\right)^*}_{IV}$	$\underbrace{\frac{\partial}{\partial y}\left(\overline{u'v'}\right)^*}_{V}$
Point 3	Low	$-0.63\cdot10^{-4}$	$6.62\cdot10^{-5}$	$-1.27\cdot10^{-4}$	$1.76\cdot10^{-4}$	$-1.78\cdot10^{-4}$
	Medium	$1.09\cdot10^{-4}$	$3.21\cdot10^{-5}$	$0.16\cdot10^{-4}$	$0.91\cdot10^{-4}$	$-0.31\cdot10^{-4}$
	High	$-0.03\cdot10^{-4}$	$2.64\cdot10^{-5}$	$0.00\cdot10^{-4}$	$0.16\cdot10^{-4}$	$-0.46\cdot10^{-4}$
	Roughness	$\underbrace{-\frac{1}{\rho}\frac{\partial \overline{p}^*}{\partial x}+\epsilon}_{I}$	$\underbrace{\overline{u}\frac{\partial \overline{u}^*}{\partial x}}_{II}$	$\underbrace{\overline{v}\frac{\partial \overline{u}^*}{\partial y}}_{III}$	$\underbrace{\frac{\partial}{\partial x}\left(\overline{u'^2}\right)^*}_{IV}$	$\underbrace{\frac{\partial}{\partial y}\left(\overline{u'v'}\right)^*}_{V}$
Point 4	Low	$-0.13\cdot10^{-4}$	$3.93\cdot10^{-4}$	$-4.13\cdot10^{-4}$	$0.77\cdot10^{-4}$	$-6.95\cdot10^{-5}$
	Medium	$1.82\cdot10^{-4}$	$0.05\cdot10^{-4}$	$0.64\cdot10^{-4}$	$1.64\cdot10^{-4}$	$-5.19\cdot10^{-5}$
	High	$0.16\cdot10^{-4}$	$-0.17\cdot10^{-4}$	$1.02\cdot10^{-4}$	$0.22\cdot10^{-4}$	$-9.12\cdot10^{-5}$

Table 4.17. Values at selected points for normalized terms of the RANS equations in the *y*-direction of 0° experiments.

	Roughness	$\underbrace{-\frac{1}{\rho}\frac{\partial \overline{p}^*}{\partial y}+\epsilon}_{VI}$	$\underbrace{\overline{u}\frac{\partial \overline{v}^*}{\partial x}}_{VII}$	$\underbrace{\overline{v}\frac{\partial \overline{v}^*}{\partial y}}_{VIII}$	$\underbrace{\frac{\partial}{\partial y}\left(\overline{v'^2}\right)^*}_{IX}$	$\underbrace{\frac{\partial}{\partial x}\left(\overline{u'v'}\right)^*}_{X}$
Point 1	Low	$-9.34\cdot10^{-5}$	$-4.91\cdot10^{-5}$	$-3.73\cdot10^{-5}$	$-0.72\cdot10^{-5}$	$0.29\cdot10^{-6}$
	Medium	$2.00\cdot10^{-5}$	$8.52\cdot10^{-5}$	$-5.47\cdot10^{-5}$	$-1.31\cdot10^{-5}$	$2.53\cdot10^{-6}$
	High	$-5.19\cdot10^{-5}$	$1.64\cdot10^{-5}$	$-5.52\cdot10^{-5}$	$-1.53\cdot10^{-5}$	$2.06\cdot10^{-6}$
	Roughness	$\underbrace{-\frac{1}{\rho}\frac{\partial \overline{p}^*}{\partial y}+\epsilon}_{VI}$	$\underbrace{\overline{u}\frac{\partial \overline{v}^*}{\partial x}}_{VII}$	$\underbrace{\overline{v}\frac{\partial \overline{v}^*}{\partial y}}_{VIII}$	$\underbrace{\frac{\partial}{\partial y}\left(\overline{v'^2}\right)^*}_{IX}$	$\underbrace{\frac{\partial}{\partial x}\left(\overline{u'v'}\right)^*}_{X}$
Point 2	Low	$1.07\cdot10^{-3}$	$5.25\cdot10^{-5}$	$-8.19\cdot10^{-5}$	$9.44\cdot10^{-4}$	$1.50\cdot10^{-4}$
	Medium	$0.51\cdot10^{-3}$	$-1.41\cdot10^{-5}$	$0.90\cdot10^{-5}$	$5.56\cdot10^{-4}$	$-0.39\cdot10^{-4}$
	High	$0.45\cdot10^{-3}$	$-6.00\cdot10^{-5}$	$6.83\cdot10^{-5}$	$4.73\cdot10^{-4}$	$-0.30\cdot10^{-4}$
	Roughness	$\underbrace{-\frac{1}{\rho}\frac{\partial \overline{p}^*}{\partial y}+\epsilon}_{VI}$	$\underbrace{\overline{u}\frac{\partial \overline{v}^*}{\partial x}}_{VII}$	$\underbrace{\overline{v}\frac{\partial \overline{v}^*}{\partial y}}_{VIII}$	$\underbrace{\frac{\partial}{\partial y}\left(\overline{v'^2}\right)^*}_{IX}$	$\underbrace{\frac{\partial}{\partial x}\left(\overline{u'v'}\right)^*}_{X}$
Point 3	Low	$-1.56\cdot10^{-4}$	$-7.67\cdot10^{-5}$	$0.83\cdot10^{-4}$	$-2.55\cdot10^{-4}$	$0.93\cdot10^{-4}$
	Medium	$-1.07\cdot10^{-4}$	$-0.05\cdot10^{-5}$	$1.11\cdot10^{-4}$	$-3.28\cdot10^{-4}$	$1.11\cdot10^{-4}$
	High	$-2.23\cdot10^{-4}$	$5.74\cdot10^{-5}$	$0.50\cdot10^{-4}$	$-3.22\cdot10^{-4}$	$-0.08\cdot10^{-4}$
	Roughness	$\underbrace{-\frac{1}{\rho}\frac{\partial \overline{p}^*}{\partial y}+\epsilon}_{VI}$	$\underbrace{\overline{u}\frac{\partial \overline{v}^*}{\partial x}}_{VII}$	$\underbrace{\overline{v}\frac{\partial \overline{v}^*}{\partial y}}_{VIII}$	$\underbrace{\frac{\partial}{\partial y}\left(\overline{v'^2}\right)^*}_{IX}$	$\underbrace{\frac{\partial}{\partial x}\left(\overline{u'v'}\right)^*}_{X}$
Point 4	Low	$-6.15\cdot10^{-4}$	$-5.79\cdot10^{-4}$	$4.89\cdot10^{-4}$	$-0.73\cdot10^{-3}$	$2.06\cdot10^{-4}$
	Medium	$-8.49\cdot10^{-4}$	$-2.23\cdot10^{-4}$	$2.90\cdot10^{-4}$	$-1.20\cdot10^{-3}$	$2.84\cdot10^{-4}$
	High	$-3.13\cdot10^{-4}$	$1.15\cdot10^{-4}$	$0.23\cdot10^{-4}$	$-0.57\cdot10^{-3}$	$1.20\cdot10^{-4}$

Table 4.18. Values at selected points for normalized terms of the RANS equations in the *y*-direction of 10° experiments.

	Roughness	$\underbrace{-\frac{1}{\rho}\frac{\partial \overline{p}^*}{\partial y}+\epsilon}_{VI}$	$\underbrace{\overline{u}\frac{\partial \overline{v}^*}{\partial x}}_{VII}$	$\underbrace{\overline{v}\frac{\partial \overline{v}^*}{\partial y}}_{VIII}$	$\underbrace{\frac{\partial}{\partial y}\left(\overline{v'^2}\right)^*}_{IX}$	$\underbrace{\frac{\partial}{\partial x}\left(\overline{u'v'}\right)^*}_{X}$
Point 1	Low	$2.66\cdot10^{-4}$	$2.62\cdot10^{-4}$	$-1.17\cdot10^{-5}$	$1.30\cdot10^{-5}$	$3.59\cdot10^{-6}$
	Medium	$0.33\cdot10^{-4}$	$0.51\cdot10^{-4}$	$-1.50\cdot10^{-5}$	$-0.67\cdot10^{-5}$	$3.62\cdot10^{-6}$
	High	$3.79\cdot10^{-4}$	$3.71\cdot10^{-4}$	$0.78\cdot10^{-5}$	$0.33\cdot10^{-5}$	$-3.53\cdot10^{-6}$
	Roughness	$\underbrace{-\frac{1}{\rho}\frac{\partial \overline{p}^*}{\partial y}+\epsilon}_{VI}$	$\underbrace{\overline{u}\frac{\partial \overline{v}^*}{\partial x}}_{VII}$	$\underbrace{\overline{v}\frac{\partial \overline{v}^*}{\partial y}}_{VIII}$	$\underbrace{\frac{\partial}{\partial y}\left(\overline{v'^2}\right)^*}_{IX}$	$\underbrace{\frac{\partial}{\partial x}\left(\overline{u'v'}\right)^*}_{X}$
Point 2	Low	$3.24\cdot10^{-4}$	$-9.04\cdot10^{-5}$	$1.50\cdot10^{-4}$	$2.28\cdot10^{-4}$	$3.67\cdot10^{-5}$
	Medium	$-0.44\cdot10^{-4}$	$-5.98\cdot10^{-5}$	$0.46\cdot10^{-4}$	$0.29\cdot10^{-4}$	$-5.98\cdot10^{-5}$
	High	$-1.73\cdot10^{-4}$	$-1.09\cdot10^{-5}$	$0.07\cdot10^{-4}$	$-2.63\cdot10^{-4}$	$9.38\cdot10^{-5}$
	Roughness	$\underbrace{-\frac{1}{\rho}\frac{\partial \overline{p}^*}{\partial y}+\epsilon}_{VI}$	$\underbrace{\overline{u}\frac{\partial \overline{v}^*}{\partial x}}_{VII}$	$\underbrace{\overline{v}\frac{\partial \overline{v}^*}{\partial y}}_{VIII}$	$\underbrace{\frac{\partial}{\partial y}\left(\overline{v'^2}\right)^*}_{IX}$	$\underbrace{\frac{\partial}{\partial x}\left(\overline{u'v'}\right)^*}_{X}$
Point 3	Low	$-1.28\cdot10^{-4}$	$8.44\cdot10^{-5}$	$2.56\cdot10^{-4}$	$-4.87\cdot10^{-4}$	$1.87\cdot10^{-5}$
	Medium	$1.38\cdot10^{-4}$	$1.55\cdot10^{-5}$	$2.05\cdot10^{-4}$	$-1.18\cdot10^{-4}$	$3.57\cdot10^{-5}$
	High	$-2.46\cdot10^{-4}$	$-3.24\cdot10^{-5}$	$0.35\cdot10^{-4}$	$-2.01\cdot10^{-4}$	$-4.81\cdot10^{-5}$
	Roughness	$\underbrace{-\frac{1}{\rho}\frac{\partial \overline{p}^*}{\partial y}+\epsilon}_{VI}$	$\underbrace{\overline{u}\frac{\partial \overline{v}^*}{\partial x}}_{VII}$	$\underbrace{\overline{v}\frac{\partial \overline{v}^*}{\partial y}}_{VIII}$	$\underbrace{\frac{\partial}{\partial y}\left(\overline{v'^2}\right)^*}_{IX}$	$\underbrace{\frac{\partial}{\partial x}\left(\overline{u'v'}\right)^*}_{X}$
Point 4	Low	$0.94\cdot10^{-4}$	$0.10\cdot10^{-4}$	$1.91\cdot10^{-4}$	$-1.44\cdot10^{-4}$	$3.73\cdot10^{-5}$
	Medium	$1.21\cdot10^{-4}$	$-1.45\cdot10^{-4}$	$3.90\cdot10^{-4}$	$-1.74\cdot10^{-4}$	$5.03\cdot10^{-5}$
	High	$-0.69\cdot10^{-4}$	$-1.25\cdot10^{-4}$	$0.59\cdot10^{-4}$	$0.56\cdot10^{-4}$	$-5.90\cdot10^{-5}$

Table 4.19. Values at selected points for normalized terms of the RANS equations in the *y*-direction of 17° experiments.

	Roughness	$\underbrace{-\frac{1}{\rho}\frac{\partial \overline{p}^*}{\partial y}+\epsilon}_{VI}$	$\underbrace{\overline{u}\frac{\partial \overline{v}^*}{\partial x}}_{VII}$	$\underbrace{\overline{v}\frac{\partial \overline{v}^*}{\partial y}}_{VIII}$	$\underbrace{\frac{\partial}{\partial y}\left(\overline{v'^2}\right)^*}_{IX}$	$\underbrace{\frac{\partial}{\partial x}\left(\overline{u'v'}\right)^*}_{X}$
Point 1	Low	$0.70\cdot10^{-3}$	$0.93\cdot10^{-3}$	$-4.06\cdot10^{-4}$	$1.18\cdot10^{-4}$	$6.34\cdot10^{-5}$
	Medium	$1.34\cdot10^{-3}$	$1.20\cdot10^{-3}$	$-0.02\cdot10^{-4}$	$1.30\cdot10^{-4}$	$1.07\cdot10^{-5}$
	High	$1.07\cdot10^{-3}$	$0.99\cdot10^{-3}$	$-0.07\cdot10^{-4}$	$0.65\cdot10^{-4}$	$2.08\cdot10^{-5}$
	Roughness	$\underbrace{-\frac{1}{\rho}\frac{\partial \overline{p}^*}{\partial y}+\epsilon}_{VI}$	$\underbrace{\overline{u}\frac{\partial \overline{v}^*}{\partial x}}_{VII}$	$\underbrace{\overline{v}\frac{\partial \overline{v}^*}{\partial y}}_{VIII}$	$\underbrace{\frac{\partial}{\partial y}\left(\overline{v'^2}\right)^*}_{IX}$	$\underbrace{\frac{\partial}{\partial x}\left(\overline{u'v'}\right)^*}_{X}$
Point 2	Low	$2.16\cdot10^{-4}$	$1.12\cdot10^{-5}$	$9.38\cdot10^{-5}$	$1.54\cdot10^{-4}$	$-4.28\cdot10^{-5}$
	Medium	$0.55\cdot10^{-4}$	$4.18\cdot10^{-5}$	$0.89\cdot10^{-5}$	$0.01\cdot10^{-4}$	$0.28\cdot10^{-5}$
	High	$0.38\cdot10^{-4}$	$-0.14\cdot10^{-5}$	$0.86\cdot10^{-5}$	$0.58\cdot10^{-4}$	$-2.67\cdot10^{-5}$
	Roughness	$\underbrace{-\frac{1}{\rho}\frac{\partial \overline{p}^*}{\partial y}+\epsilon}_{VI}$	$\underbrace{\overline{u}\frac{\partial \overline{v}^*}{\partial x}}_{VII}$	$\underbrace{\overline{v}\frac{\partial \overline{v}^*}{\partial y}}_{VIII}$	$\underbrace{\frac{\partial}{\partial y}\left(\overline{v'^2}\right)^*}_{IX}$	$\underbrace{\frac{\partial}{\partial x}\left(\overline{u'v'}\right)^*}_{X}$
Point 3	Low	$1.44\cdot10^{-4}$	$-5.50\cdot10^{-5}$	$3.15\cdot10^{-5}$	$2.28\cdot10^{-4}$	$-6.04\cdot10^{-5}$
	Medium	$0.50\cdot10^{-4}$	$3.48\cdot10^{-5}$	$0.22\cdot10^{-5}$	$0.38\cdot10^{-4}$	$-2.50\cdot10^{-5}$
	High	$2.14\cdot10^{-4}$	$8.63\cdot10^{-5}$	$0.25\cdot10^{-5}$	$1.24\cdot10^{-4}$	$0.19\cdot10^{-5}$
	Roughness	$\underbrace{-\frac{1}{\rho}\frac{\partial \overline{p}^*}{\partial y}+\epsilon}_{VI}$	$\underbrace{\overline{u}\frac{\partial \overline{v}^*}{\partial x}}_{VII}$	$\underbrace{\overline{v}\frac{\partial \overline{v}^*}{\partial y}}_{VIII}$	$\underbrace{\frac{\partial}{\partial y}\left(\overline{v'^2}\right)^*}_{IX}$	$\underbrace{\frac{\partial}{\partial x}\left(\overline{u'v'}\right)^*}_{X}$
Point 4	Low	$2.97\cdot10^{-5}$	$-9.28\cdot10^{-5}$	$1.28\cdot10^{-4}$	$7.14\cdot10^{-5}$	$-7.64\cdot10^{-5}$
	Medium	$3.65\cdot10^{-5}$	$0.00\cdot10^{-5}$	$-0.15\cdot10^{-4}$	$7.76\cdot10^{-5}$	$-2.60\cdot10^{-5}$
	High	$9.10\cdot10^{-5}$	$2.82\cdot10^{-5}$	$-0.27\cdot10^{-4}$	$8.32\cdot10^{-5}$	$0.69\cdot10^{-5}$

Table 4.20. Figure numbers for each RANS term contour plot in the Appendix. Each number is prefaced by "Figure A-".

	Terms									
	I	**II**	**III**	**IV**	**V**	**VI**	**VII**	**VIII**	**IX**	**X**
Low Roughness - 0°	21	30	39	48	57	66	75	84	93	102
Low Roughness - 10°	22	31	40	49	58	67	76	85	94	103
Low Roughness - 17°	23	32	41	50	59	68	77	86	95	104
Medium Roughness - 0°	24	33	42	51	60	69	78	87	96	105
Medium Roughness - 10°	25	34	43	52	61	70	79	88	97	106
Medium Roughness - 17°	26	35	44	53	62	71	80	89	98	107
High Roughness - 0°	27	36	45	54	63	72	81	90	99	108
High Roughness - 10°	28	37	46	55	64	73	82	91	100	109
High Roughness - 17°	29	38	47	56	65	74	83	92	101	110

Table 4.21. Color-scales for RANS terms plots.

Angle	*x* direction	*y* direction
0°	$\pm$-2.5·10^{-3}	$\pm$-2.0·10^{-3}
10°	$\pm$-2.5·10^{-3}	$\pm$-1.5·10^{-3}
17°	$\pm$-2.5·10^{-3}	$\pm$-2.5·10^{-3}

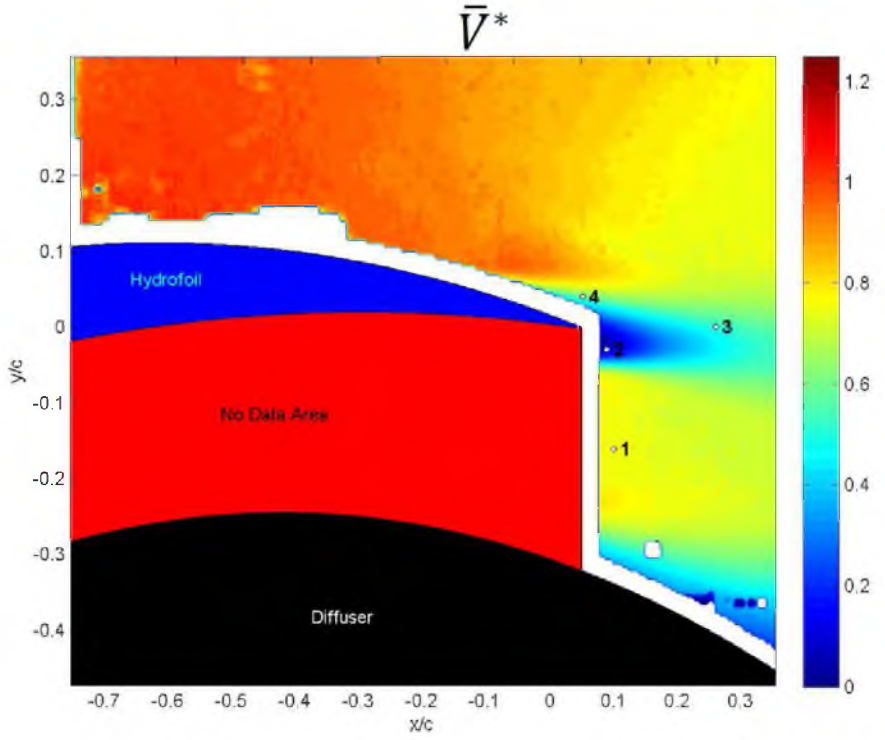

Figure 4.1. Velocity magnitude contour plot of medium roughness at 0° showing location of tabled values for all 0° experiments.

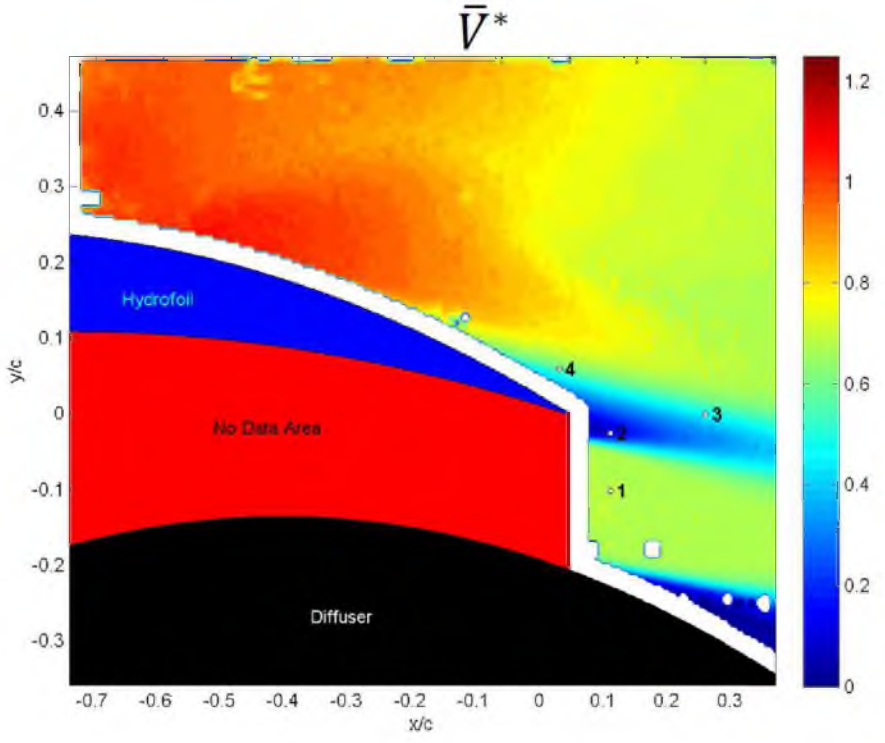

Figure 4.2. Velocity magnitude contour plot of medium roughness at 10° showing location of tabled values for all 10° experiments.

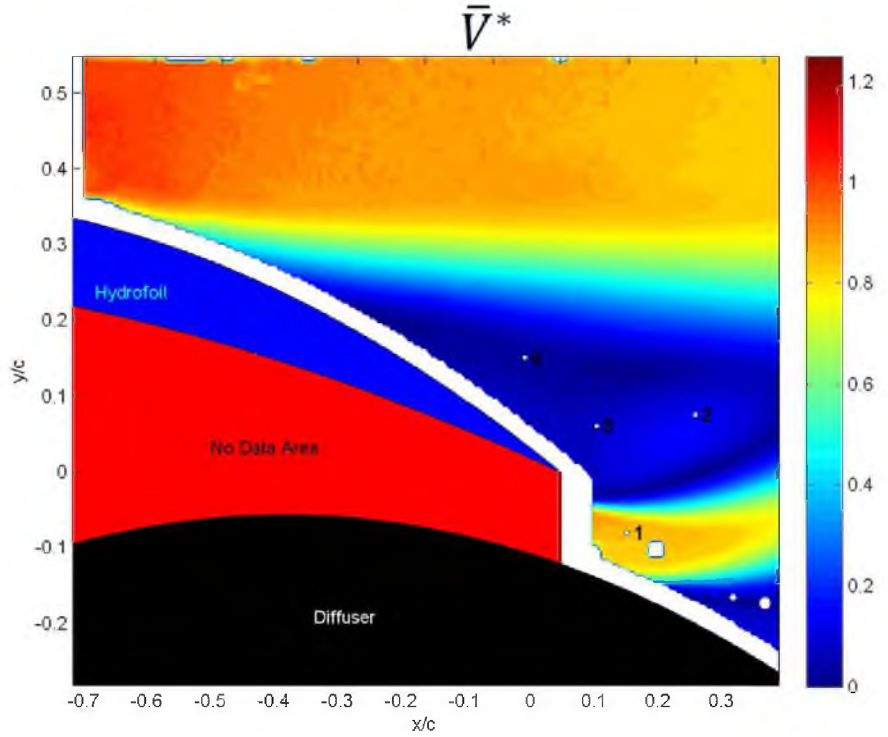

Figure 4.3. Velocity magnitude contour plot of medium roughness at 17° showing location of tabled values for all 17° experiments.

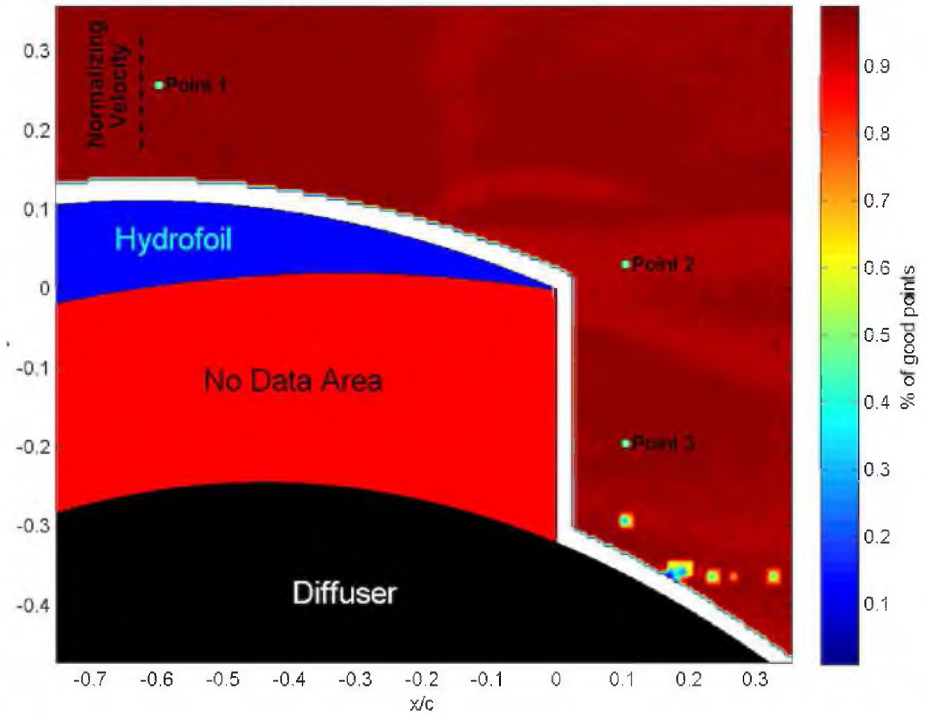

Figure 4.4. "Choice Code" contour plot for low roughness at 0° indicating the percentage of good vectors at each data processing spot.

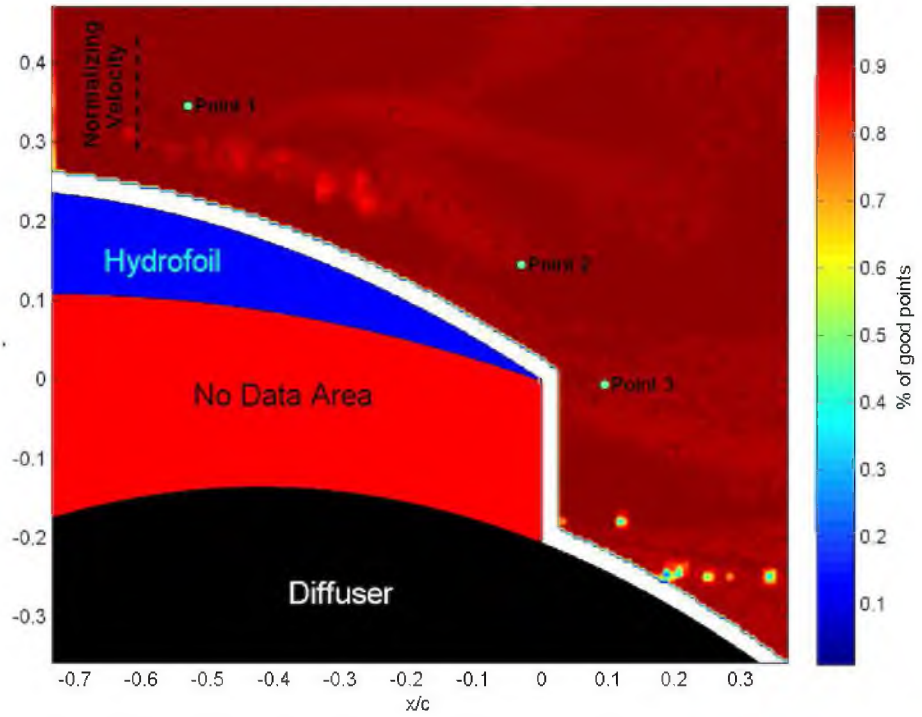

Figure 4.5. Same as 4.1 except for a 10° angle of attack.

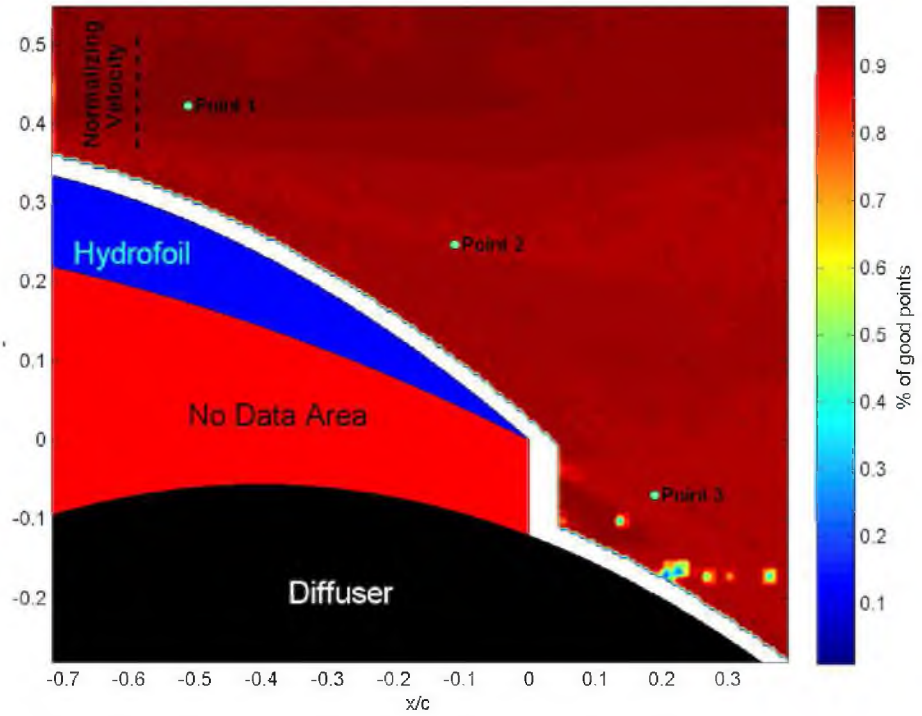

Figure 4.6. Same as 4.1 except for a 17° angle of attack.

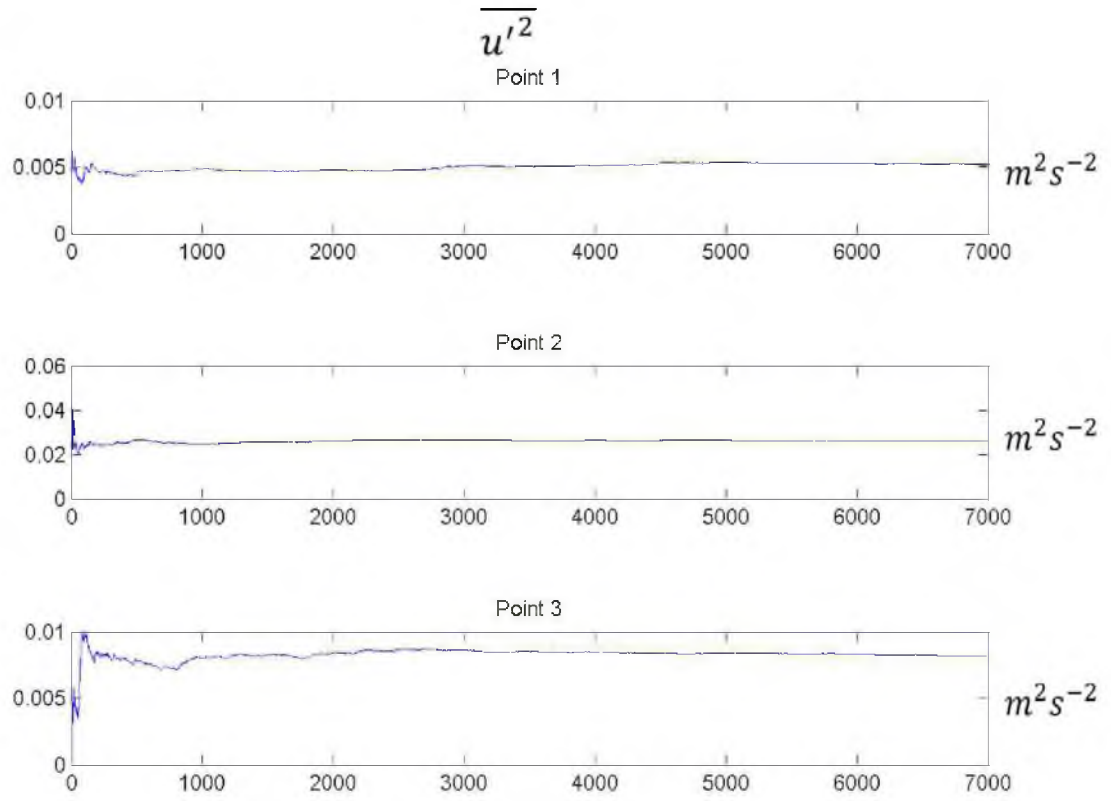

Figure 4.7. Convergence plot for mean Reynolds normal stress in the streamwise direction as a function of number of images considered for high roughness at 17°.

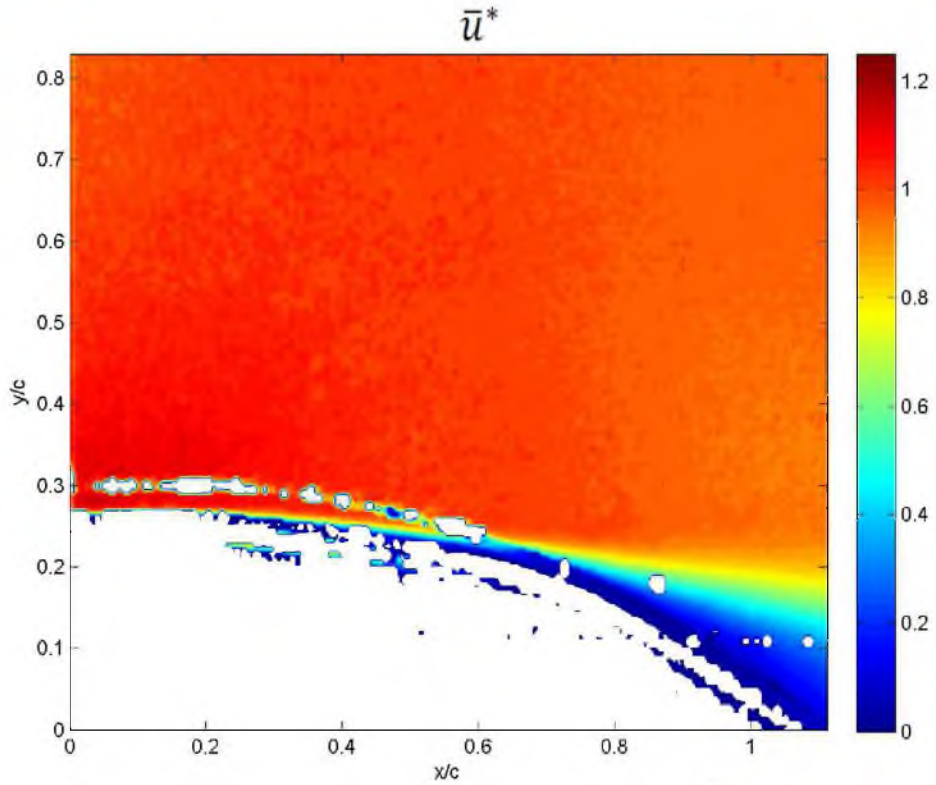

Figure 4.8. Contours of nondimensional streamwise velocity ($\bar{u}^*$) for the data set with no hydrofoil present.

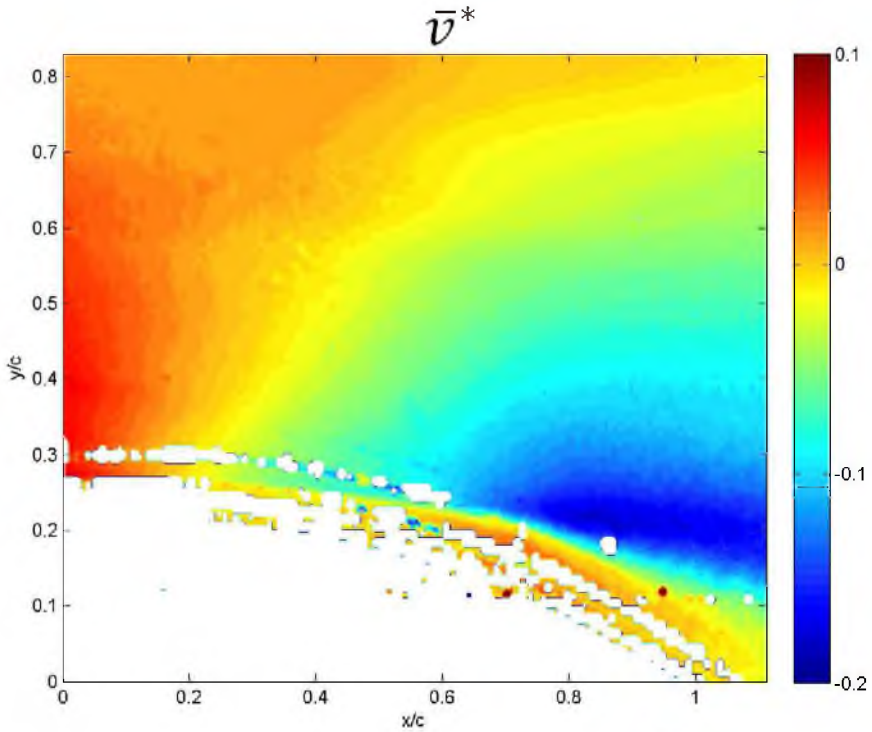

Figure 4.9. Contours of nondimensional cross-flow velocity ($\bar{v}^*$) for the data set with no hydrofoil present.

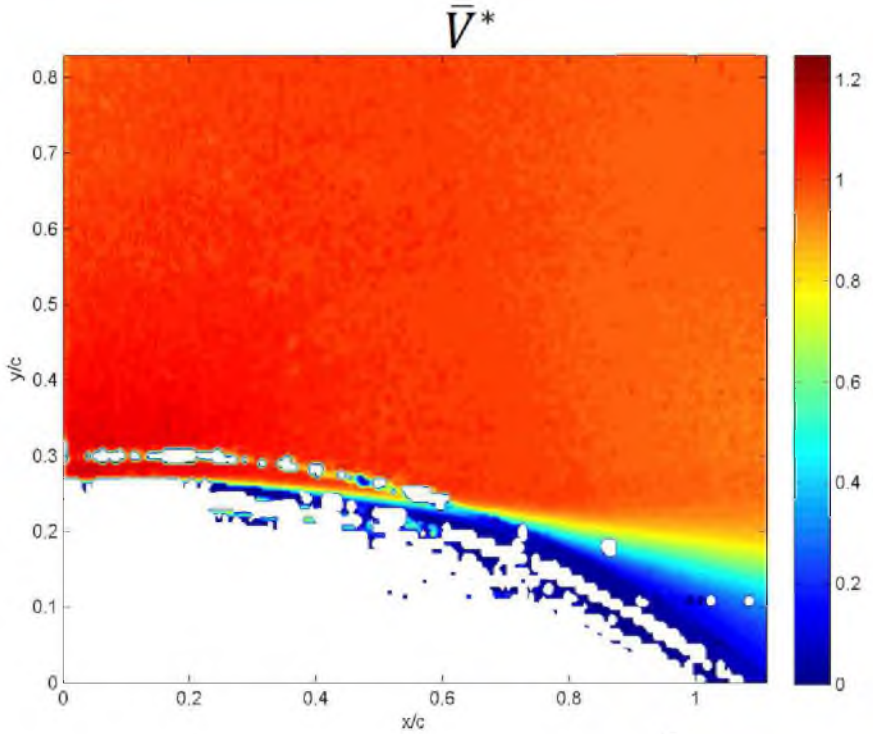

Figure 4.10. Contours of nondimensional velocity magnitude ($\bar{V}^*$) for the data set with no hydrofoil present.

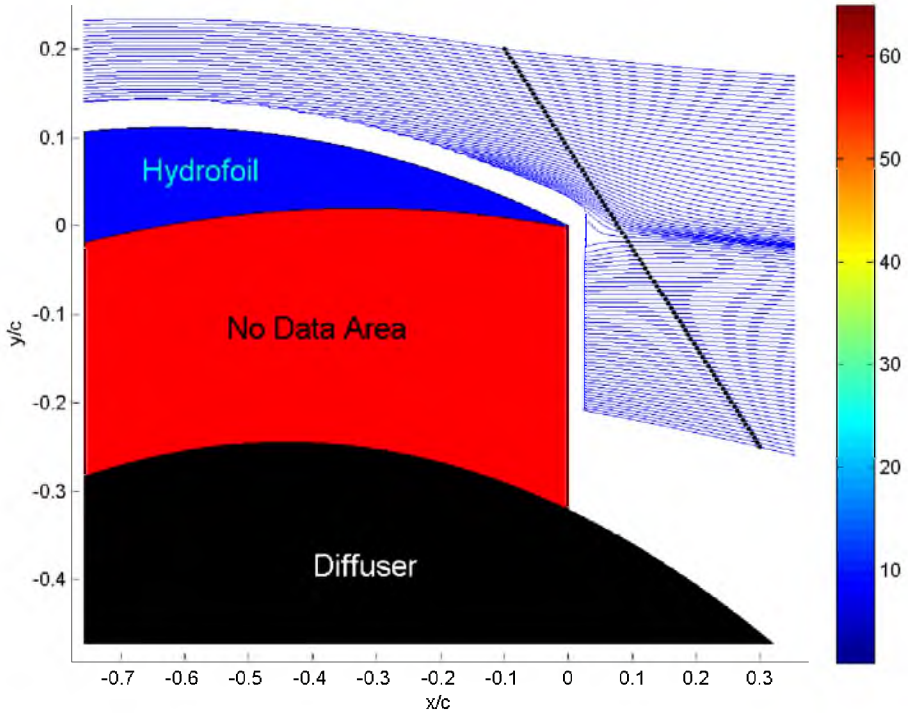

Figure 4.11. Streamlines for the low roughness experiment at 0°.

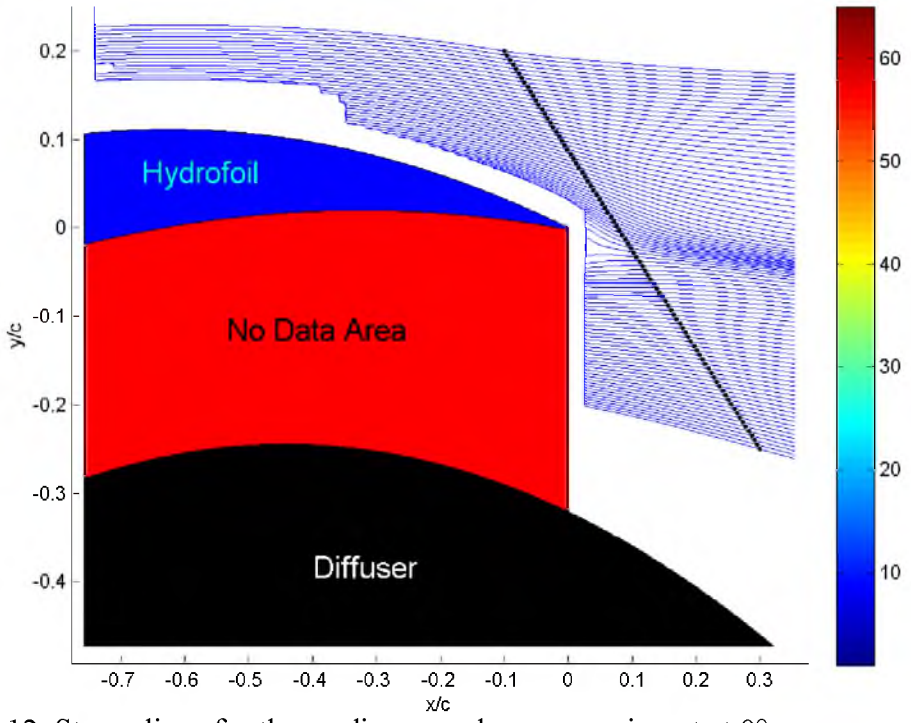

Figure 4.12. Streamlines for the medium roughness experiment at 0°.

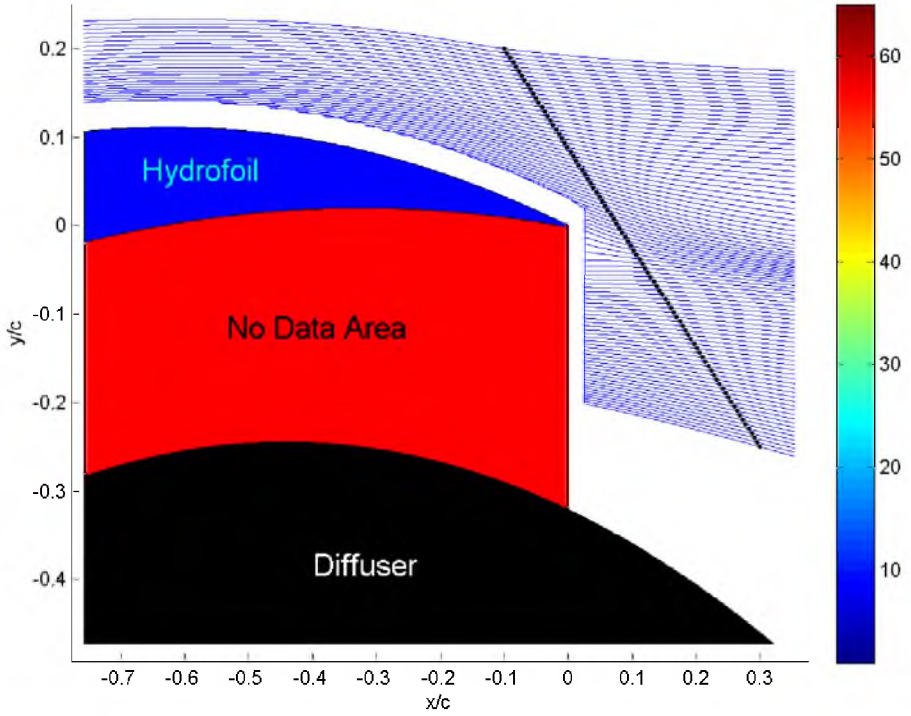

Figure 4.13. Streamlines for the high roughness experiment at 0°.

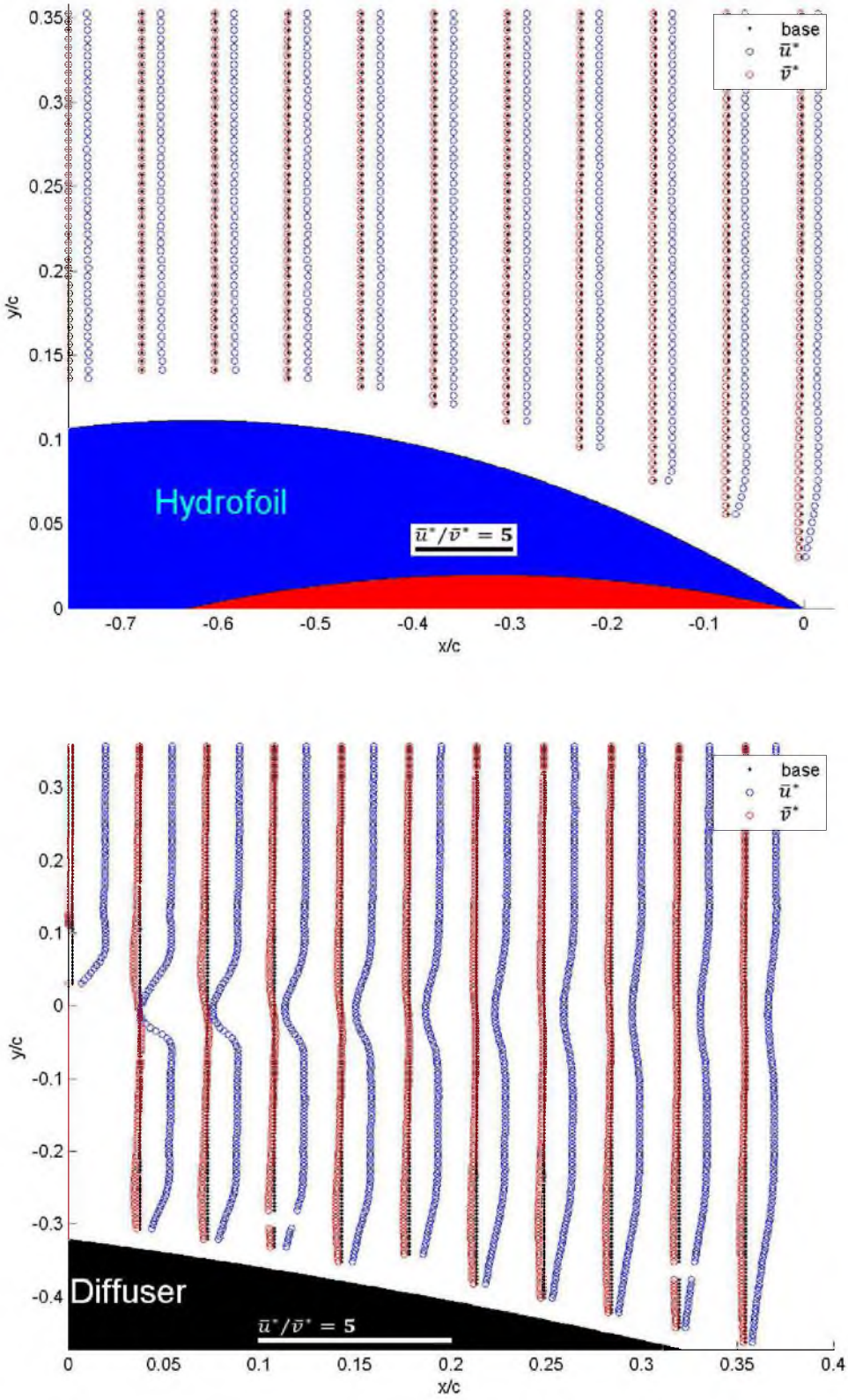

Figure 4.14. Velocity profiles for the low roughness experiment at 0°. A) (top) Above the hydrofoil. B) (bottom) Downstream of the hydrofoil.

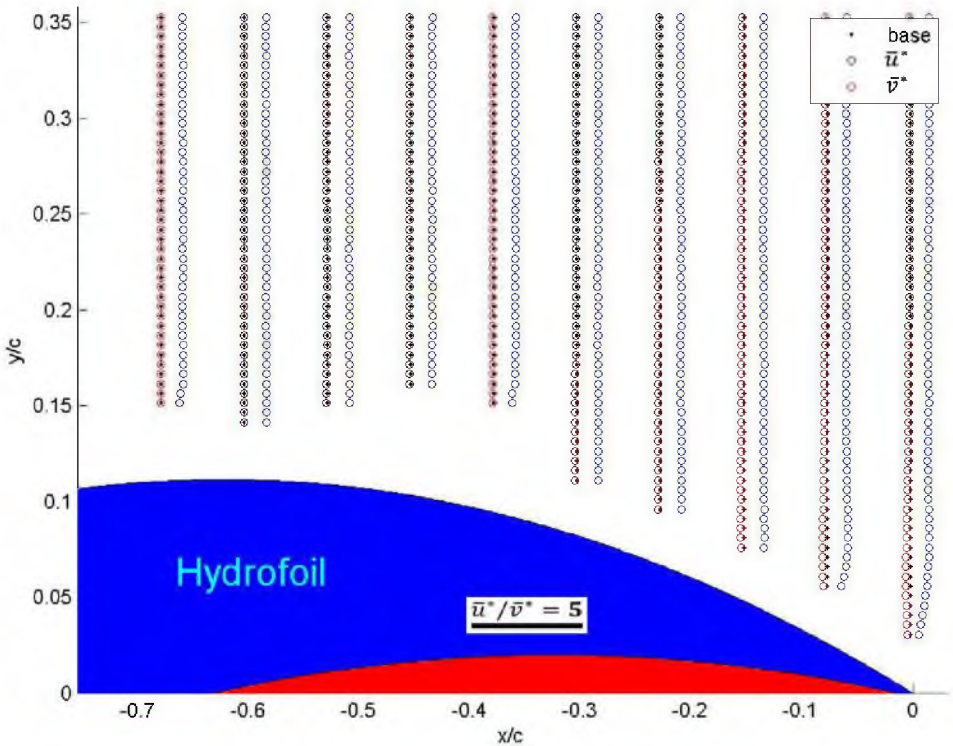
base
$\bar{u}^*$
$\bar{v}^*$
Hydrofoil
$\bar{u}^*/\bar{v}^* = 5$
y/c
x/c
0.35
0.3
0.25
0.2
0.15
0.1
0.05
0
-0.7
-0.6
-0.5
-0.4
-0.3
-0.2
-0.1
0

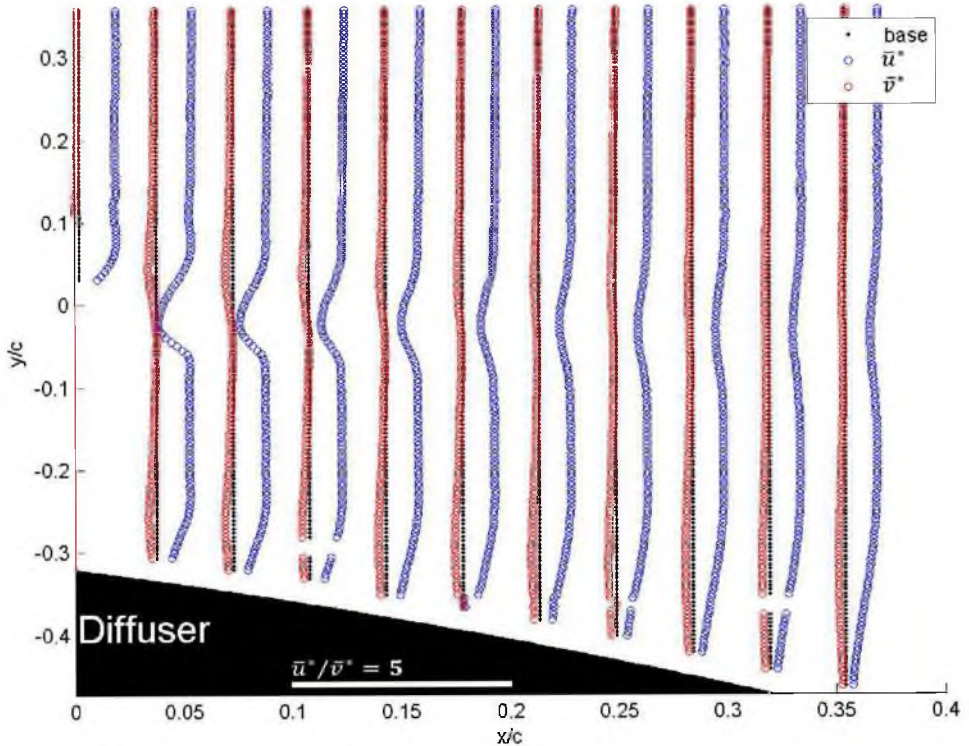

Figure 4.15. Velocity profiles for the medium roughness experiment at 0°. A) (top) Above the hydrofoil. B) (bottom) Downstream of the hydrofoil.

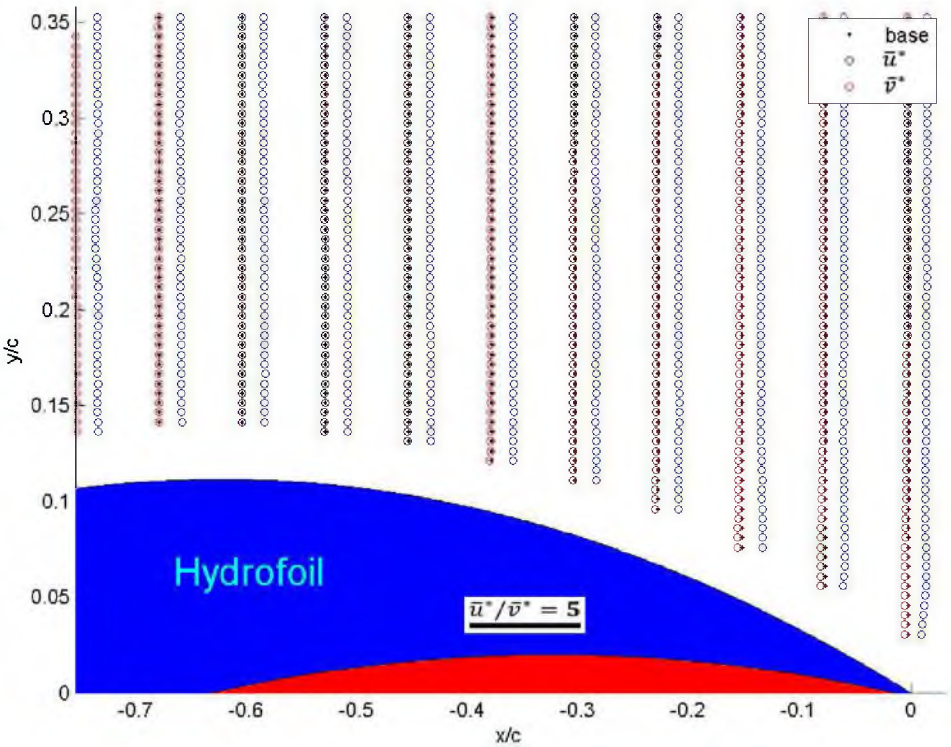
base
$\bar{u}^*$
$\bar{v}^*$
Hydrofoil
$\bar{u}^*/\bar{v}^* = 5$
y/c
x/c
0.35
0.3
0.25
0.2
0.15
0.1
0.05
0
-0.7
-0.6
-0.5
-0.4
-0.3
-0.2
-0.1
0

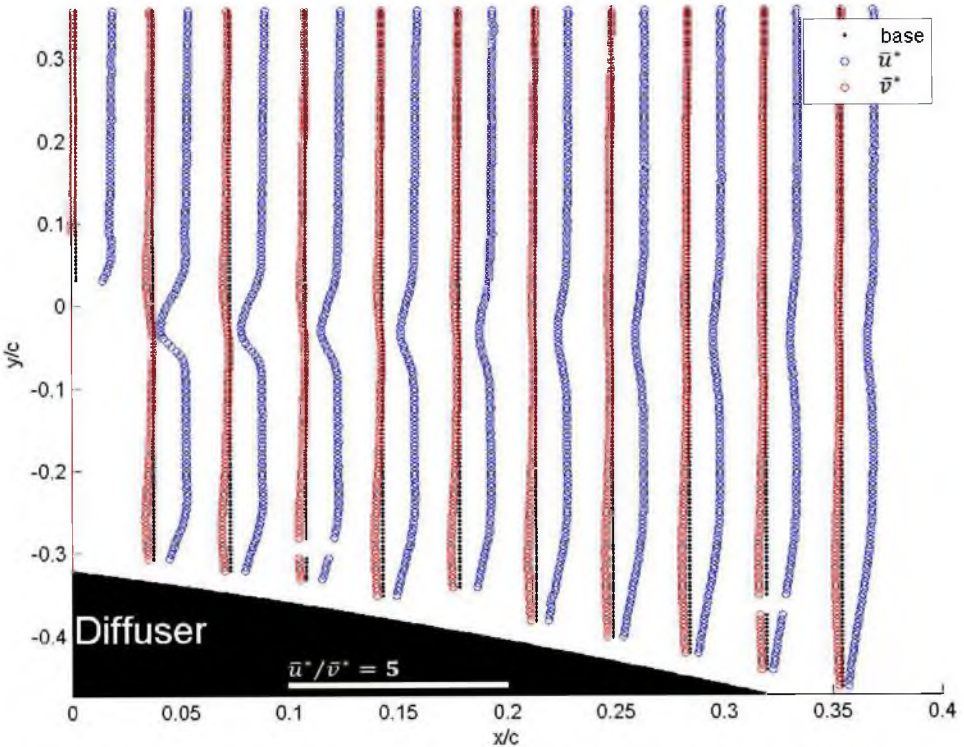

Figure 4.16. Velocity profiles for the high roughness experiment at 0°. A) (top) Above the hydrofoil. B) (bottom) Downstream of the hydrofoil.

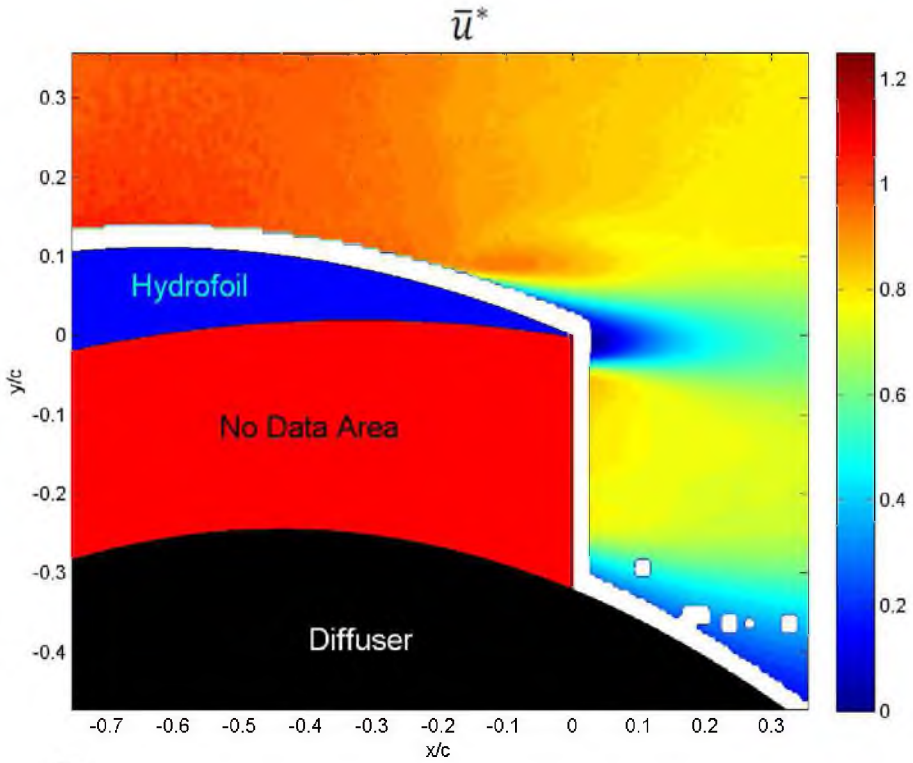

Figure 4.17. $\bar{u}^*$ contour plot of low roughness at 0°.

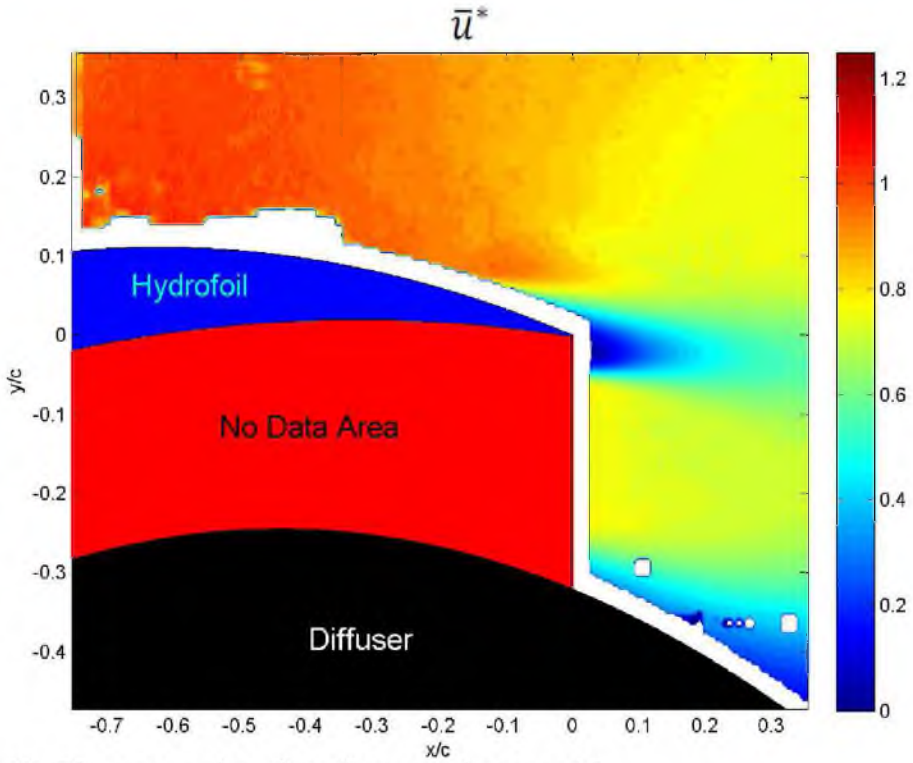

Figure 4.18. $\bar{u}^*$ contour plot of medium roughness at 0°.

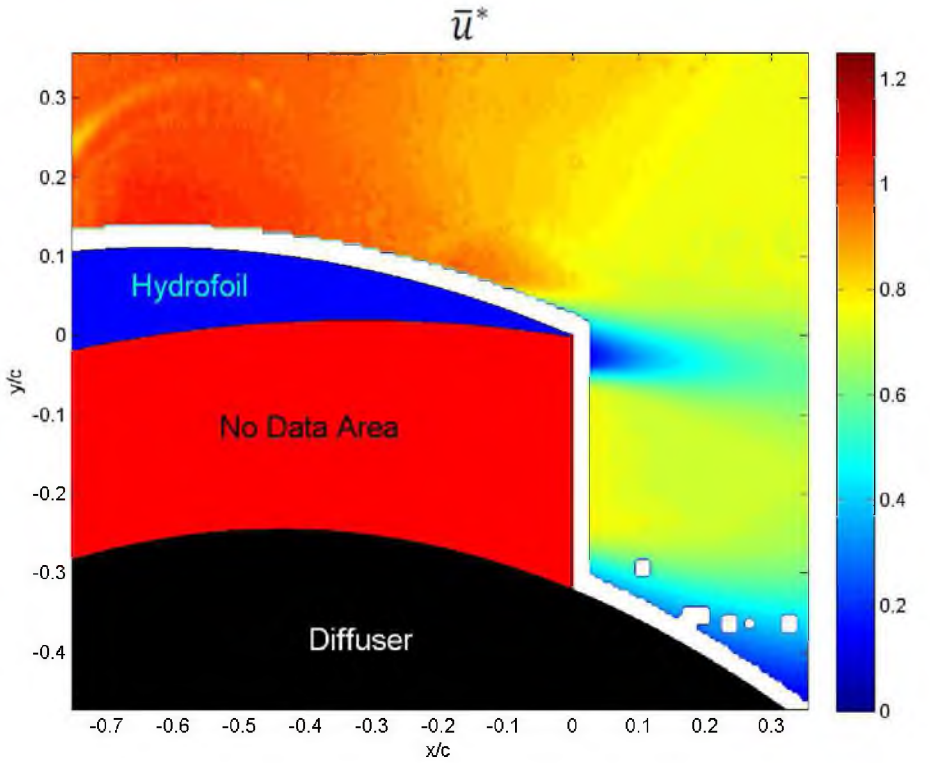

Figure 4.19. $\bar{u}^*$ contour plot of high roughness at 0°.

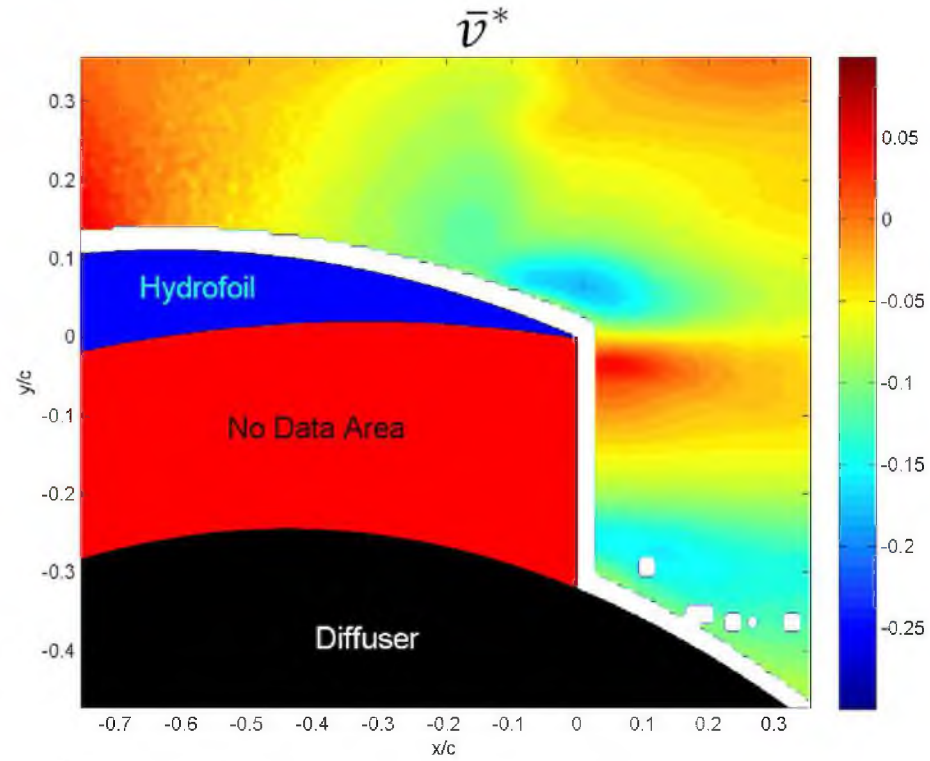

Figure 4.20. $\bar{v}^*$ contour plot of low roughness at 0°.

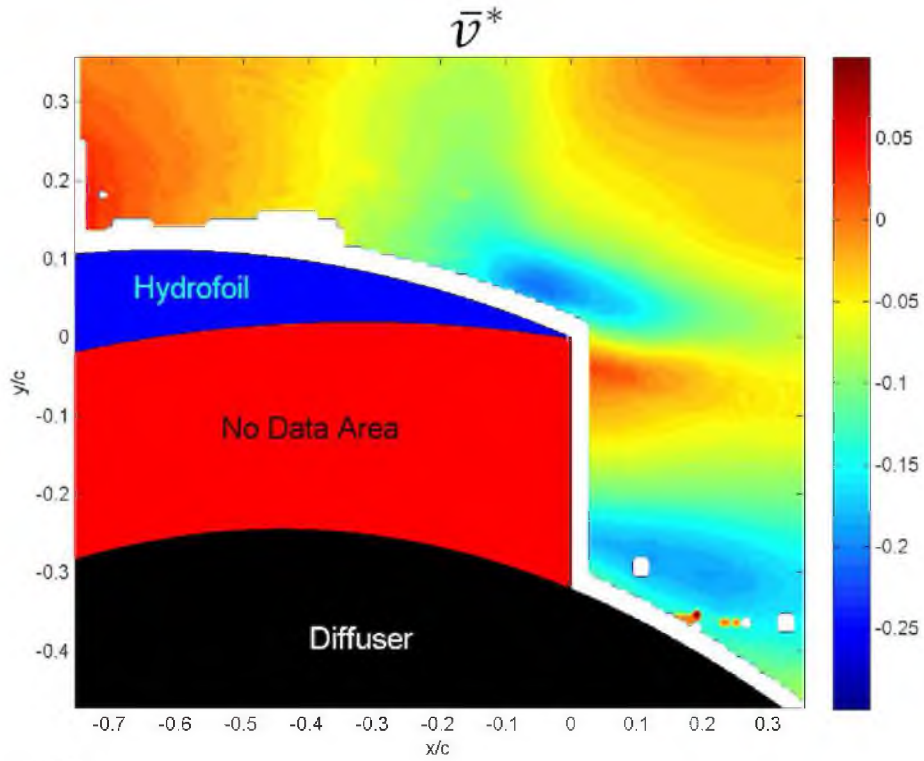

Figure 4.21. $\bar{v}^*$ contour plot of medium roughness at 0°.

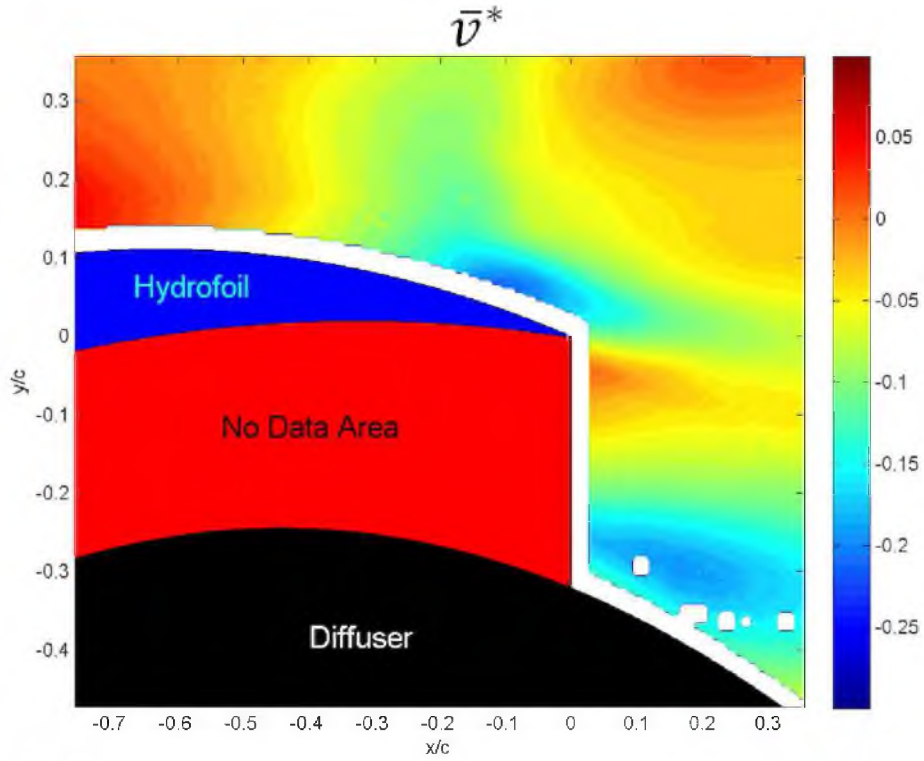

Figure 4.22. $\bar{v}^*$ contour plot of high roughness at 0°.

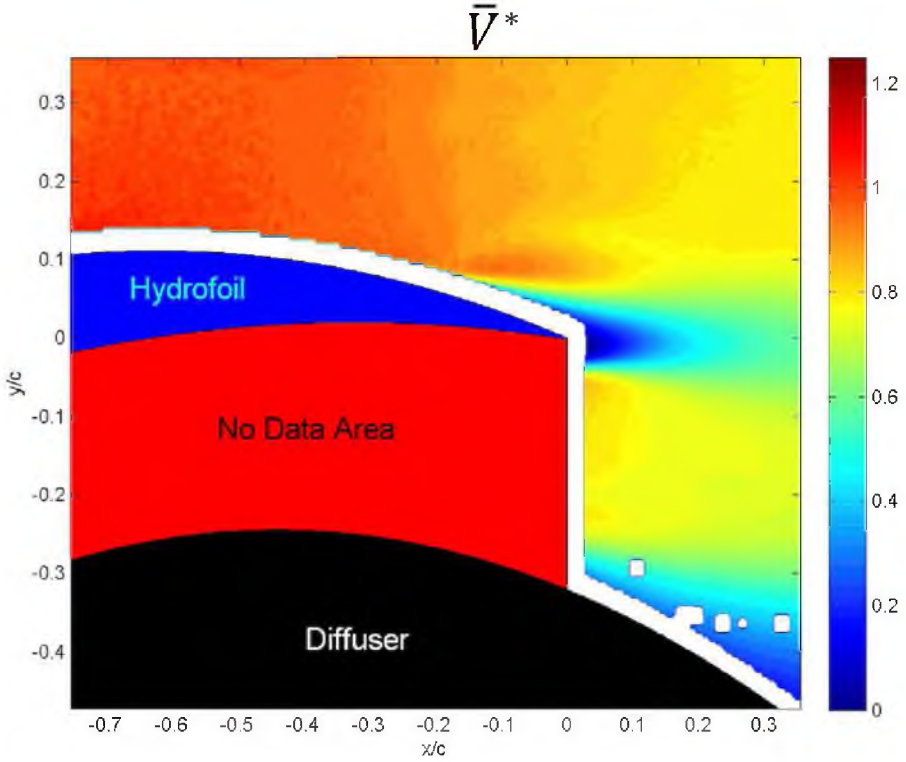

Figure 4.23. $\bar{V}^*$ contour plot of low roughness at 0°.

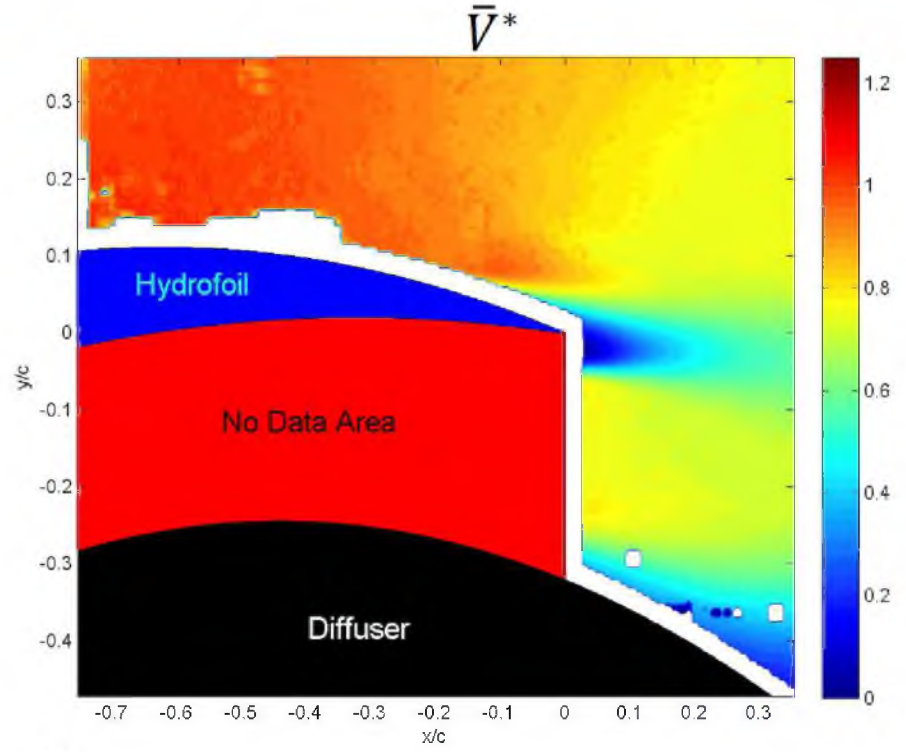

Figure 4.24. $\bar{V}^*$ contour plot of medium roughness at 0°.

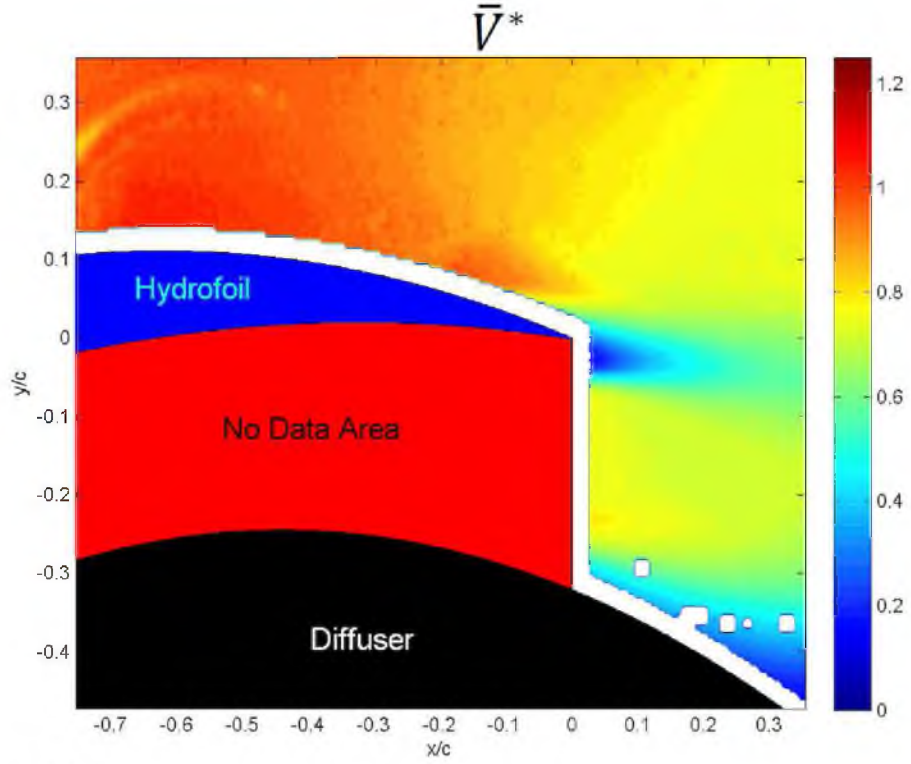

Figure 4.25. $\bar{V}^*$ contour plot of high roughness at 0°.

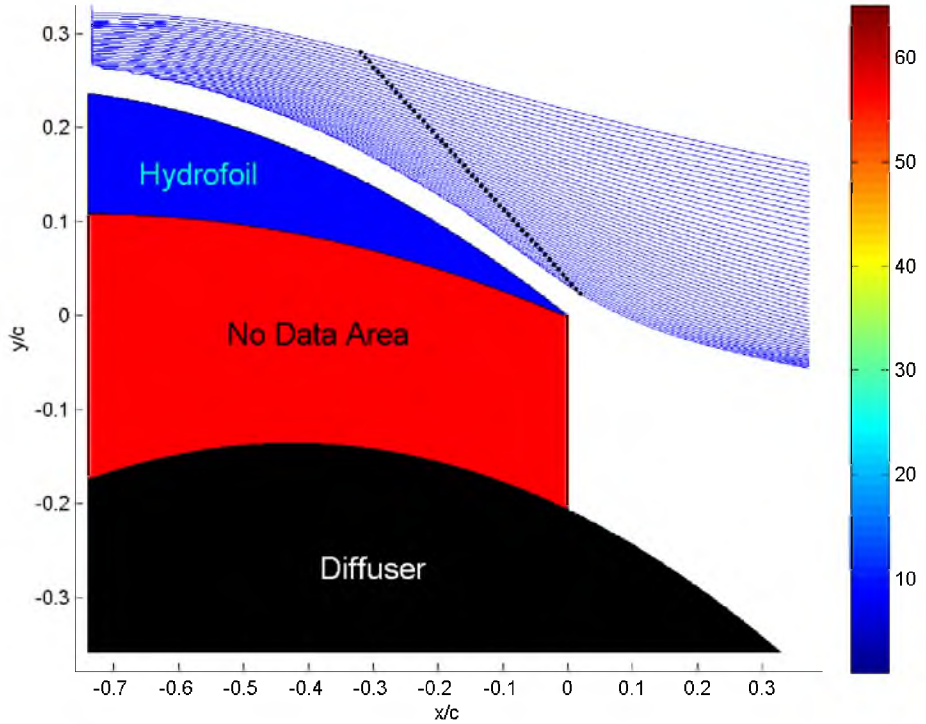

Figure 4.26. Streamlines for the low roughness experiment at 10°.

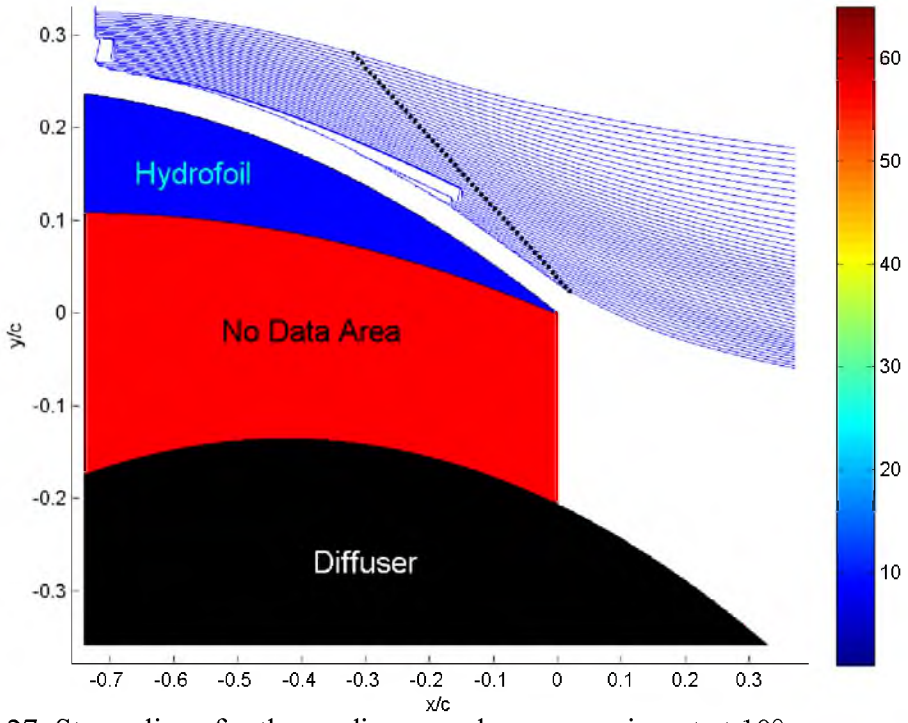

Figure 4.27. Streamlines for the medium roughness experiment at 10°.

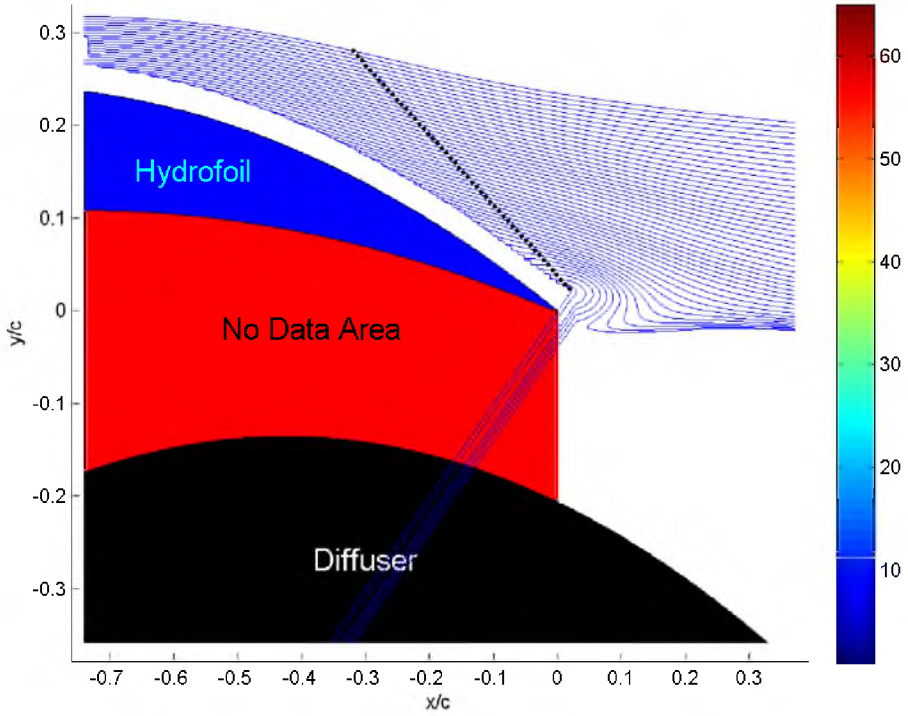

Figure 4.28. Streamlines for the high roughness experiment at 10°.

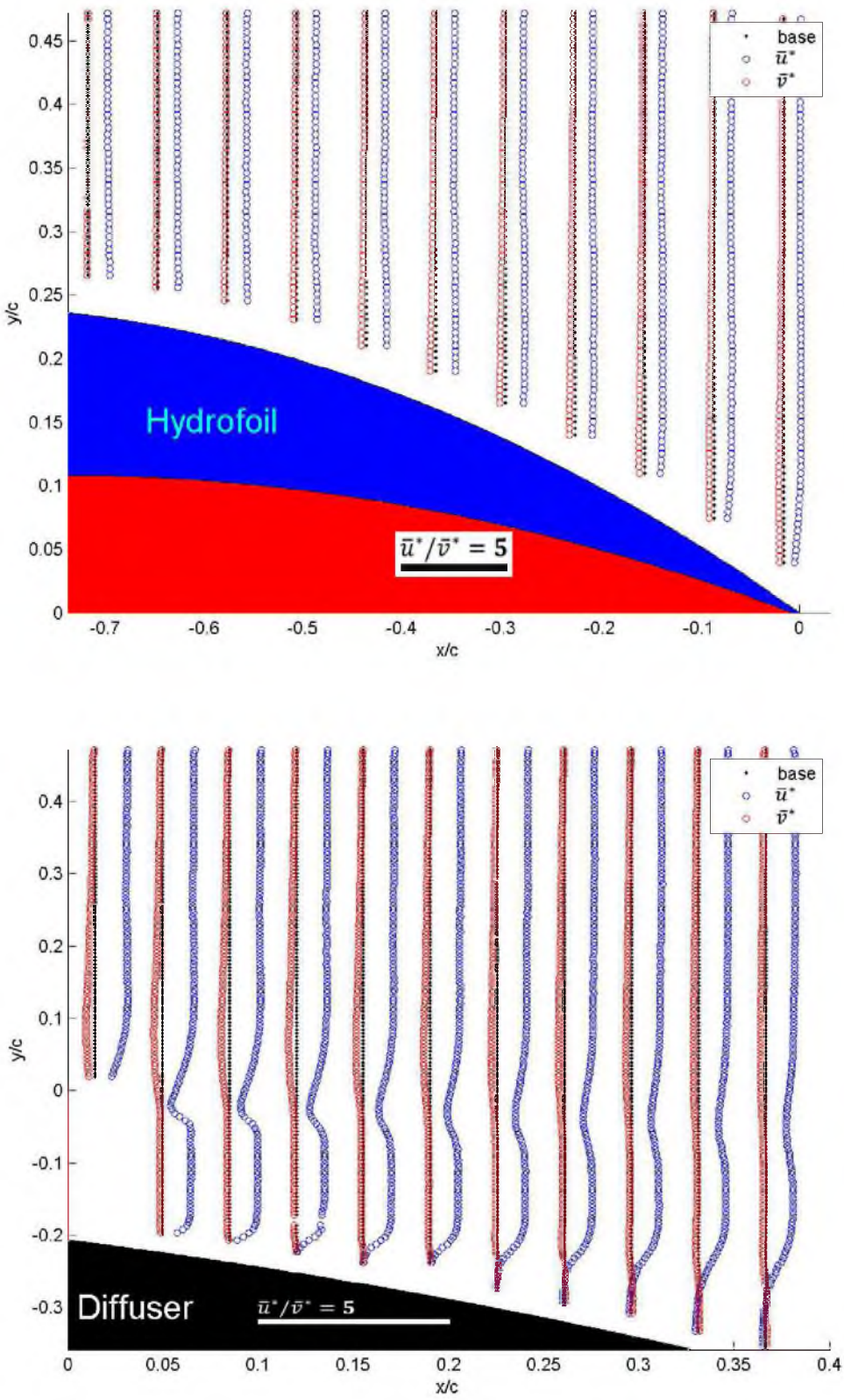

Figure 4.29. Velocity profiles for the low roughness experiment at 10°. A) (top) Above the hydrofoil. B) (bottom) Downstream of the hydrofoil.

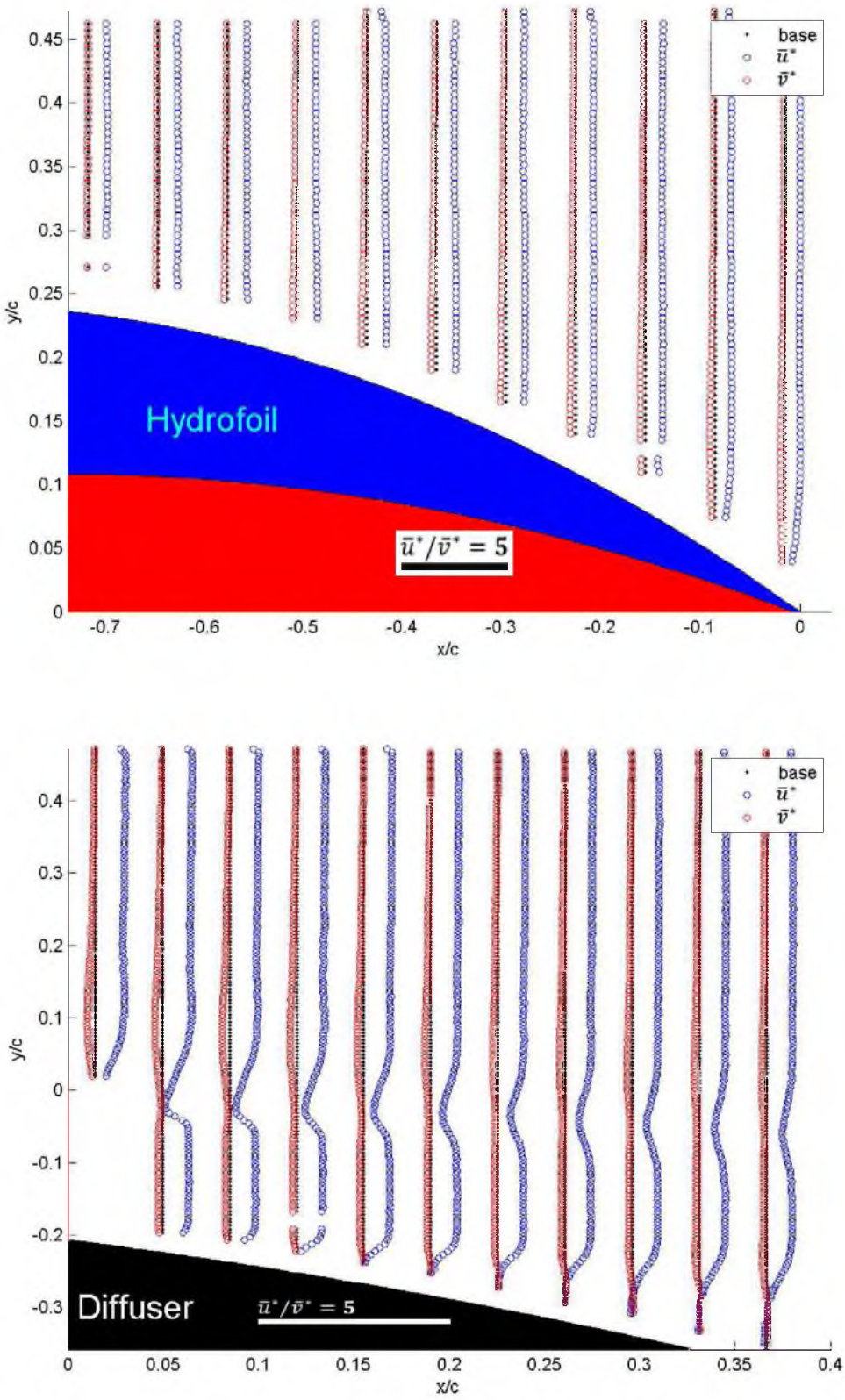

Figure 4.30. Velocity profiles for the medium roughness experiment at 10°. A) (top) Above the hydrofoil. B) (bottom) Downstream of the hydrofoil.

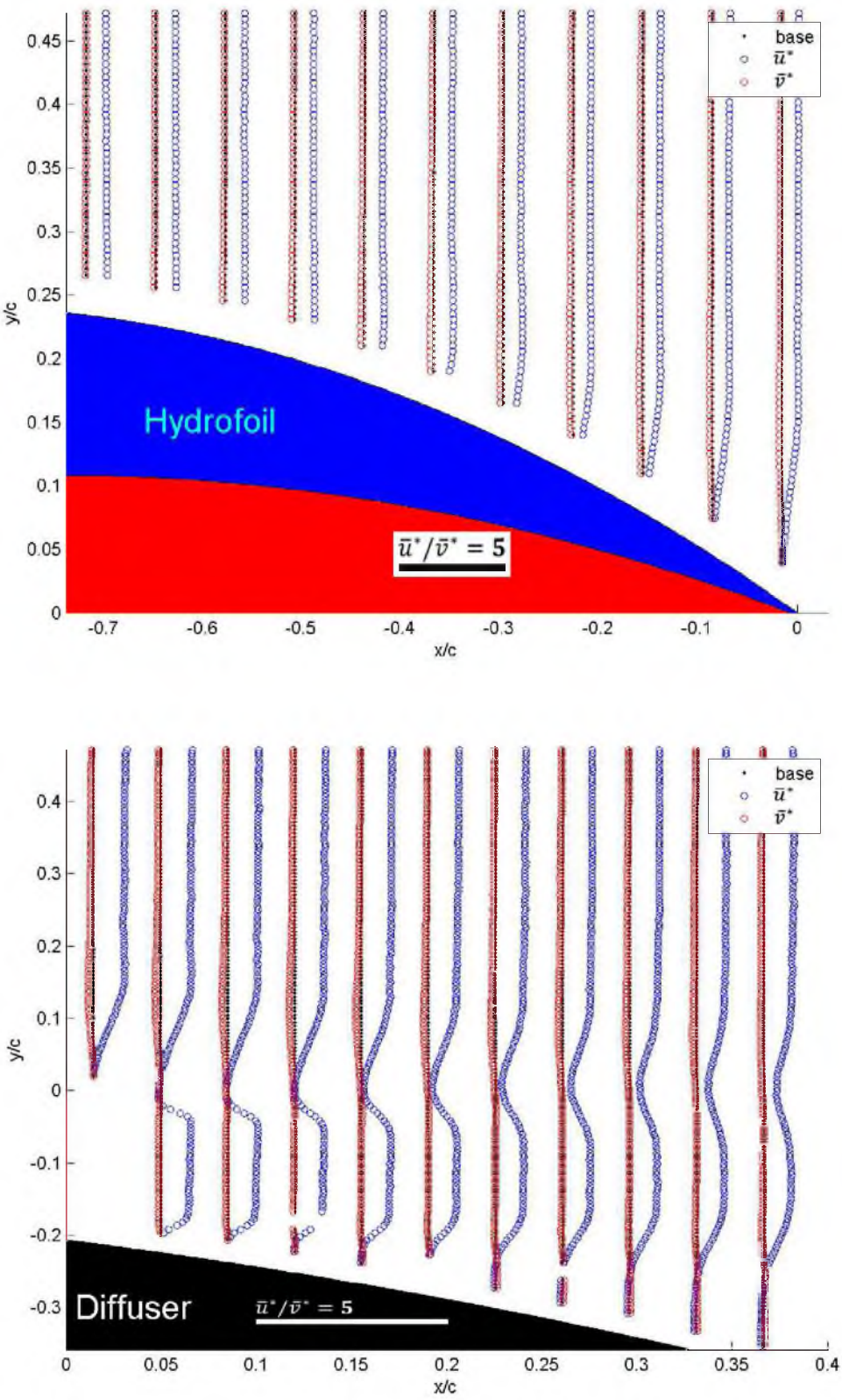

Figure 4.31. Velocity profiles for the high roughness experiment at 10°. A) (top) Above the hydrofoil. B) (bottom) Downstream of the hydrofoil.

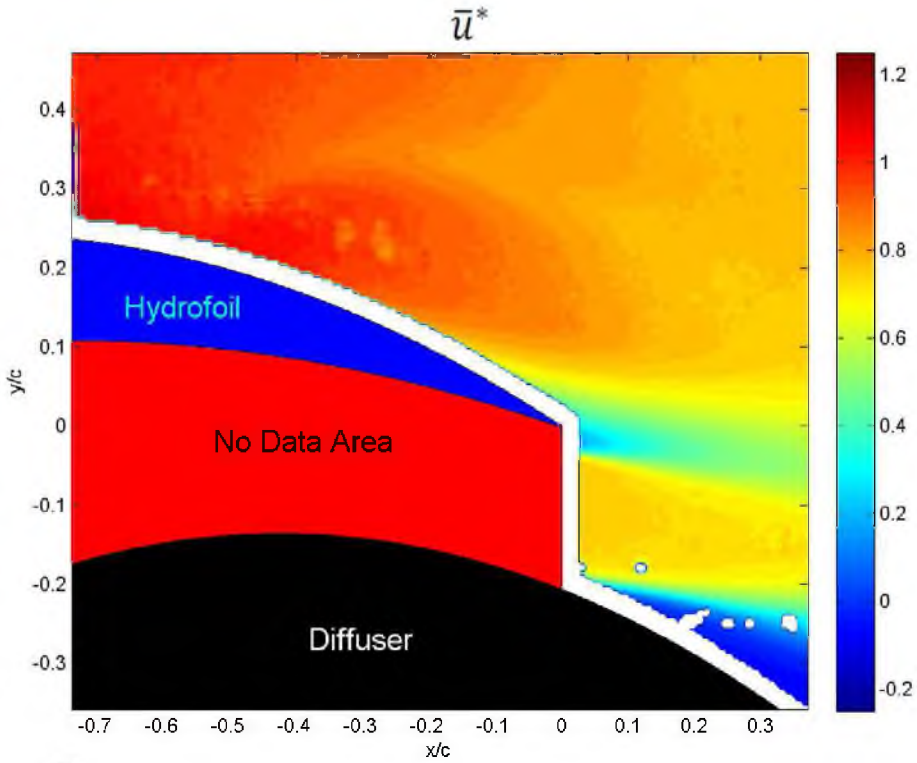

Figure 4.32. $\bar{u}^*$ contour plot of low roughness at 10°.

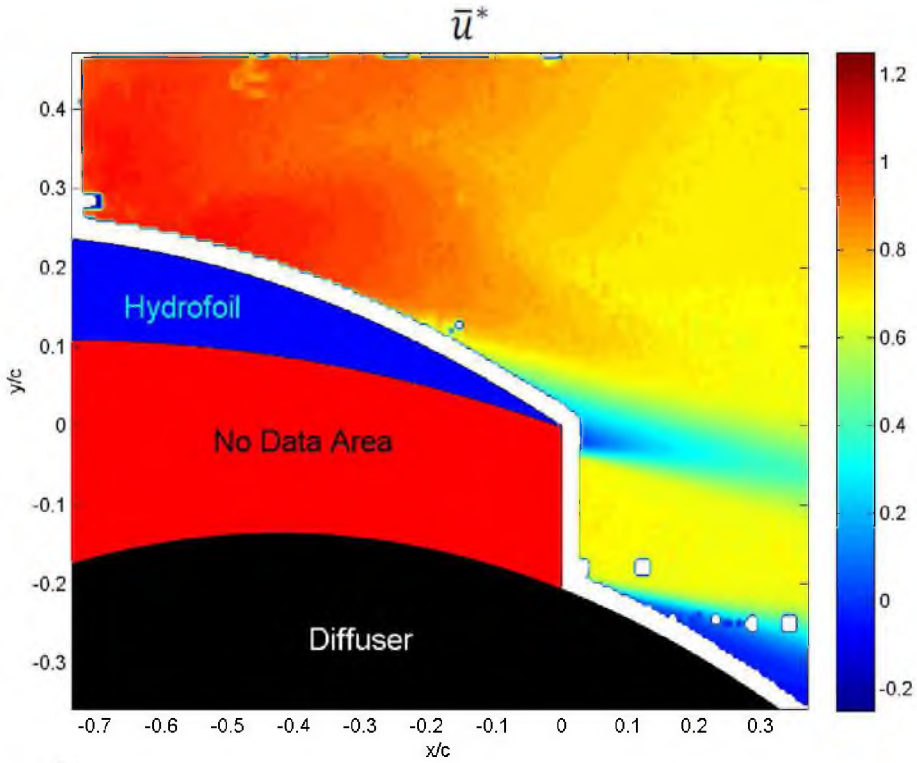

Figure 4.33. $\bar{u}^*$ contour plot of medium roughness at 10°.

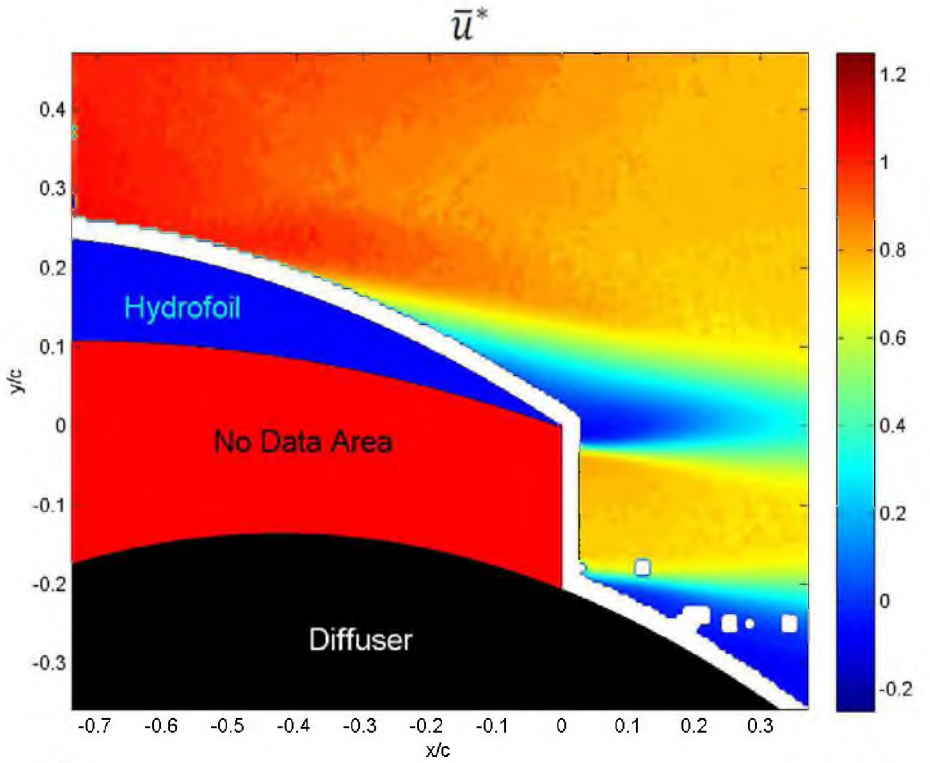

Figure 4.34. $\bar{u}^*$ contour plot of high roughness at 10°.

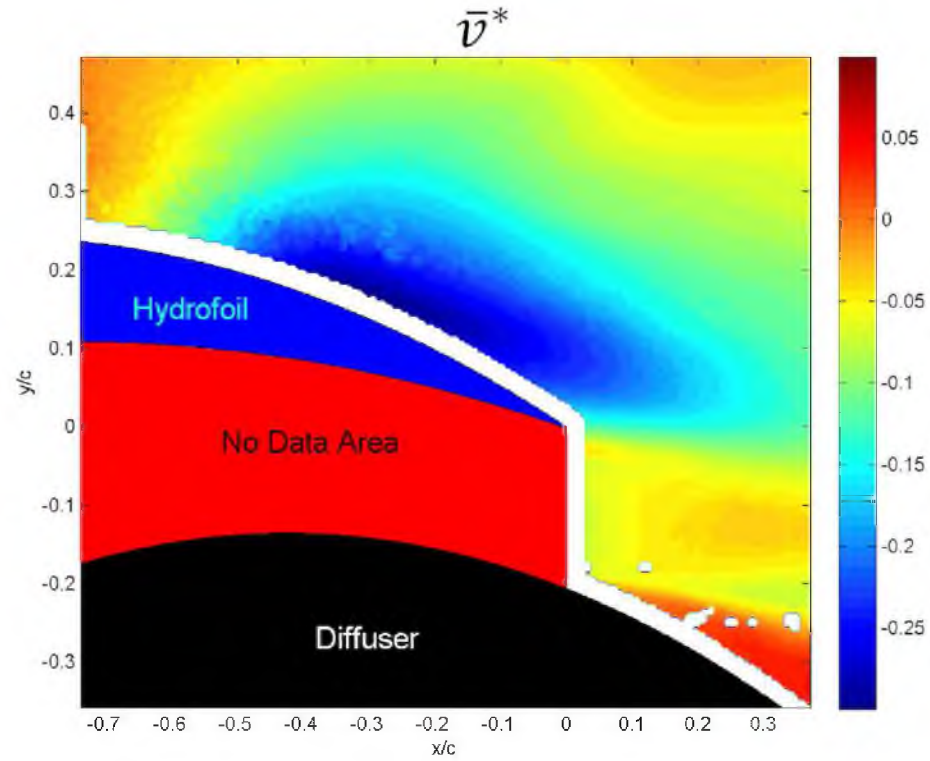

Figure 4.35. $\bar{v}^*$ contour plot of low roughness at 10°.

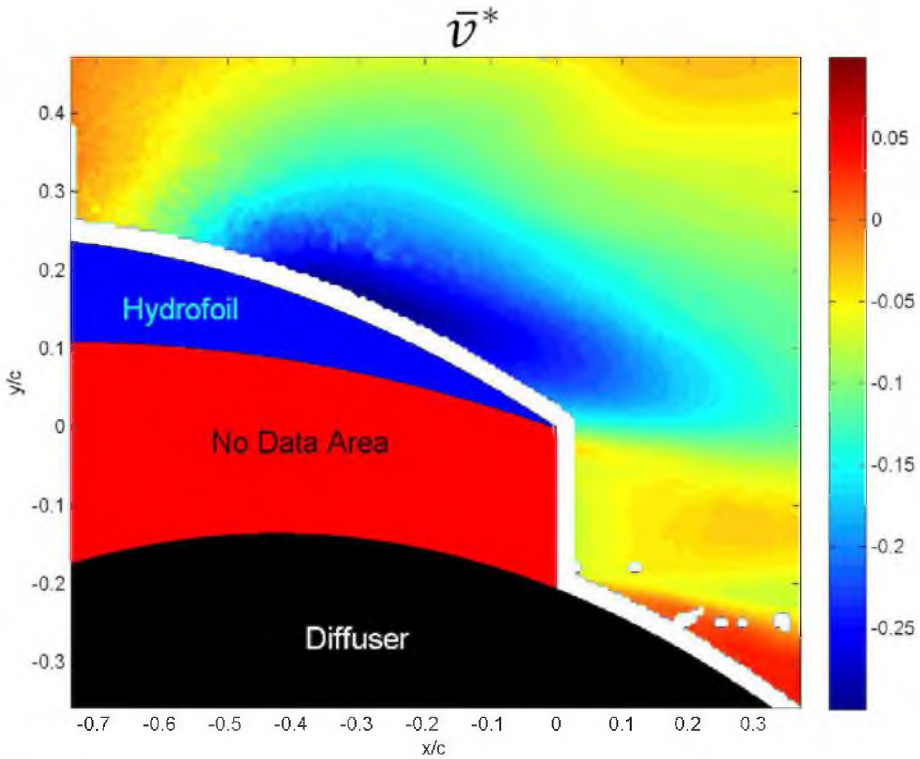

Figure 4.36. $\bar{v}^*$ contour plot of medium roughness at 10°.

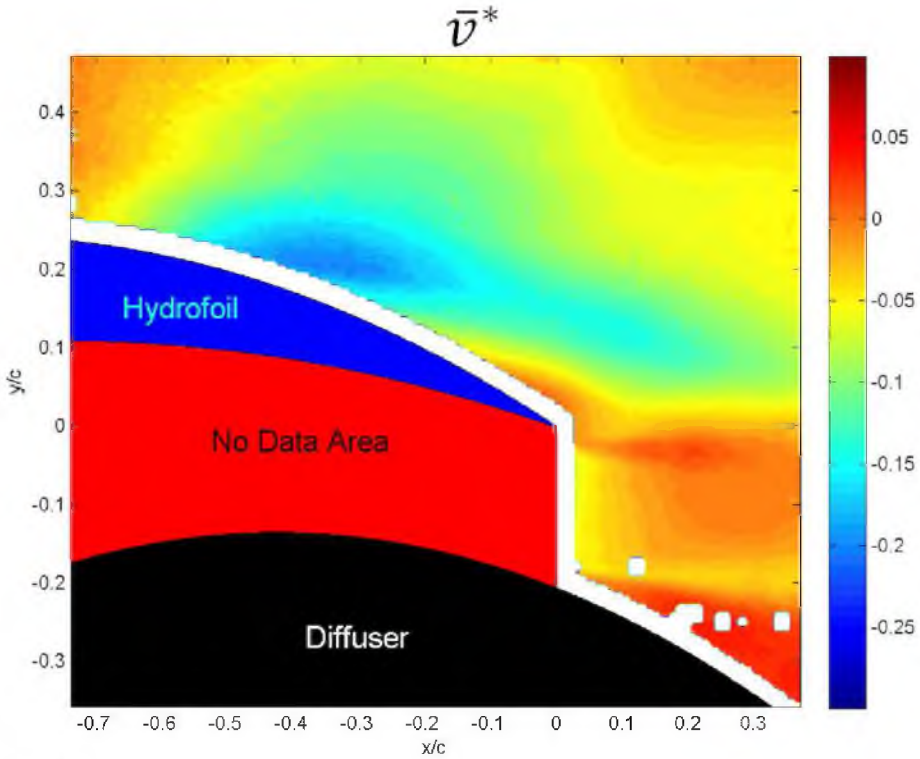

Figure 4.37. $\bar{v}^*$ contour plot of high roughness at 10°.

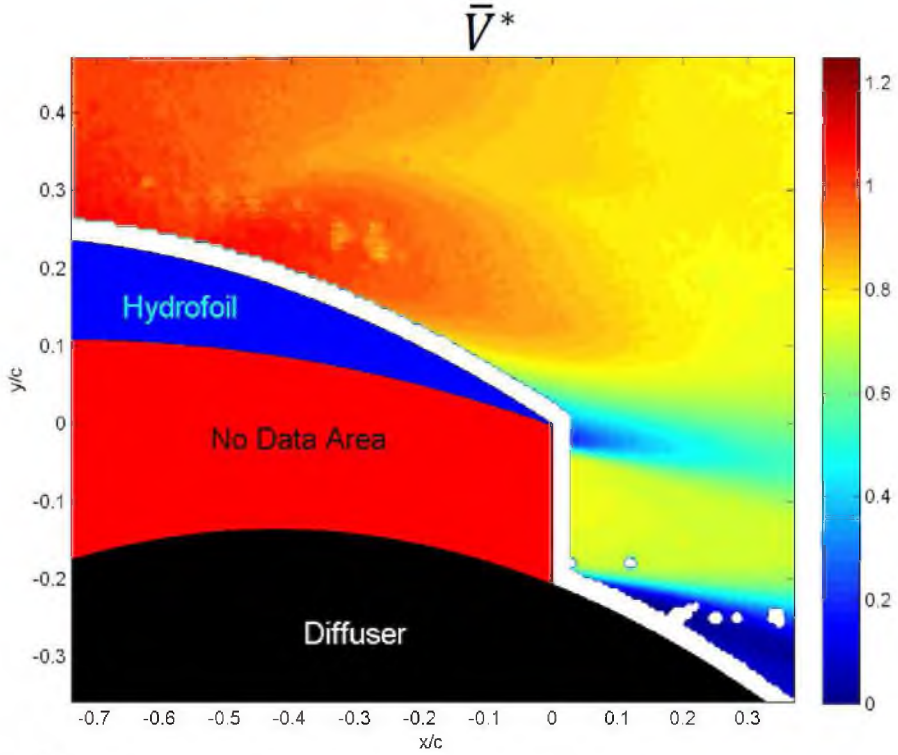

Figure 4.38. $\bar{V}^*$ contour plot of low roughness at 10°.

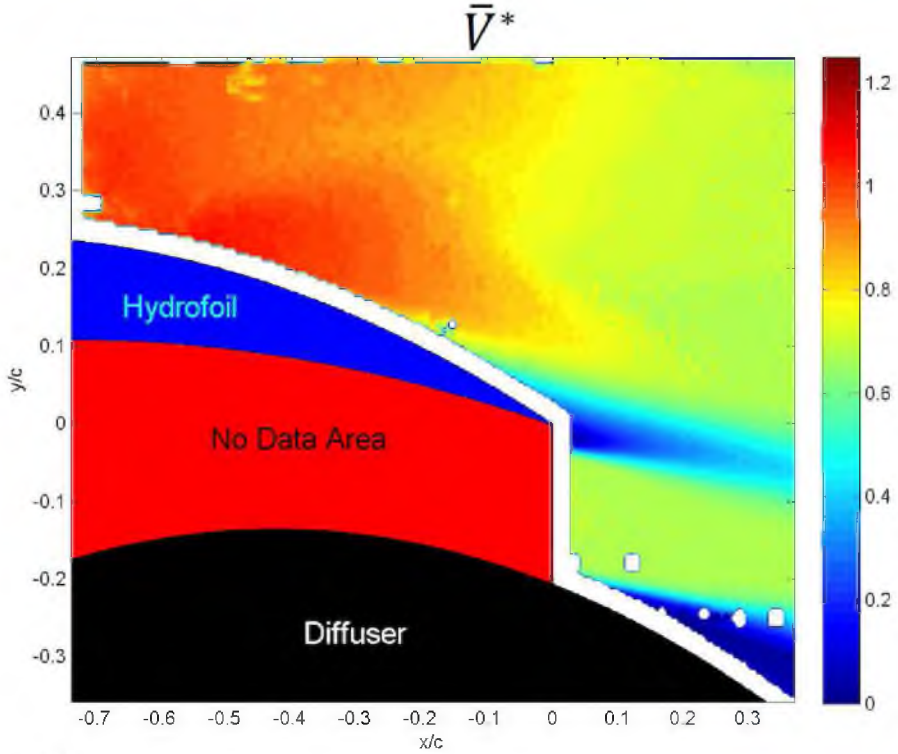

Figure 4.39. $\bar{V}^*$ contour plot of medium roughness at 10°.

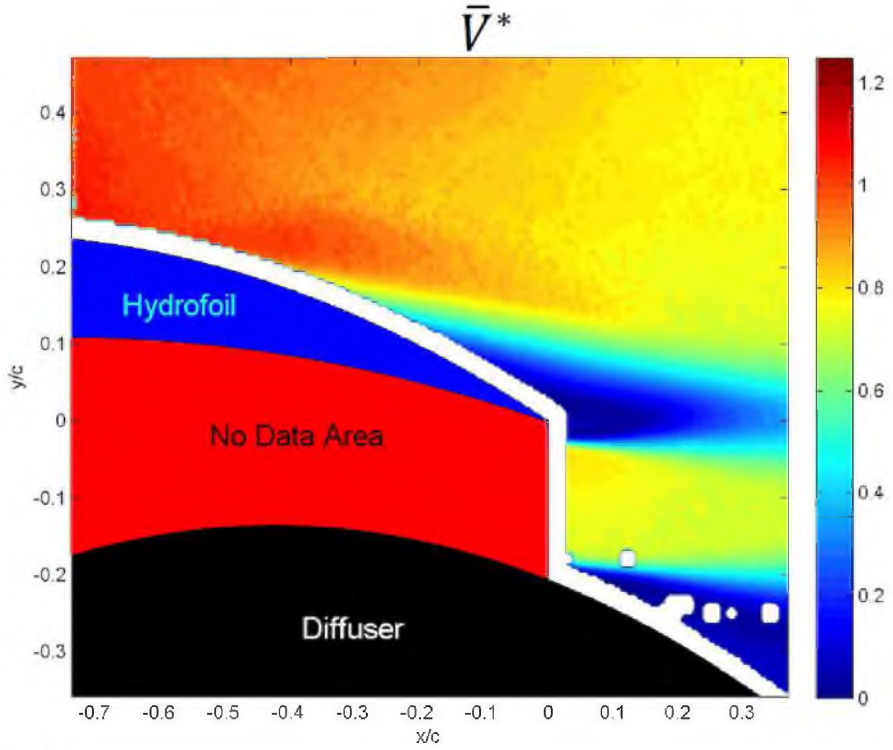

Figure 4.40. $\bar{V}^*$ contour plot of high roughness at 0°.

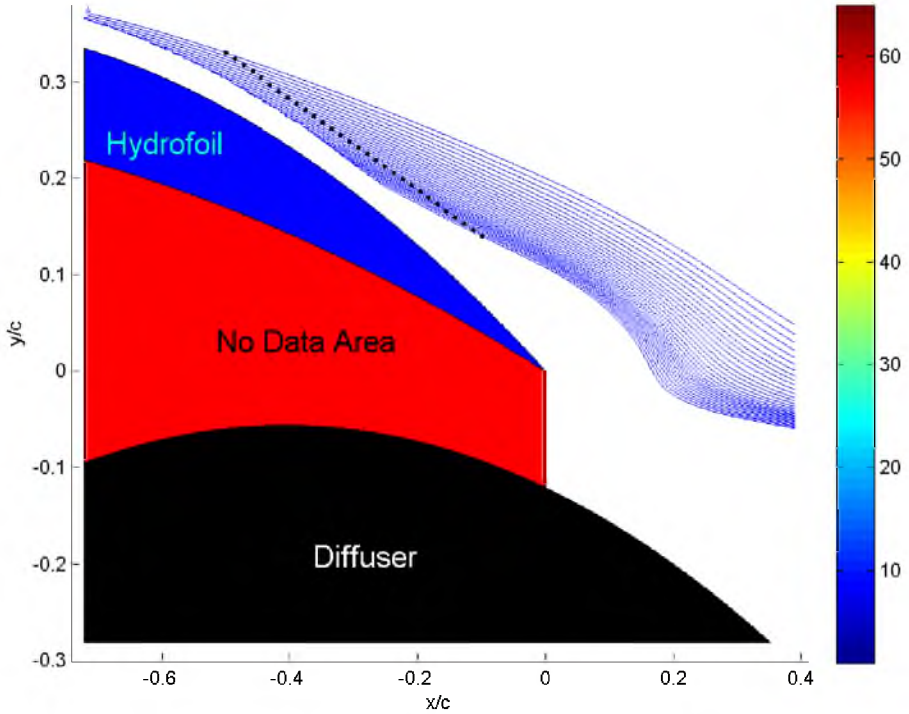

Figure 4.41. Streamlines for the low roughness experiment at 17°.

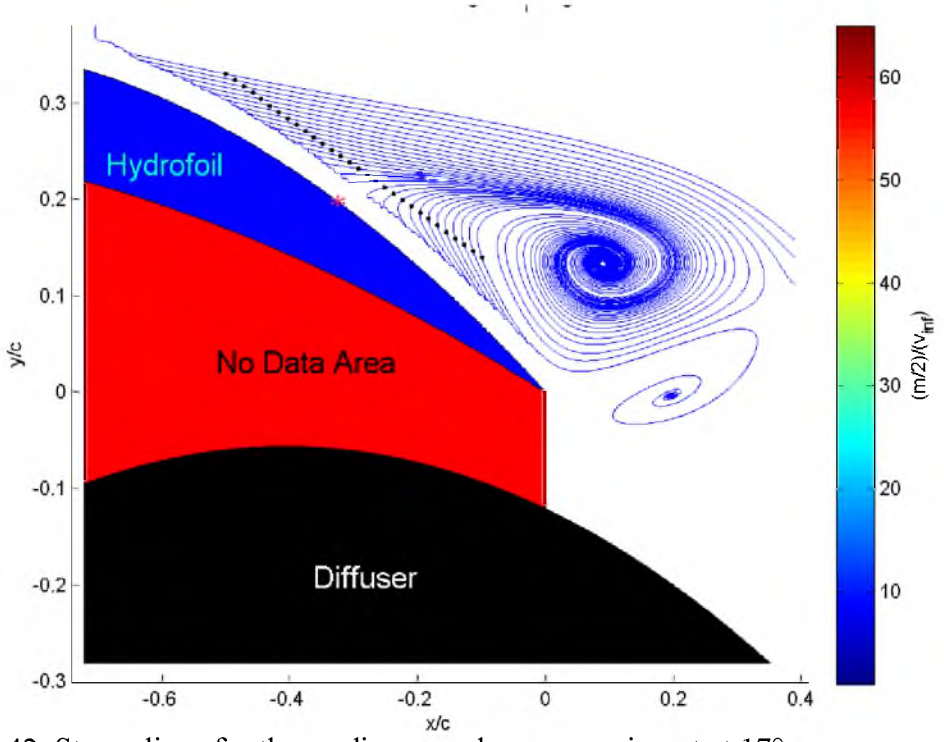

Figure 4.42. Streamlines for the medium roughness experiment at 17°.

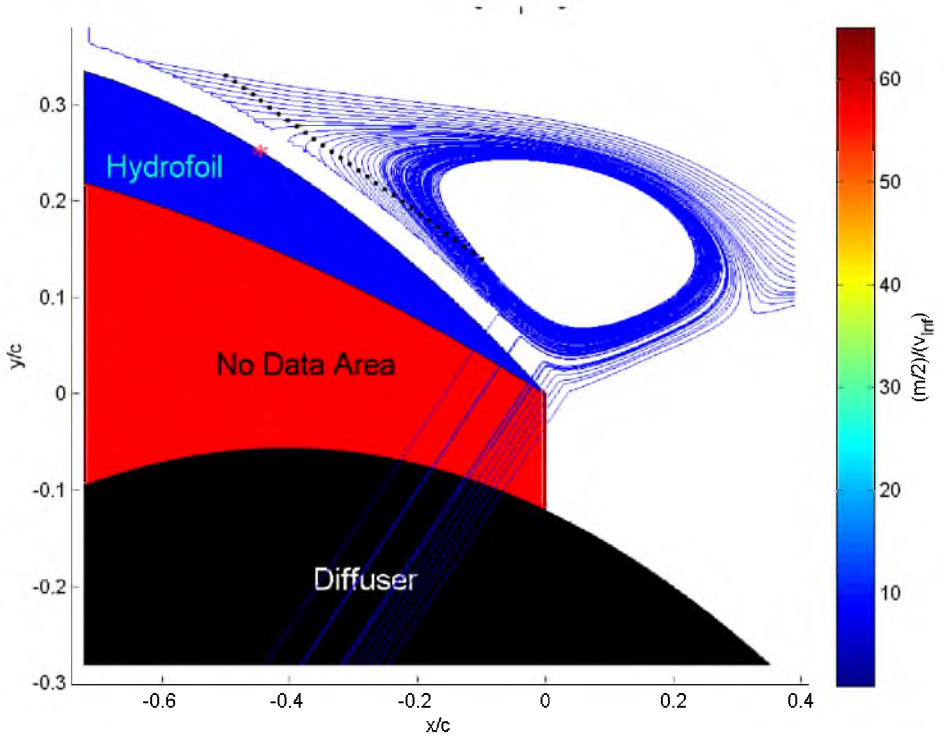

Figure 4.43. Streamlines for the high roughness experiment at 17°.

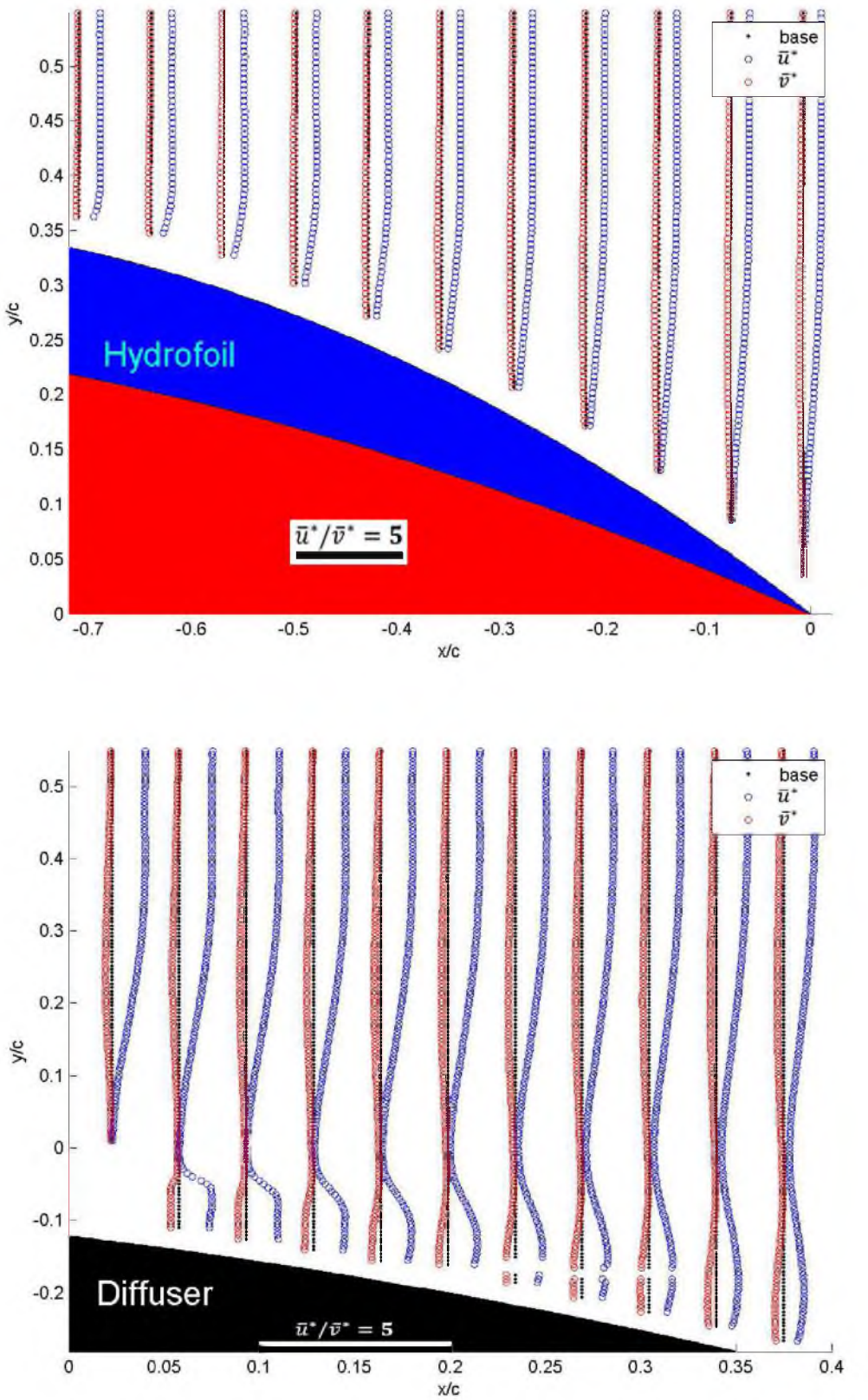

Figure 4.44. Velocity profiles for the low roughness experiment at 17°. A) (top) Above the hydrofoil. B) (bottom) Downstream of the hydrofoil.

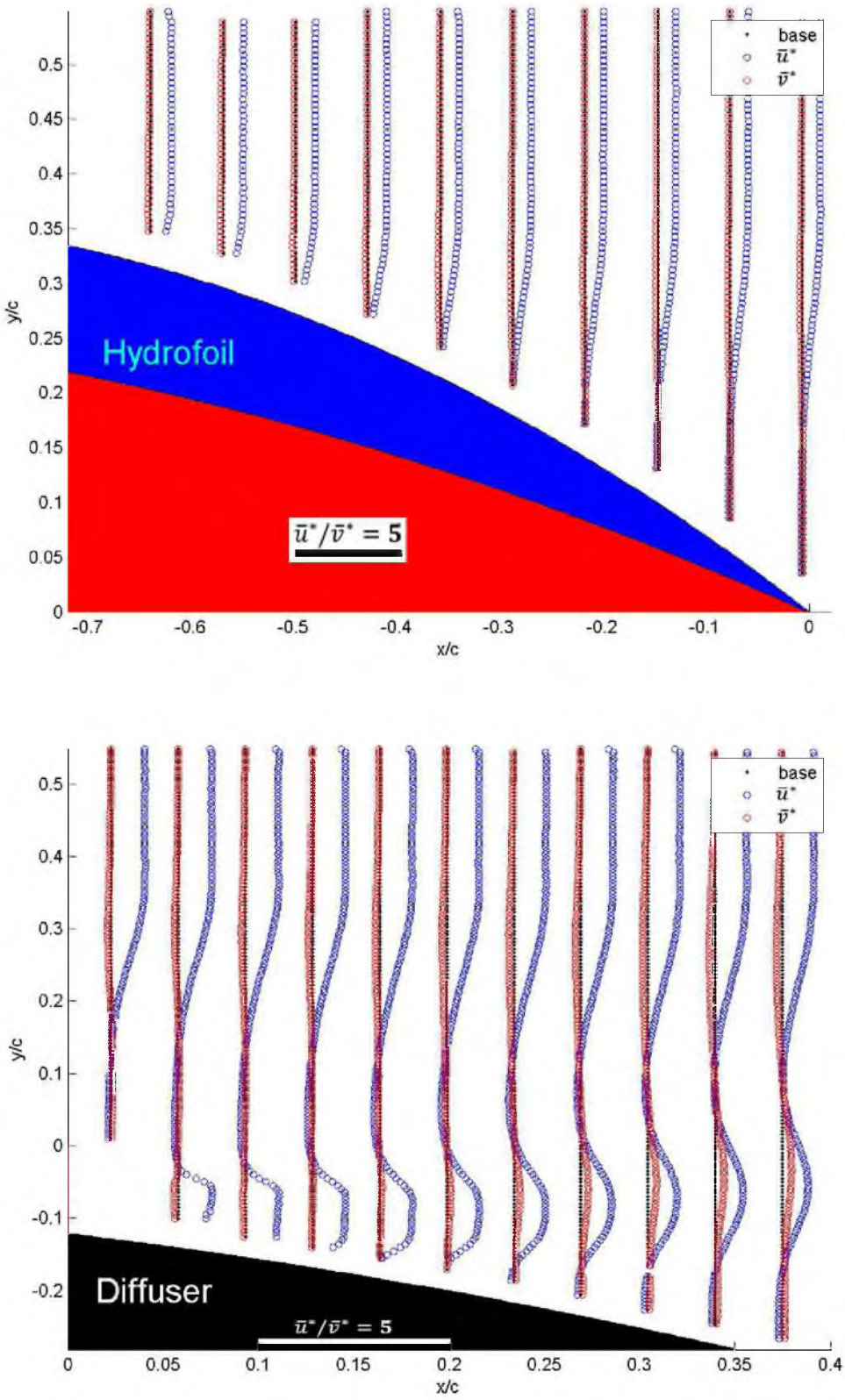

Figure 4.45. Velocity profiles for the medium roughness experiment at 17°. A) (top) Above the hydrofoil. B) (bottom) Downstream of the hydrofoil.

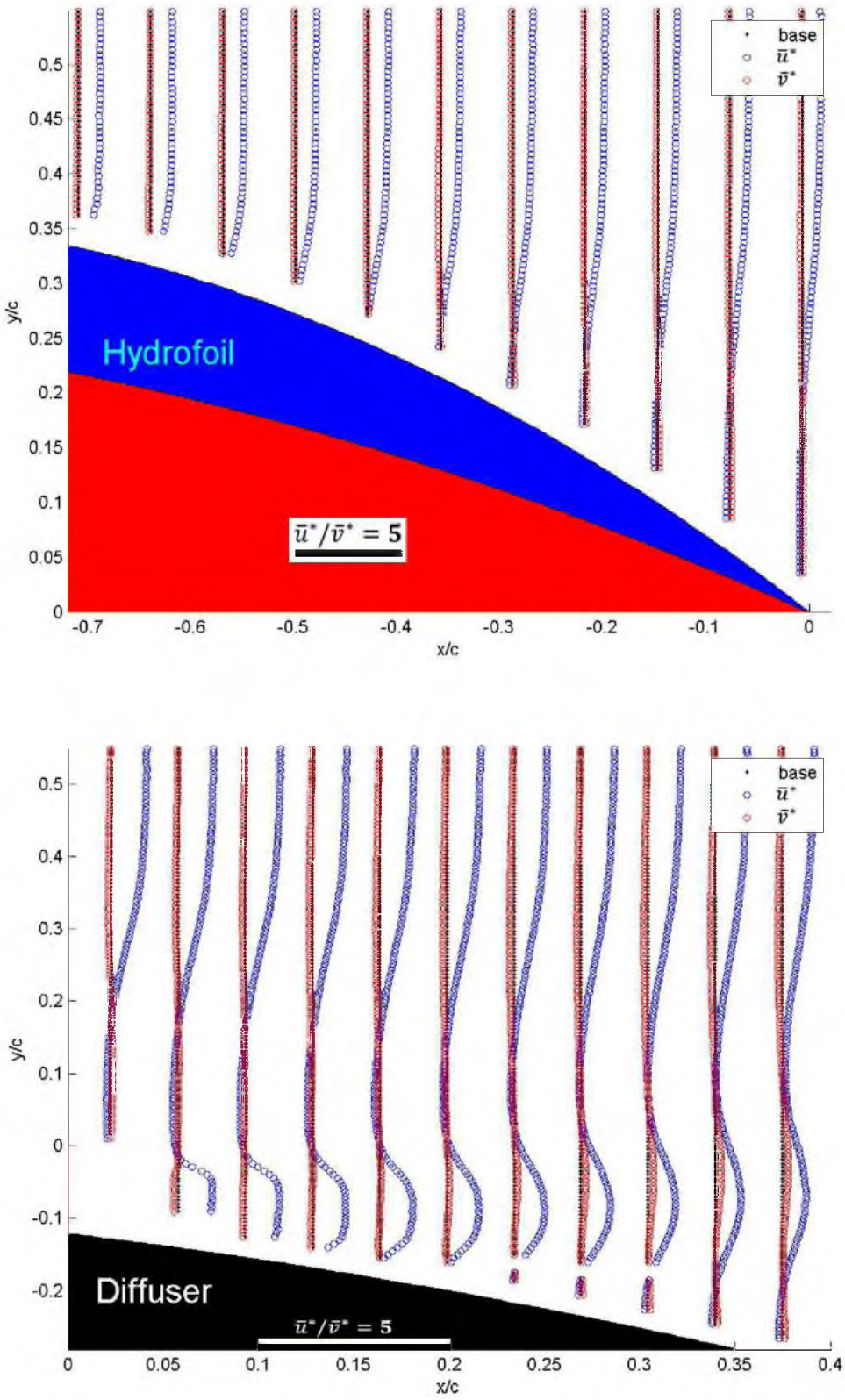

Figure 4.46. Velocity profiles for the high roughness experiment at 17°. A) (top) Above the hydrofoil. B) (bottom) Downstream of the hydrofoil.

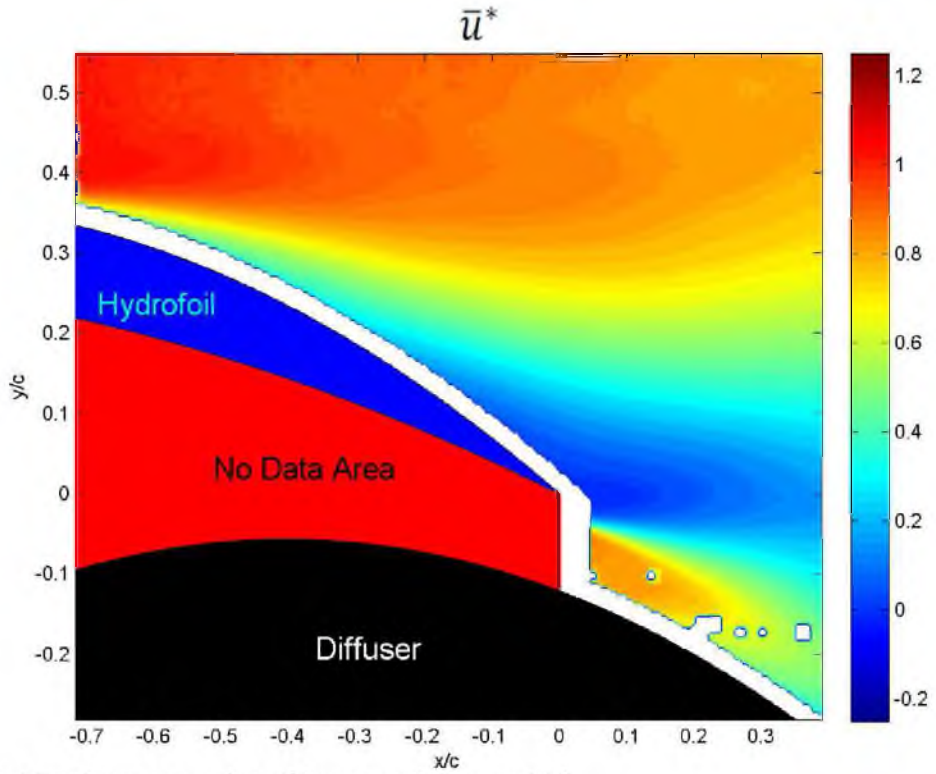

Figure 4.47. $\bar{u}^*$ contour plot of low roughness at 17°.

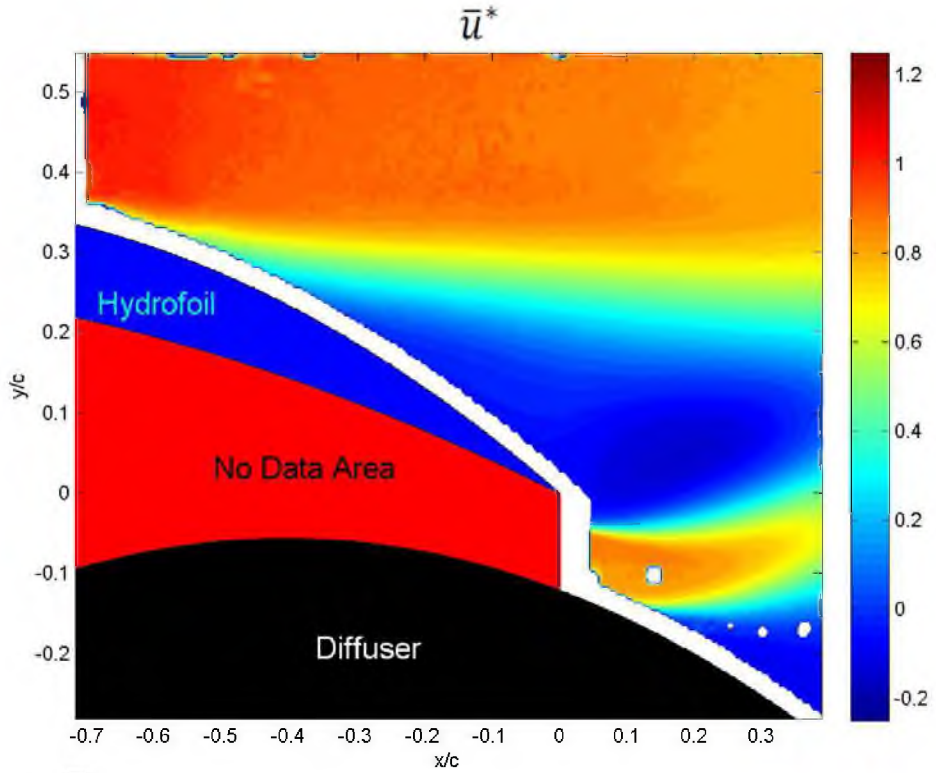

Figure 4.48. $\bar{u}^*$ contour plot of medium roughness at 17°.

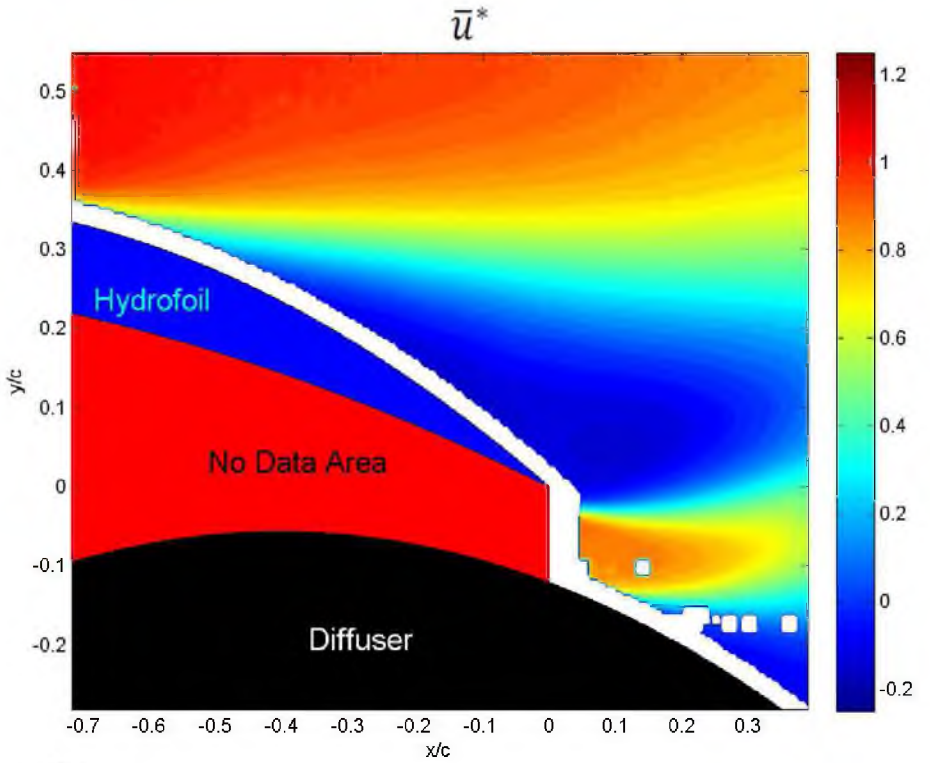

Figure 4.49. $\bar{u}^*$ contour plot of high roughness at 17°.

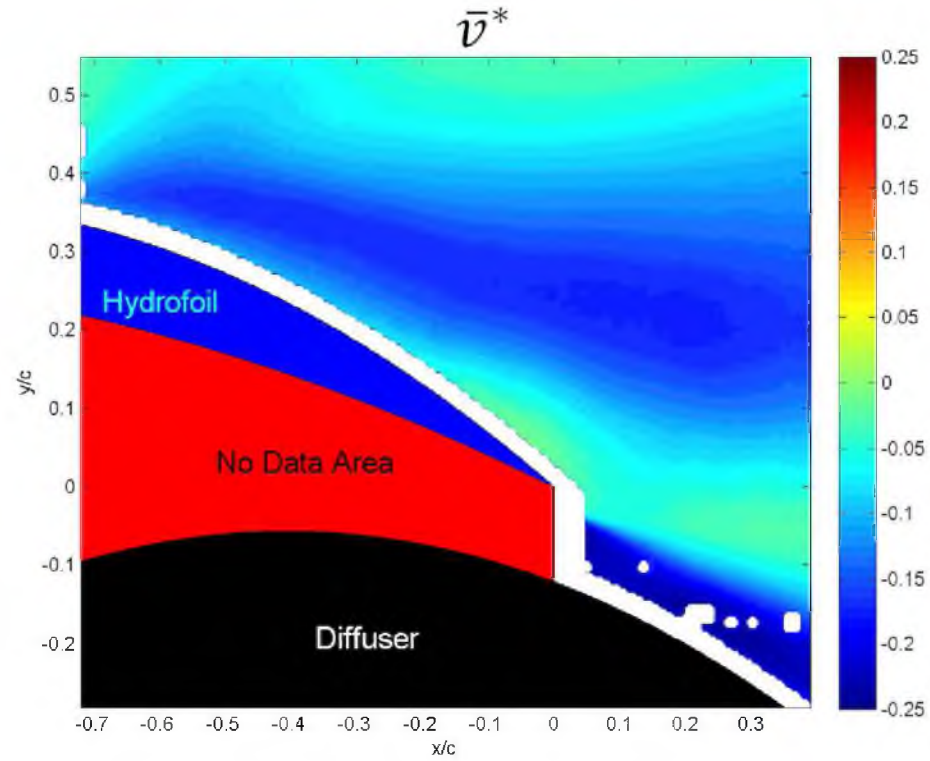

Figure 4.50. $\bar{v}^*$ contour plot of low roughness at 17°.

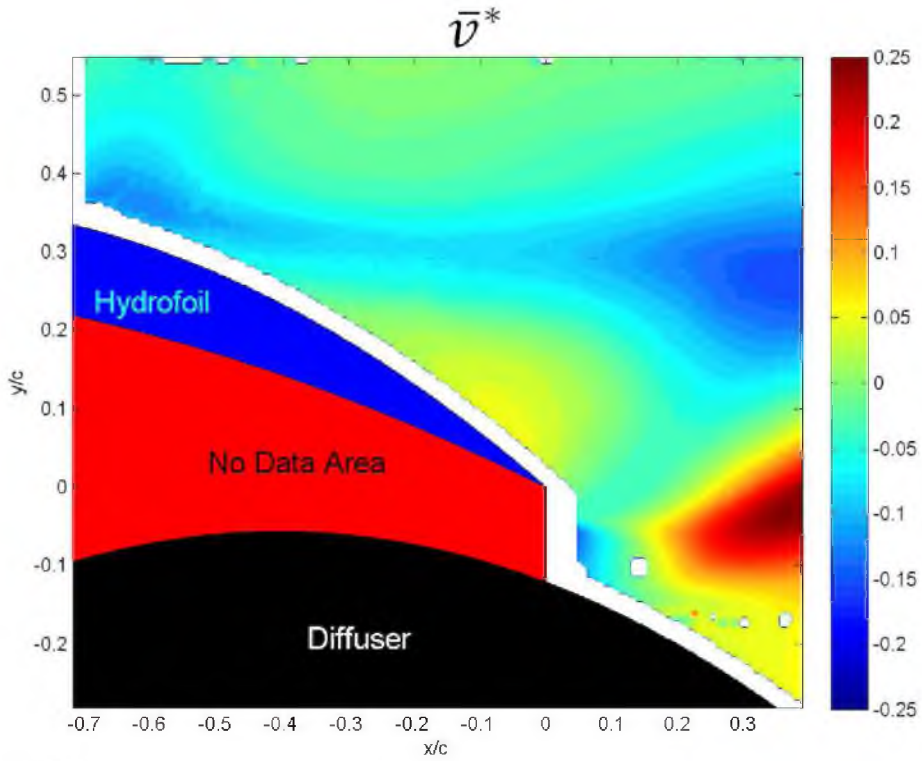

Figure 4.51. $\bar{v}^*$ contour plot of medium roughness at 17°.

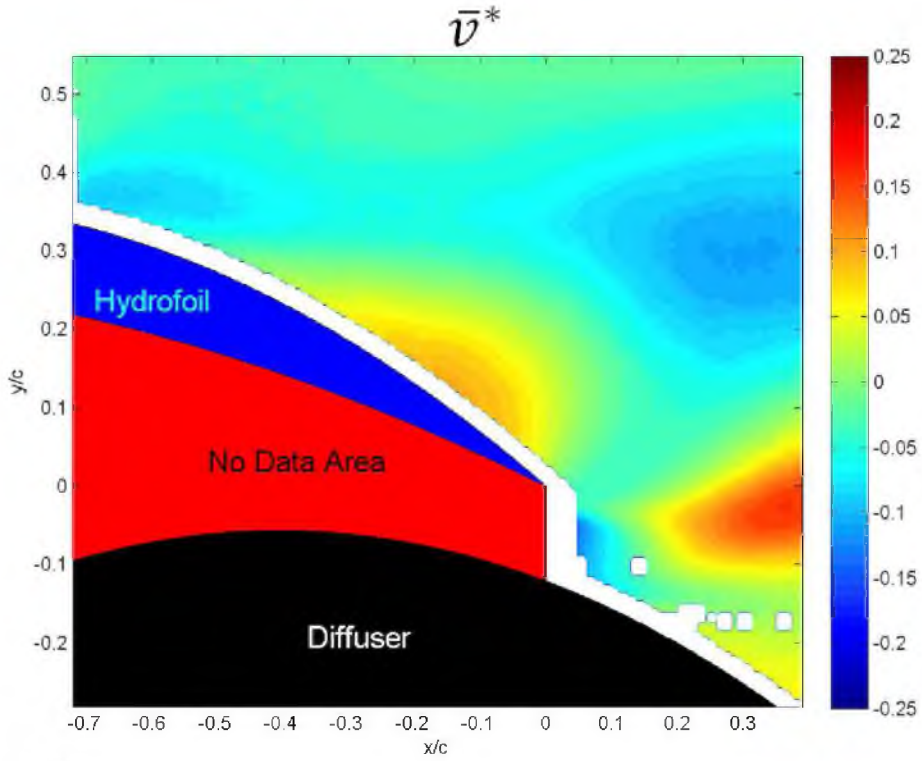

Figure 4.52. $\bar{v}^*$ contour plot of high roughness at 17°.

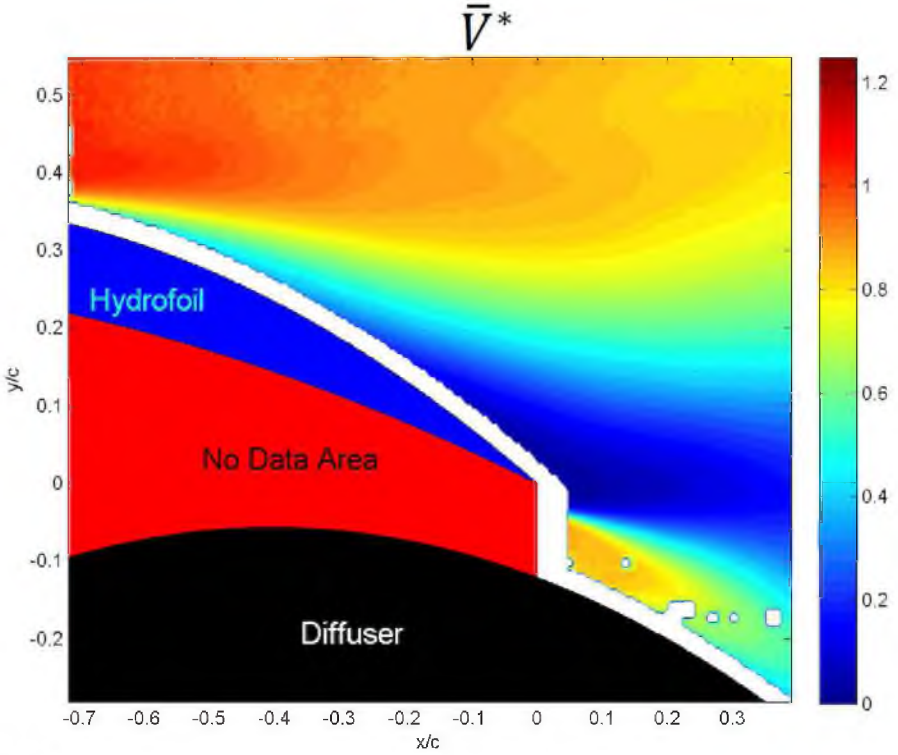

Figure 4.53. $\bar{V}^*$ contour plot of low roughness at 17°.

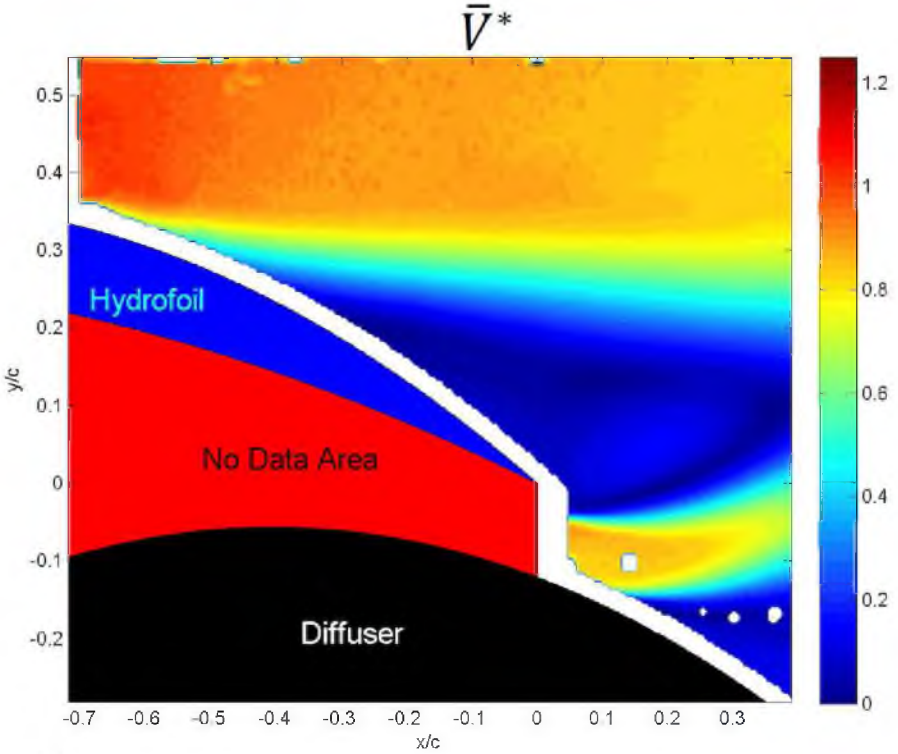

Figure 4.54. $\bar{V}^*$ contour plot of medium roughness at 17°.

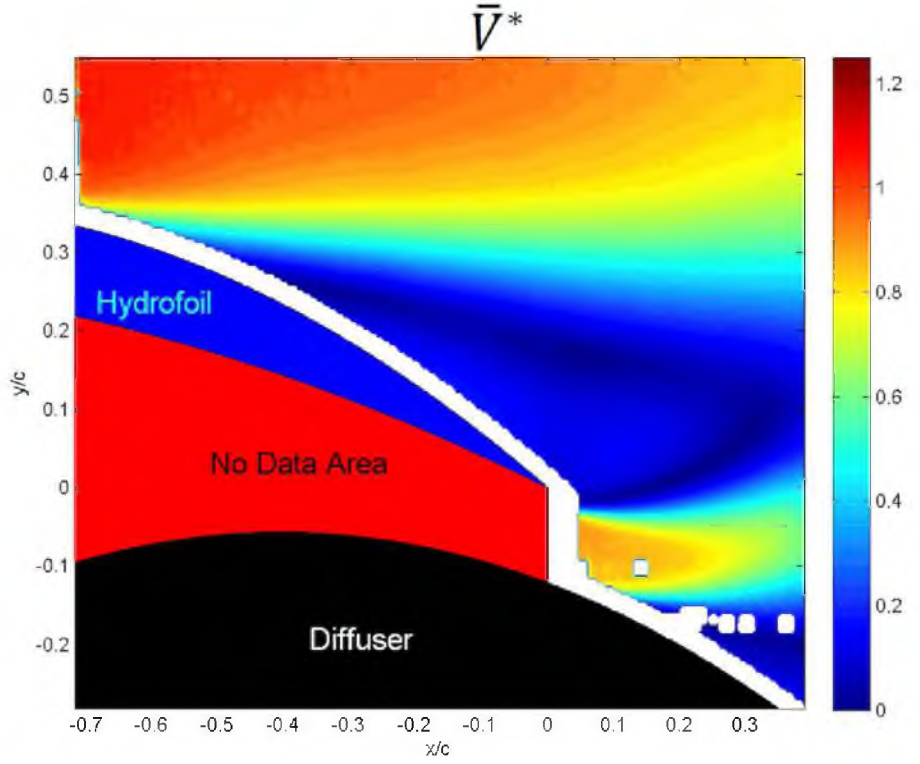

Figure 4.55. $\bar{V}^*$ contour plot of high roughness at 17°.

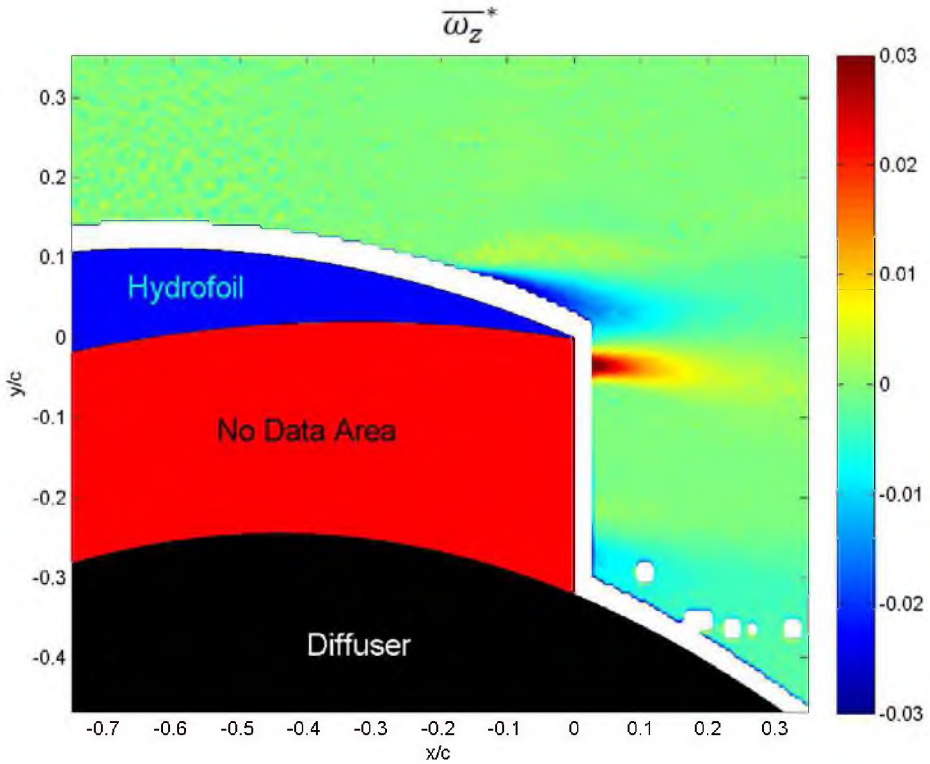

Figure 4.56. Mean Vorticity $\overline{\omega_z}^*$ for low roughness at 0°.

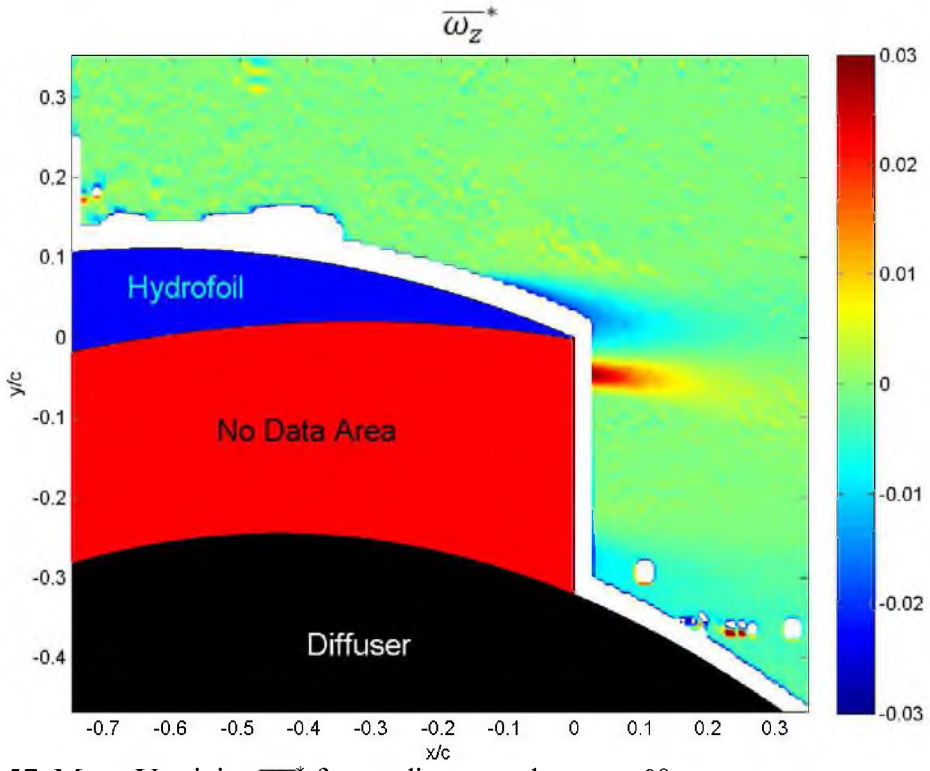

Figure 4.57. Mean Vorticity $\overline{\omega_z}^*$ for medium roughness at 0°.

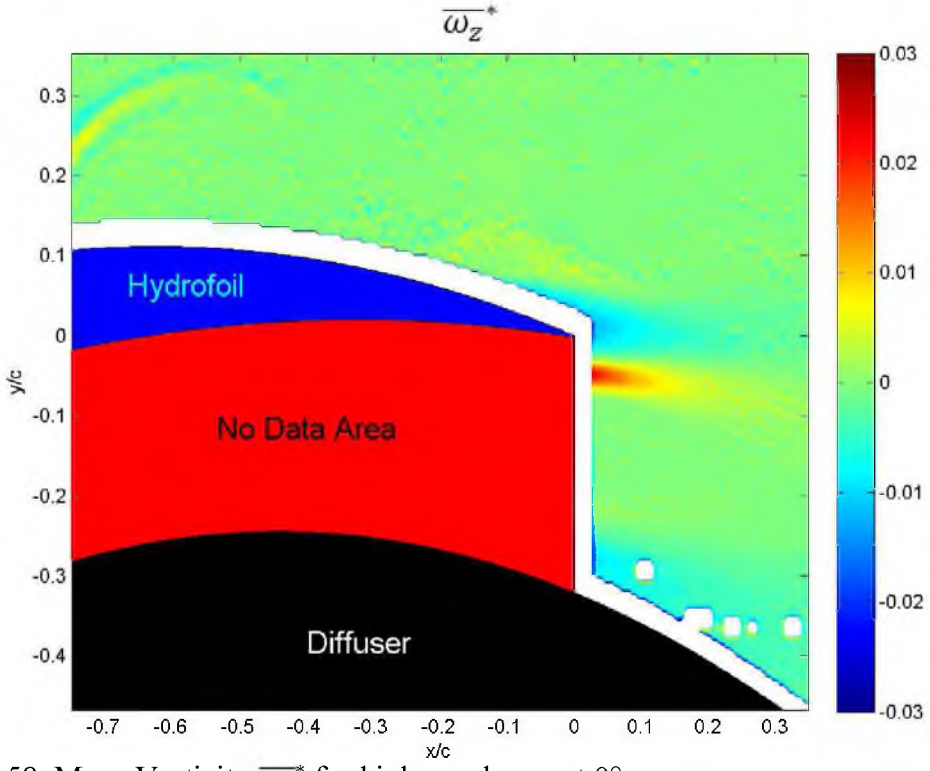

Figure 4.58. Mean Vorticity $\overline{\omega_z}^*$ for high roughness at 0°.

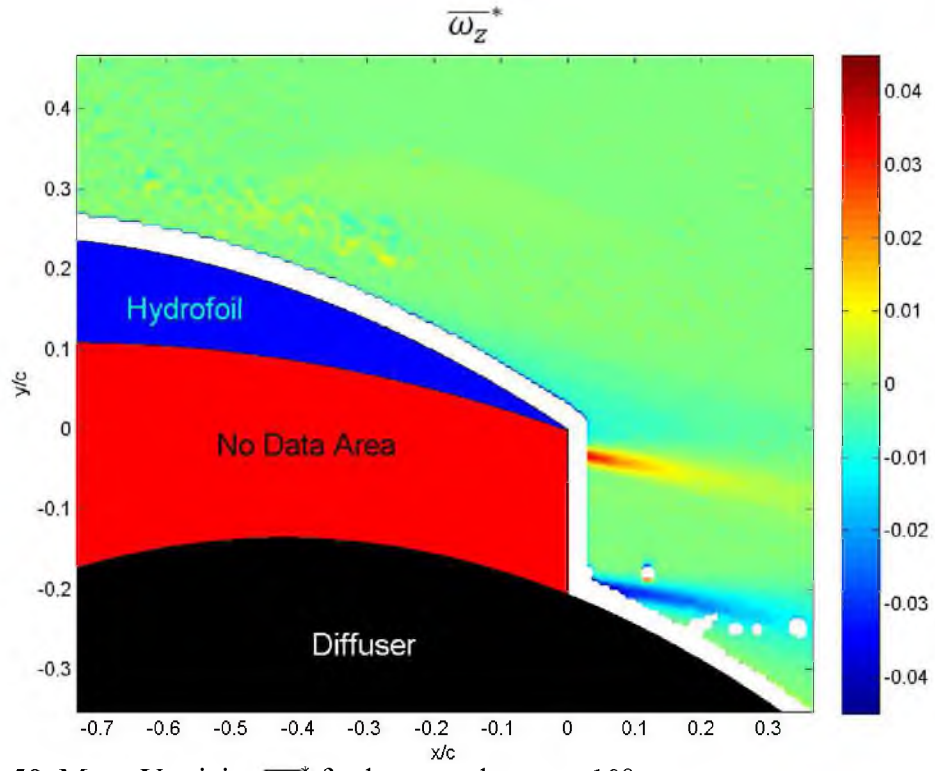

Figure 4.59. Mean Vorticity $\overline{\omega_z}^*$ for low roughness at 10°.

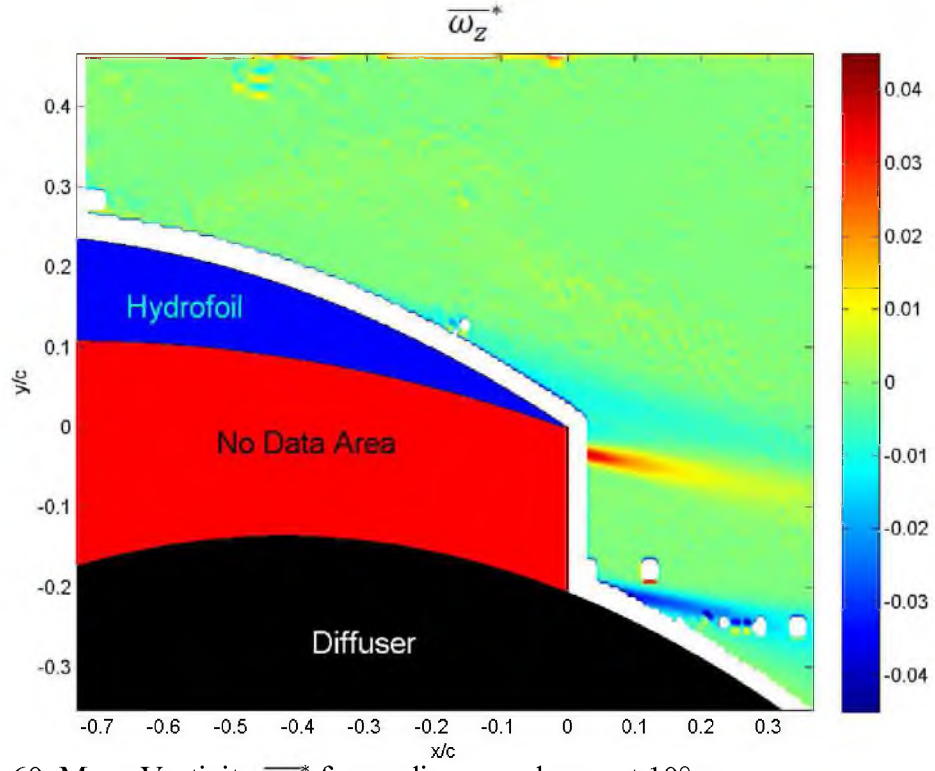

Figure 4.60. Mean Vorticity $\overline{\omega_z}^*$ for medium roughness at 10°.

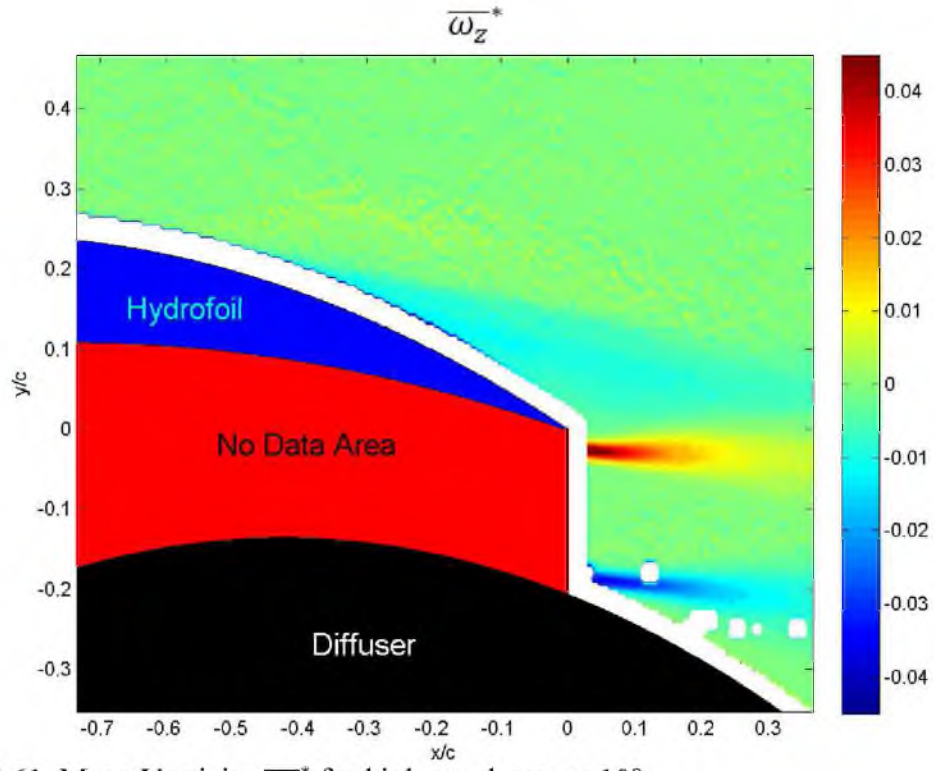

Figure 4.61. Mean Vorticity $\overline{\omega_z}^*$ for high roughness at 10°.

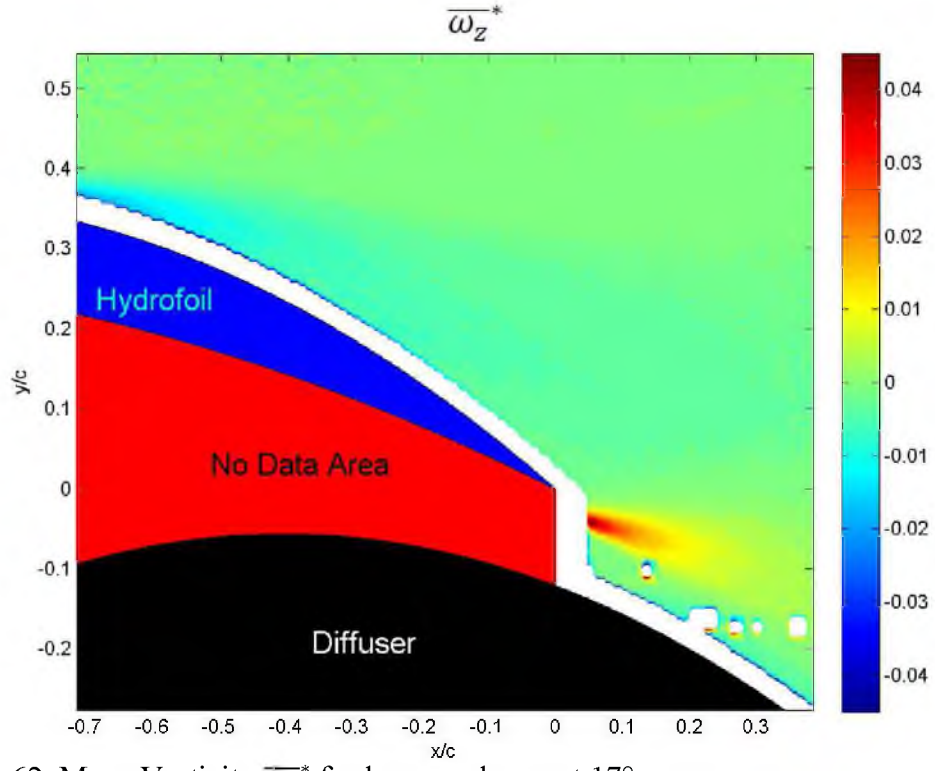

Figure 4.62. Mean Vorticity $\overline{\omega_z}^*$ for low roughness at 17°.

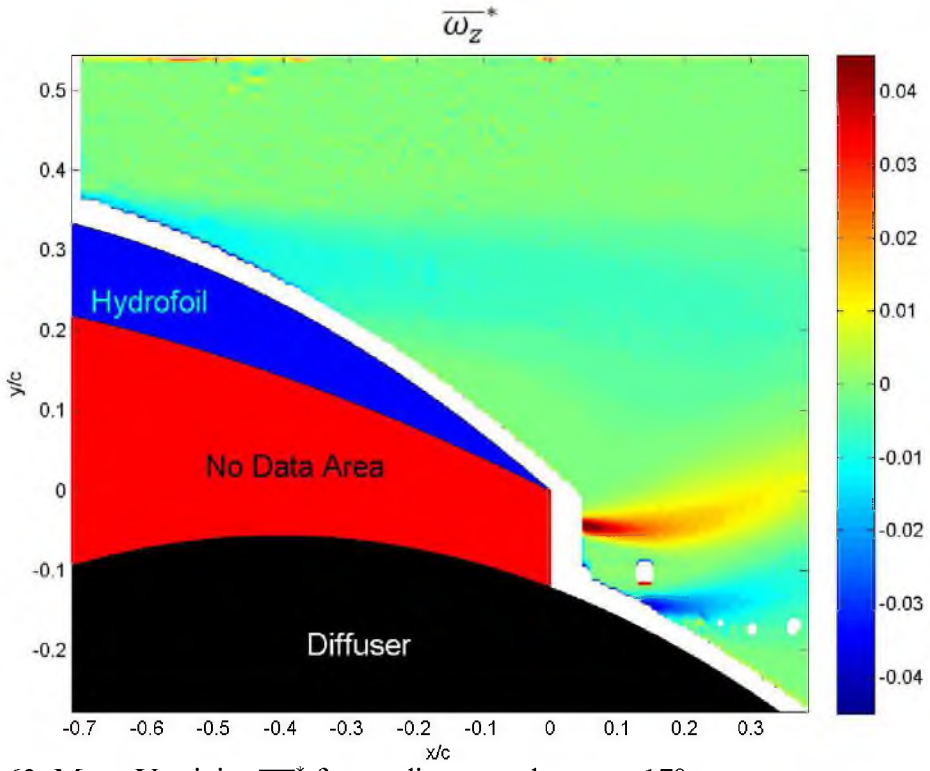

Figure 4.63. Mean Vorticity $\overline{\omega_z}^*$ for medium roughness at 17°.

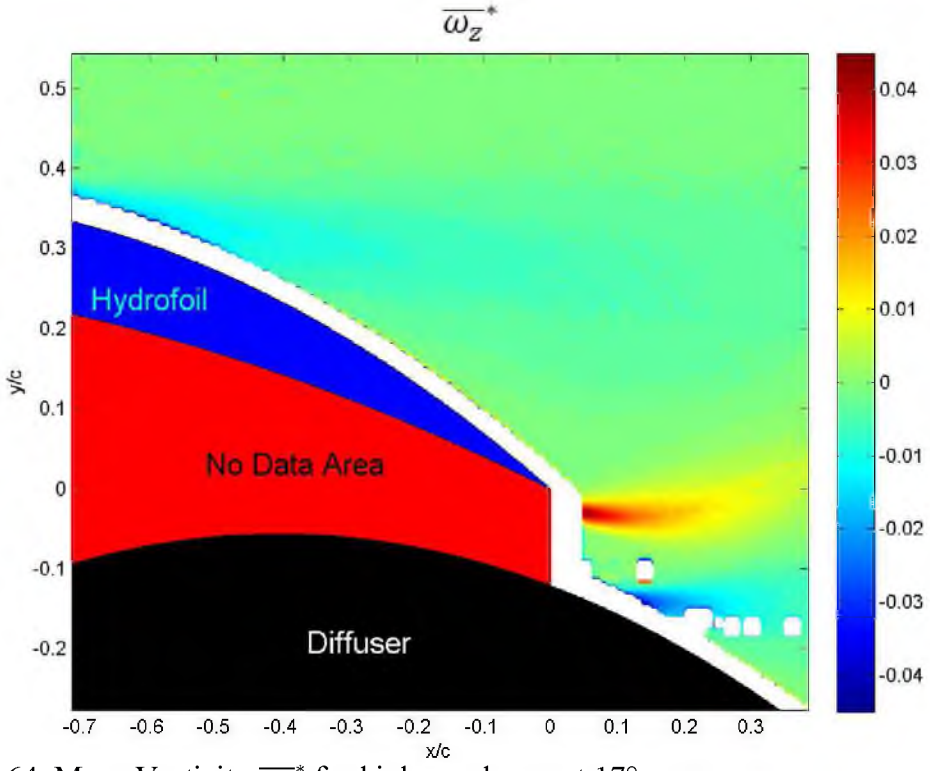

Figure 4.64. Mean Vorticity $\overline{\omega_z}^*$ for high roughness at 17°.

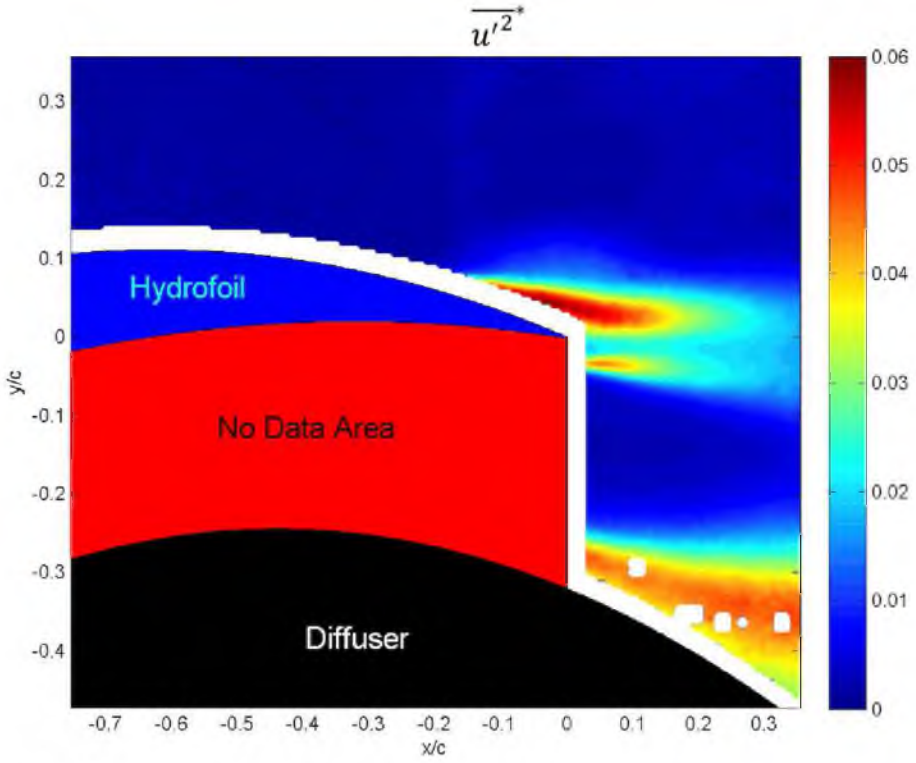

Figure 4.65 $\overline{u'^2}^*$ for low roughness at 0°.

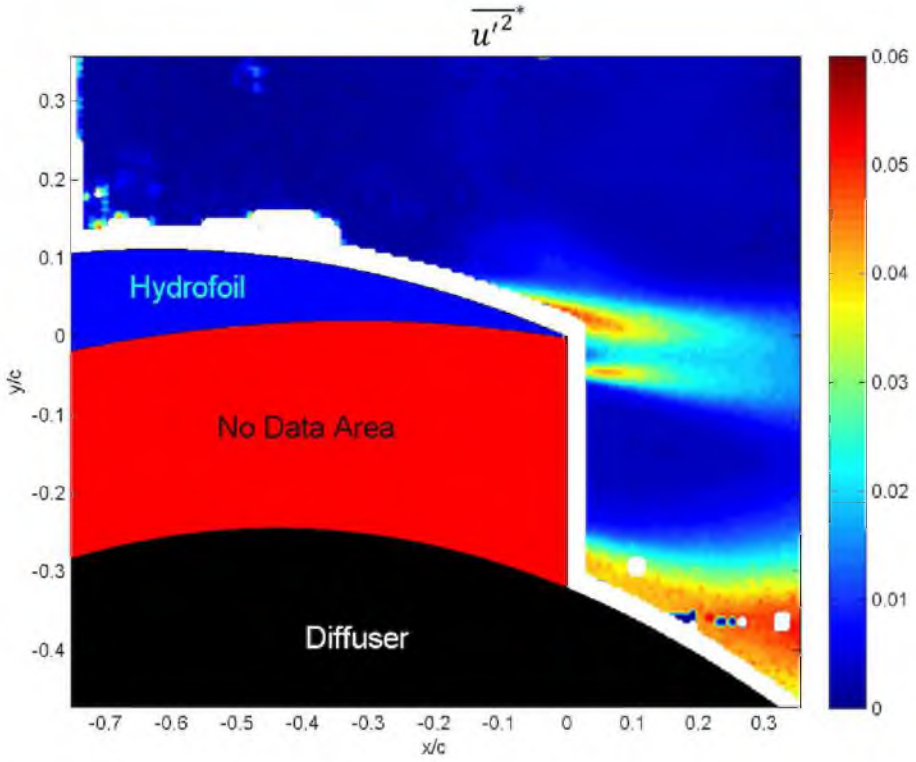

Figure 4.66 $\overline{u'^2}^*$ for medium roughness at 0°.

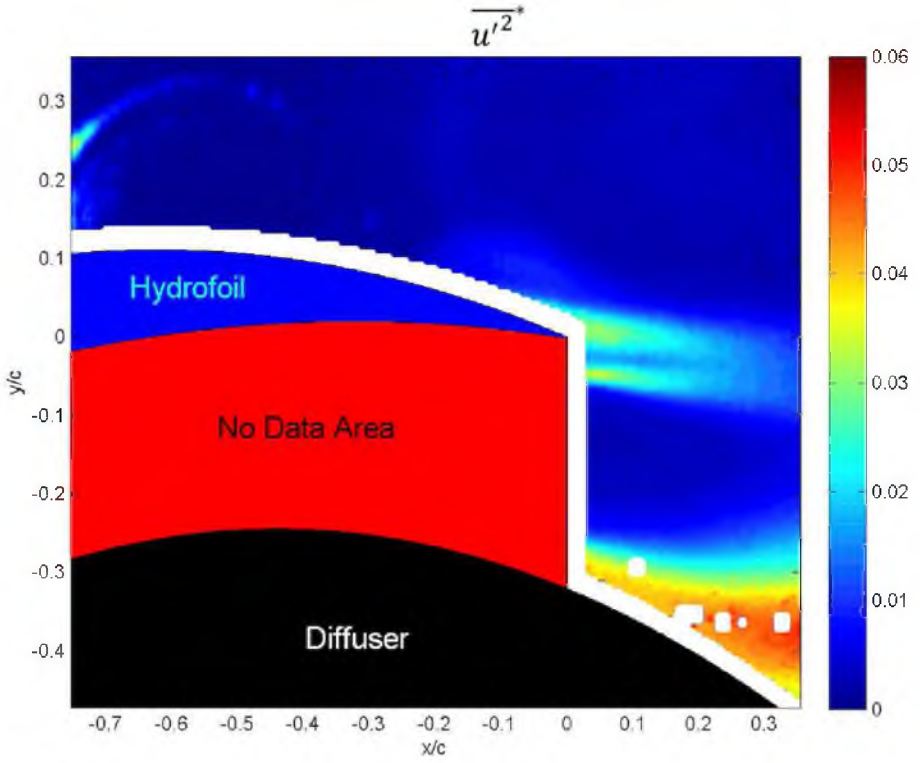

Figure 4.67 $\overline{u'^2}^*$ for high roughness at 0°.

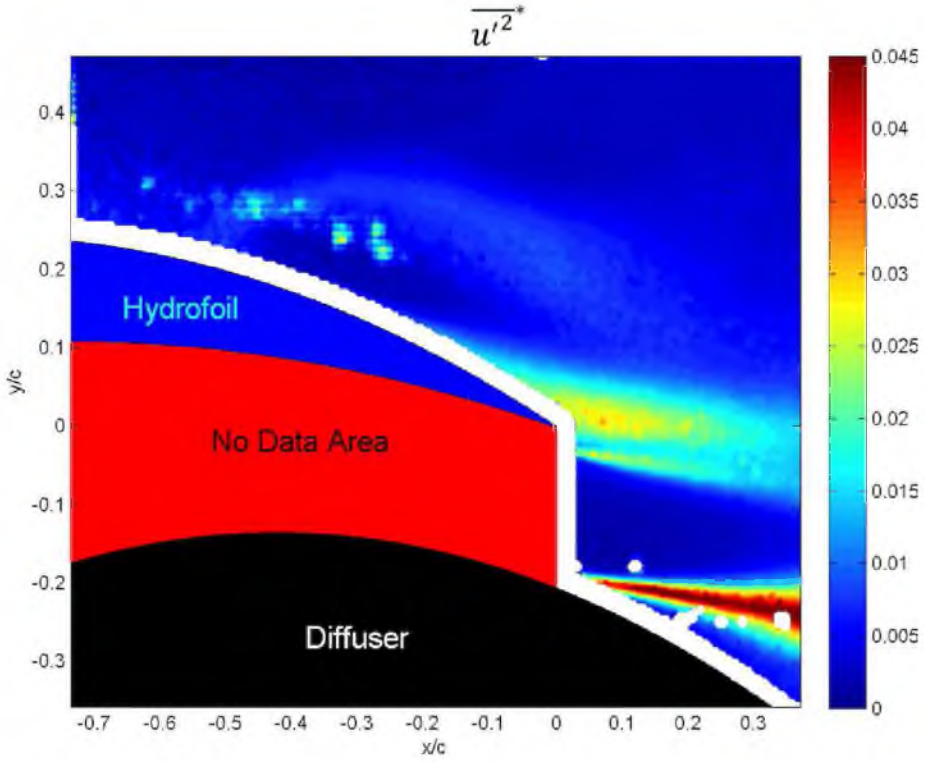

Figure 4.68 $\overline{u'^2}^*$ for low roughness at 10°.

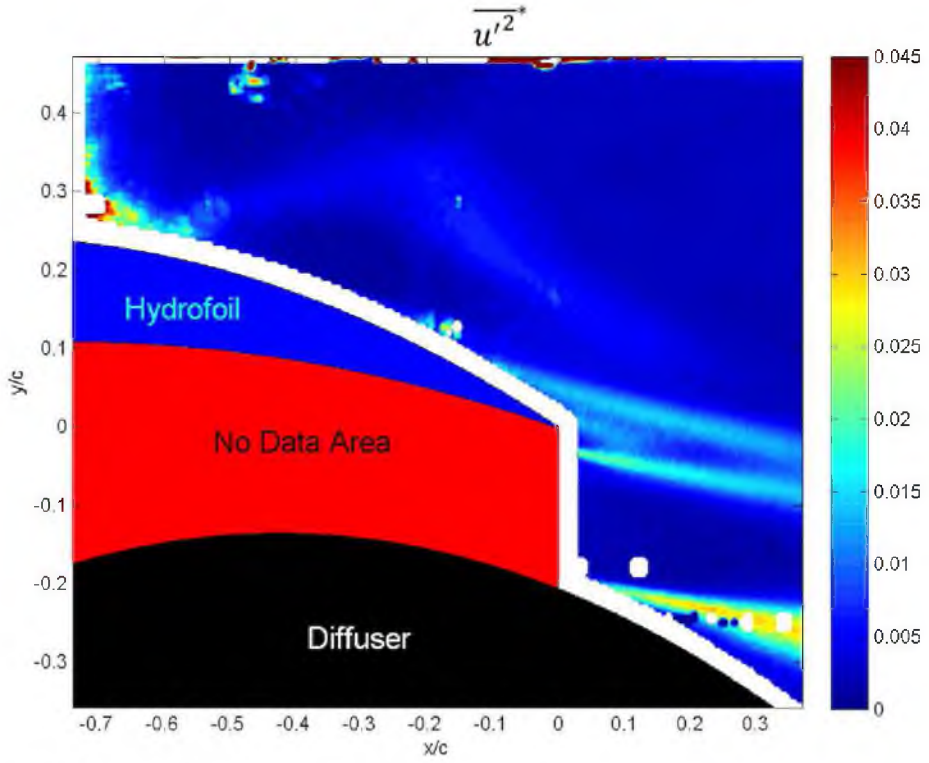

Figure 4.69 $\overline{u'^2}^*$ for medium roughness at 10°.

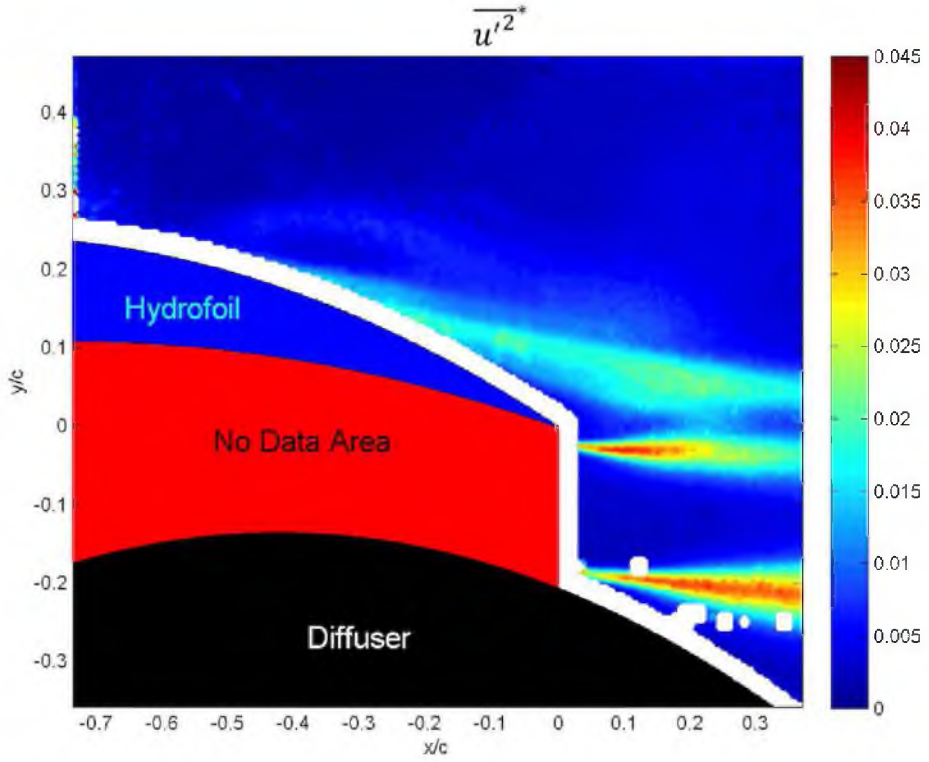

Figure 4.70 $\overline{u'^2}^*$ for high roughness at 10°.

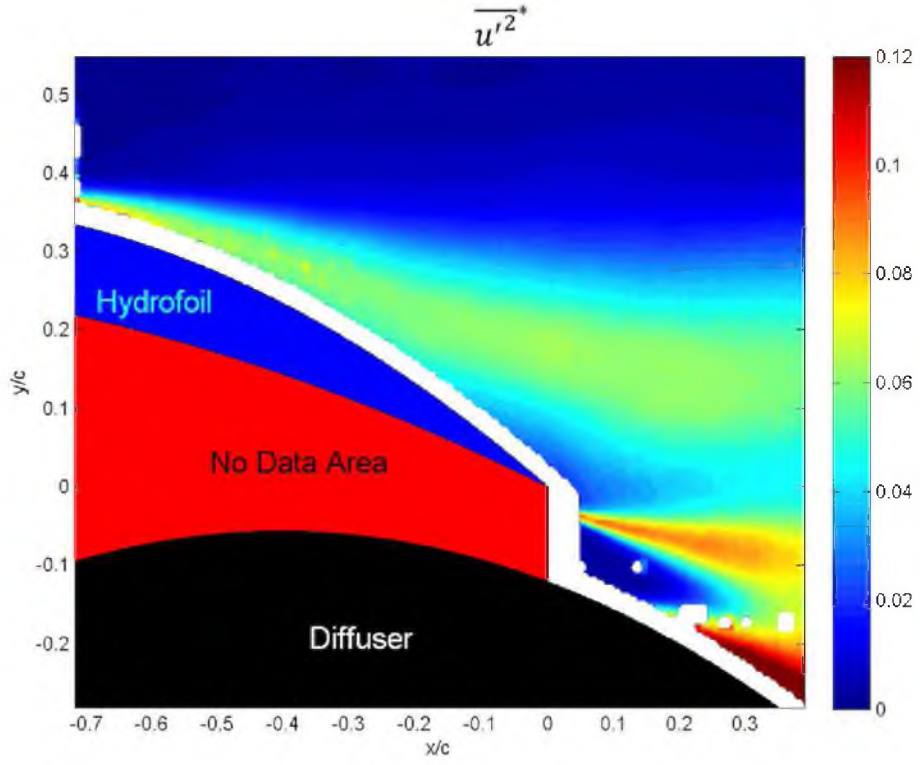

Figure 4.71 $\overline{u'^2}^*$ for low roughness at 17°.

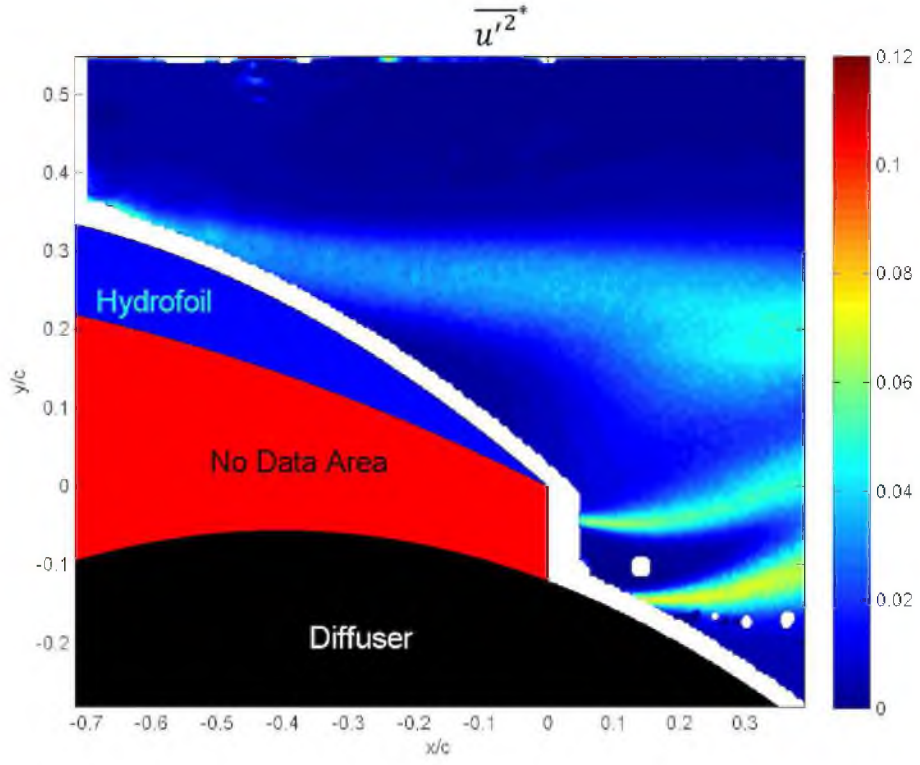

Figure 4.72 $\overline{u'^2}^*$ for medium roughness at 17°.

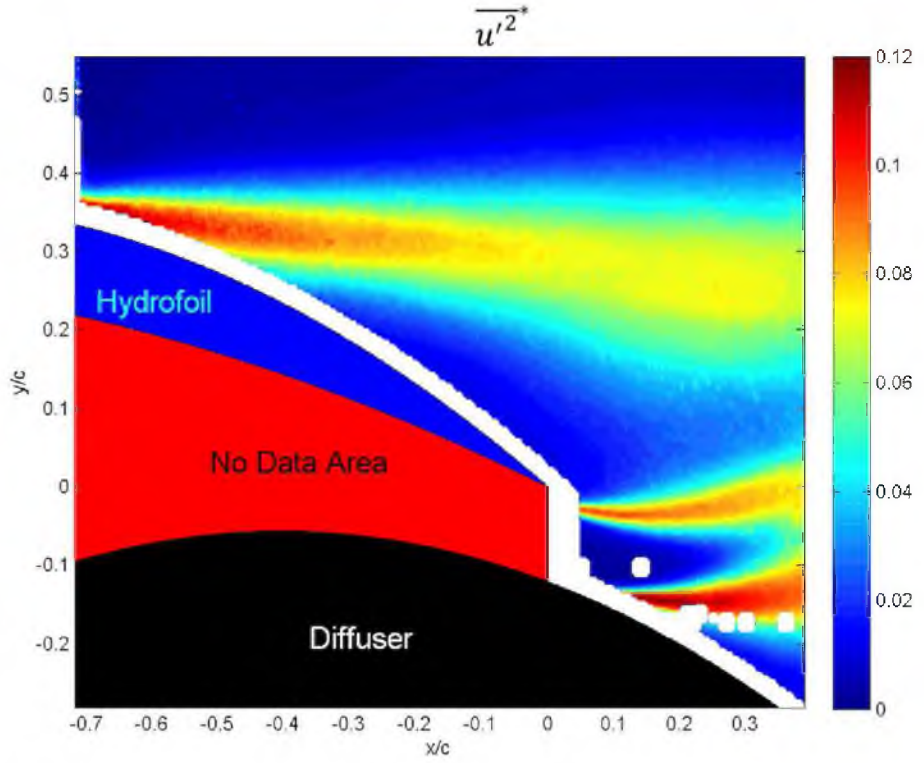

Figure 4.73 $\overline{u'^2}^*$ for high roughness at 17°.

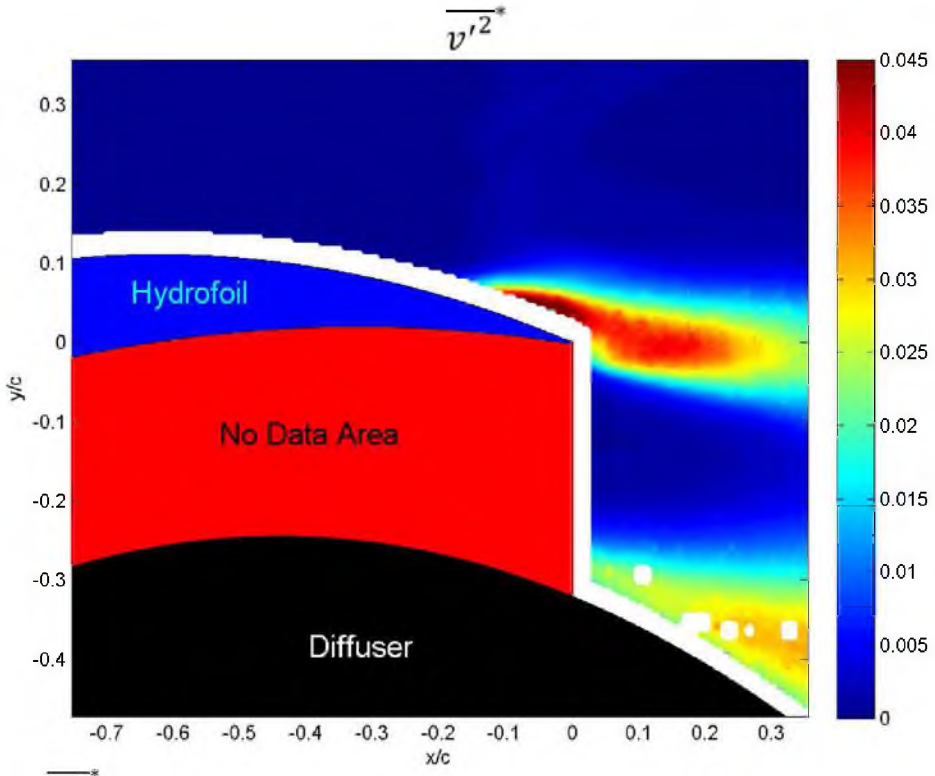

Figure 4.74 $\overline{v'^2}^*$ for low roughness at 0°.

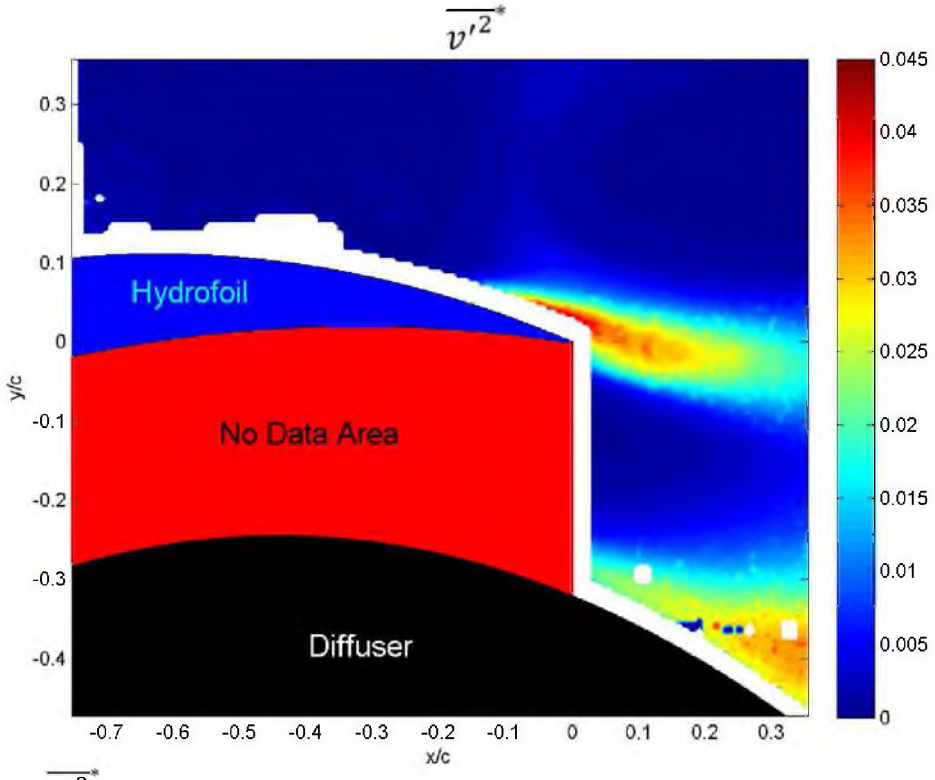

Figure 4.75 $\overline{v'^2}^*$ for medium roughness at 0°.

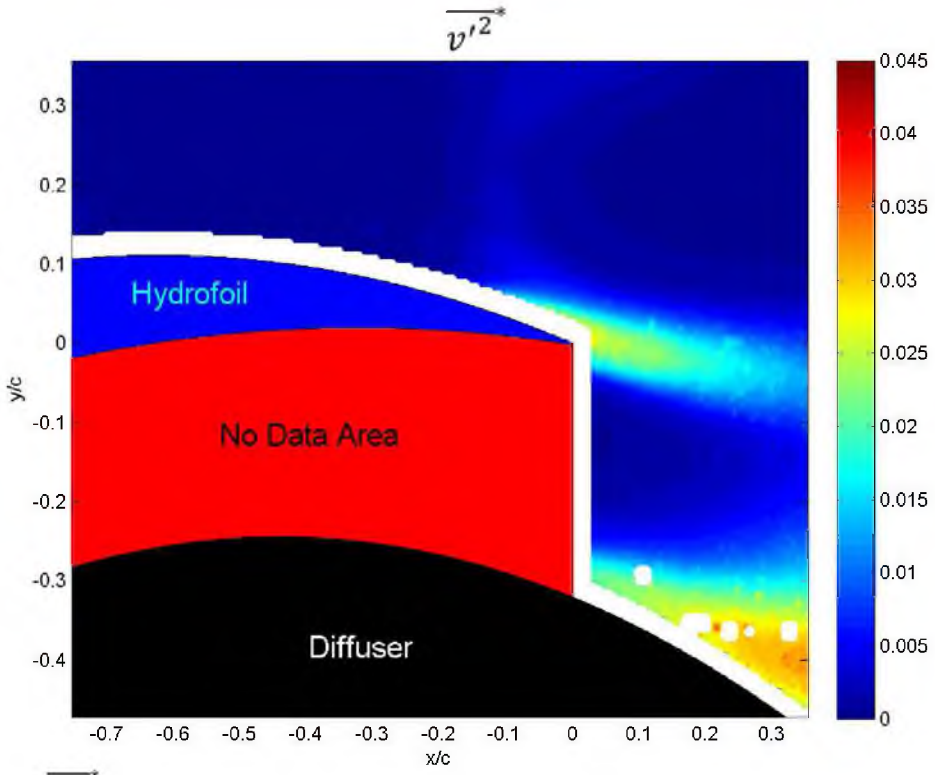

Figure 4.76 $\overline{v'^2}^*$ for high roughness at 0°.

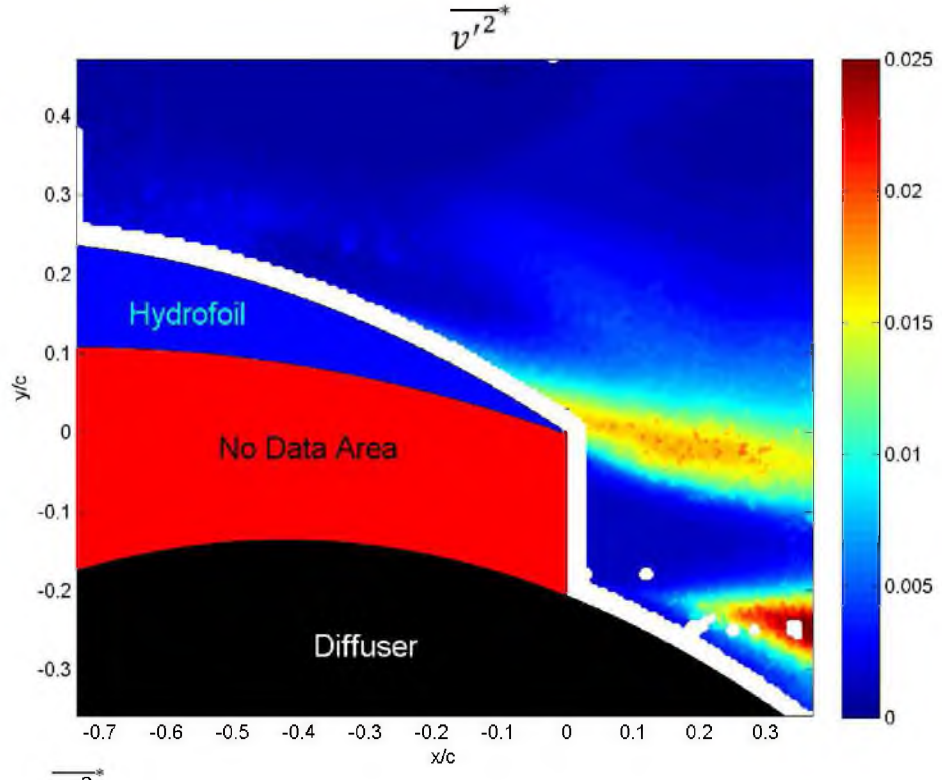

Figure 4.77 $\overline{v'^2}^*$ for low roughness at 10°.

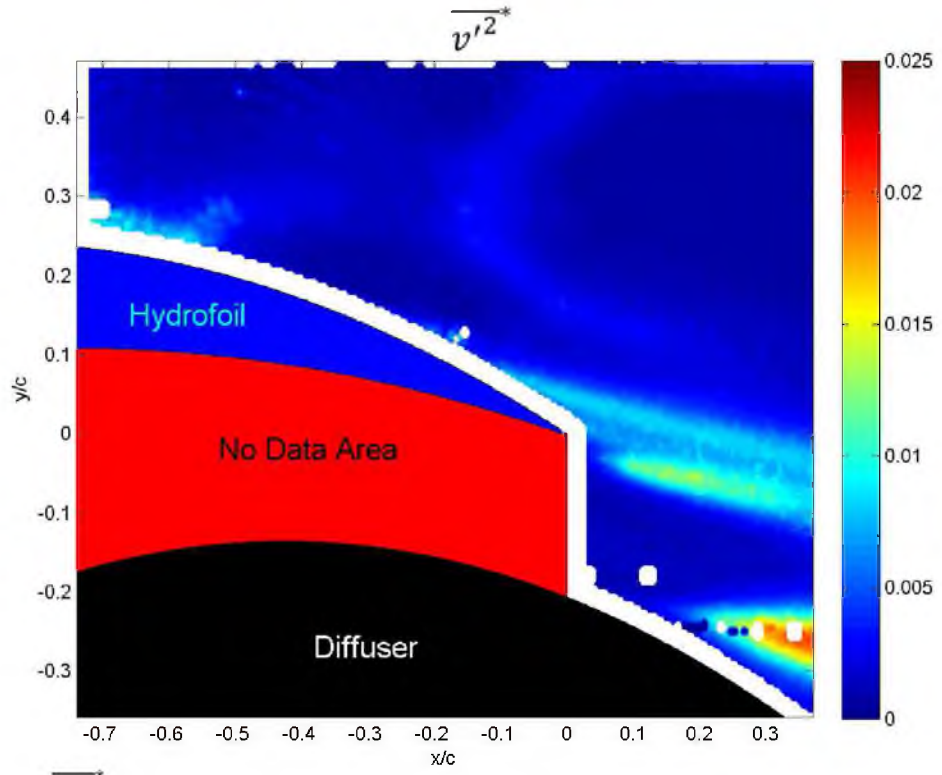

Figure 4.78 $\overline{v'^2}^*$ for medium roughness at 10°.

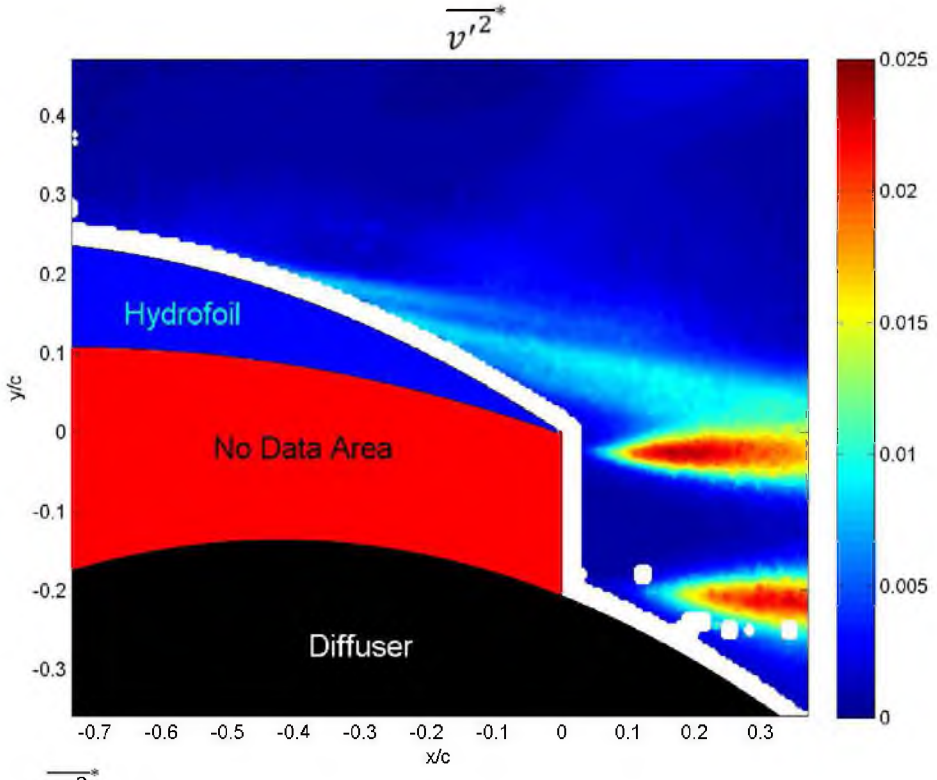

Figure 4.79 $\overline{v'^2}^*$ for high roughness at 10°.

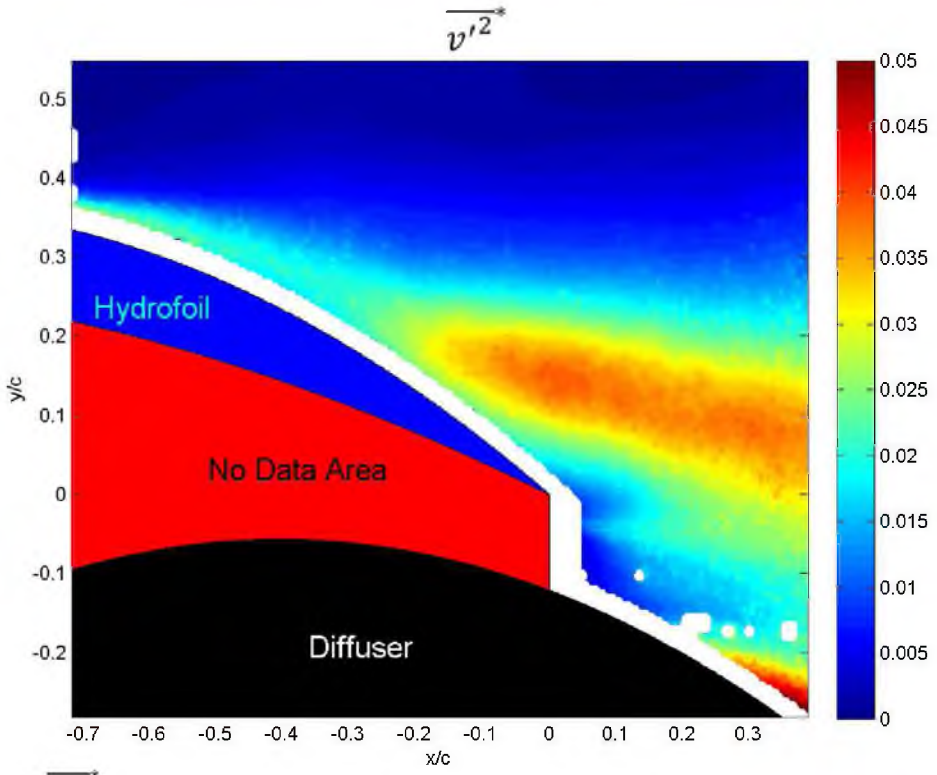

Figure 4.80 $\overline{v'^2}^*$ for low roughness at 17°.

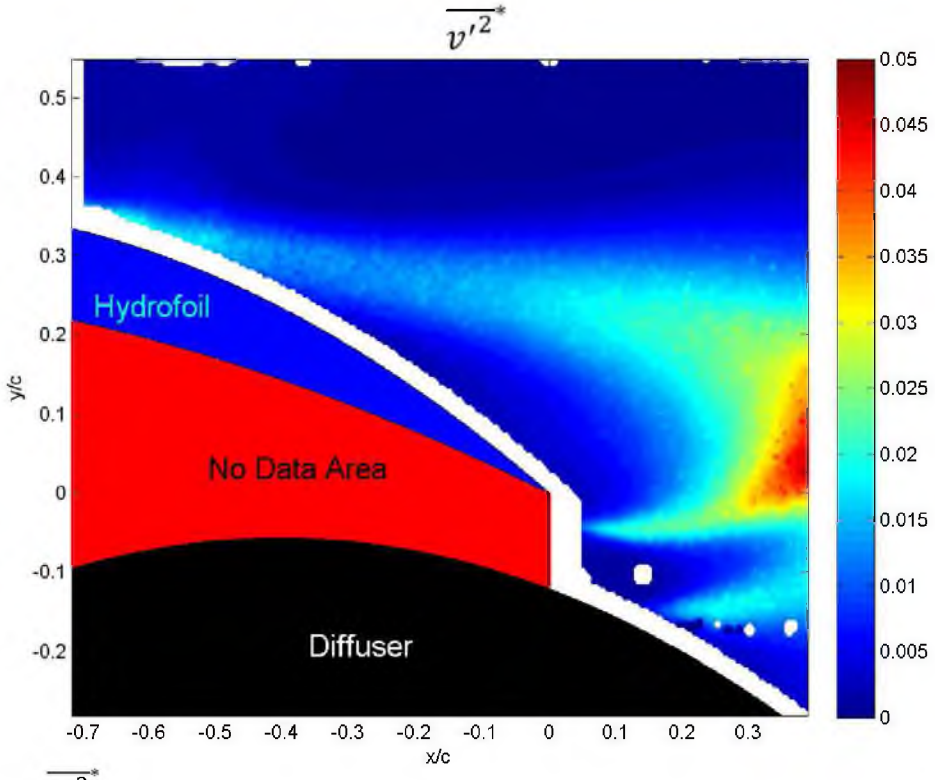

Figure 4.81 $\overline{v'^2}^*$ for medium roughness at 17°.

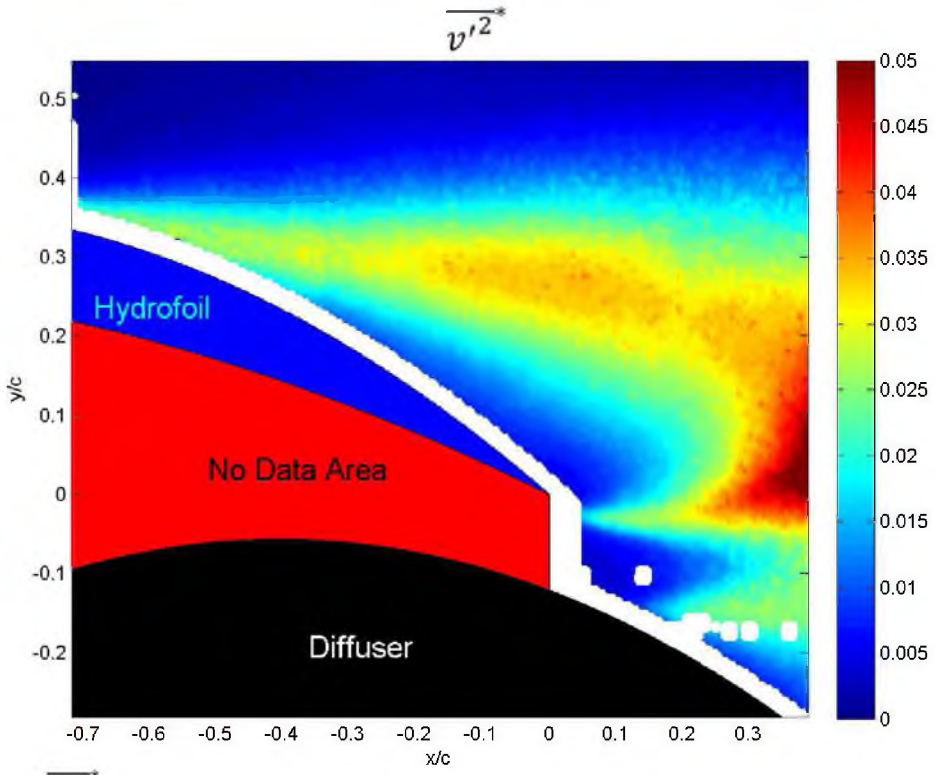

Figure 4.82 $\overline{v'^2}^*$ for high roughness at 17°.

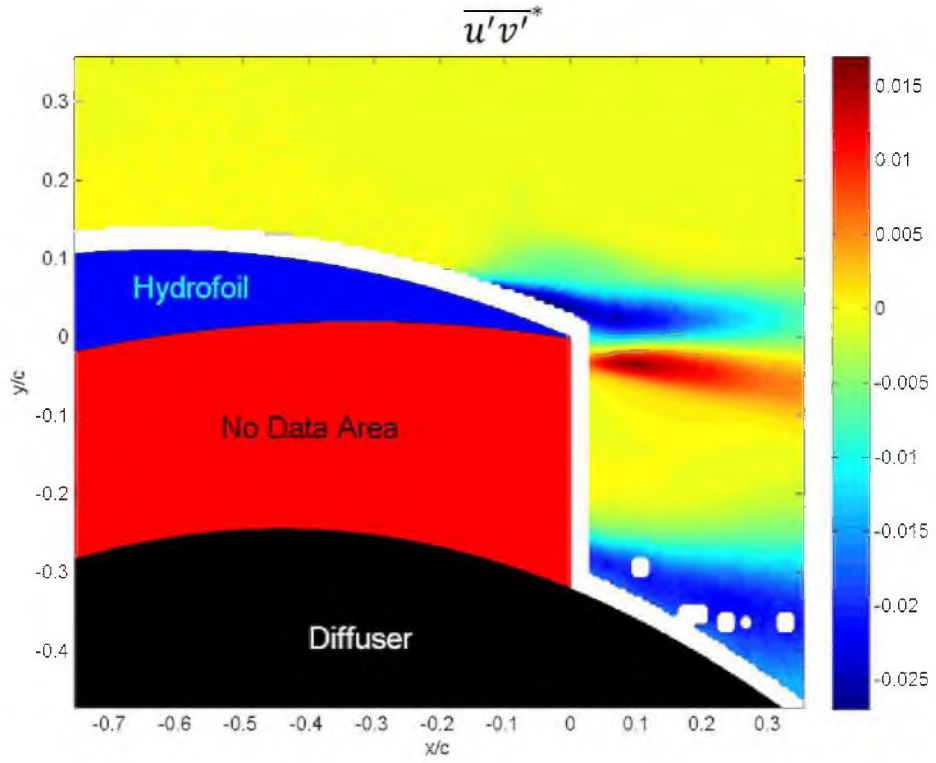

Figure 4.83 $\overline{u'v'}^*$ for low roughness at 0°.

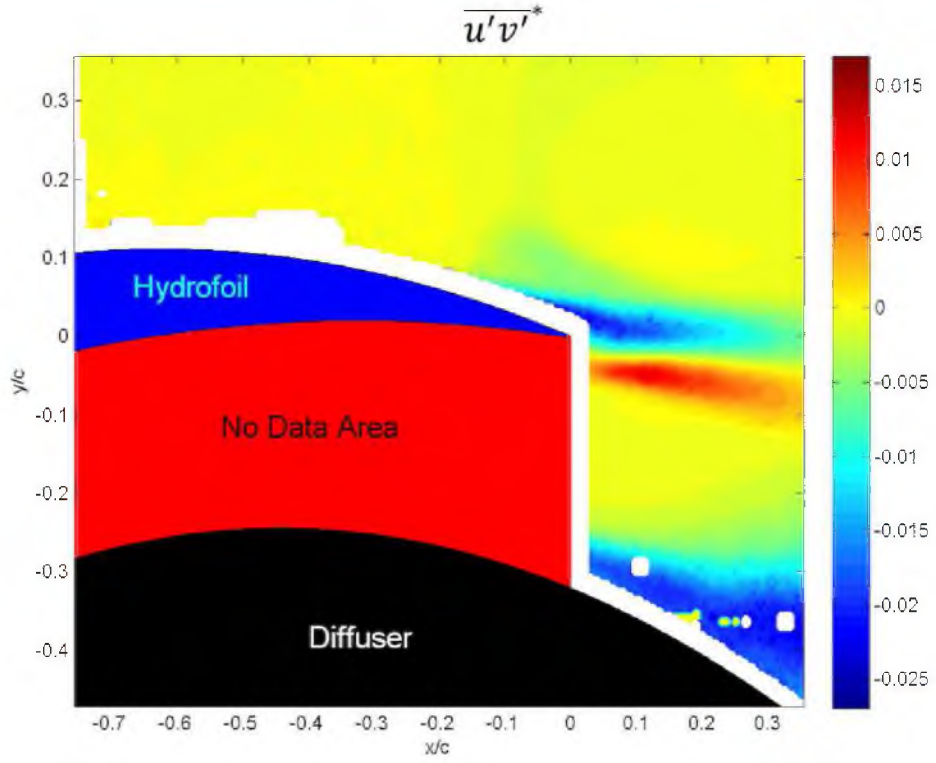

Figure 4.84 $\overline{u'v'}^*$ for medium roughness at 0°.

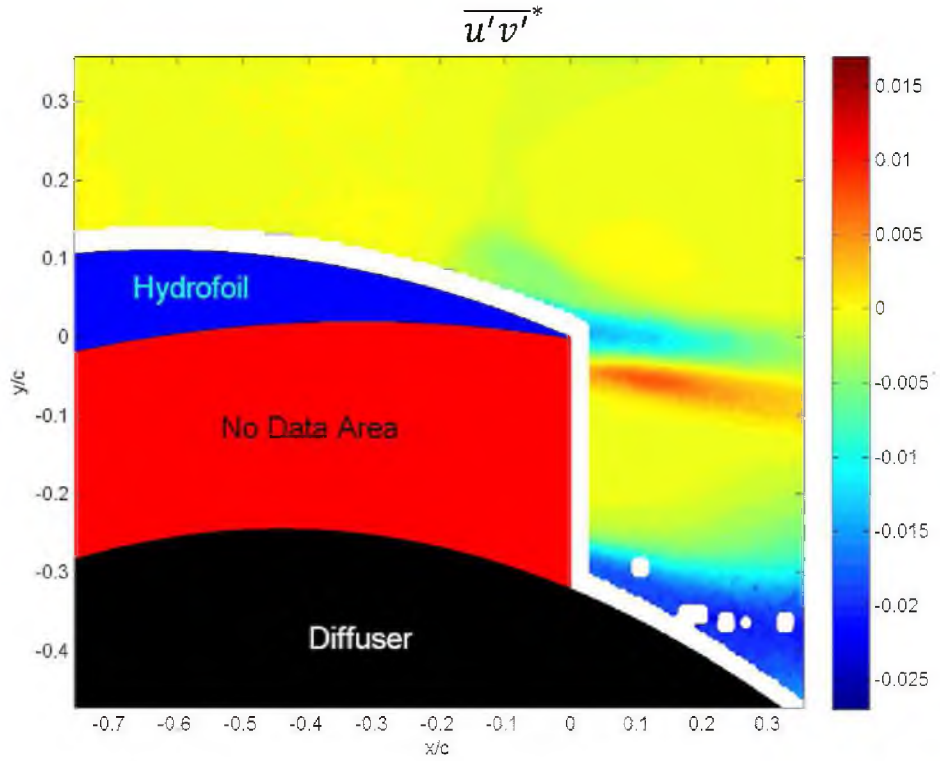

Figure 4.85 $\overline{u'v'}^*$ for high roughness at 0°.

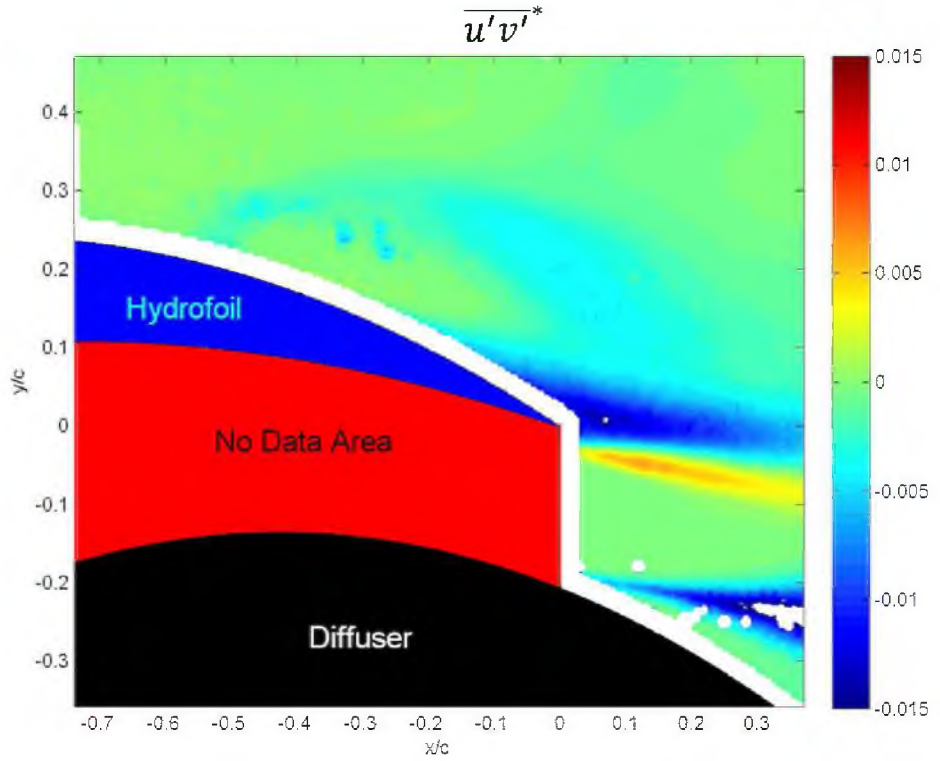

Figure 4.86 $\overline{u'v'}^*$ for low roughness at 10°.

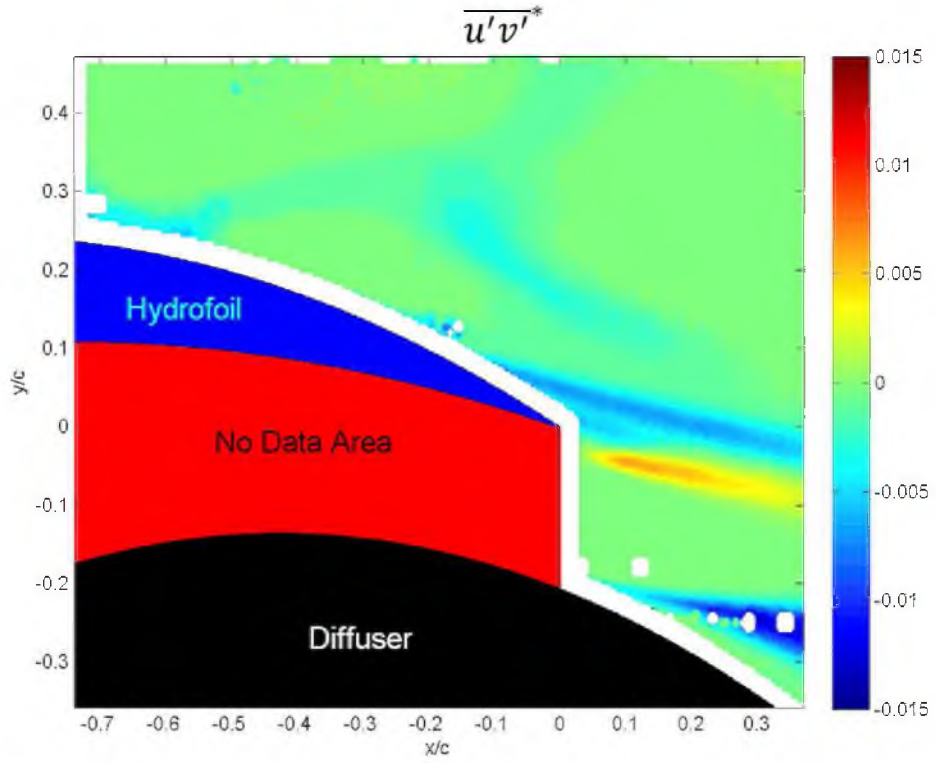

Figure 4.87 $\overline{u'v'}^*$ for medium roughness at 10°.

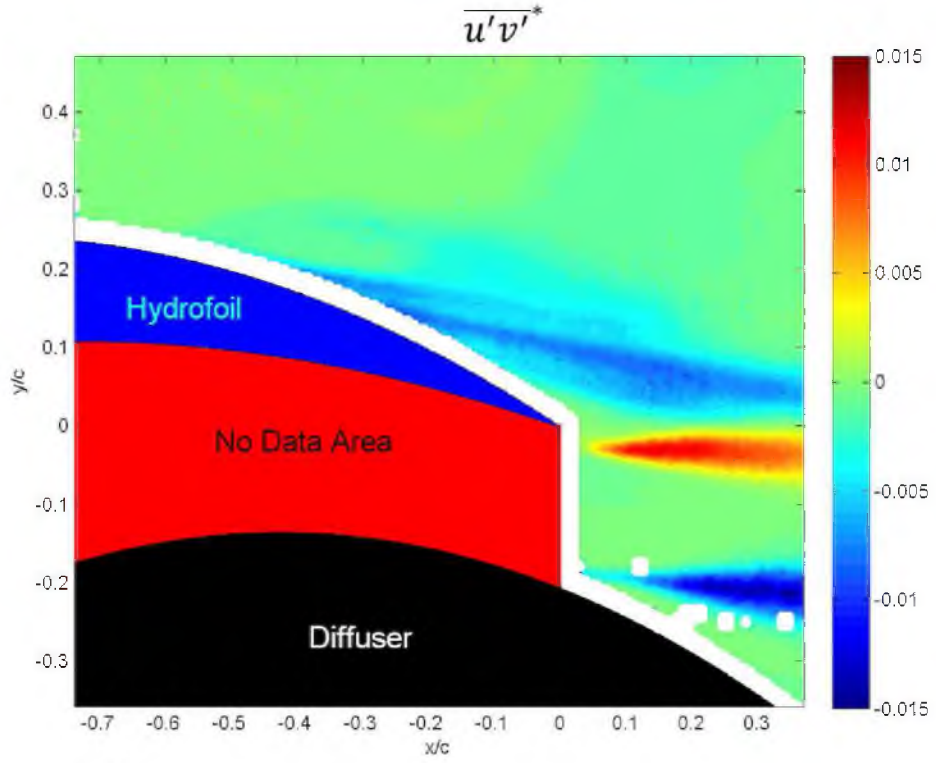

Figure 4.88 $\overline{u'v'}^*$ for high roughness at 10°.

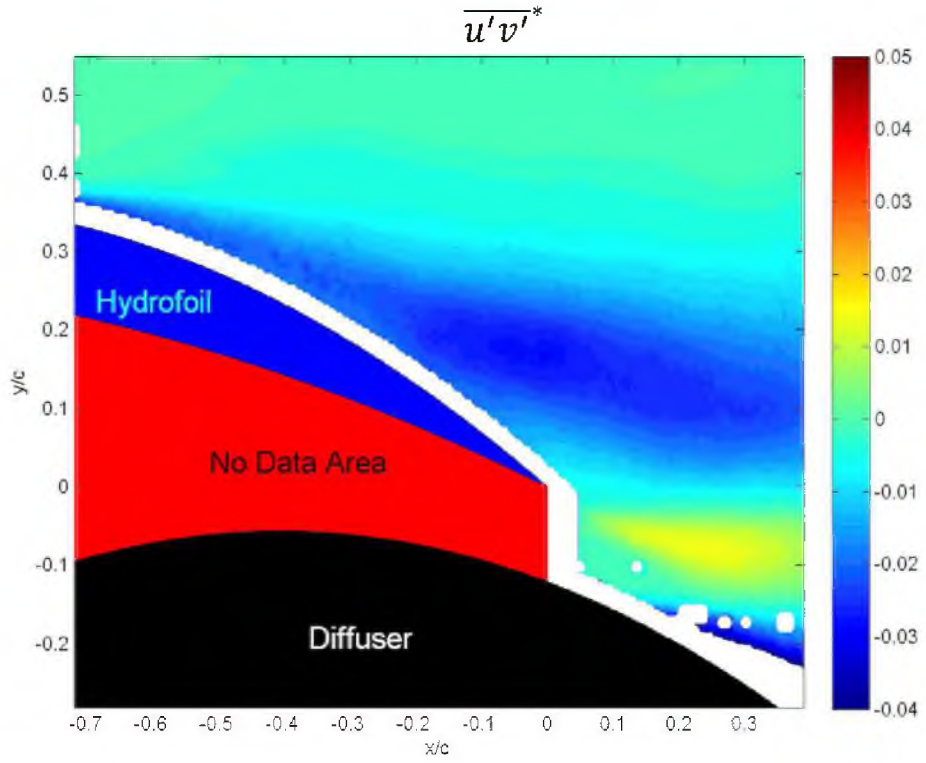

Figure 4.89 $\overline{u'v'}^*$ for low roughness at 17°.

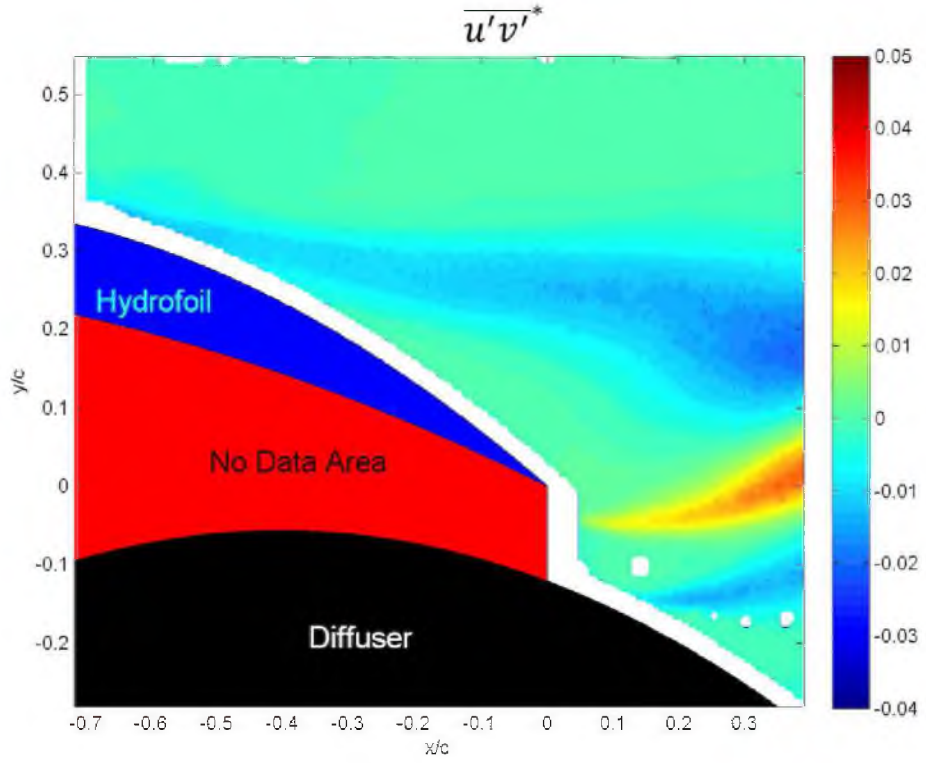

Figure 4.90 $\overline{u'v'}^*$ for medium roughness at 17°.

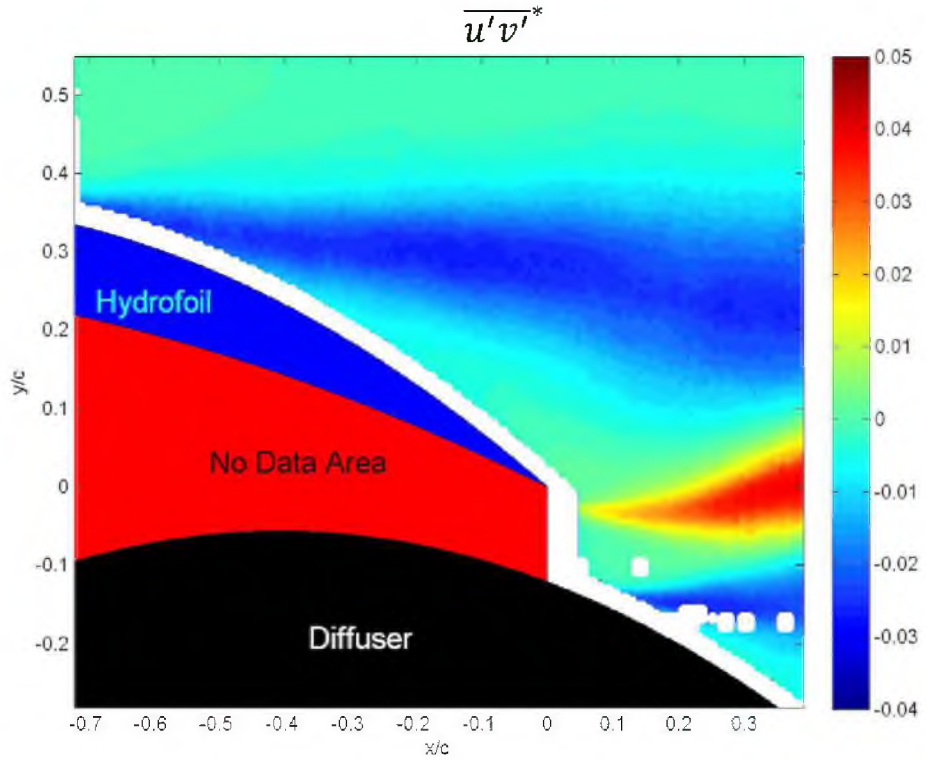

Figure 4.91 $\overline{u'v'}^*$ for high roughness at 17°.

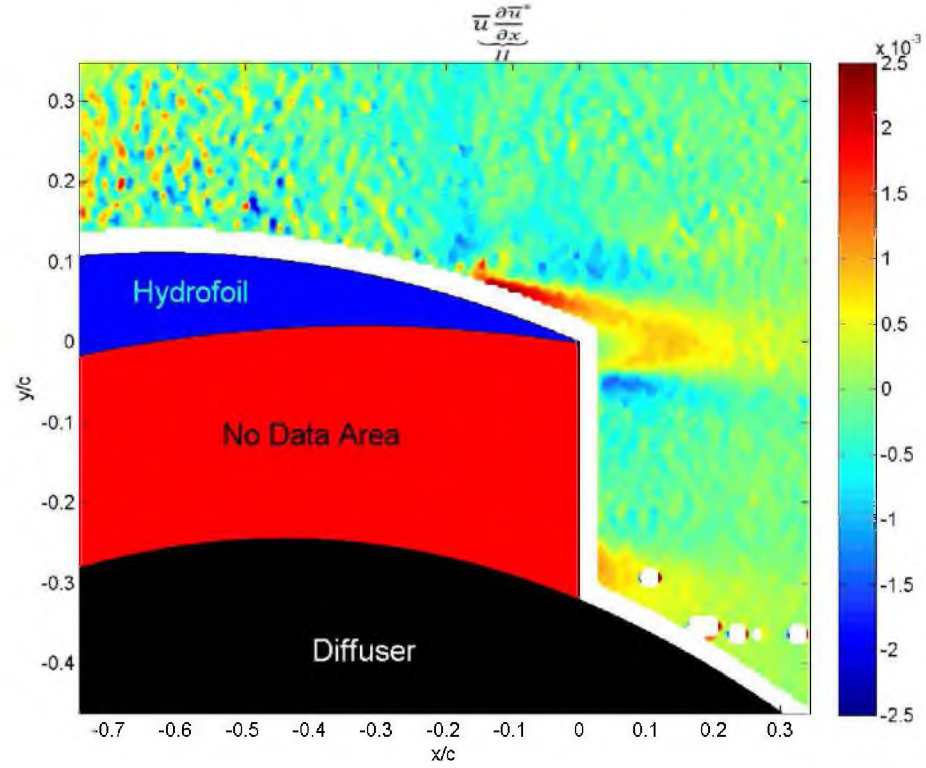

Figure 4.92 Term II for low roughness at 0°.

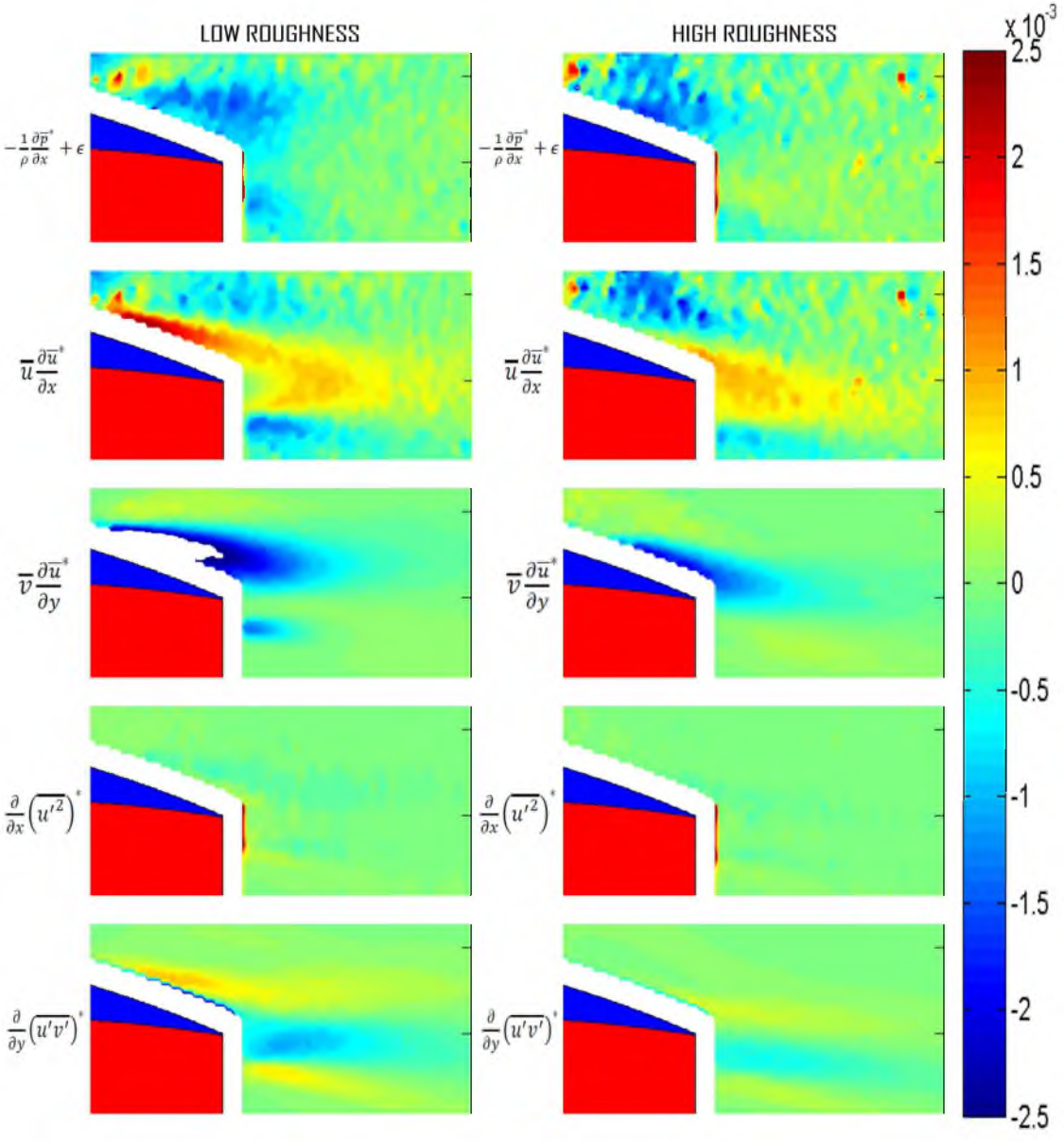

Figure 4.93. Cutout view of terms of the RANS equation in the x-direction around the trailing edge region for low roughness and high roughness at 0°.

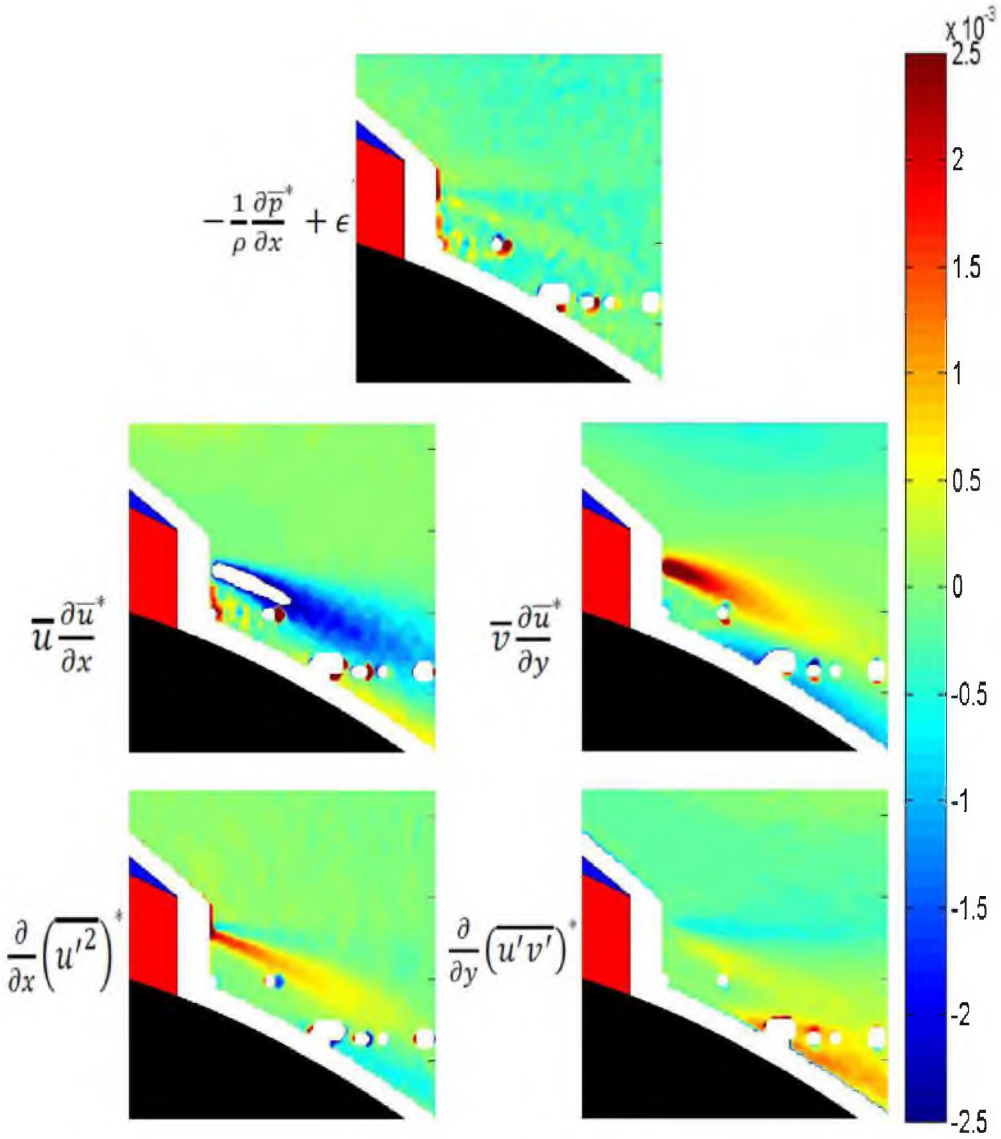

Figure 4.94. Cutout view of terms of the RANS equation in the *x*-direction around the trailing edge region for low roughness at 17°

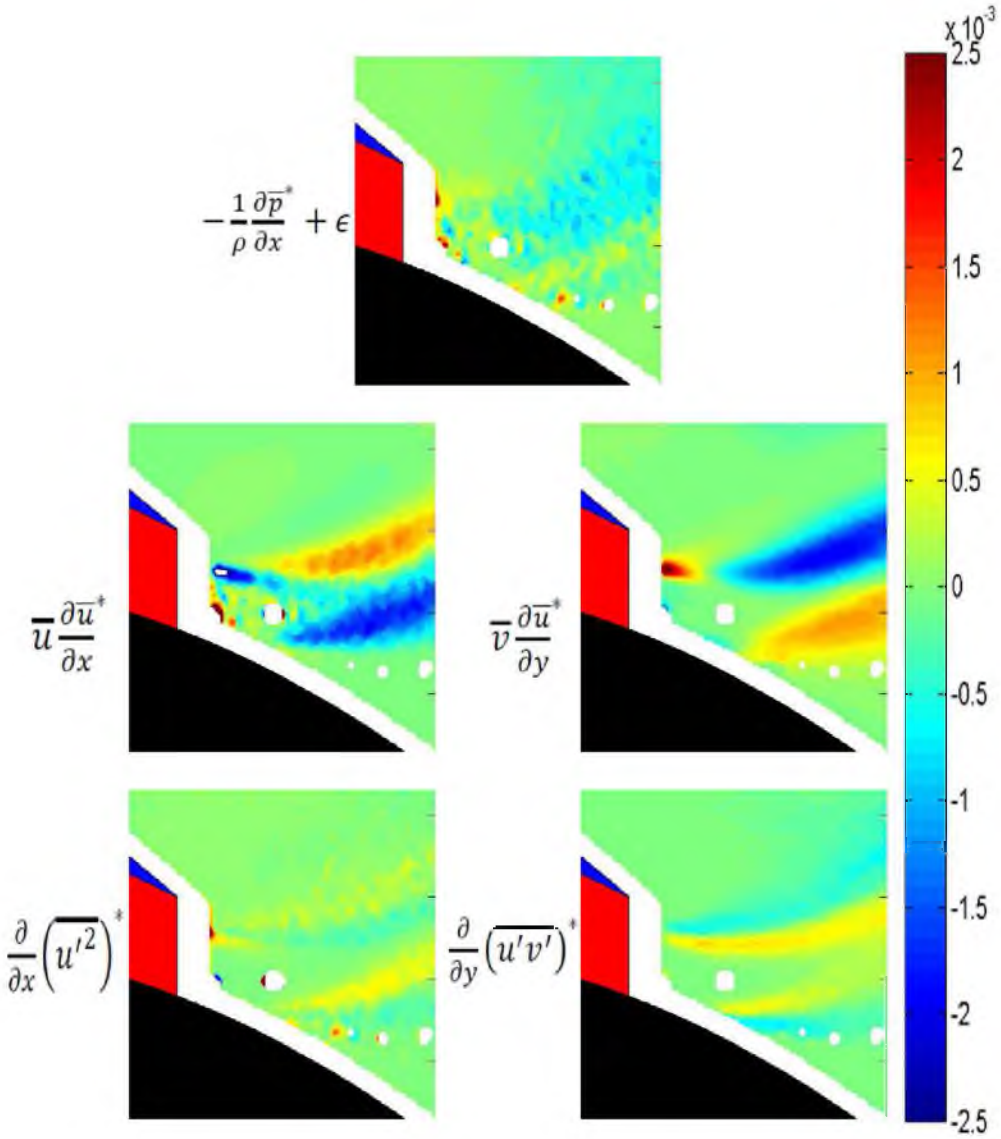

Figure 4.95. Cutout view of terms of the RANS equation in the *x*-direction around the trailing edge region for medium roughness at 17°.

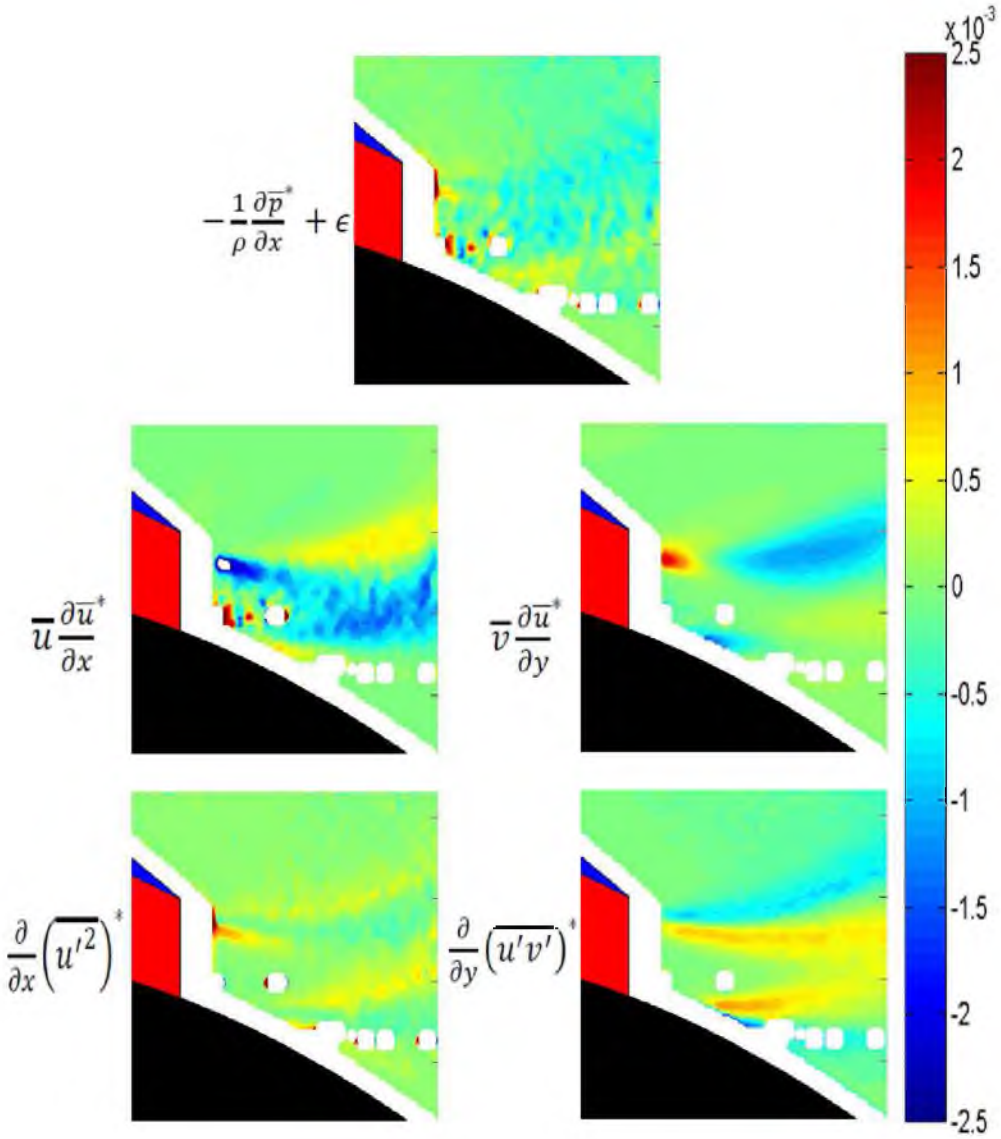

Figure 4.96. Cutout view of terms of the RANS equation in the *x*-direction around the trailing edge region for high roughness at 17°.

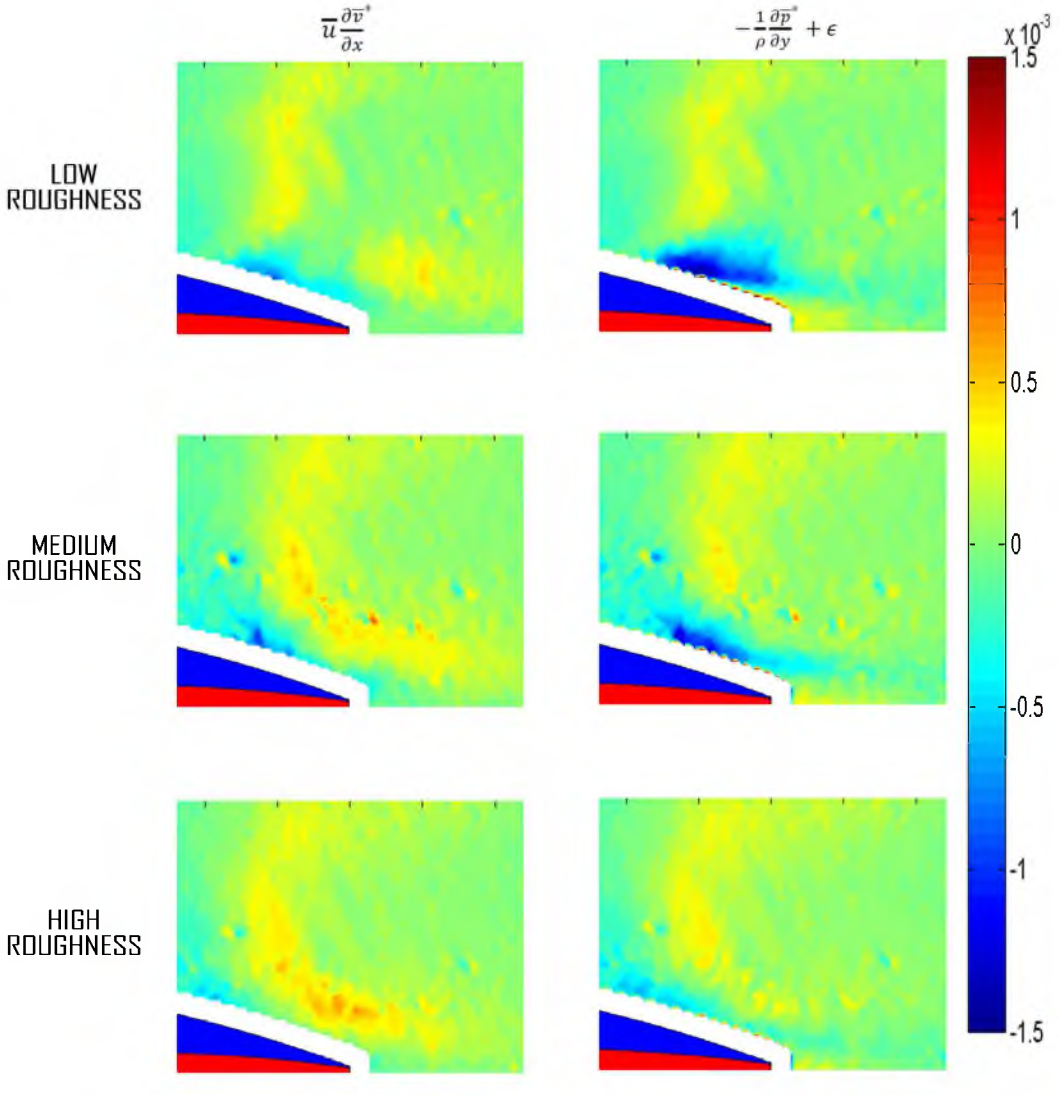

Figure 4.97. Cutout view showing contours of Term VII (left side) and Term VI (right side) from the RANS equations in the *y*-direction around the trailing edge for all three roughnesses at 0°.

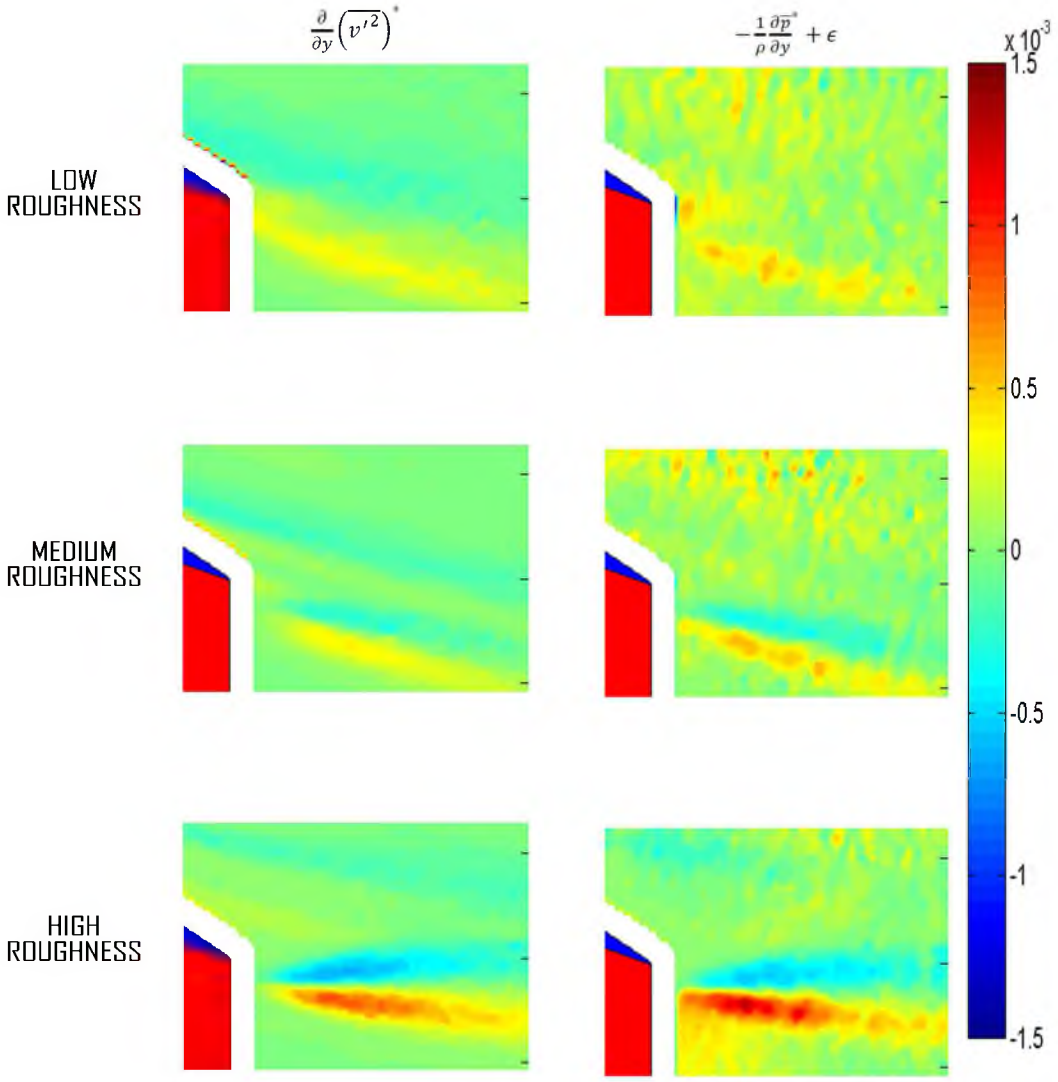

Figure 4.98. Cutout view showing contours of Term IX (left side) and Term VI (right side) from the RANS equations in the *y*-direction around the trailing edge for all three roughnesses at 10°.

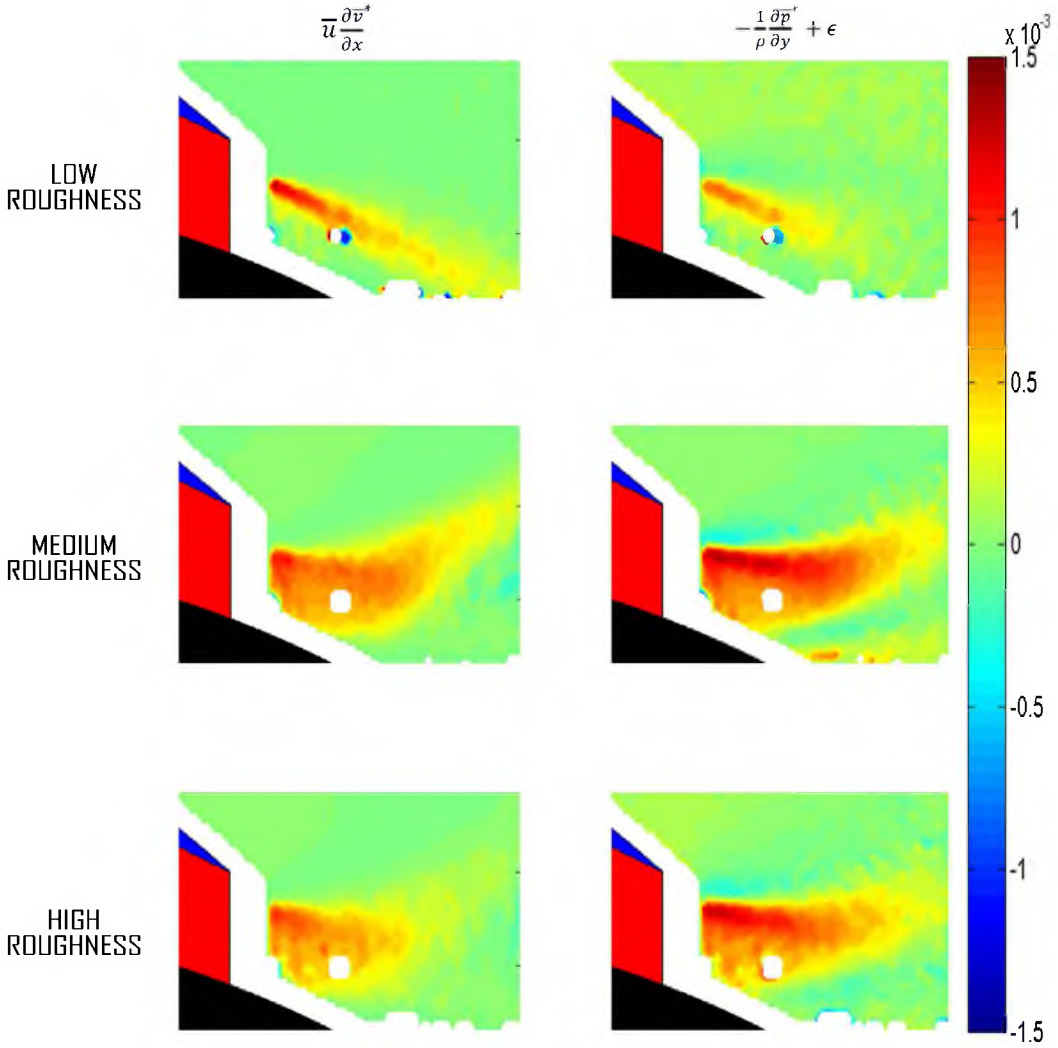

Figure 4.99. Cutout view showing contours of Term VII (left side) and Term VI (right side) from the RANS equations in the *y*-direction around the trailing edge for all three roughnesses at 17°.

CHAPTER 5

CONCLUSIONS

Experiments were conducted in order to further the knowledge of roughness and how it affects the flow of fluid in confined spaces such as those found in turbomachinery. This work was partially motivated by the work of Park et al. (2009) regarding the problems associated with deep-sea mining of raw minerals. PIV was used to explore in a more fundamental matter the behavior of the flow by looking at the mean vorticity, terms of the Reynolds stress tensor, and terms of the RANS equations.

The study of roughness effects on wall-bounded flows is generally considered to have started with Nikuradse (1933) and Schlicting (1936). From their work came the concept of *equivalent sand grain roughness* (k_s) that is still used today. For flow behavior, the shape and density of roughness elements play as big of a role as their size. Therefore, it is not sufficient to simply compare roughness heights (k). While researchers since then have re-evaluated the results of Schlicting's original experiment, the concept remains an important way to compare roughnesses between different fluid experiments. This thesis uses the Van Rij (2002) adaptation of the Sigal and Danberg (1988) model to determine the appropriate relationship between k and k_s. The experiments performed for this thesis involved flow over a hydrofoil inside a confined water channel with a diffuser present to create strong pressure gradients and cross-sectional area changes such as those found in turbomachinery. The test section was approximately 99 cm long with a square cross-

section with 15.2 cm per side, designed such that the hydrofoils could be easily substituted and the angle adjusted. Three identically shaped hydrofoils were used with three different sand-paper surfaces, resulting in relative roughnesses (using equivalent sand grain roughness—RR_s) of approximately $1.26 \cdot 10^{-3}$, $1.85 \cdot 10^{-3}$, and $2.12 \cdot 10^{-3}$, which are referred to as low roughness, medium roughness, and high roughness, respectively. 2D PIV experiments were conducted showing details of the flow field on the pressure side of the hydrofoil as well as the near wake region.

This work was exploratory in nature, and thus did not necessarily give definitive answers to the questions posed. However, some key and definite conclusions can be made from it. PIV is an effective tool to characterize—both qualitatively and *quantitatively*—turbulent flow. Its ability to capture entire flow fields makes it much more powerful than many of the traditional methods such as hot wire probes. By looking at the turbulent quantities in an entire region—instead of just the areas where they are *believed to be meaningful*—areas of interest are discovered that otherwise might be overlooked. For the most part, the results of experiments involving airfoils in unconfined flow and those involving hydrofoils near an air/water surface cannot be accurately used to predict the behavior of confined flow such as that found in turbomachinery. This work did not focus on one particular variable and how it compares across different roughness values. Instead, the fundamental objective was to begin to understand how roughness affects the flow of fluid in a confined, nonuniform, irregular shaped flow such as that found in turbomachinery beyond simply looking at head loss. To that end, PIV provided the opportunity to explore numerous flow quantities by developing a complete vector field of the flow in a plane. By assuming that the flow was statistically steady,

taking multiple images at the same plane and under the same flow conditions allowed for the ability to look at quantities of turbulence as well. Primarily, this research focused on three categories of flow quantities: Vorticity, the Reynolds stress tensor, and the terms of the RANS equations. The data were considered to have converged satisfactorily by looking at the Reynolds normal stress in the streamwise direction.

Perhaps the most significant finding of this was work is that at a high angle of attack—in this case, 17°—roughness causes separation to occur 'earlier', or closer to the leading edge. While no data were taken inside the boundary layer, streamline plots of the medium roughness and high roughness experiments at 17° show clear indication that separation had occurred and where. When separation occurs, it becomes a dominant element of the flow, and it is usually an undesirable quality. Large wake regions that develop behind the hydrofoil can cause significant drag.

The effects of roughness on mean vorticity for this research is dependent on the angle of attack considered. At 0°, in the area immediately above the trailing edge, the higher roughness experiments had lower magnitudes of vorticity. The 10° data were too noisy to make meaningful conclusions. The data for the 17° experiments showed the effects of hastening separation on vorticity. For the roughest case, separation causes the formation of strong vortices downstream of the trailing edge (approximately 0.2-0.3 chord lengths) and creates vortex pairs that can be seen downstream of the suction side of the hydrofoil. The smoothest case shows a constant 'stream' of negative vorticity that emanates from almost the entire visible suction side surface of the hydrofoil. This is what would be expected in a flow without complete separation because of the Kutta condition.

The Reynolds stress results are also dependent on the angle of attack. As was the case with vorticity, at 0°, in the area immediately above the trailing edge, the higher roughness experiments had lower magnitudes of all three Reynolds stress quantities. The 10° and 17° cases showed a pattern that is also evident in the velocity contours and many of the RANS equations terms: a nonmonotonic relationship from the smoothest to the roughest case, in which the middle roughness is typically of a smaller magnitude than the other two. This finding suggests that the different roughness profile for the middle roughness could have played an unknown role in certain results. Comparing the smoothest and roughest cases, one observable relationship is that for the roughest case—in which separation occurs early—there is a smaller magnitude of negative Reynolds shear stress emanating from the suction side than the smoothest case, but a greater magnitude of positive Reynolds shear stress in pressure-side jet region. For the 17° angle of attack experiments, the fact that the smoothest case does not separate (or separates very closely to the trailing edge), while the rougher cases do experience complete separation, is very easily observed. A small region of strong turbulence emanates from the apparent separation point on the roughest case and forms a jet that advects downstream, while very little turbulence is present near the surface between this point and the trailing edge.

For the terms of the RANS equations in the *x*-direction (streamwise), the pressure gradient term was very small compared to the others, although still significant in a small area concentrated above the trailing edge. The dominant terms in the equations were the two advections terms, and for the most part they balanced each other out—in the areas where one was negative, the other was positive. There was a large amount of noise above (suction side) the hydrofoil in Term II (which propagated into term I), likely resulting

from the larger mean velocity values magnifying the noise in the derivative term. This made it impossible to make decent observations in this area, or to even tell if there were meaningful nonnegligible values there at all. Other than these areas of noise, the majority of the areas of interest were in the near wake region of the hydrofoil.

For the terms of the RANS equations in the *y*-direction (cross-stream), the pressure gradient term was somewhat higher in relation to the other variables than with the *x*-direction. The advection of cross-stream velocity in the streamwise direction (Term VII) was the dominant term for most of the experiments, particular for the 17° experiments, in which everywhere showed negligible values of all terms except for the strong negative vertical pressure gradient in the near-wake jet emanating from the pressure side of the hydrofoil. For the other two angles of attack, there is a region of negative vertical pressure gradient above the trailing edge of the hydrofoil caused entirely by Term VII.

In conclusion, the work presented in this thesis gives a preliminary understanding about the effect roughness has on the flow inside of confined spaces such as turbomachinery. For small curvatures, such as the 0° angle of attack data on a curved hydrofoil presented here, roughness can dampen vorticity and other turbulent quantities—at least outside of the boundary layer and away from the near wall, where this experiment focused. For the higher angles of attack considered here (10° and 17°), there is not as clear of a monotonic relationship. In each of these cases, the middle roughness value did not show behavior that was in between the smoothest and roughest experiments in terms of most of the flow quantities considered. In general, the lowest turbulence could be observed for this middle roughness case. These conflicting results are believed to be due to one of two (or both) reasons: the roughness pattern of the middle roughness, while

in between the other two in terms of grain size, had a much smaller particle density on the surface; for the 17° experiments, the middle roughness value was the smoothest value *in which separation occurred*, putting the results from it in a different category than the smoothest hydrofoil—in essence, separation itself was an additional variable not consistent in all three experiments. Further tests should be done with finer control and similarity of the roughness elements in order to determine which of these two reasons are true. Until then, the results of the middle roughness values for both the (10° and 17°) angles of attack should be viewed skeptically. Finally, at the highest angle of attack, roughness directly correlated with complete separation farther upstream. The results from this thesis make a strong argument for further research beyond simple head loss measurements for confined flow, as they suggest that the vast research done on hydrofoils in open flow are not necessarily applicable.

APPENDIX

FIGURES

A1. Choice Code Plots

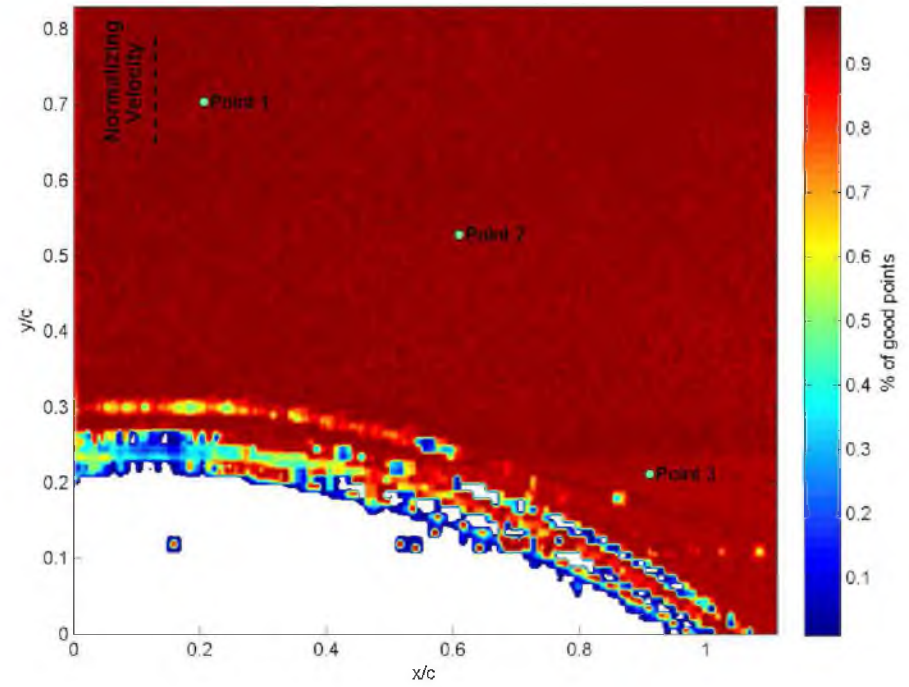

Figure A-1. "Choice Code" contour plot for experiment with no hydrofoil indicating the percentage of good vectors at each data processing spot.

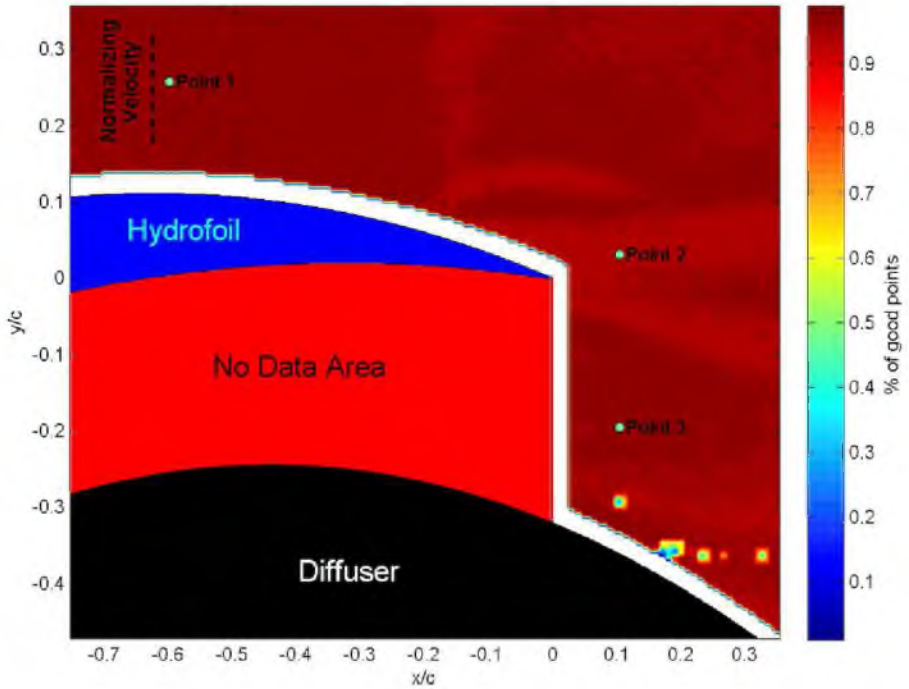

Figure A-2. "Choice Code" contour plot for low roughness at 0° indicating the percentage of good vectors at each data processing spot.

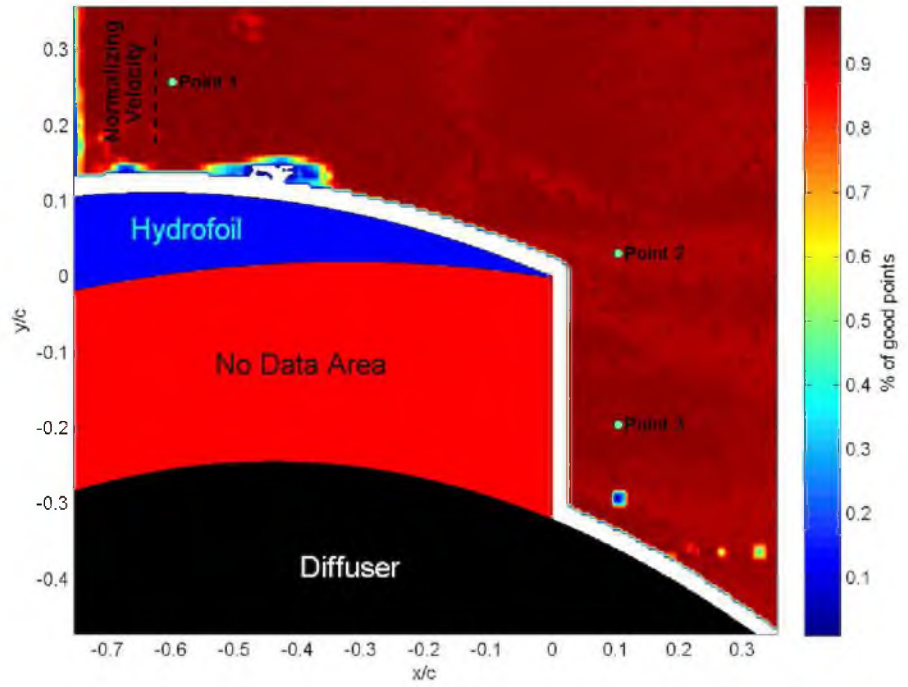

Figure A-3. "Choice Code" contour plot for medium roughness at 0° indicating the percentage of good vectors at each data processing spot.

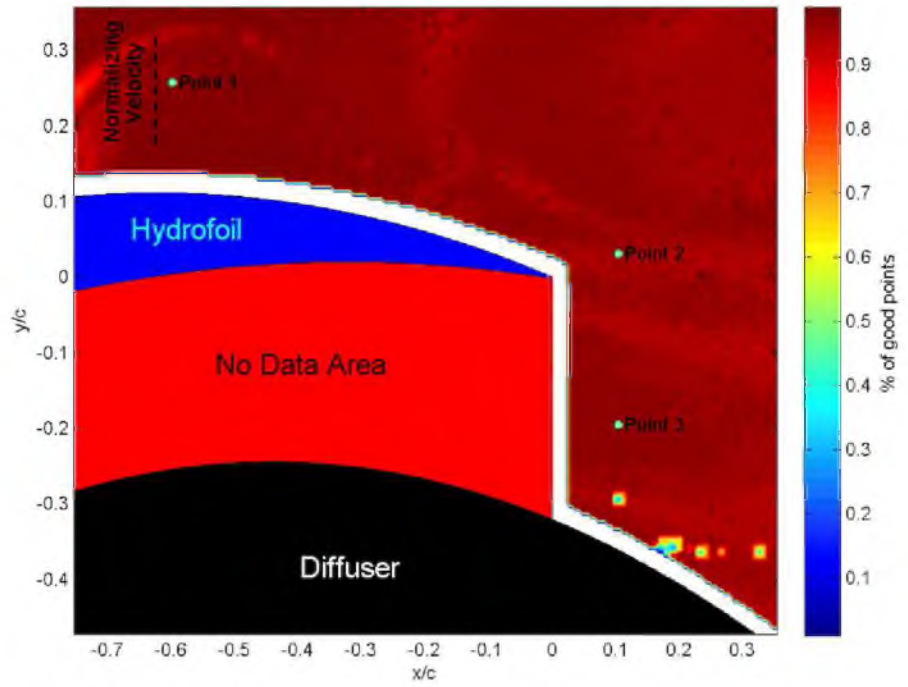

Figure A-4. "Choice Code" contour plot for high roughness at 0° indicating the percentage of good vectors at each data processing spot.

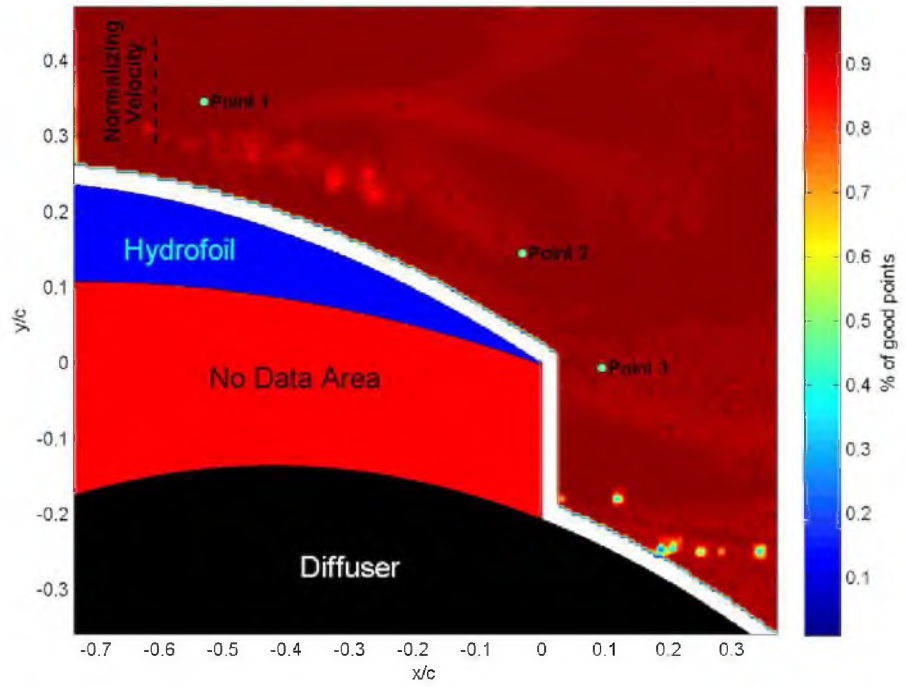

Figure A-5. "Choice Code" contour plot for low roughness at 10° indicating the percentage of good vectors at each data processing spot.

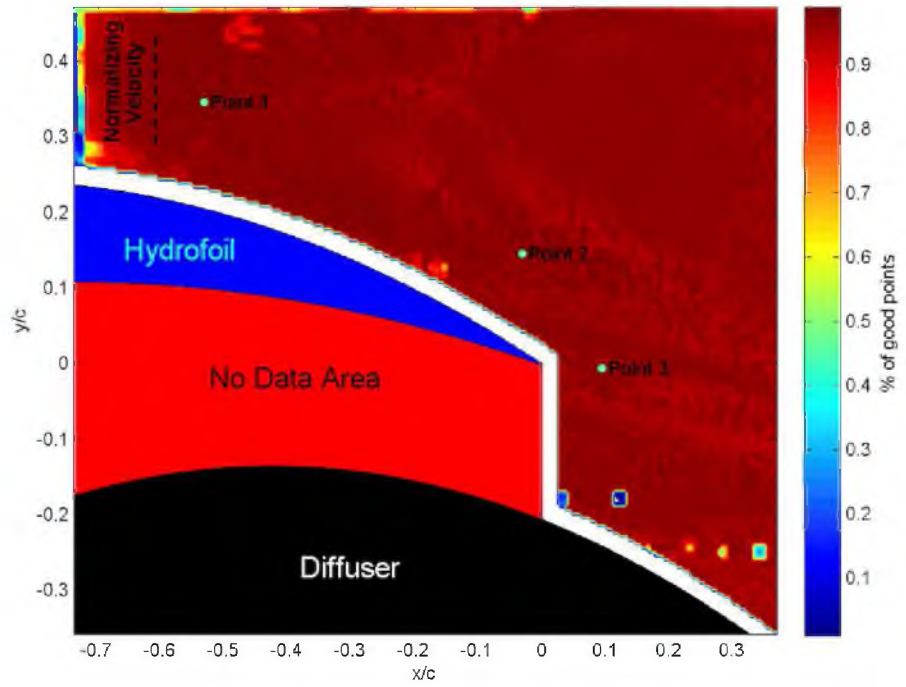

Figure A-6. "Choice Code" contour plot for medium roughness at 10° indicating the percentage of good vectors at each data processing spot.

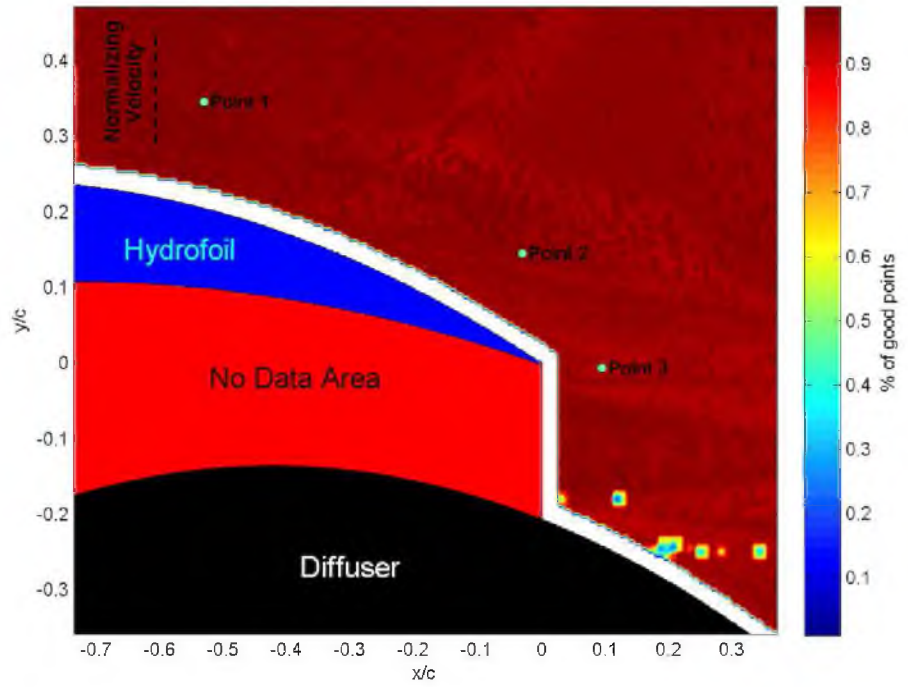

Figure A-7. "Choice Code" contour plot for high roughness at 10° indicating the percentage of good vectors at each data processing spot.

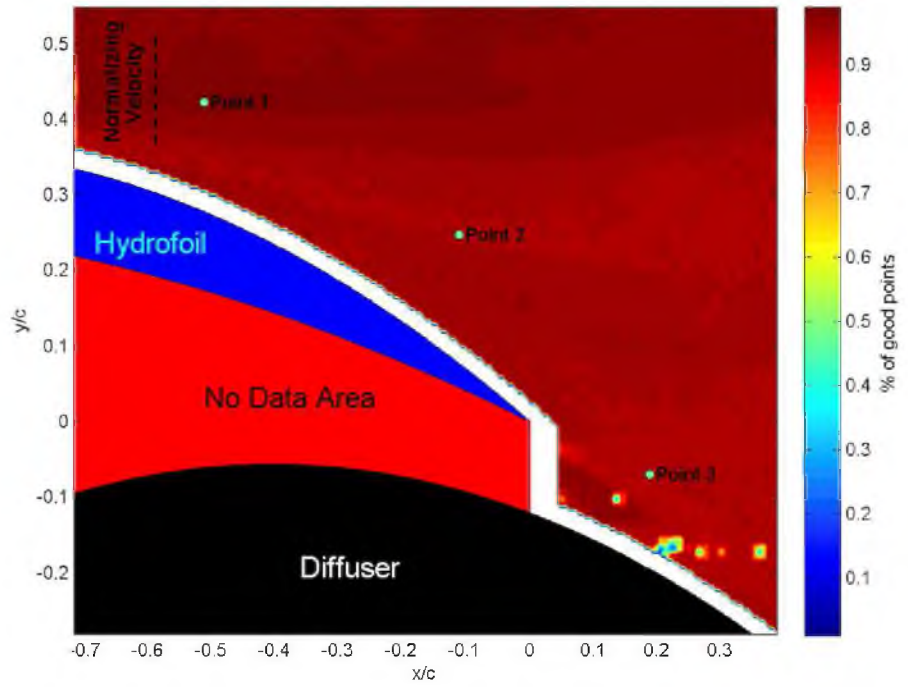

Figure A-8. "Choice Code" contour plot for low roughness at 17° indicating the percentage of good vectors at each data processing spot.

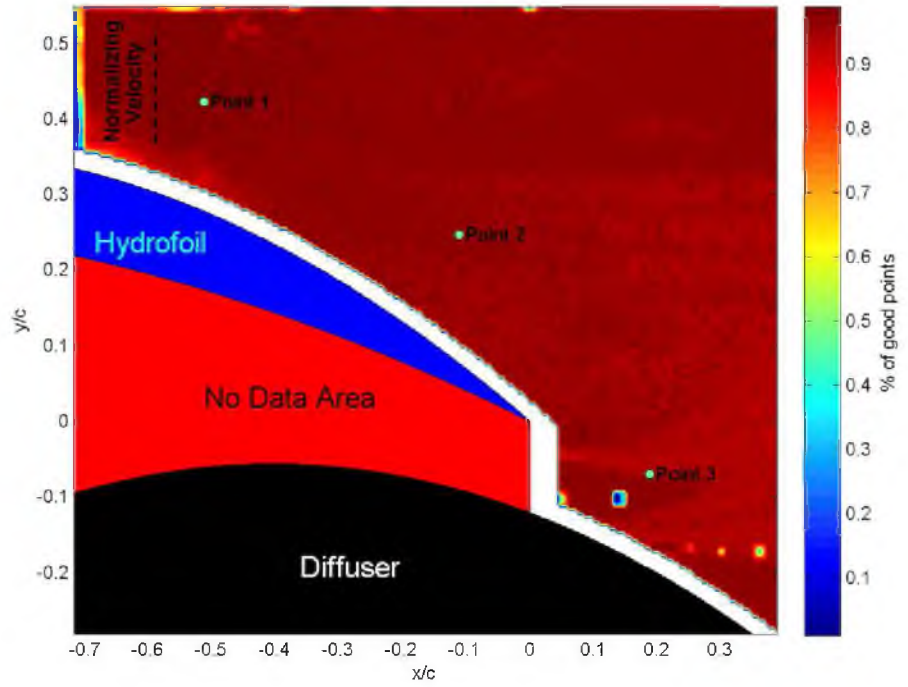

Figure A-9. "Choice Code" contour plot for medium roughness at 17° indicating the percentage of good vectors at each data processing spot.

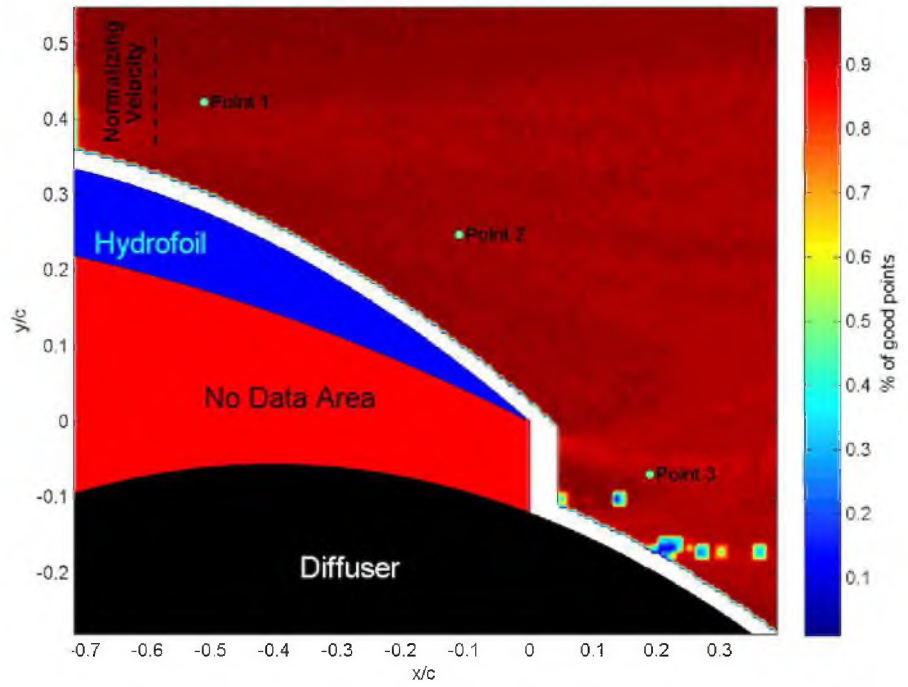

Figure A-10. "Choice Code" contour plot for high roughness at 17° indicating the percentage of good vectors at each data processing spot.

A2. Convergence Plots

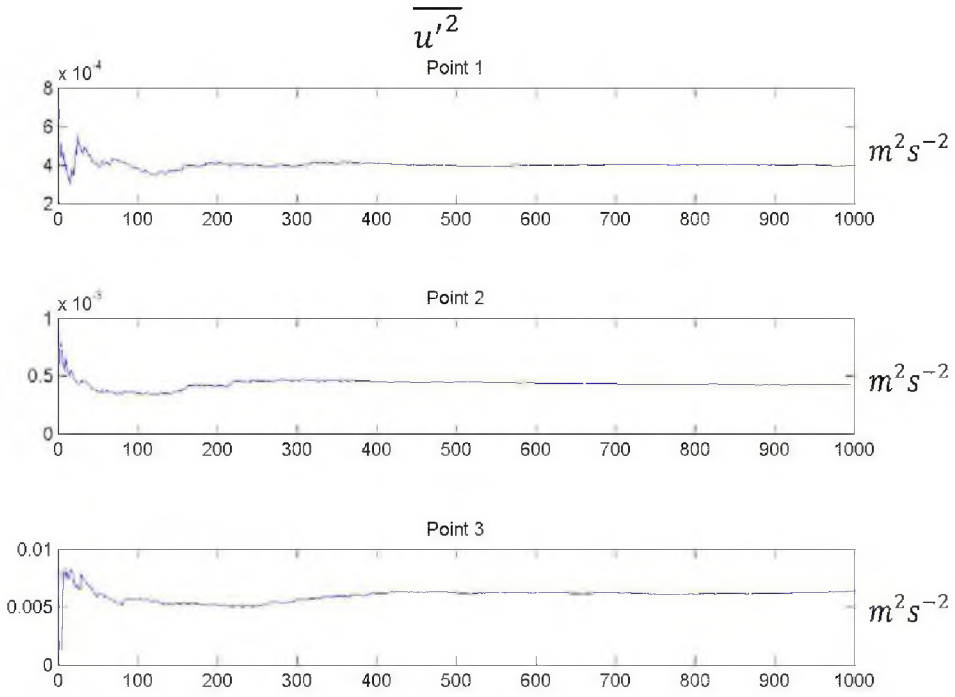

Figure A-11. Convergence plot for mean Reynolds normal stress in the streamwise direction as a function of number of images considered for experiment with no hydrofoil.

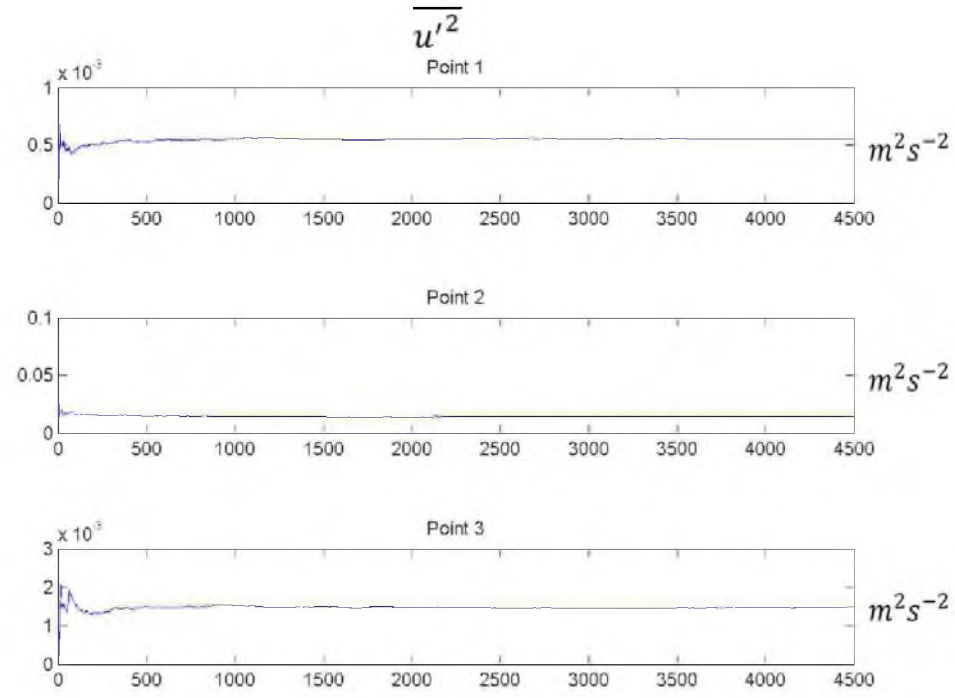

Figure A-12. Convergence plot for mean Reynolds normal stress in the streamwise direction as a function of number of images considered for low roughness at 0°.

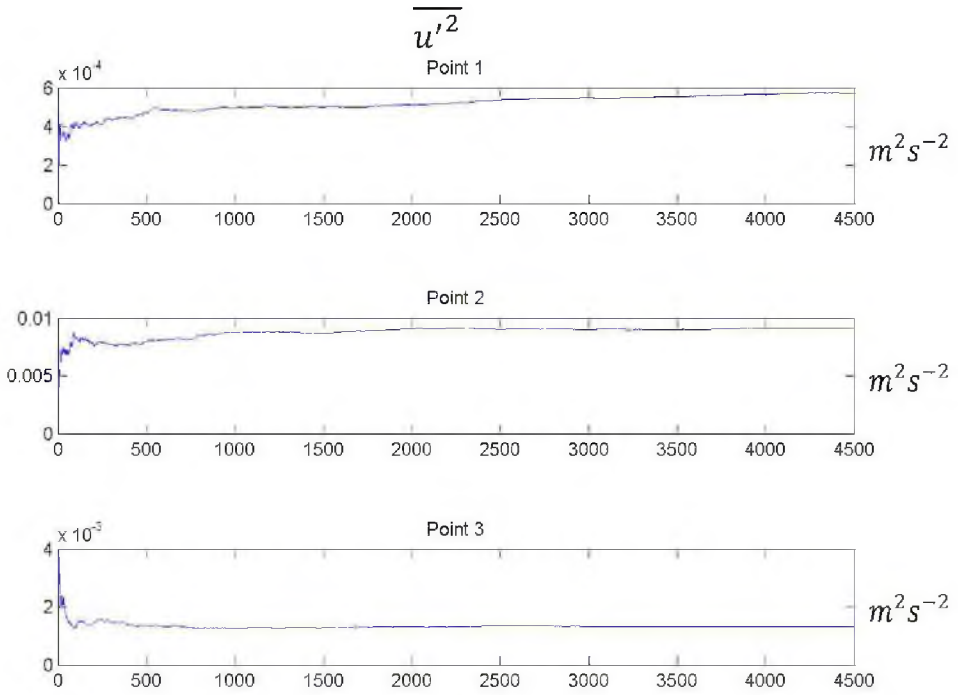

Figure A-13. Convergence plot for mean Reynolds normal stress in the streamwise direction as a function of number of images considered for medium roughness at 0°.

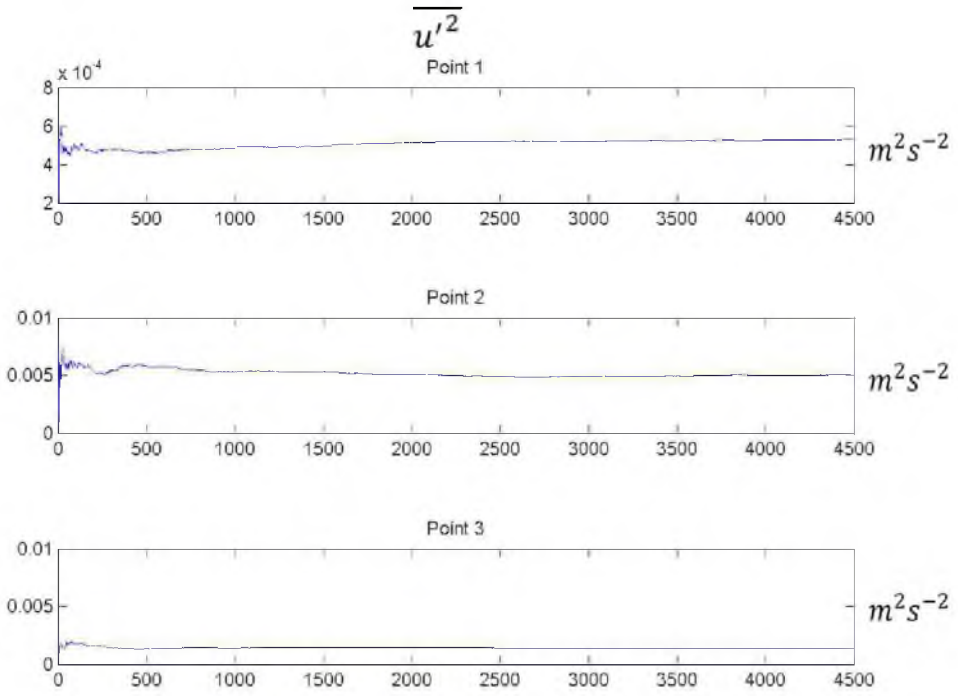

Figure A-14. Convergence plot for mean Reynolds normal stress in the streamwise direction as a function of number of images considered for high roughness at 0°.

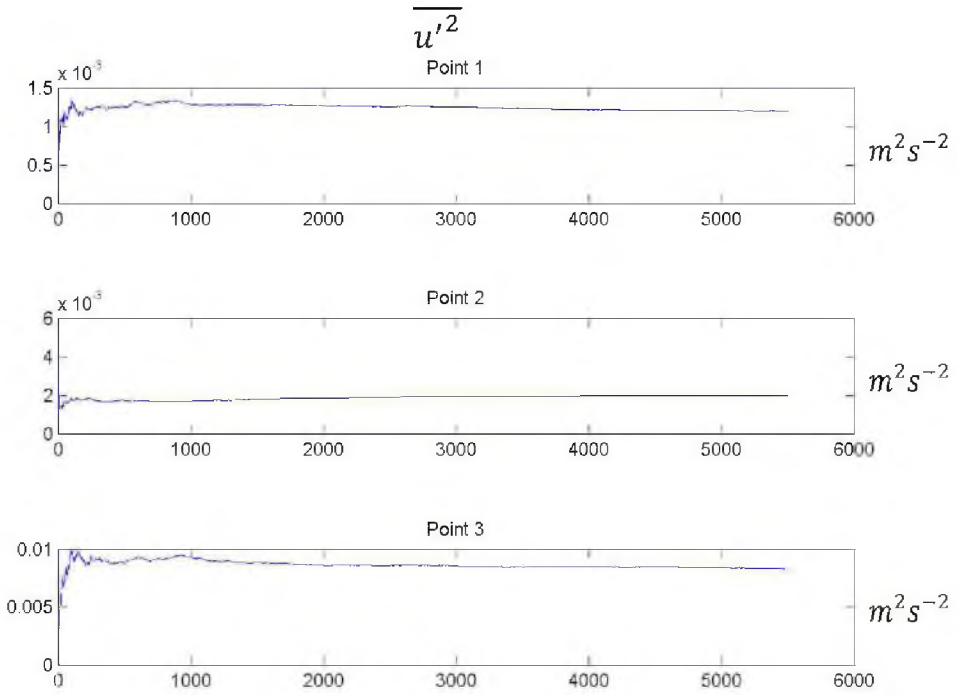

Figure A-15. Convergence plot for mean Reynolds normal stress in the streamwise direction as a function of number of images considered for low roughness at 10°.

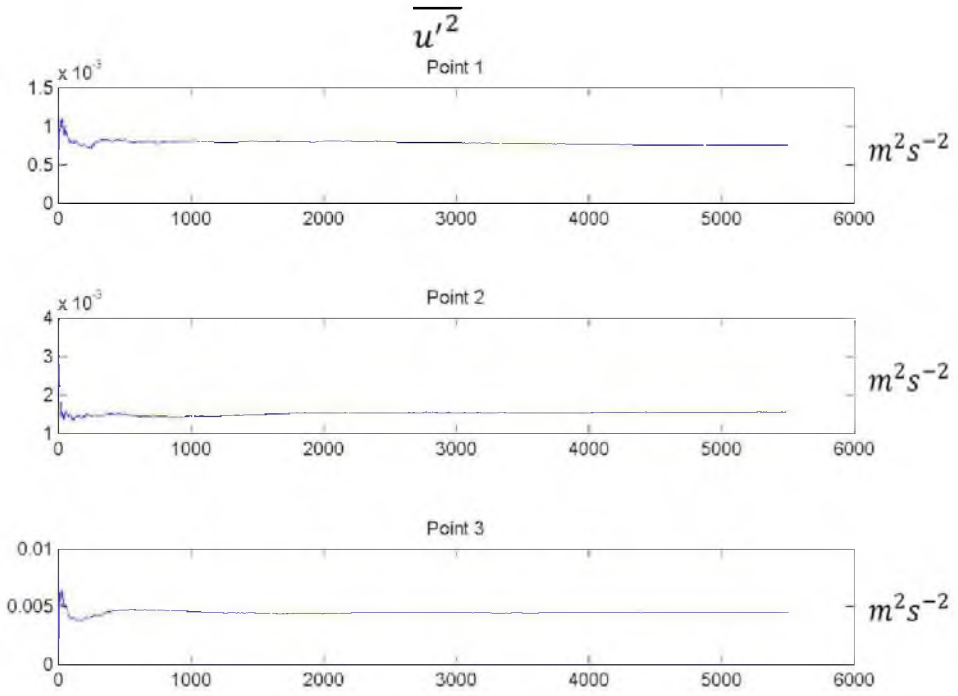

Figure A-16. Convergence plot for mean Reynolds normal stress in the streamwise direction as a function of number of images considered for medium roughness at 10°.

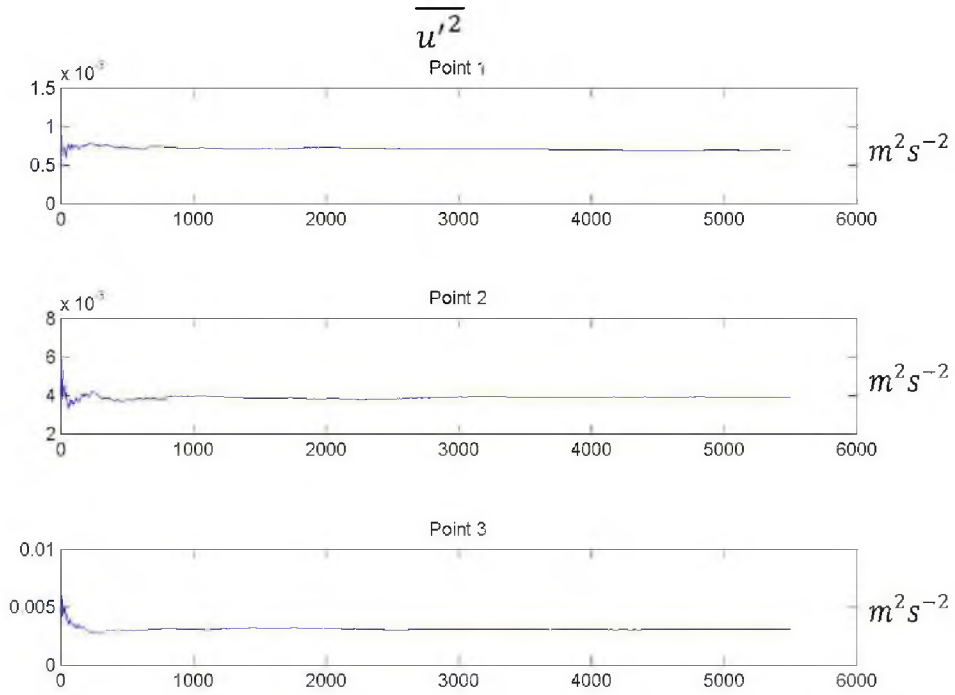

Figure A-17. Convergence plot for mean Reynolds normal stress in the streamwise direction as a function of number of images considered for high roughness at 10°.

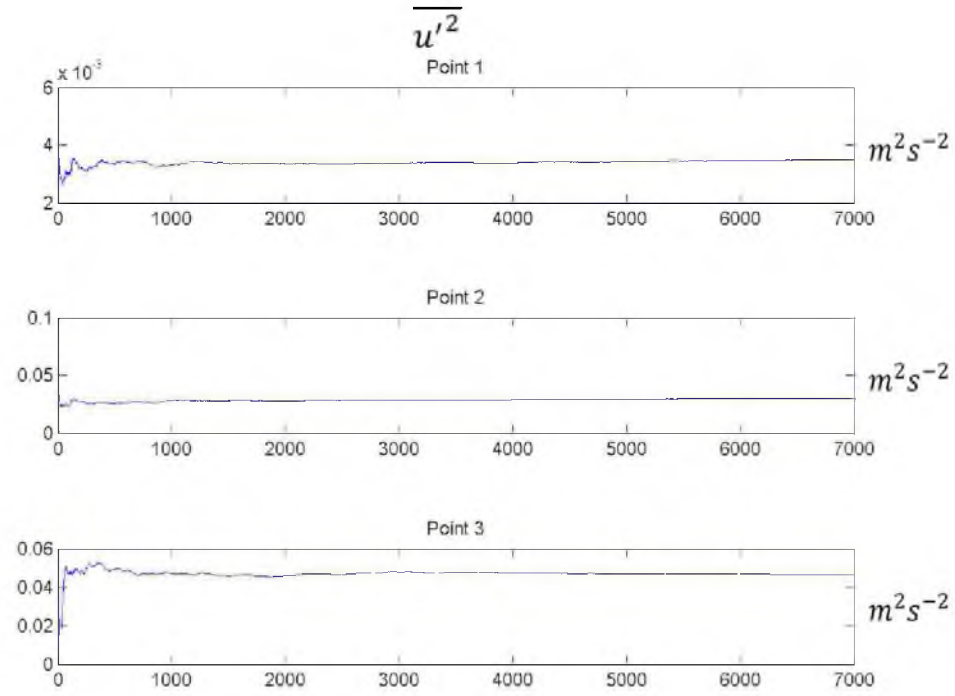

Figure A-18. Convergence plot for mean Reynolds normal stress in the streamwise direction as a function of number of images considered for low roughness at 17°.

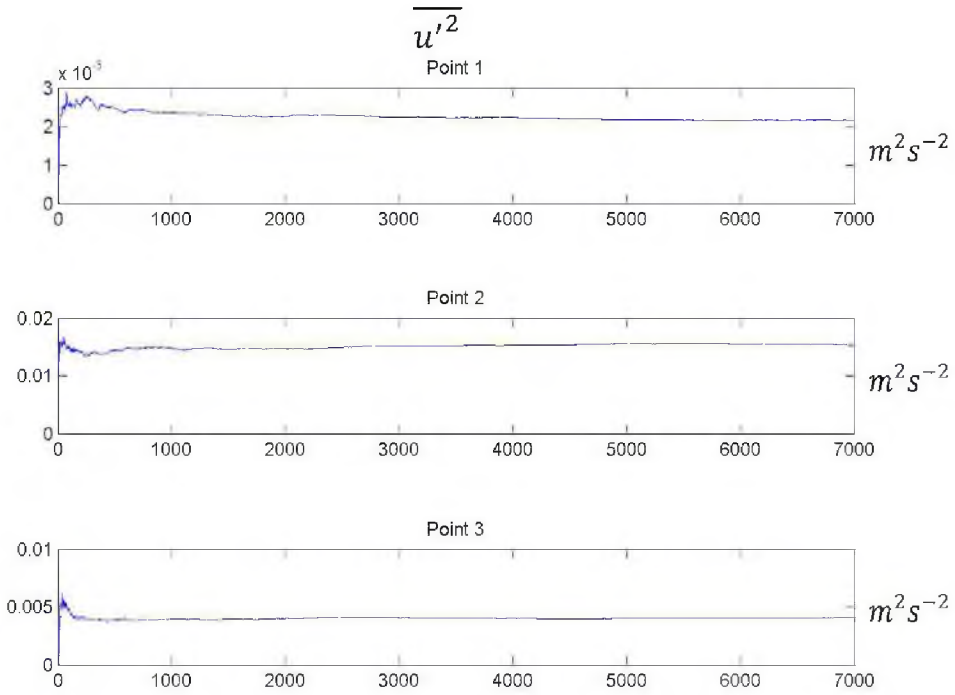

Figure A-19. Convergence plot for mean Reynolds normal stress in the streamwise direction as a function of number of images considered for medium roughness at 17°.

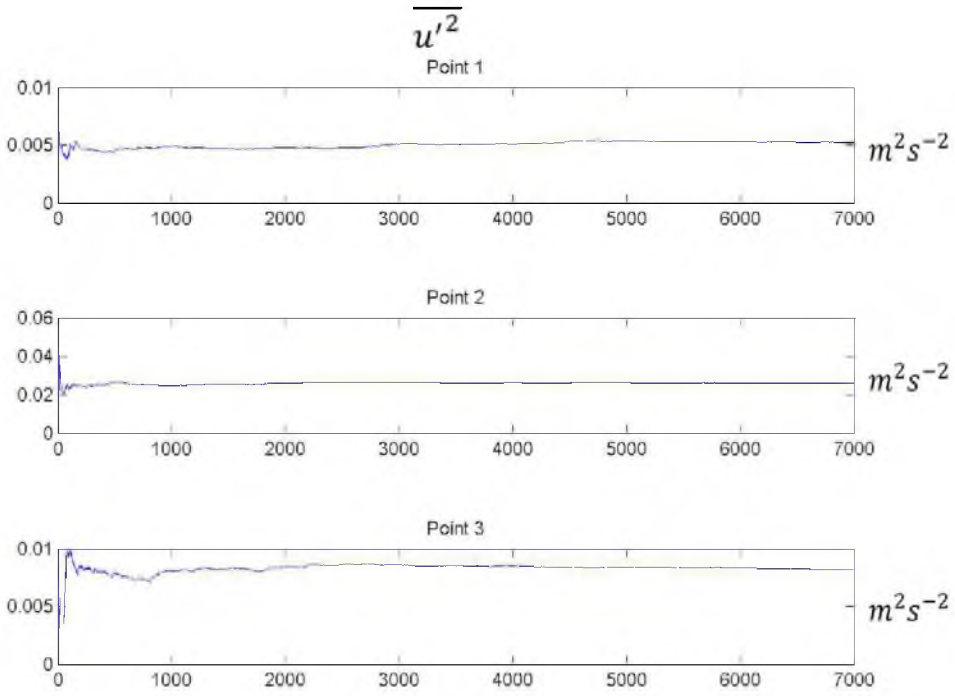

Figure A-20. Convergence plot for mean Reynolds normal stress in the streamwise direction as a function of number of images considered for high roughness at 17°.

A3. RANS Terms

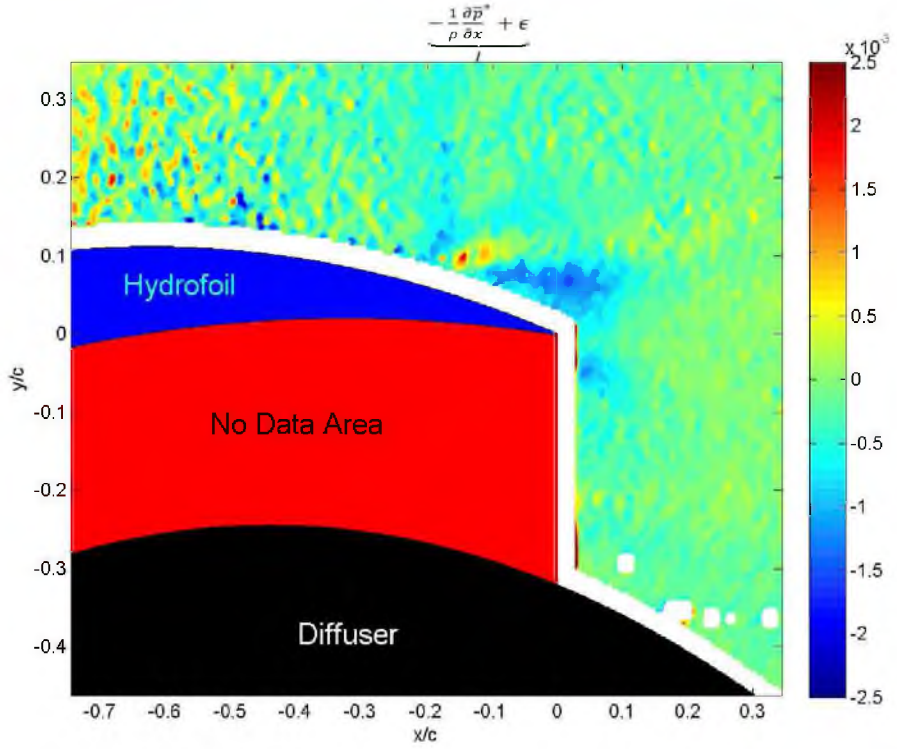

Figure A-21. 'Term I' for low roughness at 0°.

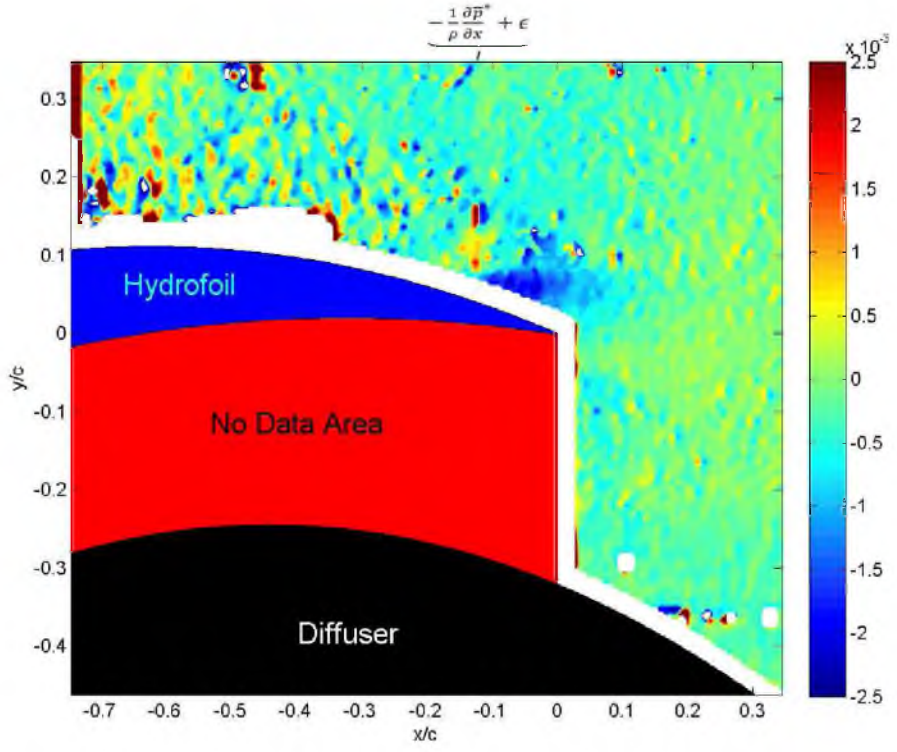

Figure A-22. 'Term I' for medium roughness at 0°.

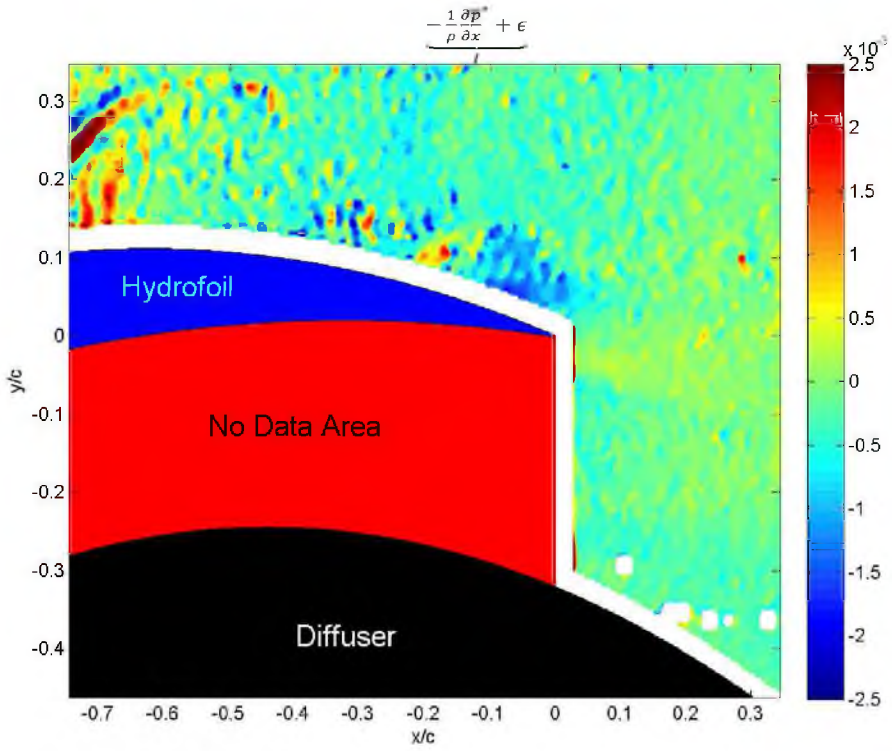

Figure A-23. 'Term I' for high roughness at 0°.

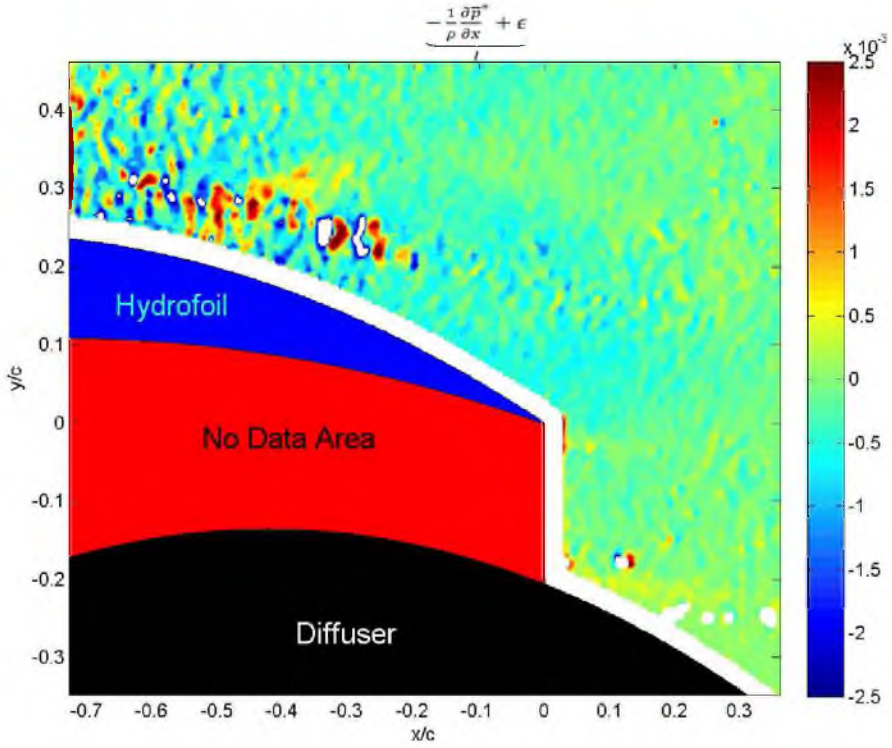

Figure A-24. 'Term I' for low roughness at 10°.

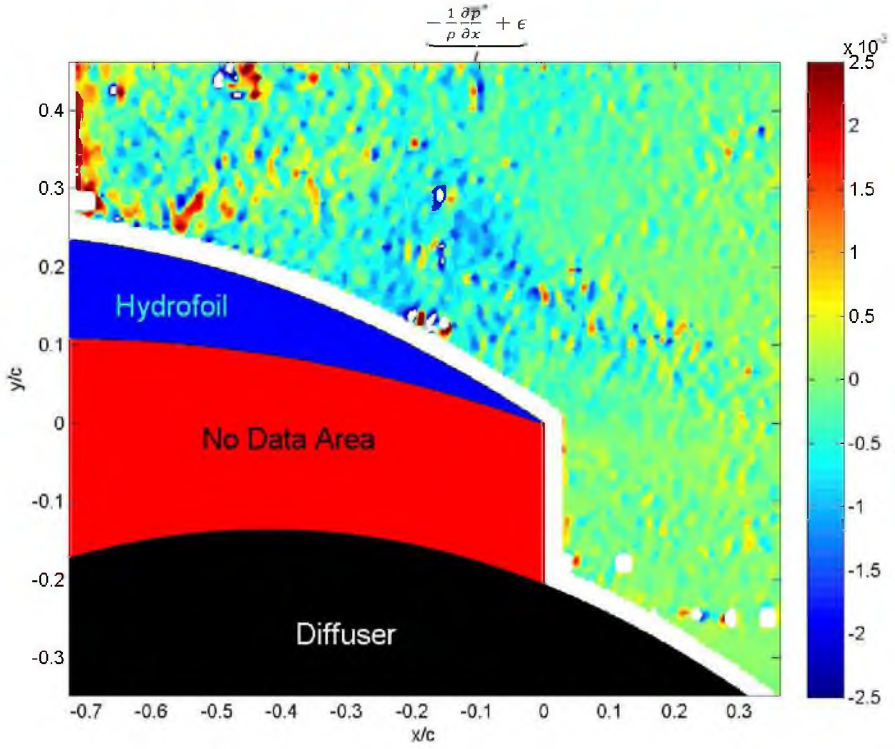

Figure A-25. 'Term I' for medium roughness at 10°.

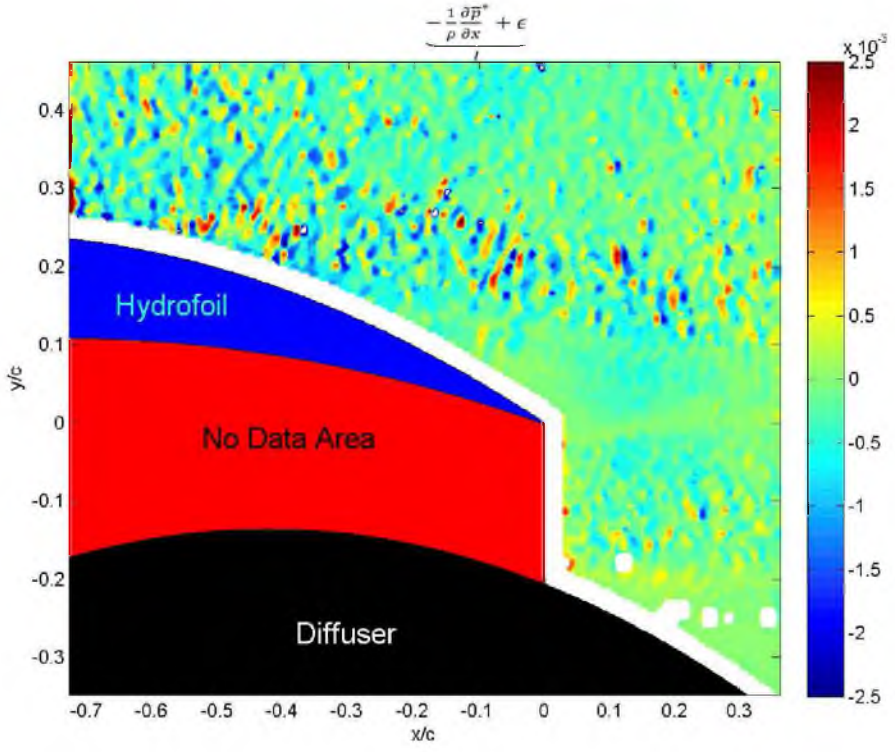

Figure A-26. 'Term I' for high roughness at 10°.

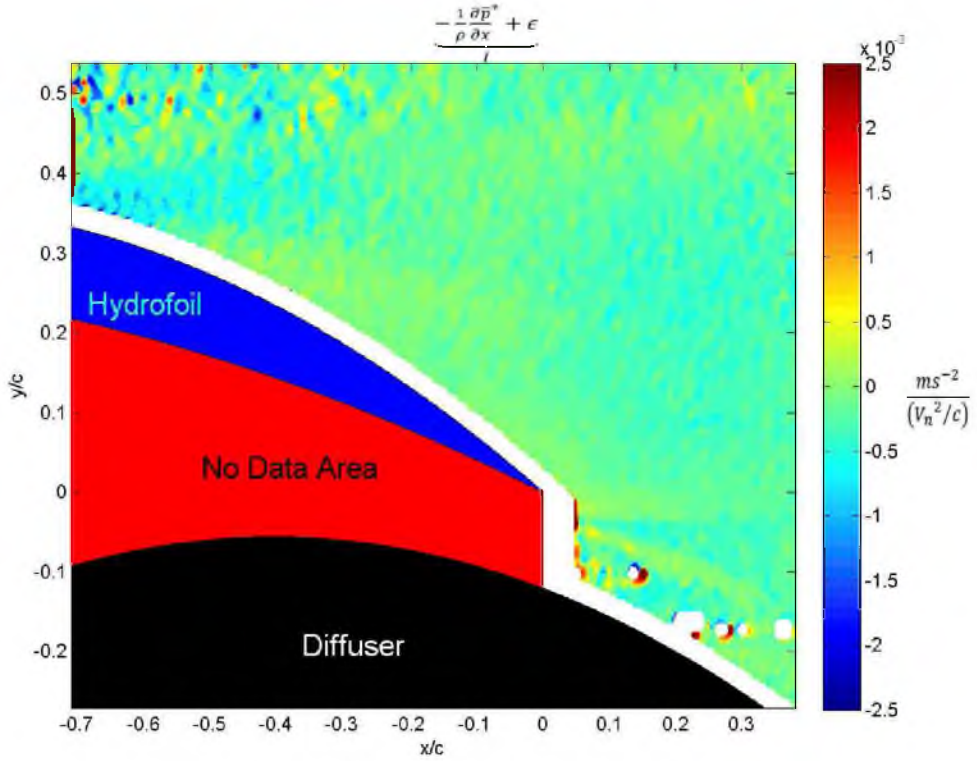

Figure A-27. 'Term I' for low roughness at 17°.

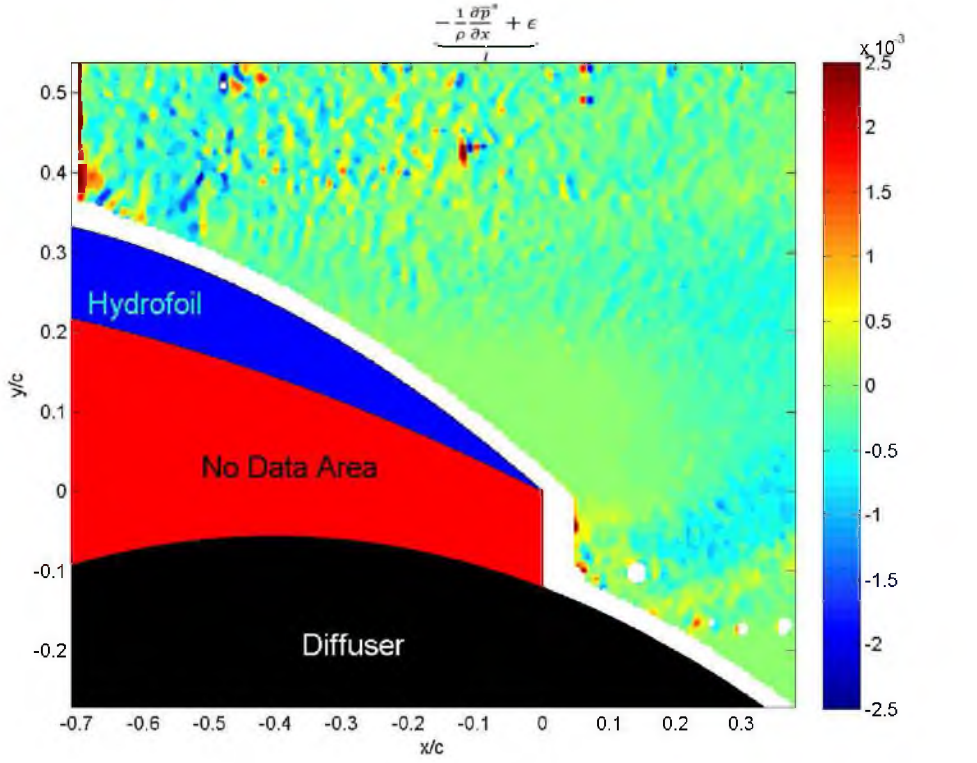

Figure A-28. 'Term I' for medium roughness at 17°.

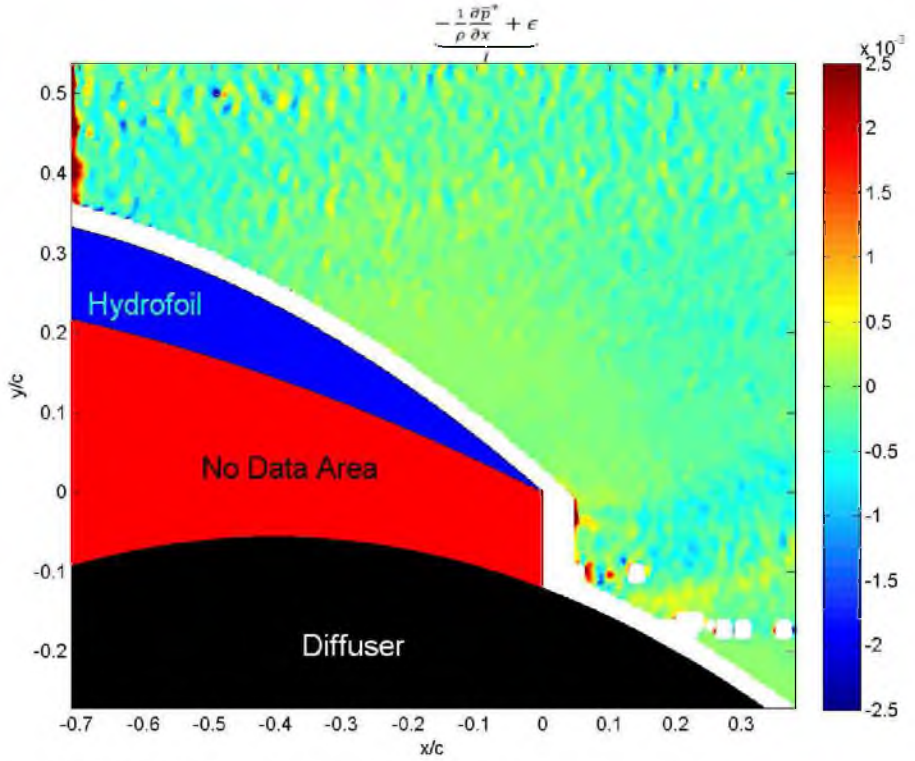

Figure A-29. 'Term I' for high roughness at 17°.

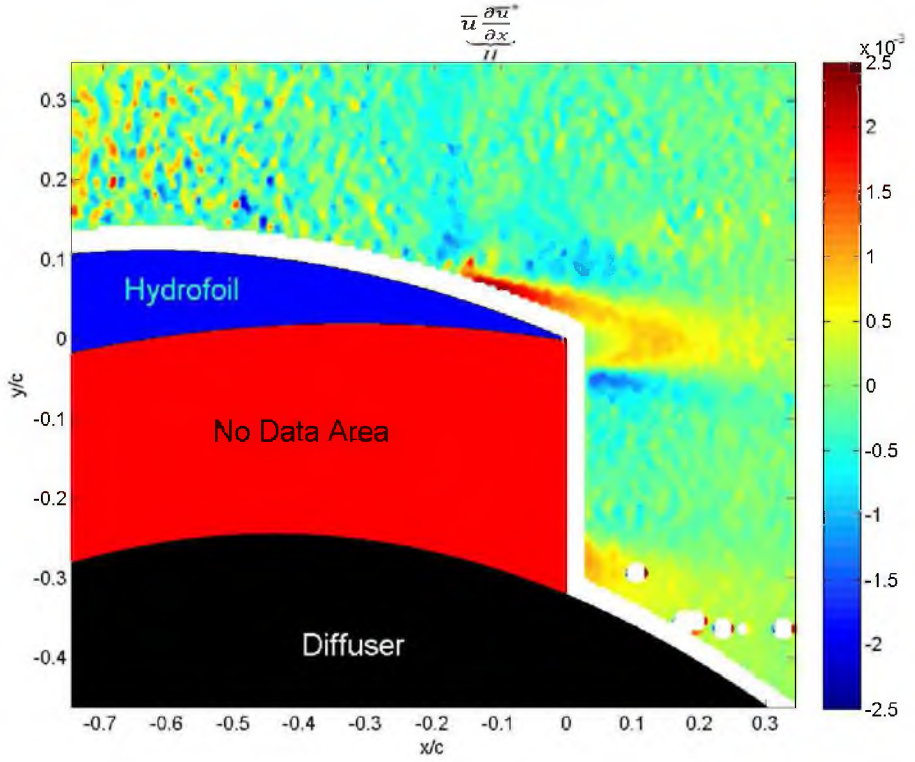

Figure A-30. 'Term II' for low roughness at 0°.

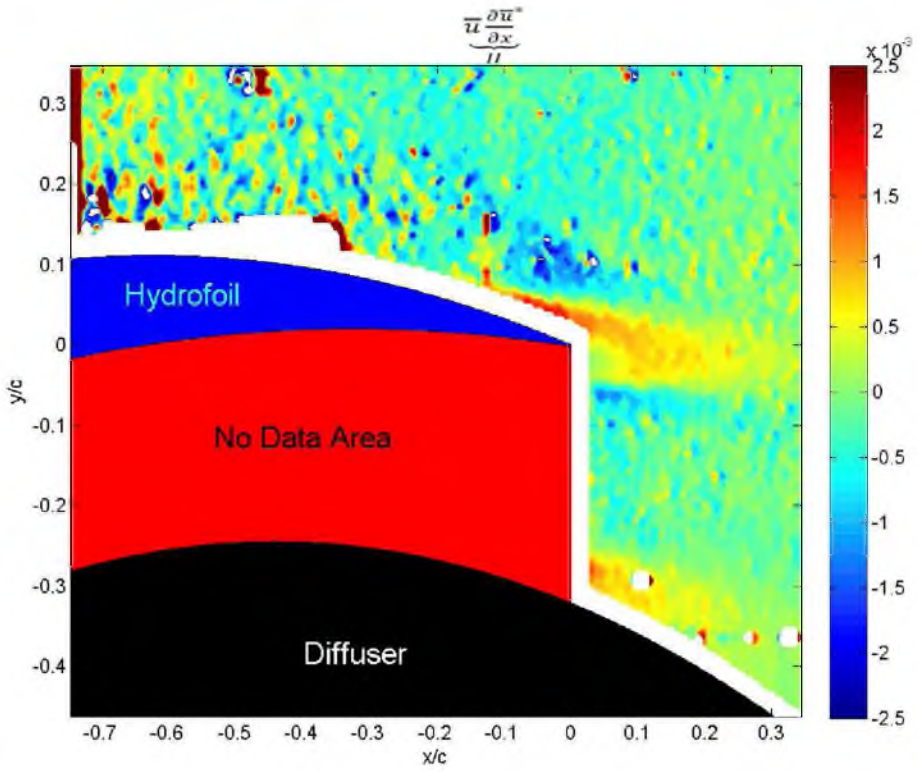

Figure A-31. 'Term II' for medium roughness at 0°.

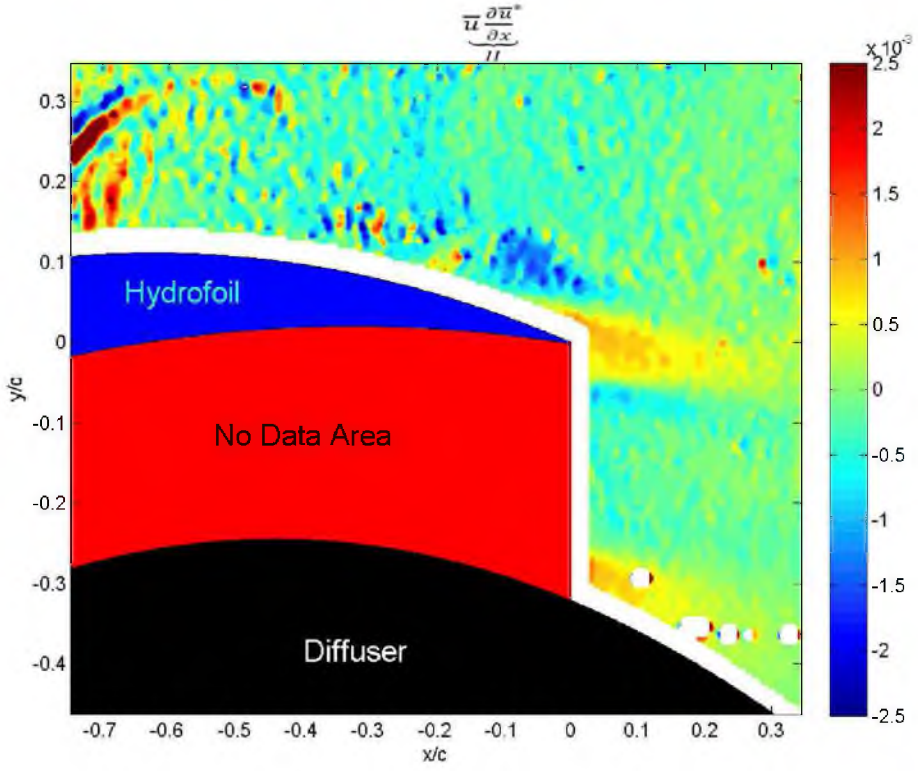

Figure A-32. 'Term II' for high roughness at 0°.

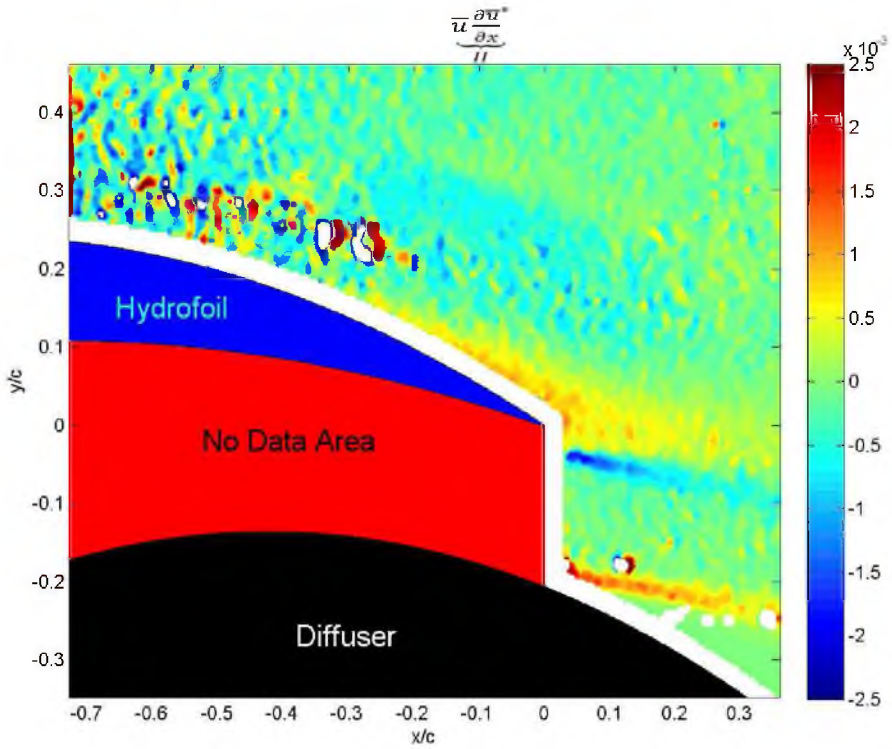

Figure A-33. 'Term II' for low roughness at 10°.

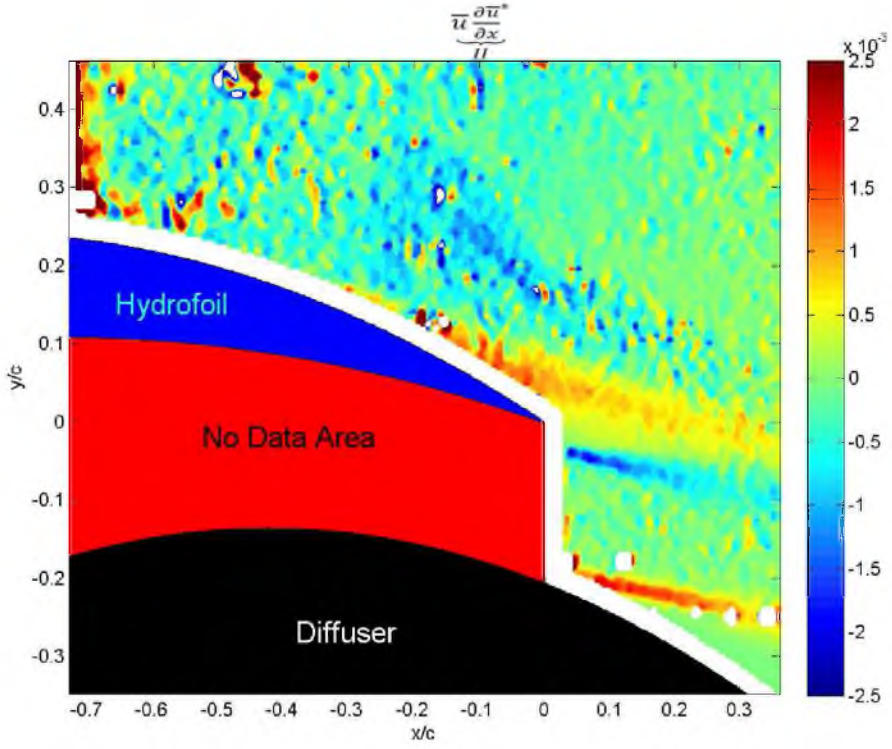

Figure A-34. 'Term II' for medium roughness at 10°.

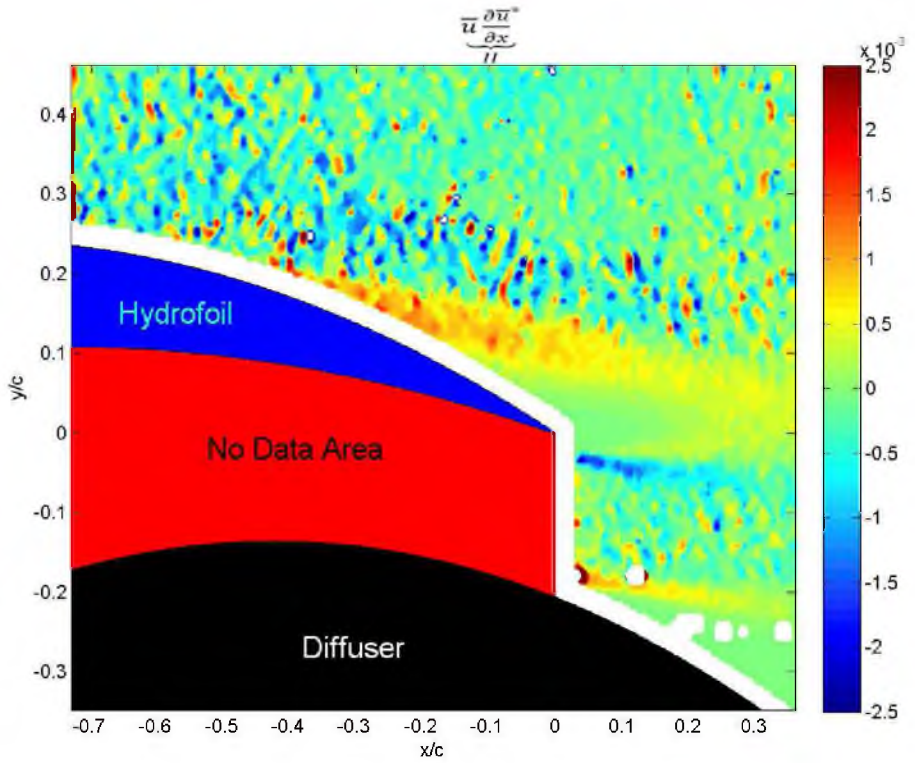

Figure A-35. 'Term II' for high roughness at 10°.

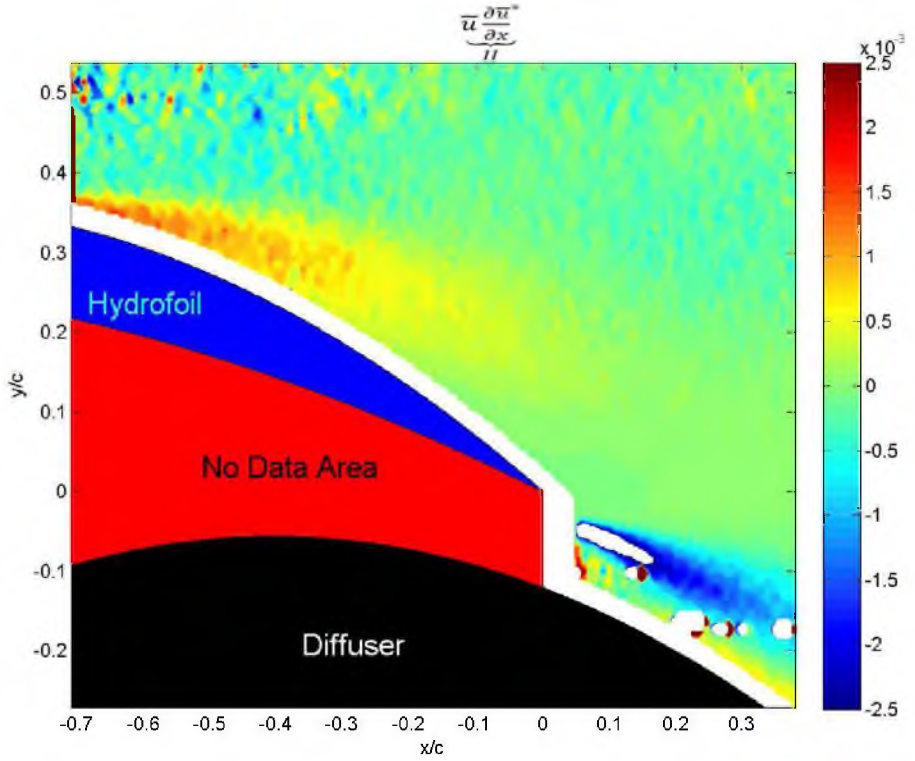

Figure A-36. 'Term II' for low roughness at 17°.

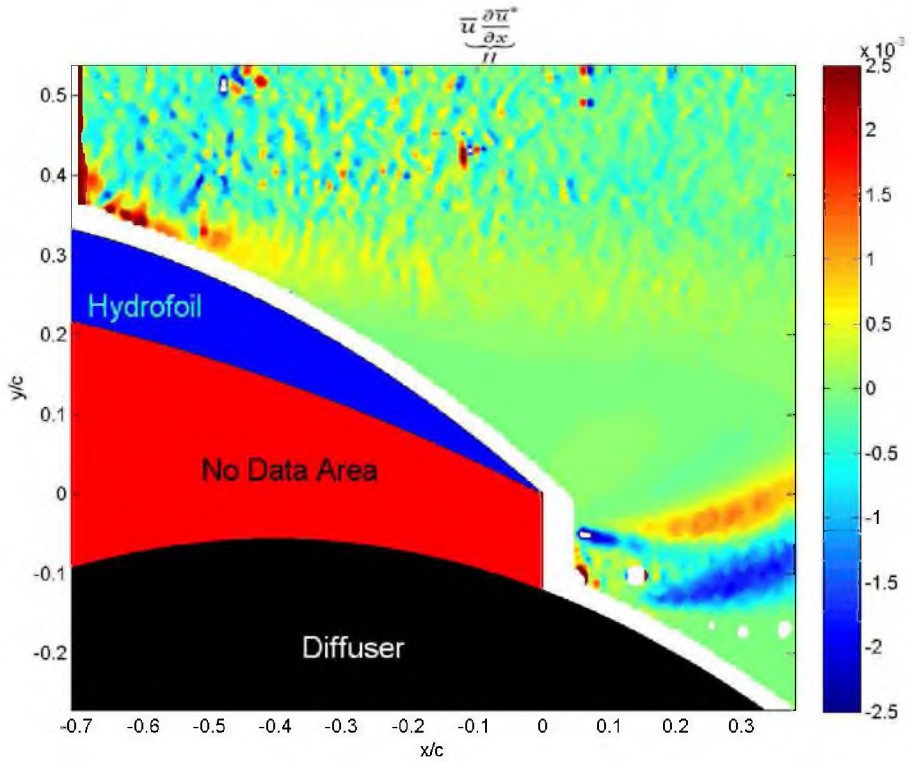

Figure A-37. 'Term II' for medium roughness at 17°.

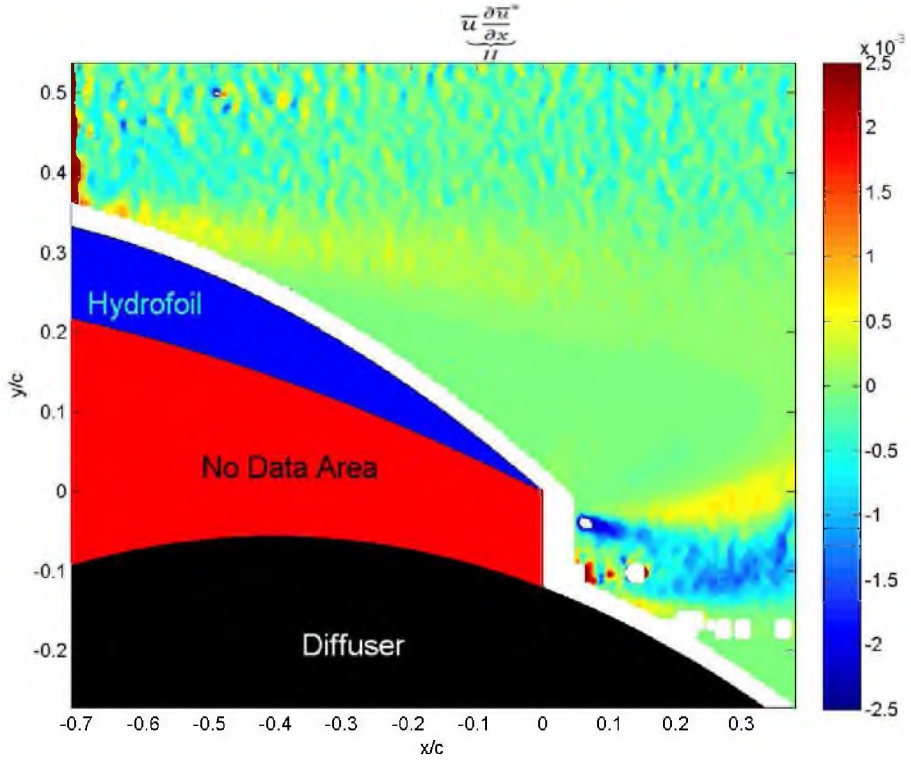

Figure A-38. 'Term II' for high roughness at 17°.

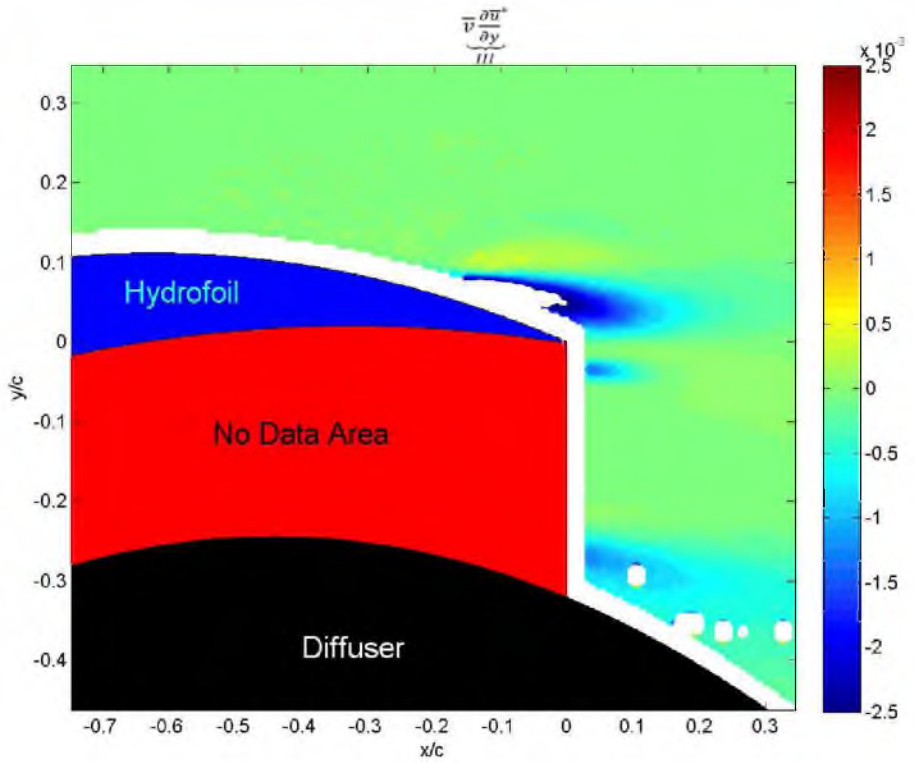

Figure A-39. 'Term III' for low roughness at 0°.

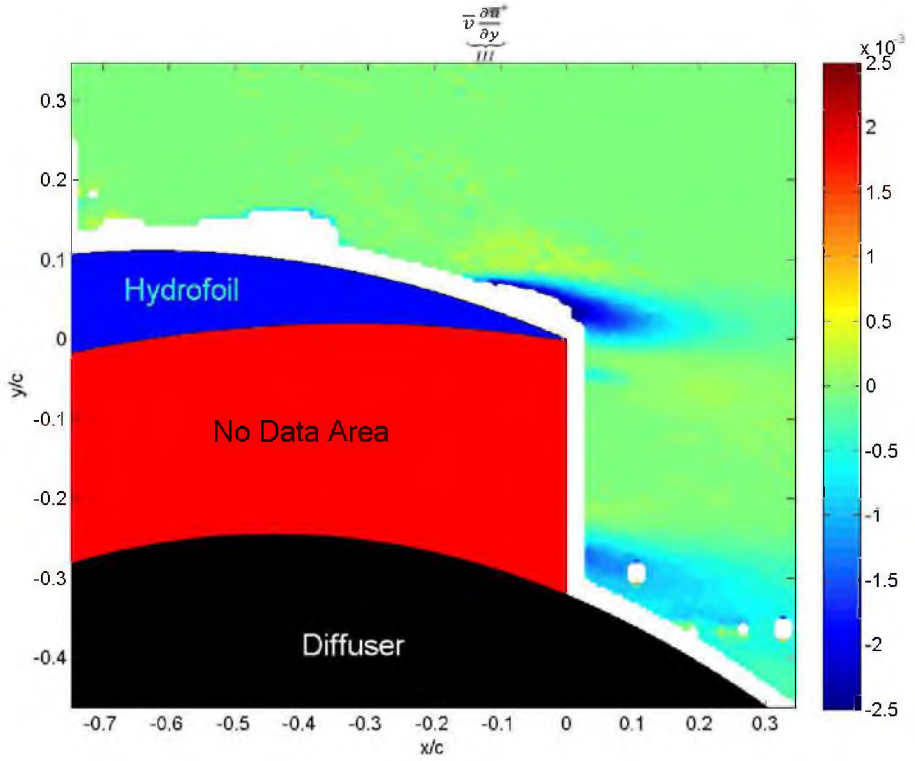

Figure A-40. 'Term III' for medium roughness at 0°.

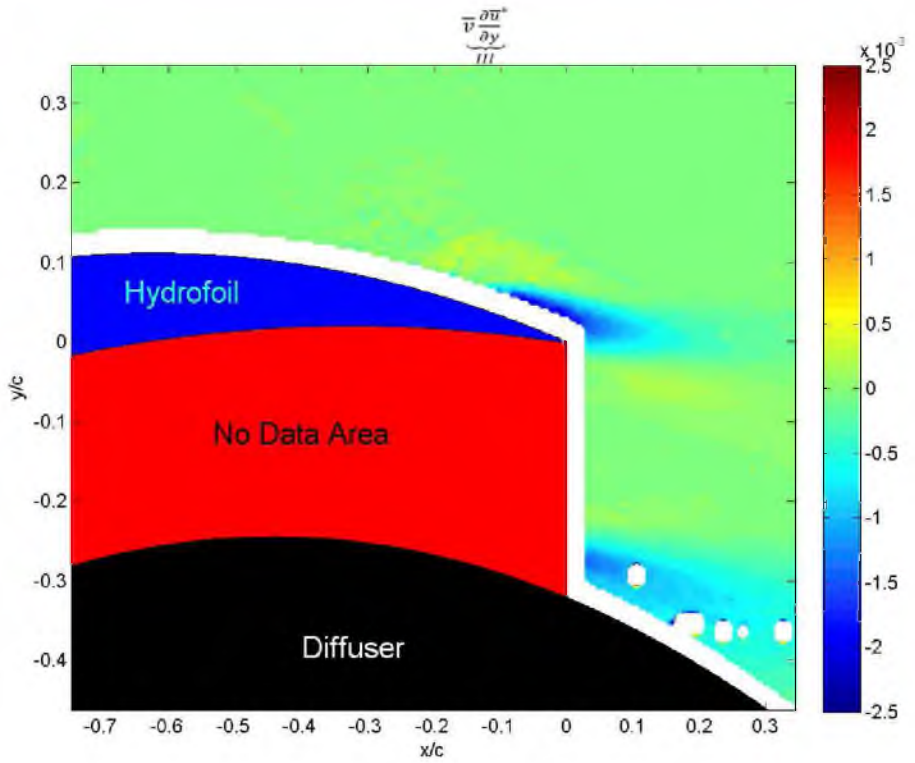

Figure A-41. 'Term III' for high roughness at 0°.

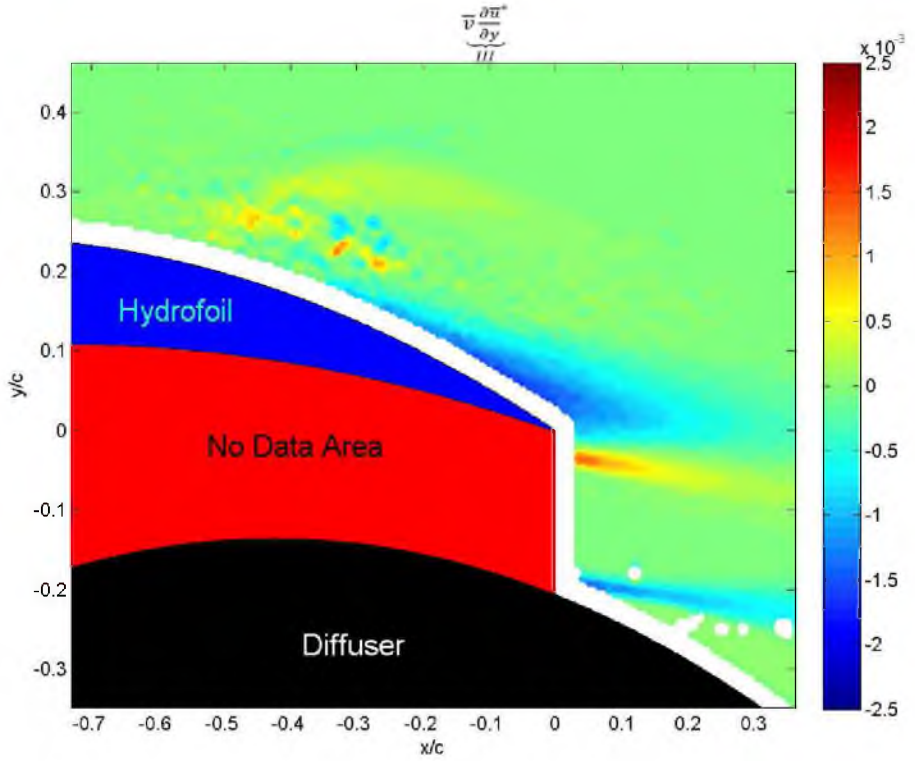

Figure A-42. 'Term III' for low roughness at 10°.

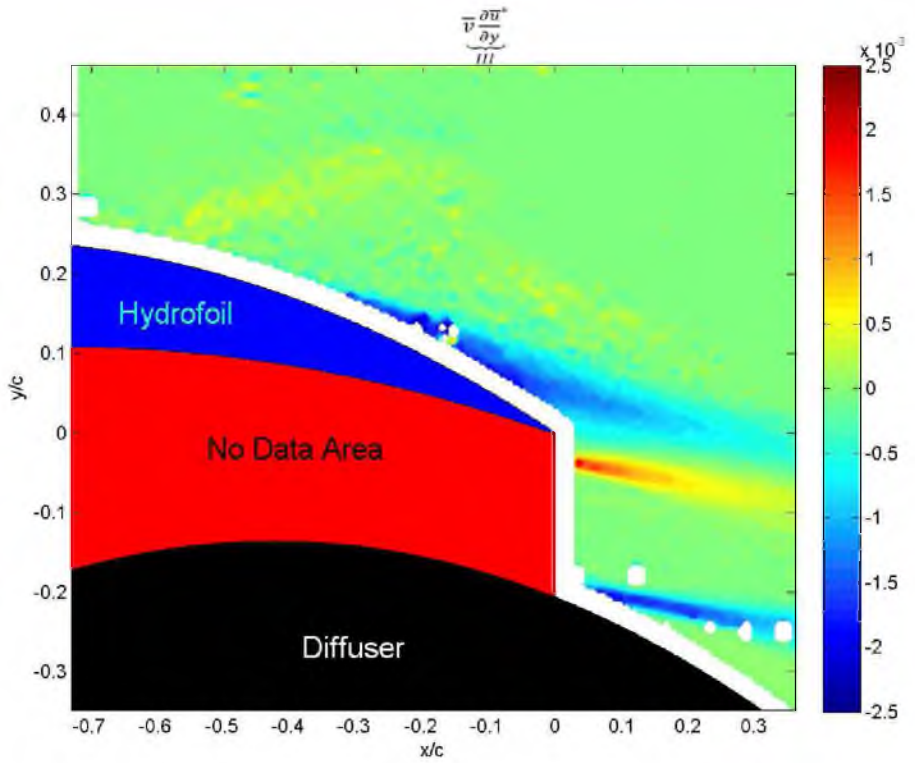

Figure A-43. 'Term III' for medium roughness at 10°.

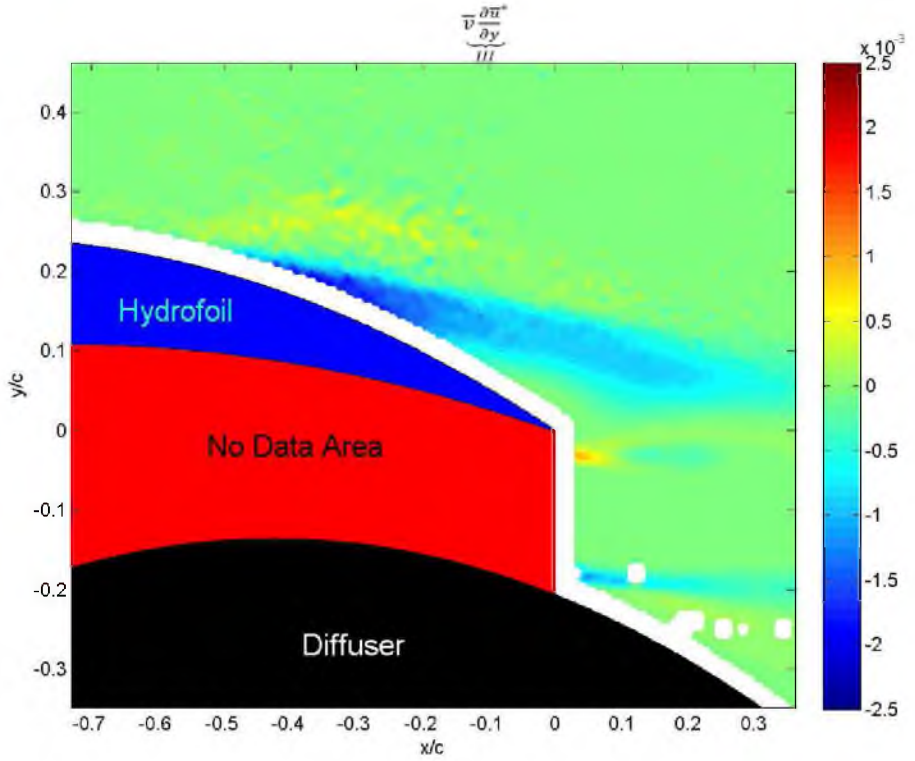

Figure A-44. 'Term III' for high roughness at 10°.

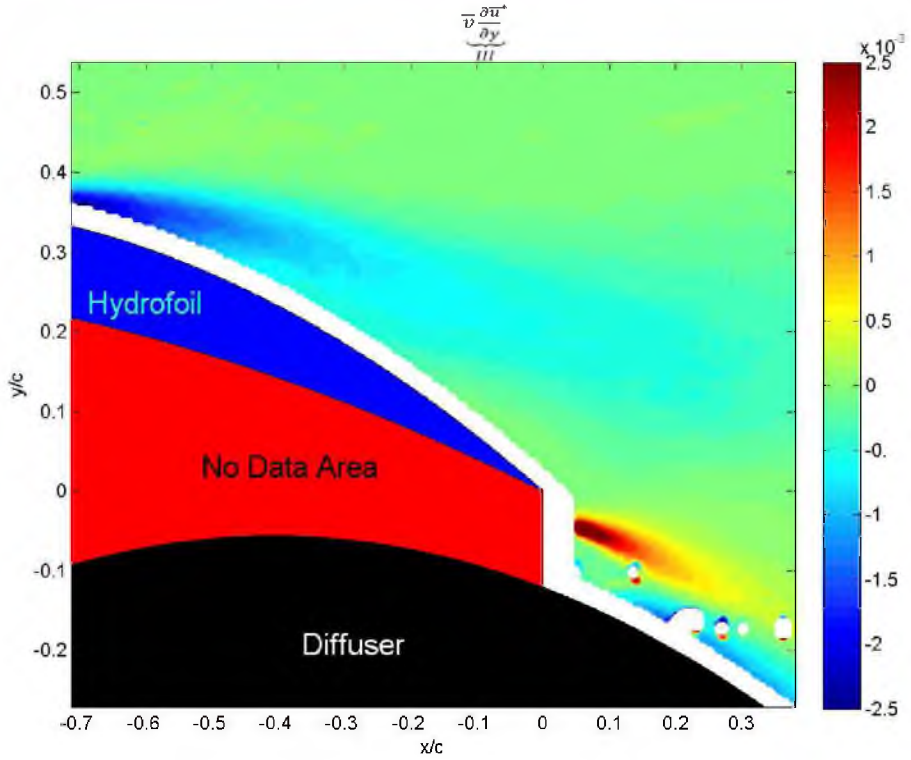

Figure A-45. 'Term III' for low roughness at 17°.

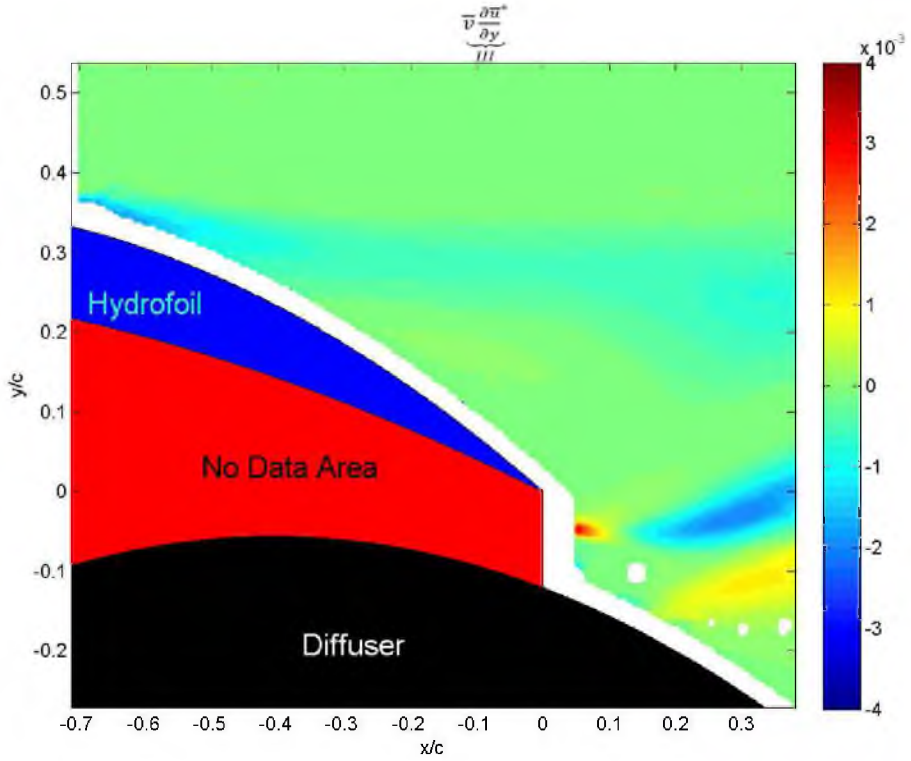

Figure A-46. 'Term III' for medium roughness at 17°.

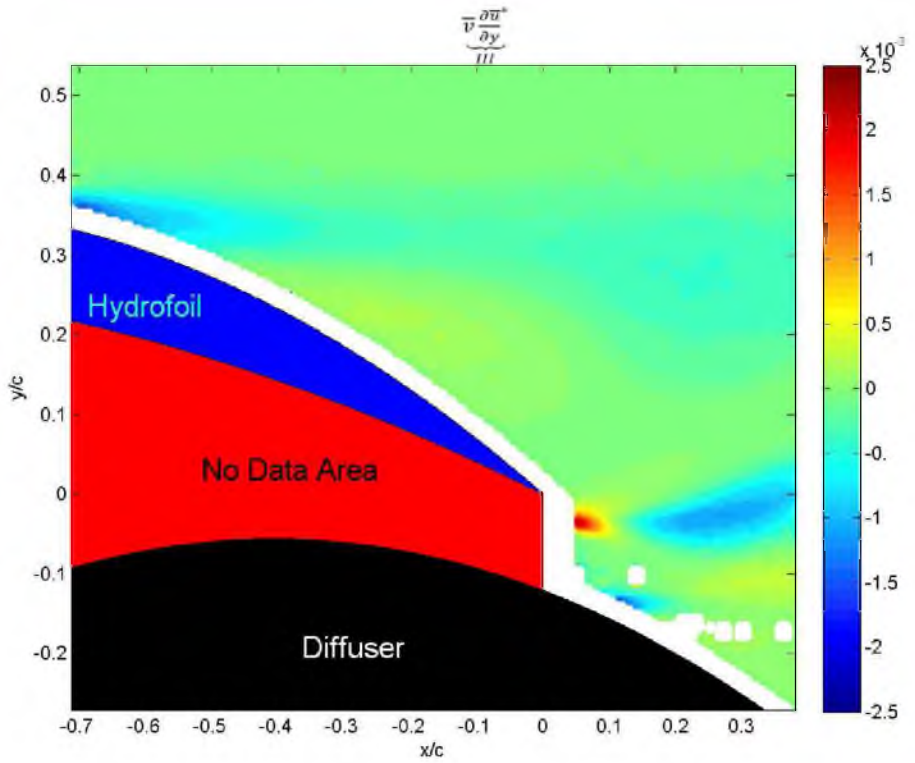

Figure A-47. 'Term III' for high roughness at 17°.

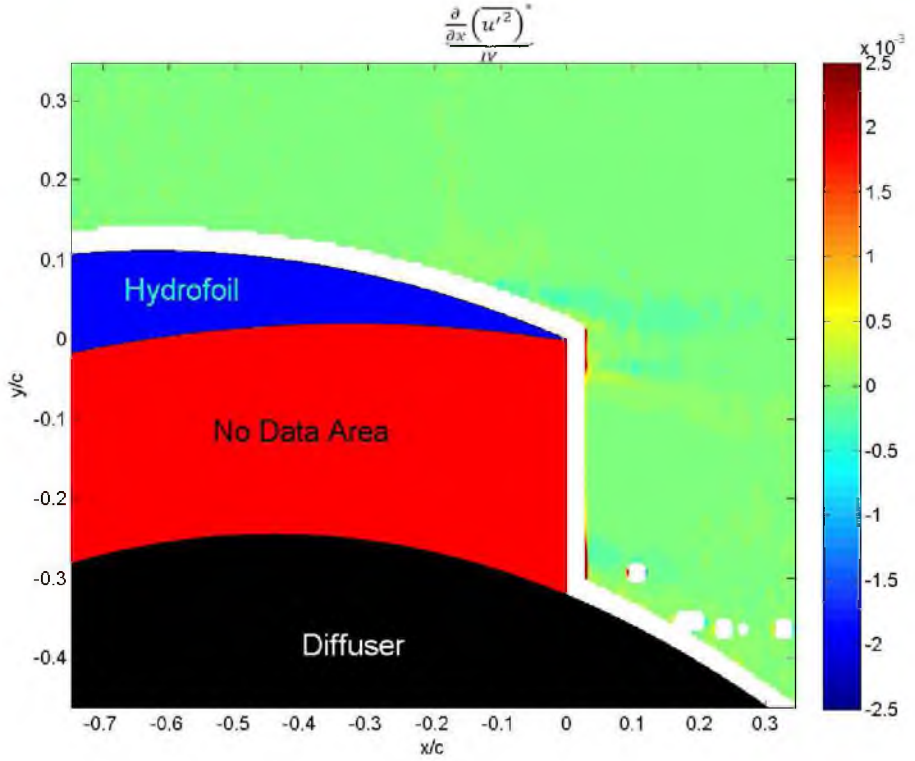

Figure A-48. 'Term IV' for low roughness at 0°.

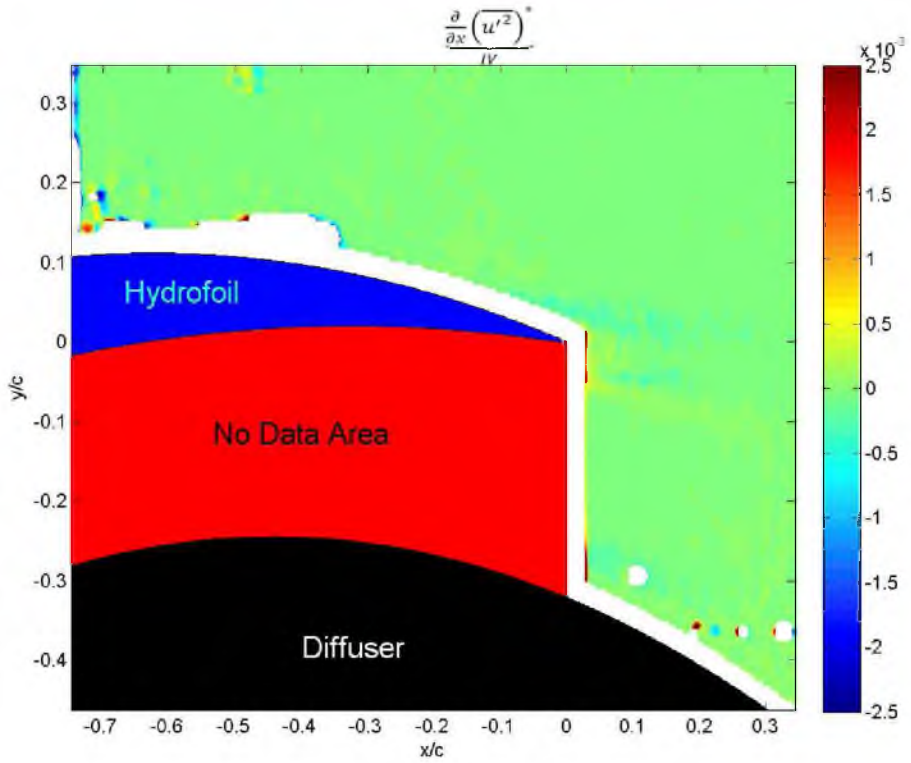

Figure A-49. 'Term IV' for medium roughness at 0°.

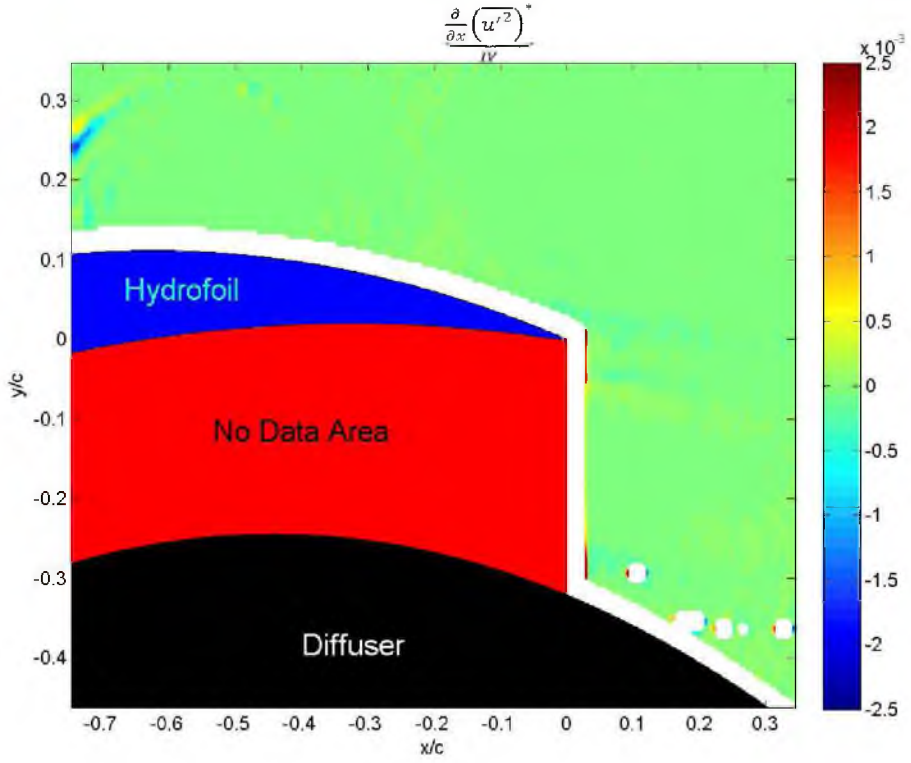

Figure A-50. 'Term IV' for high roughness at 0°.

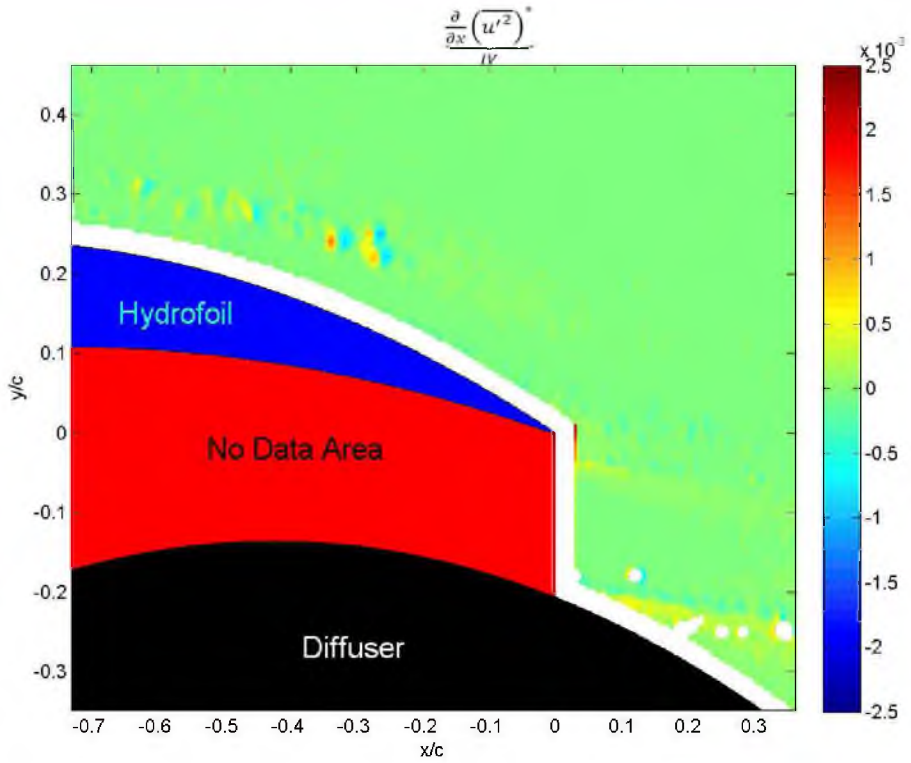

Figure A-51. 'Term IV' for low roughness at 10°.

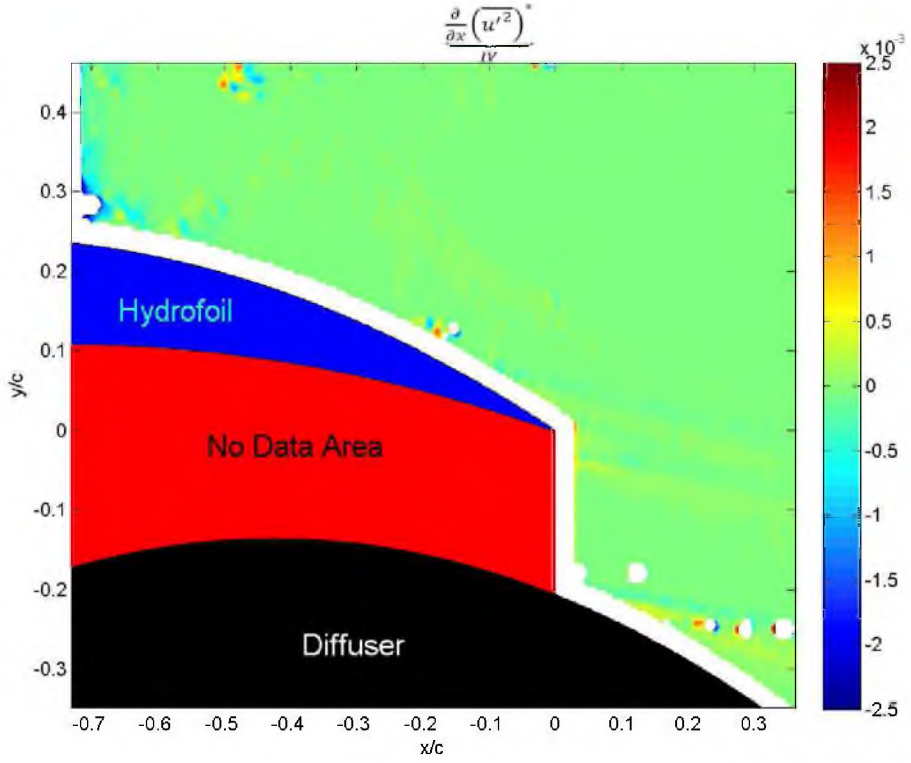

Figure A-52. 'Term IV' for medium roughness at 10°.

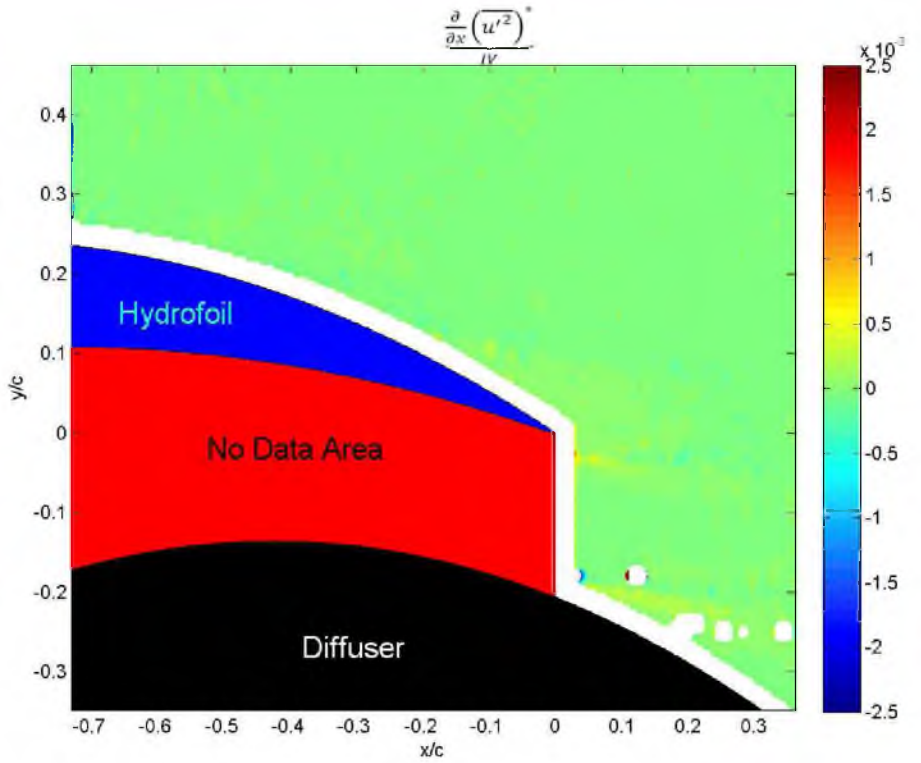

Figure A-53. 'Term IV' for high roughness at 10°.

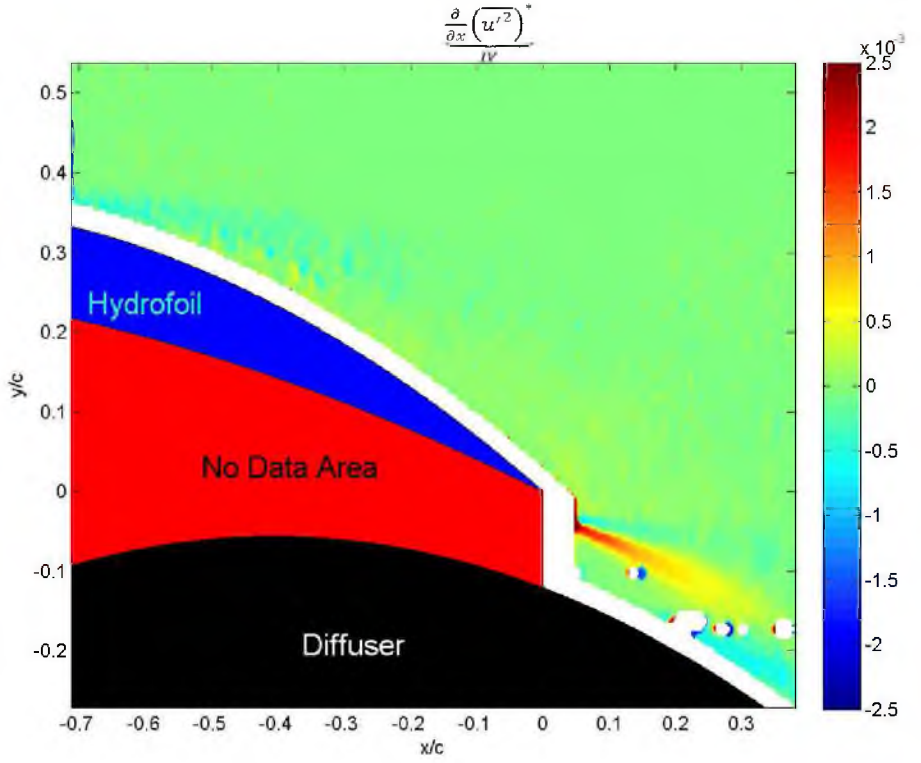

Figure A-54. 'Term IV' for low roughness at 17°.

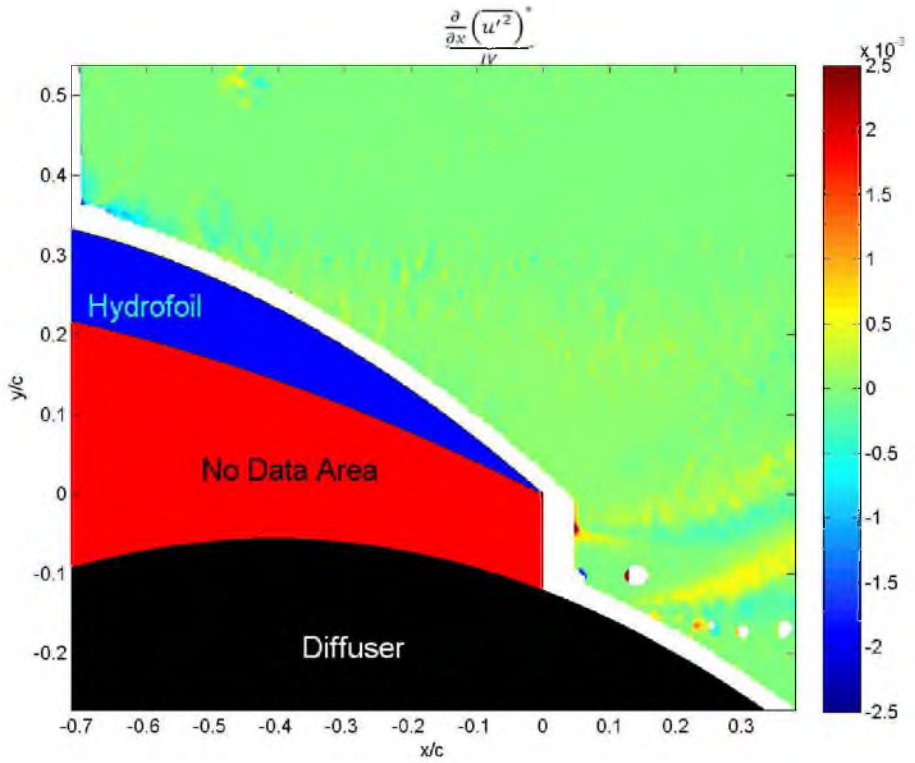

Figure A-55. 'Term IV' for medium roughness at 17°.

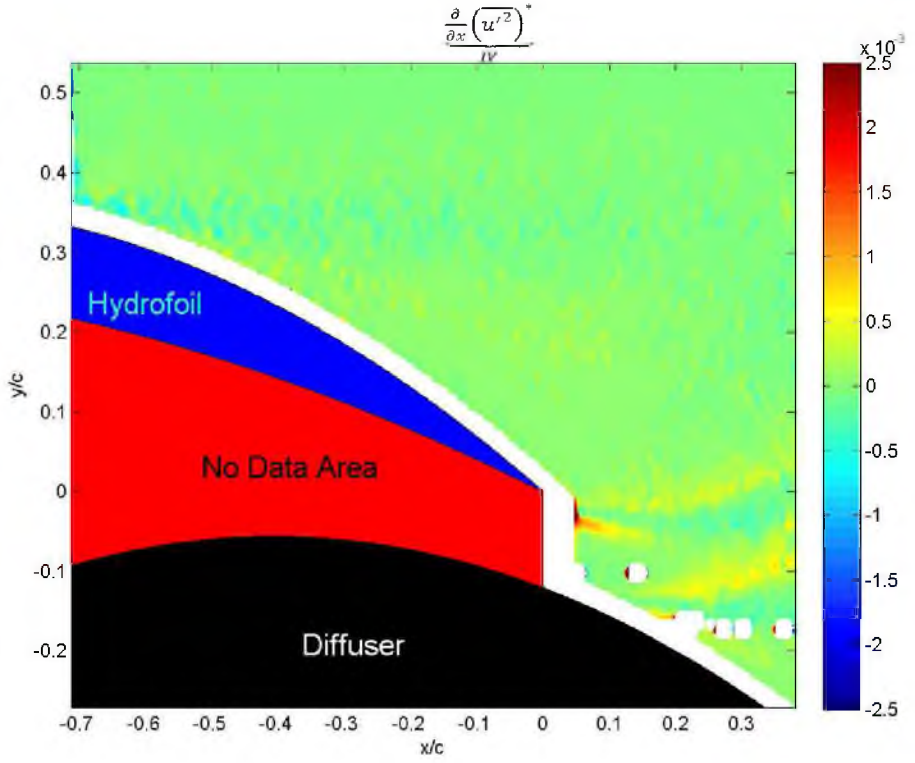

Figure A-56. 'Term IV' for high roughness at 17°.

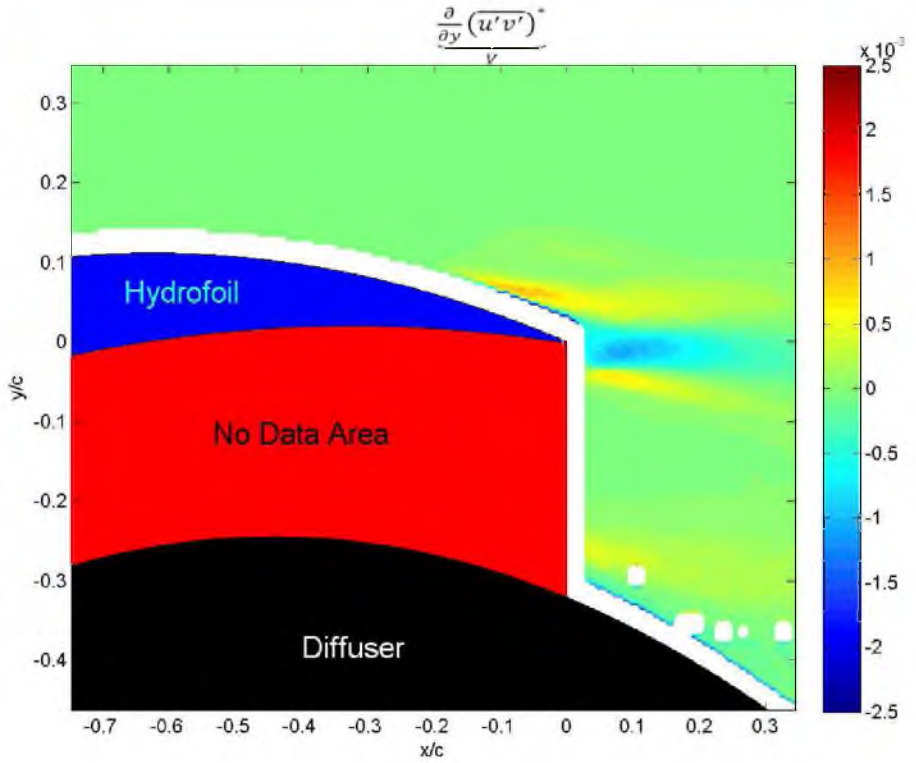

Figure A-57. 'Term V' for low roughness at 0°.

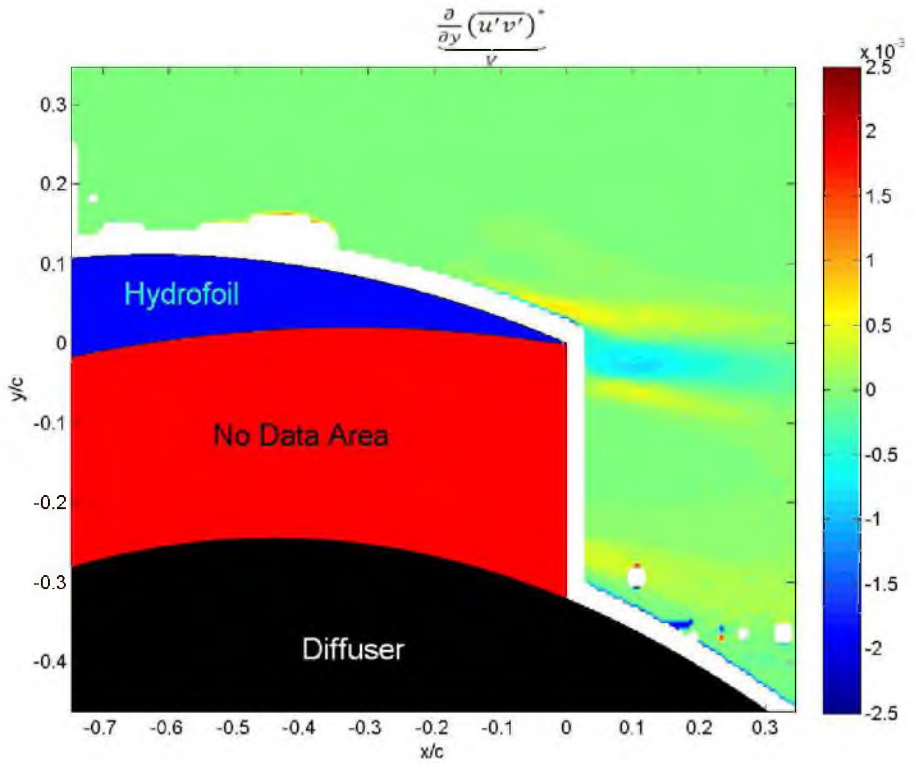

Figure A-58. 'Term V' for medium roughness at 0°.

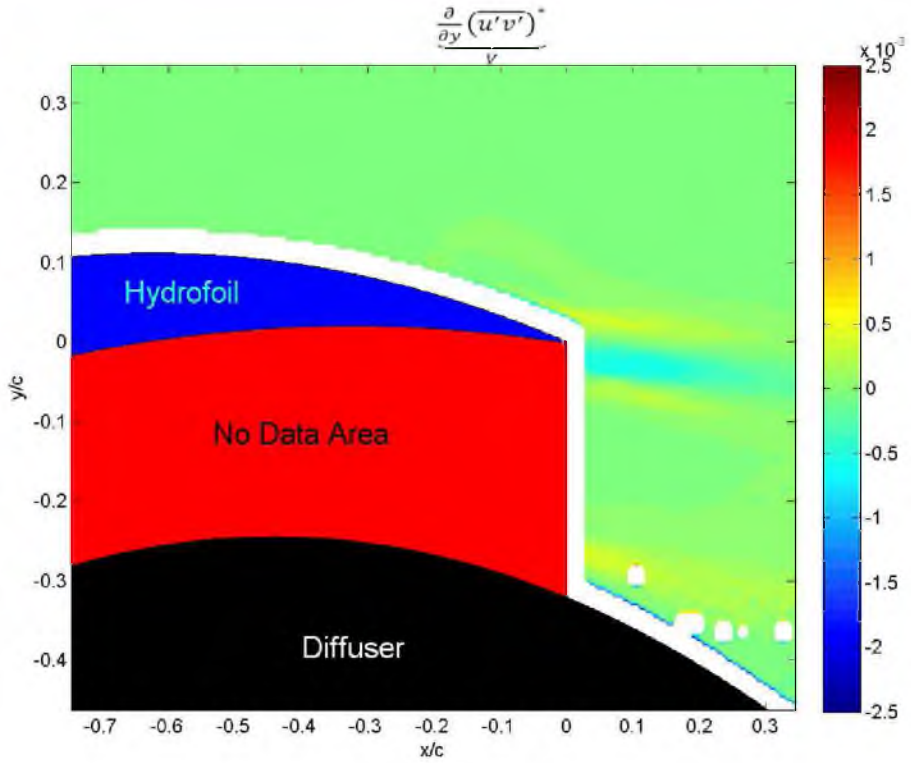

Figure A-59. 'Term V' for high roughness at 0°.

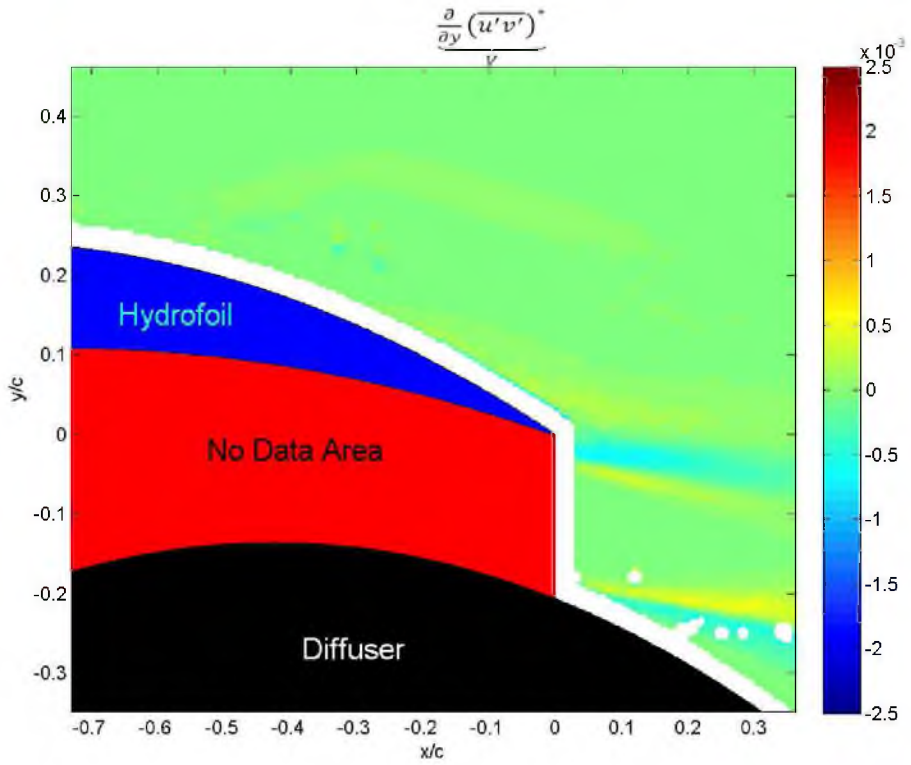

Figure A-60. 'Term V' for low roughness at 10°.

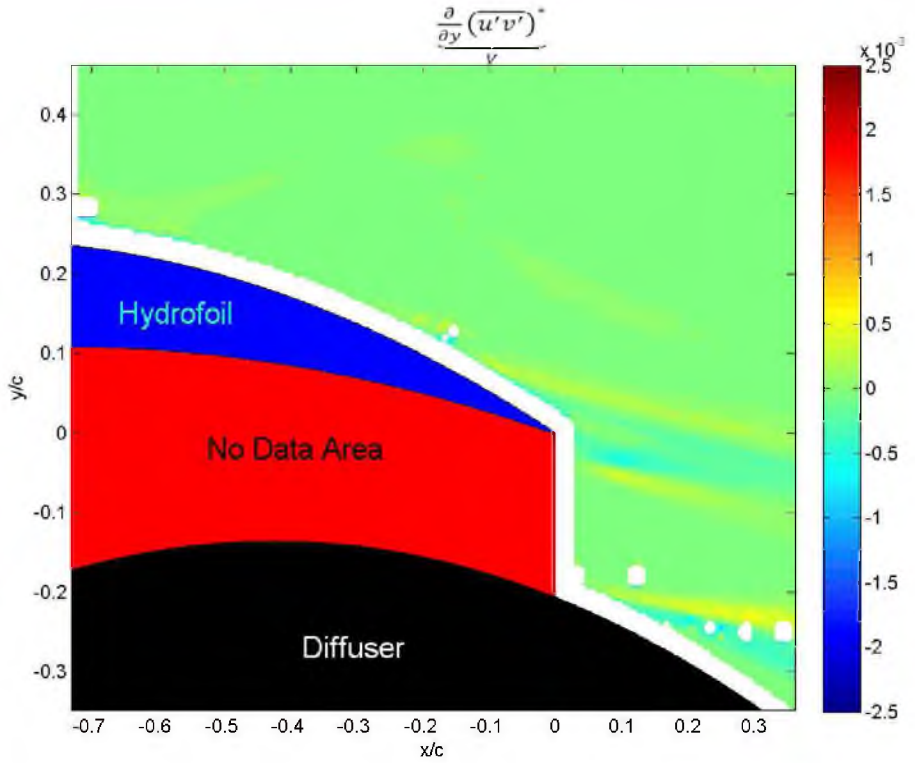

Figure A-61. 'Term V' for medium roughness at 10°.

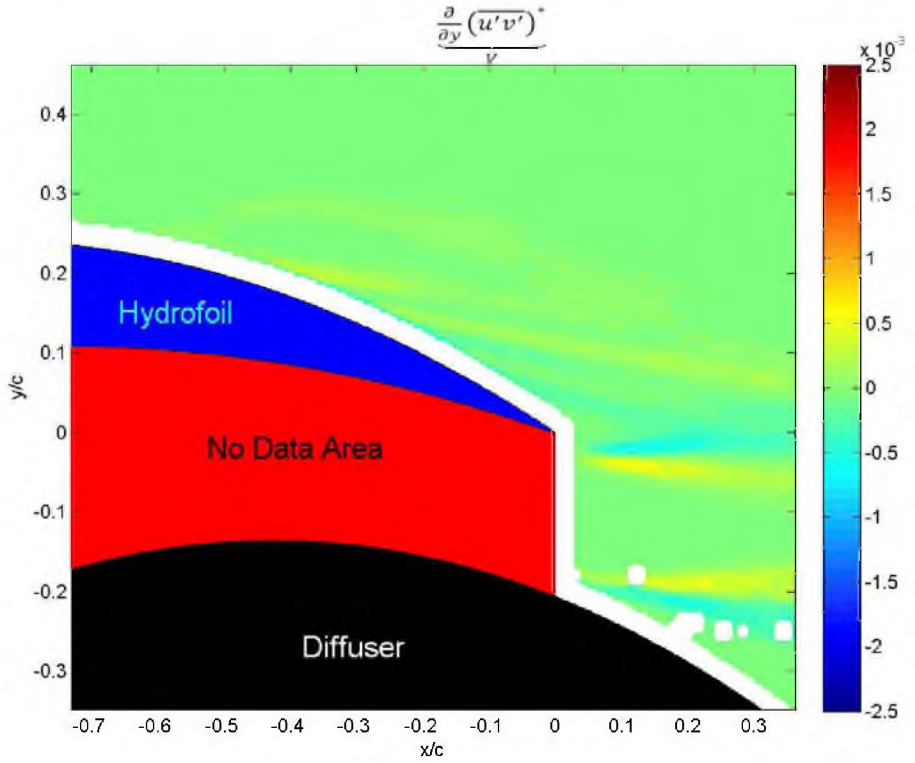

Figure A-62. 'Term V' for high roughness at 10°.

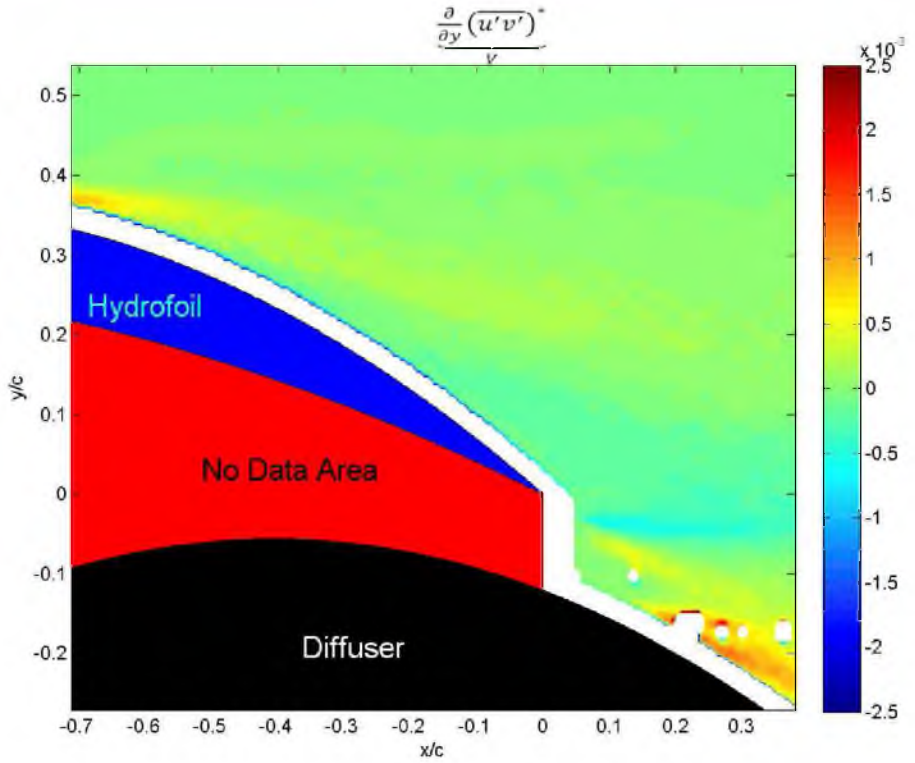

Figure A-63. 'Term V' for low roughness at 17°.

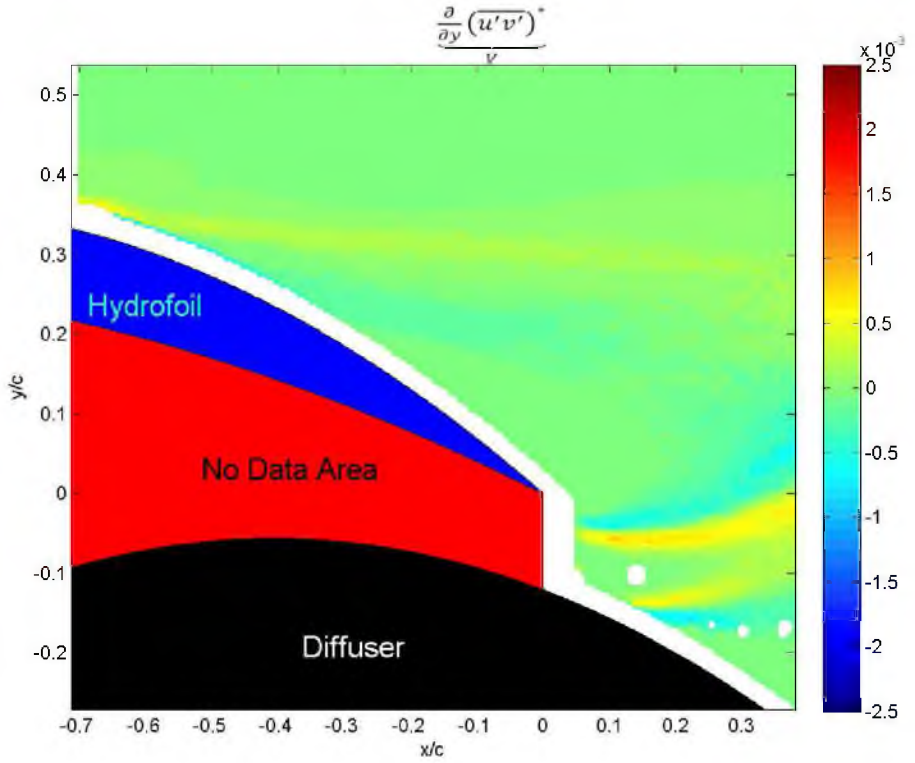

Figure A-64. 'Term V' for medium roughness at 17°.

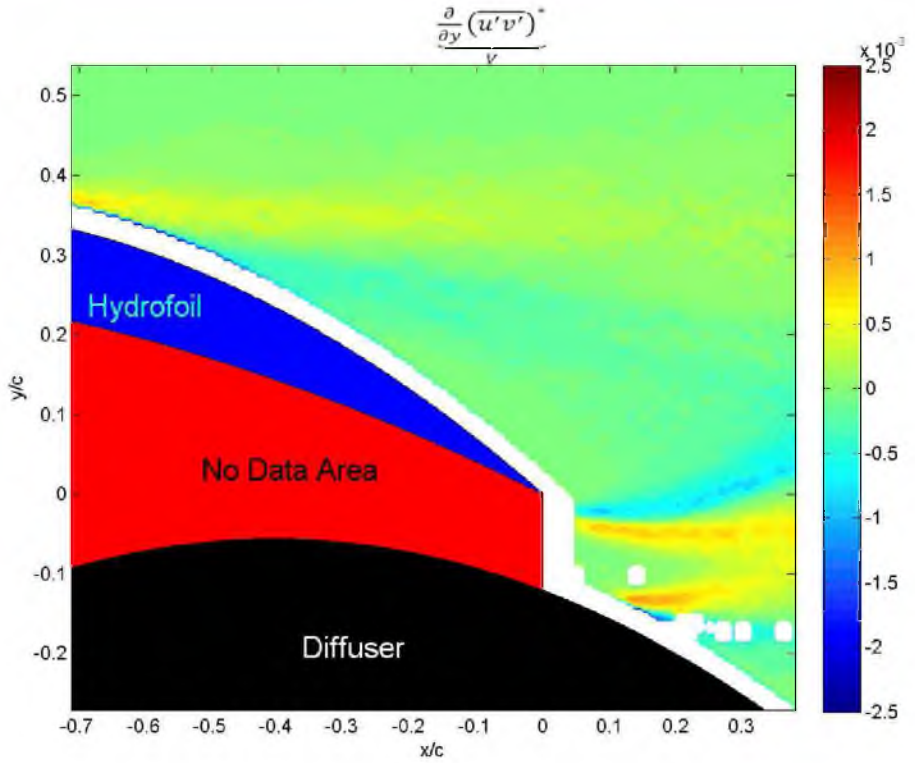

Figure A-65. 'Term V' for high roughness at 17°.

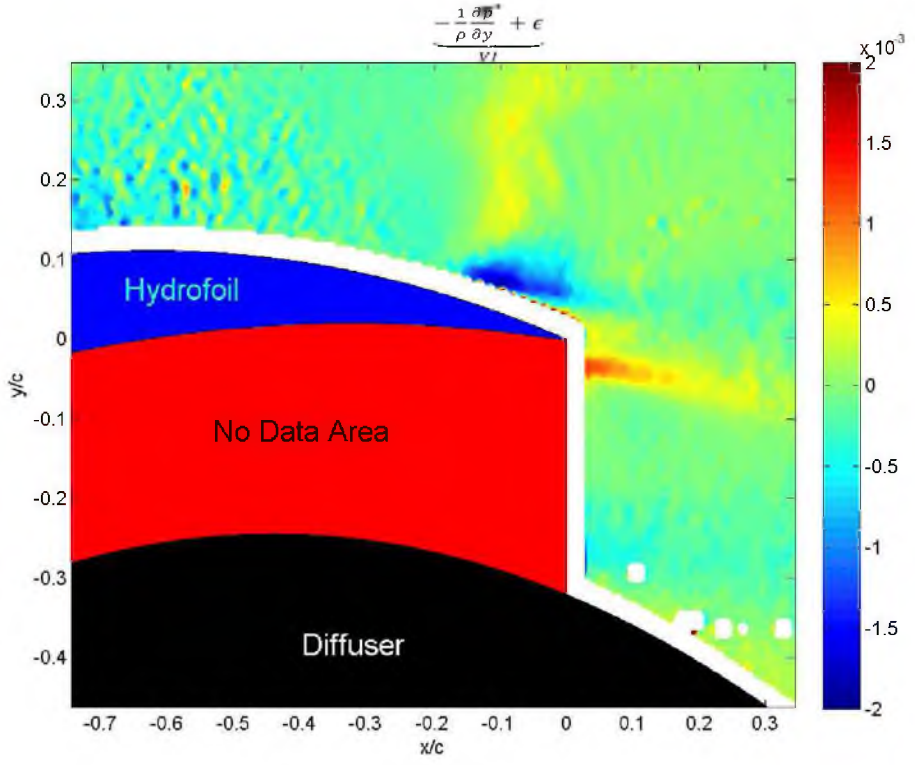

Figure A-66. 'Term VI' for low roughness at 0°.

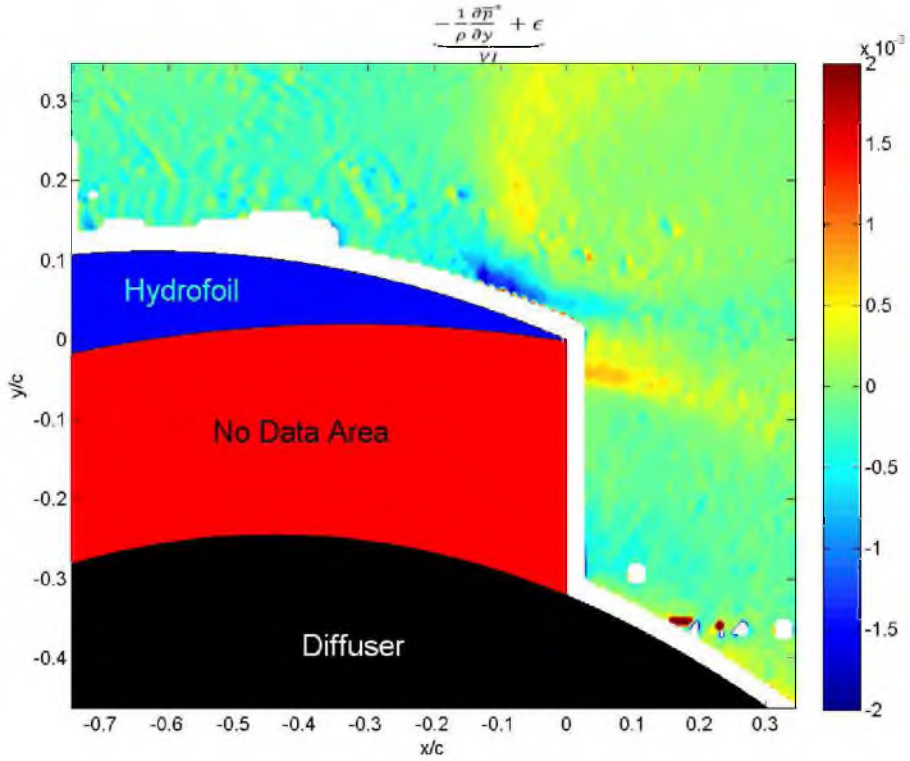

Figure A-67. 'Term VI' for medium roughness at 0°.

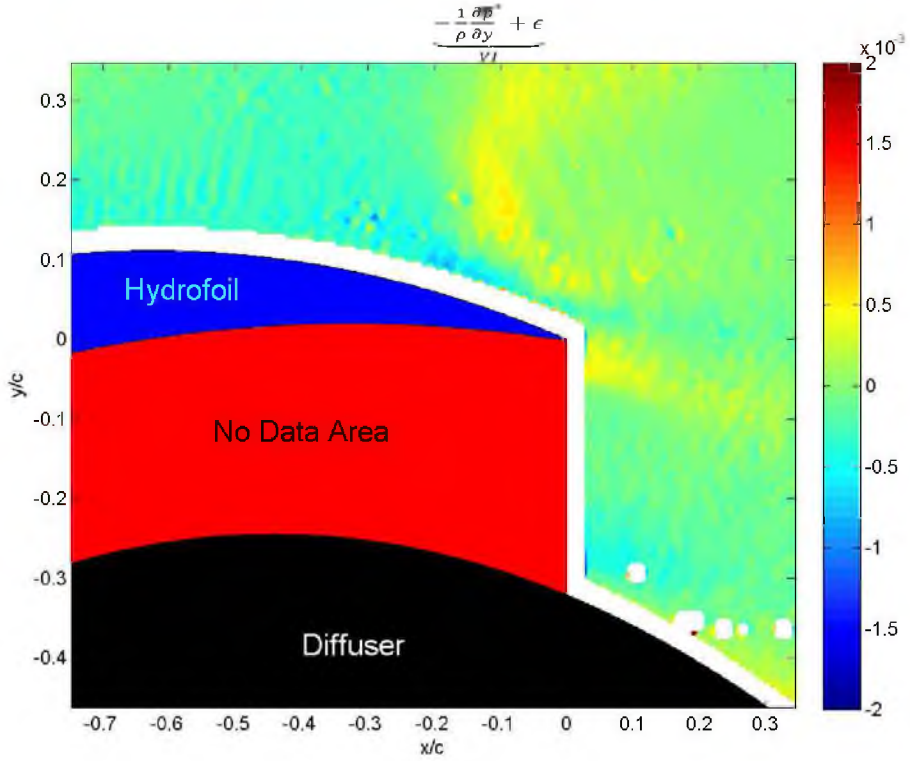

Figure A-68. 'Term VI' for high roughness at 0°.

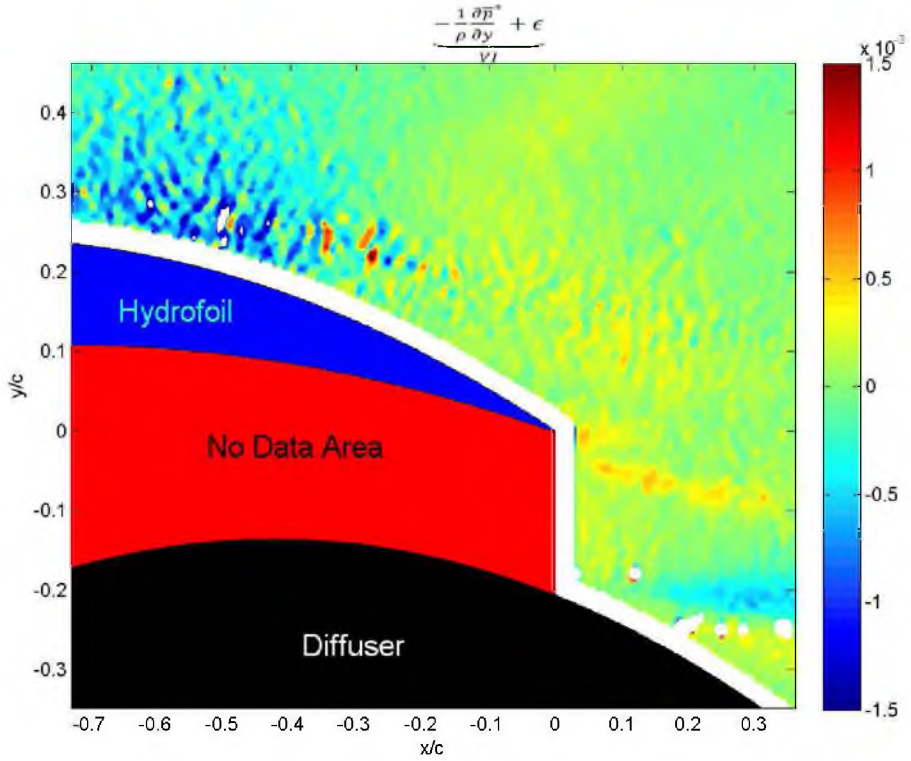

Figure A-69. 'Term VI' for low roughness at 10°.

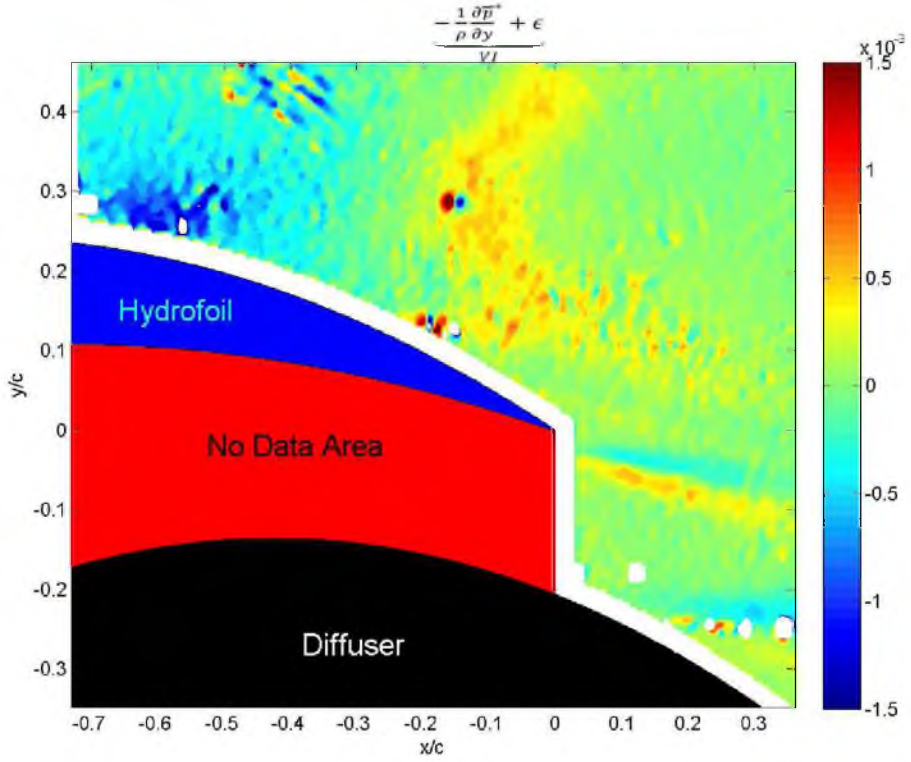

Figure A-70. 'Term VI' for medium roughness at 10°.

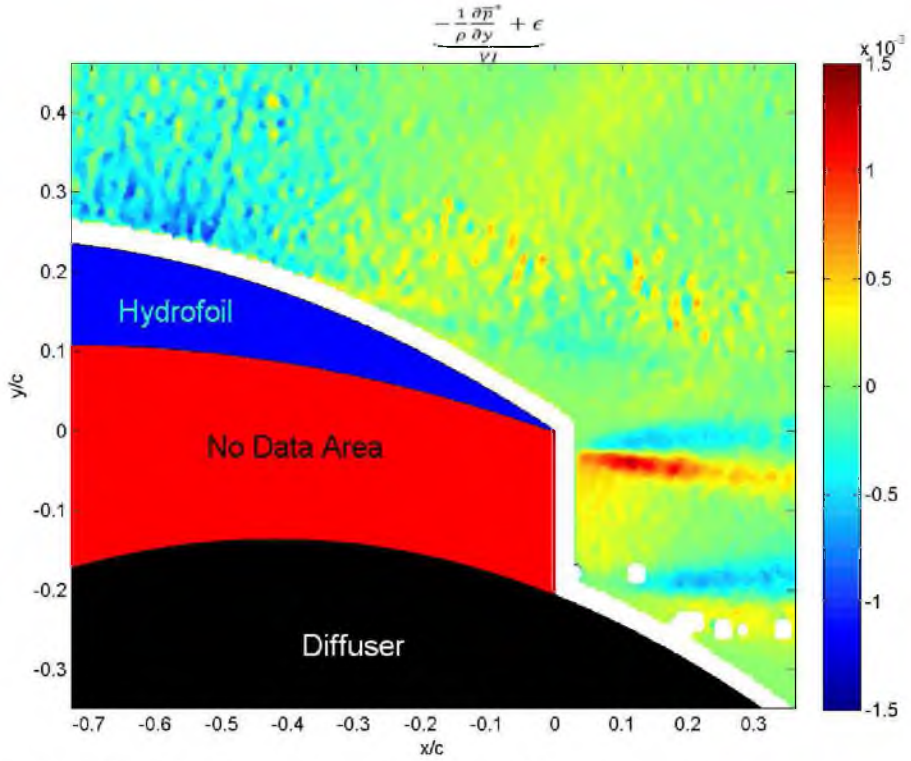

Figure A-71. 'Term VI' for high roughness at 10°.

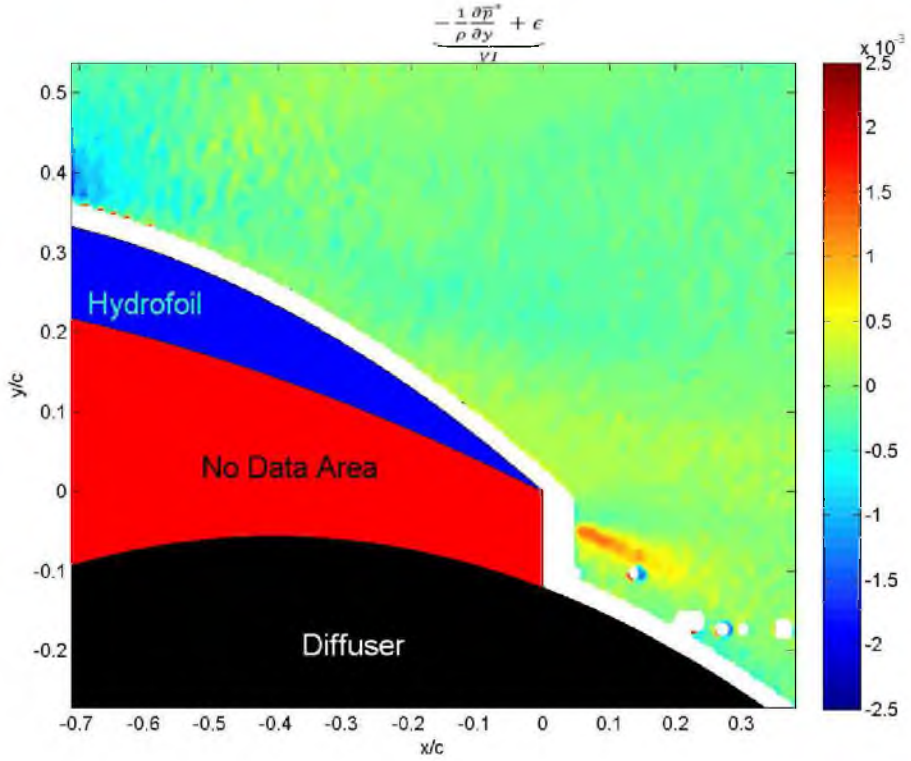

Figure A-72. 'Term VI' for low roughness at 17°.

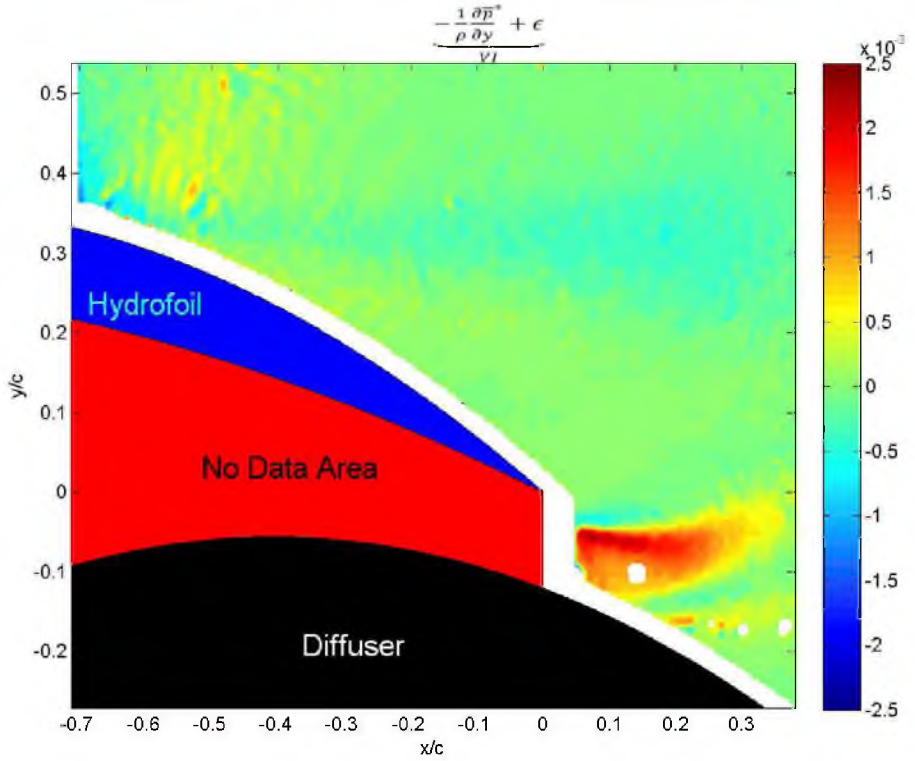

Figure A-73. 'Term VI' for medium roughness at 17°.

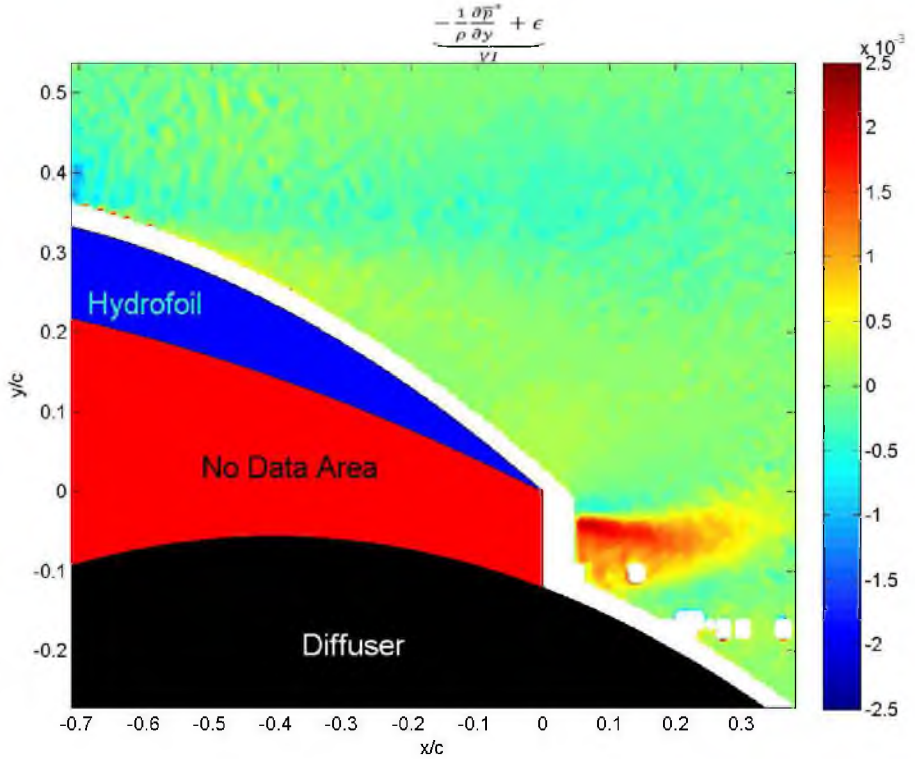

Figure A-74. 'Term VI' for high roughness at 17°.

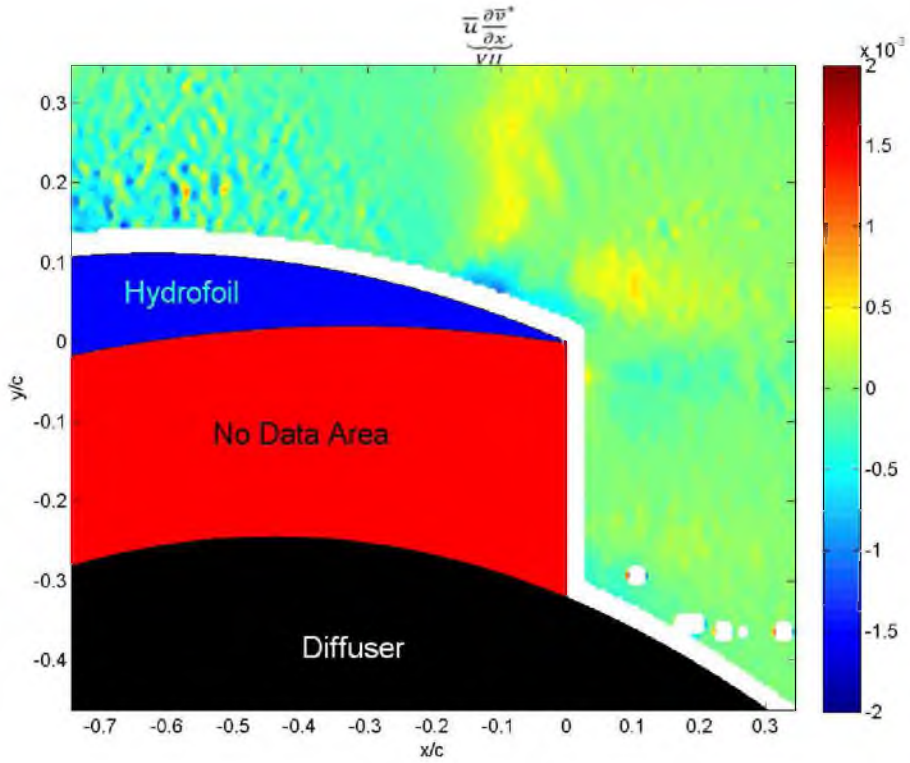

Figure A-75. 'Term VII' for low roughness at 0°.

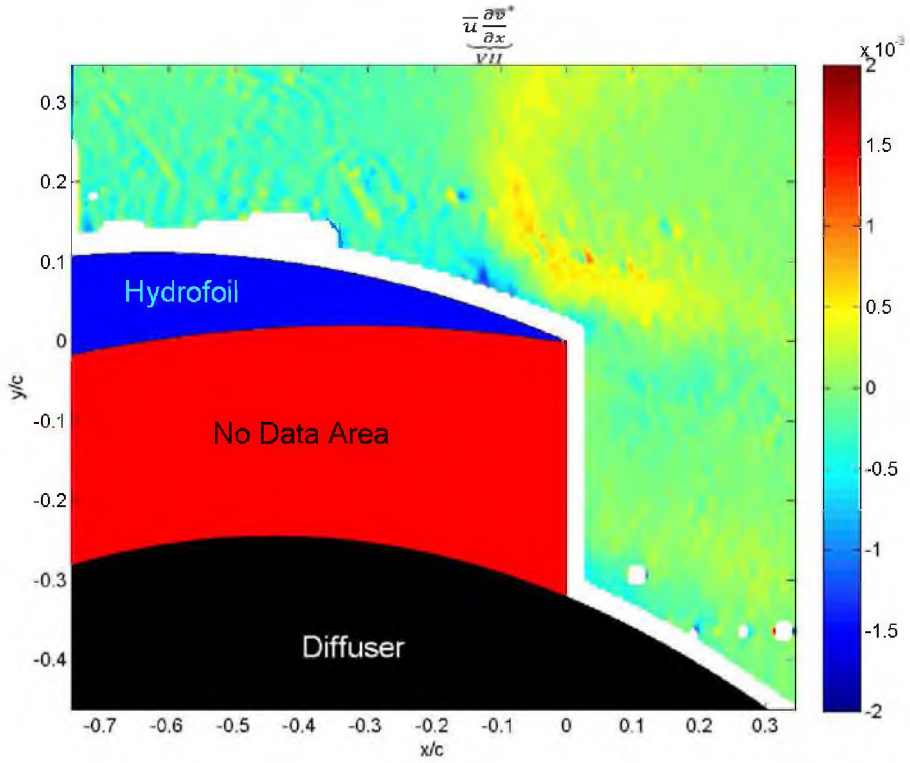

Figure A-76. 'Term VII' for medium roughness at 0°.

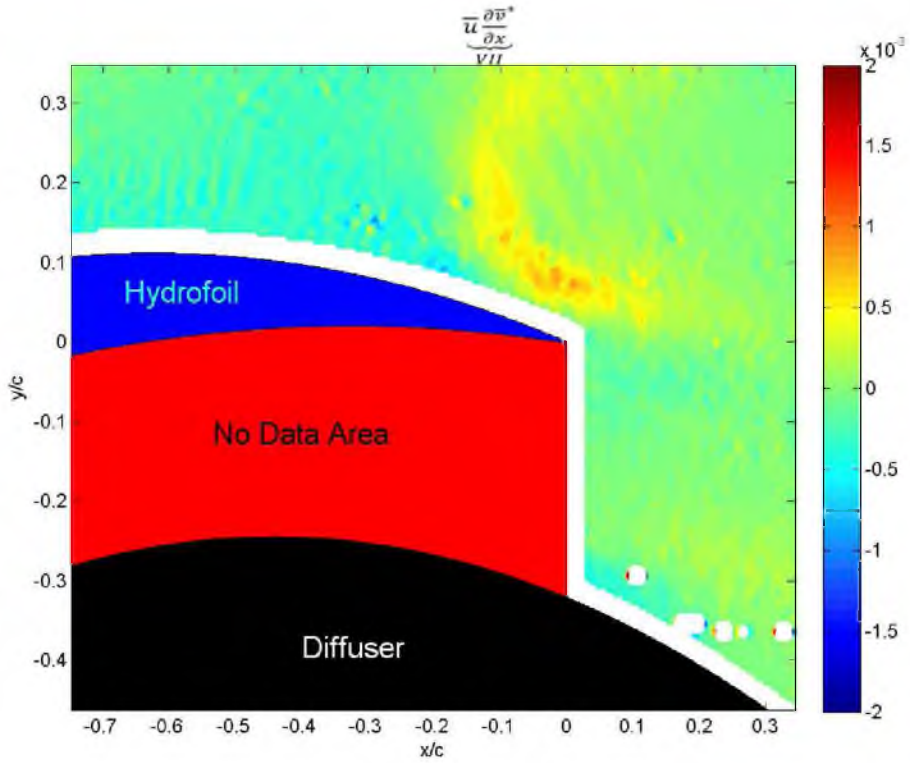

Figure A-77. 'Term VII' for high roughness at 0°.

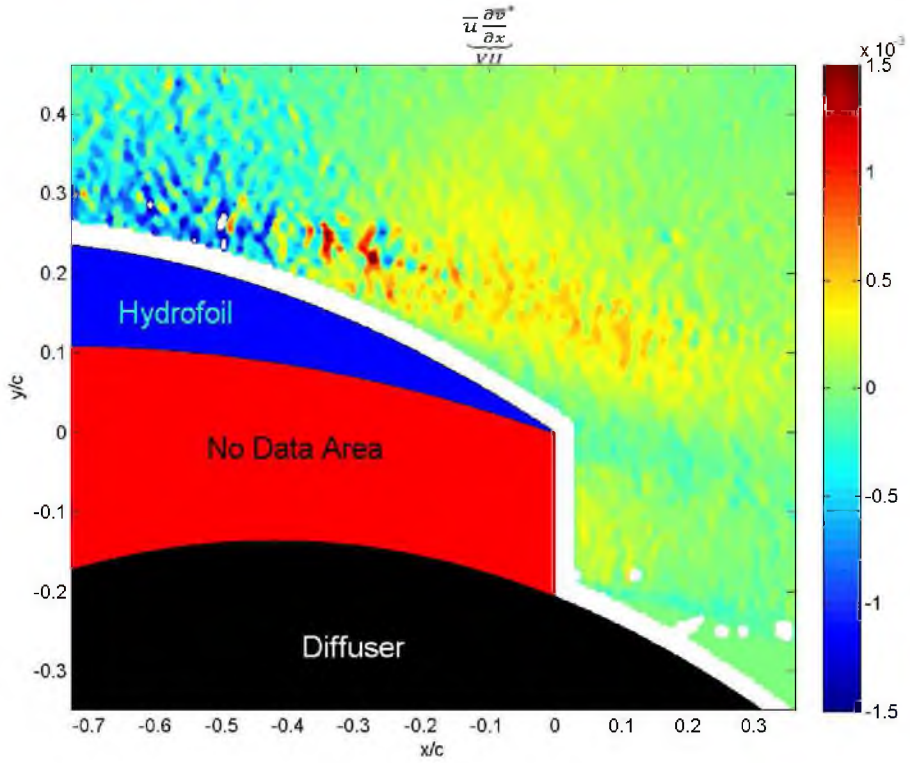

Figure A-78. 'Term VII' for low roughness at 10°.

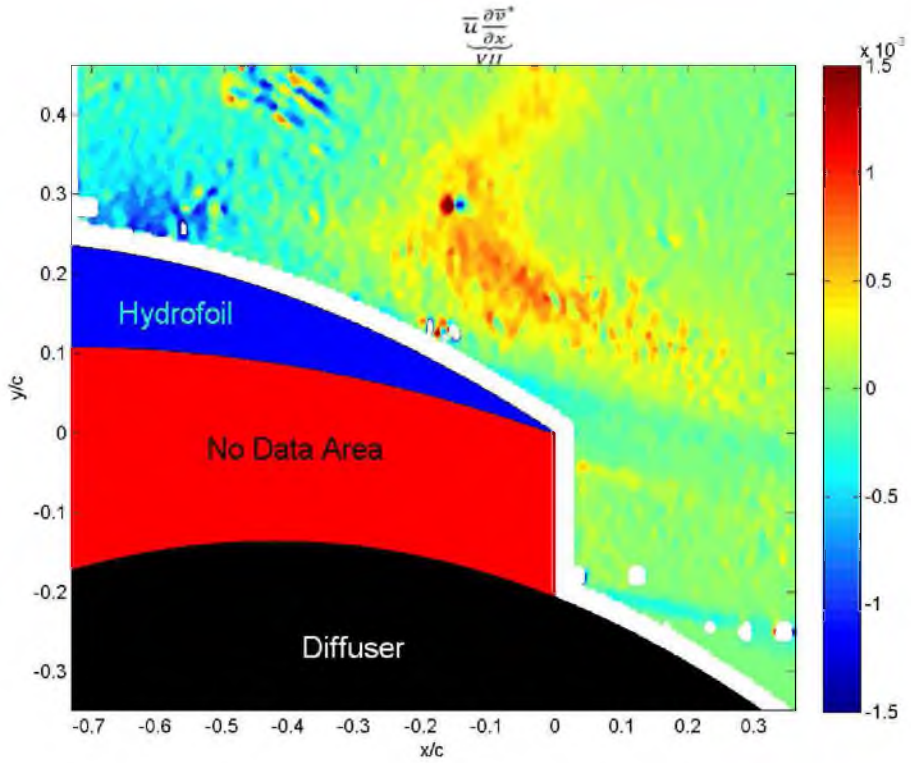

Figure A-79. 'Term VII' for medium roughness at 10°.

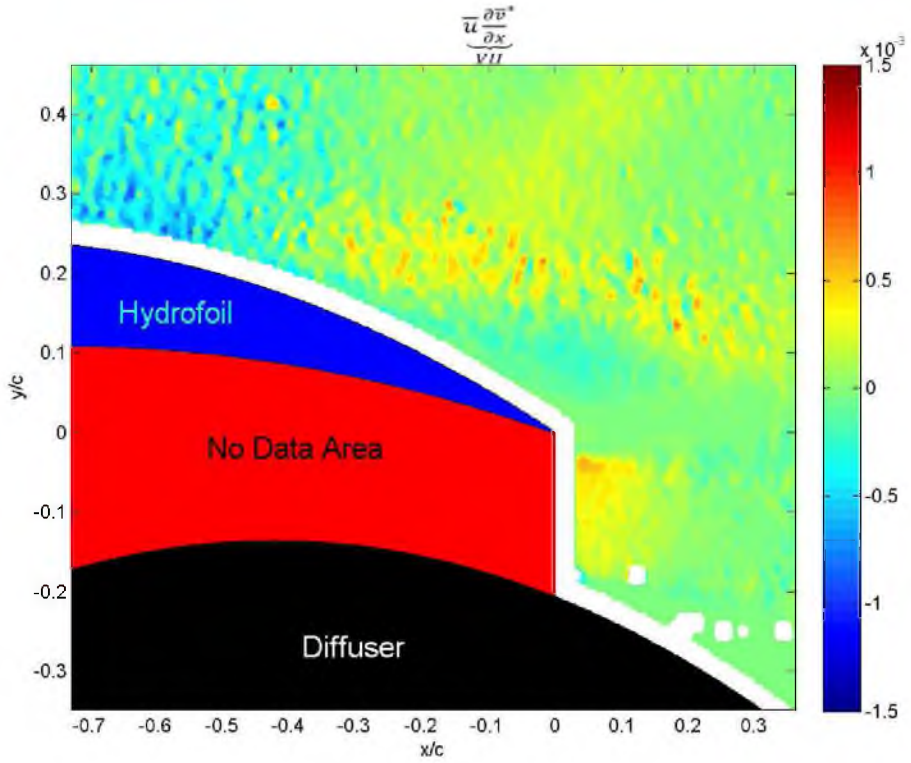

Figure A-80. 'Term VII' for high roughness at 10°.

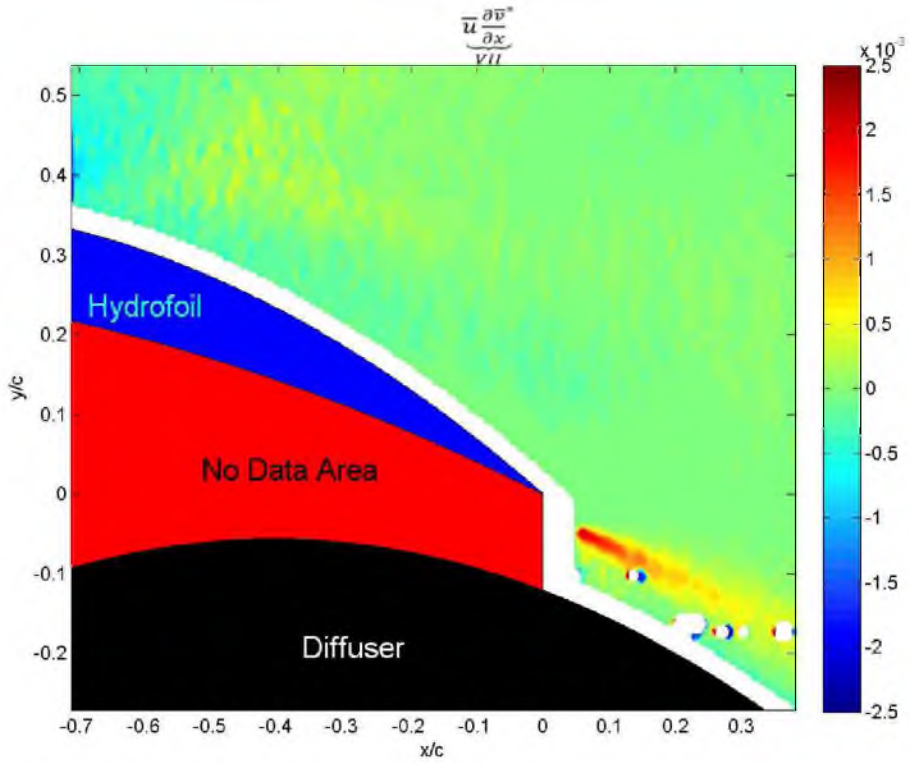

Figure A-81. 'Term VII' for low roughness at 17°.

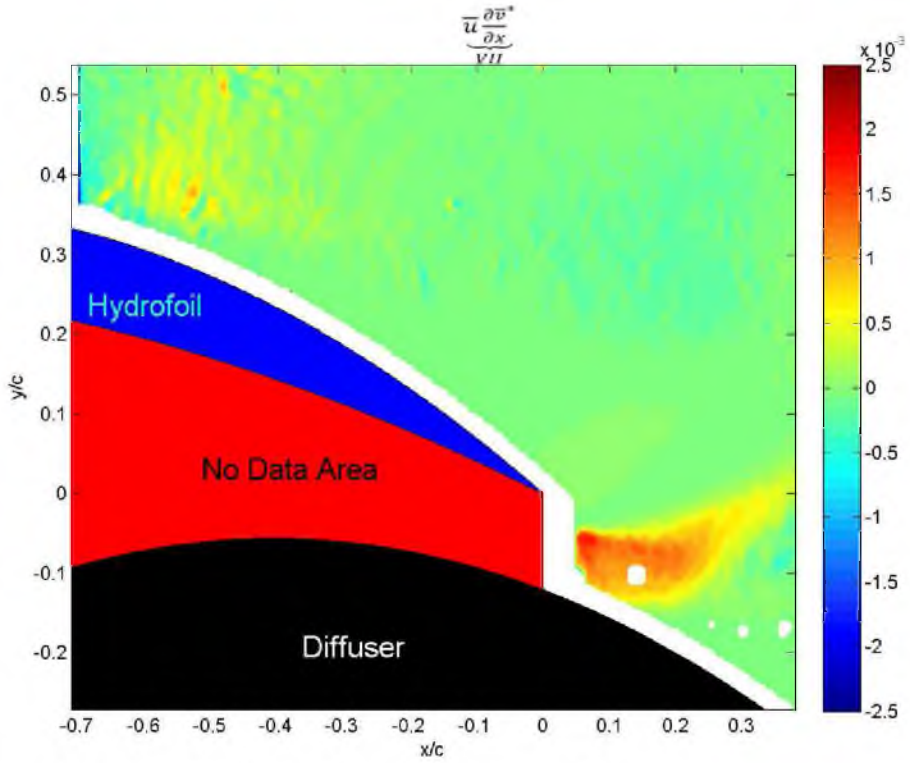

Figure A-82. 'Term VII' for medium roughness at 17°.

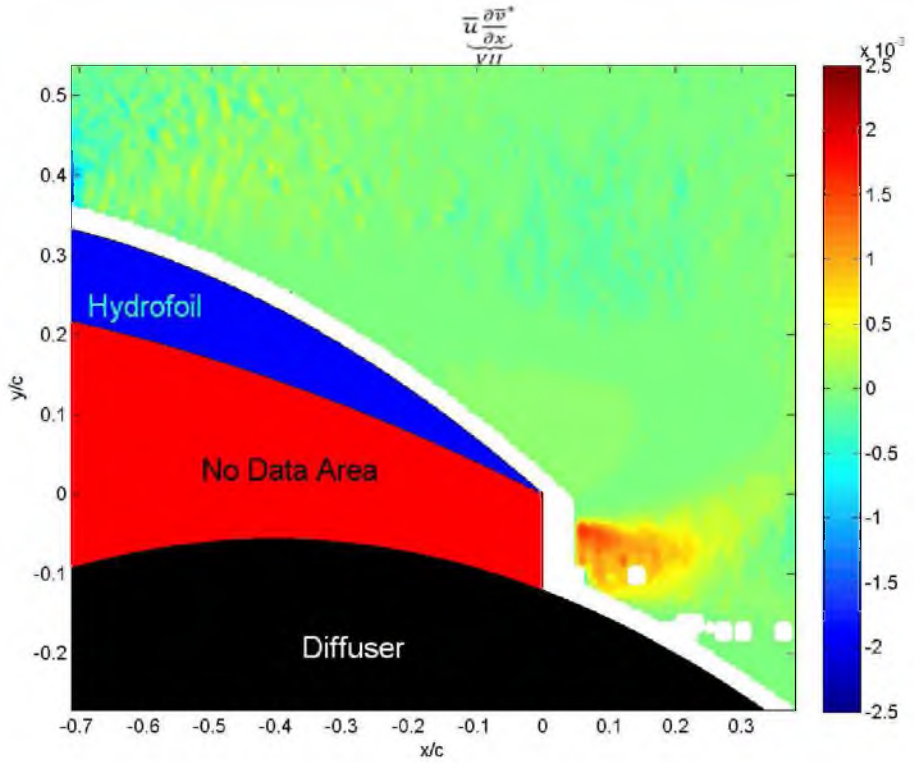

Figure A-83. 'Term VII' for high roughness at 17°.

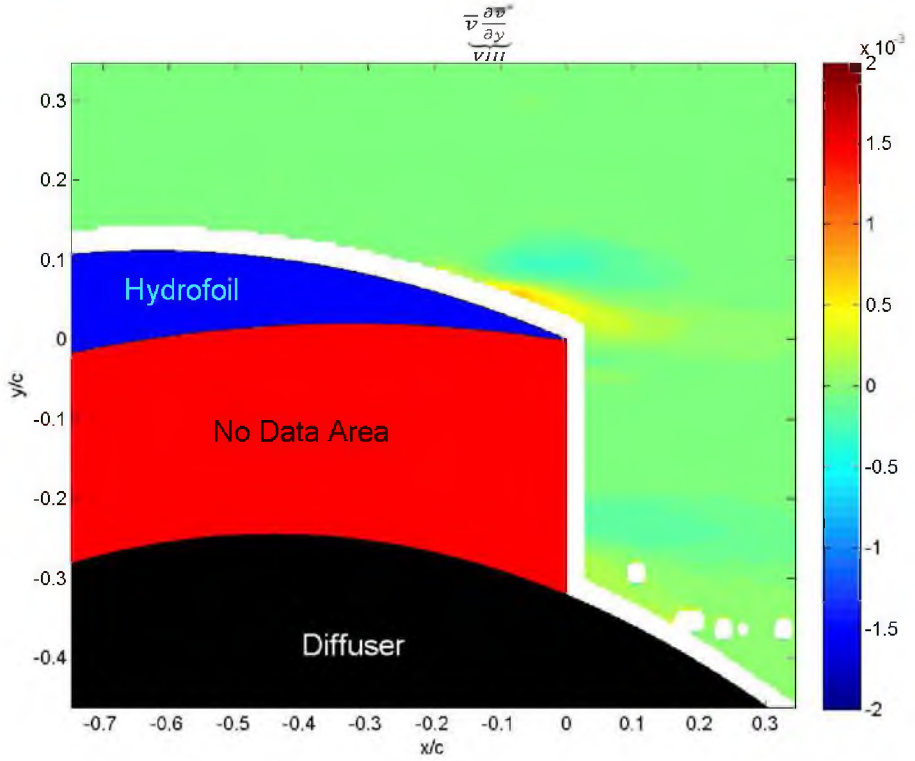

Figure A-84. 'Term VIII' for low roughness at 0°.

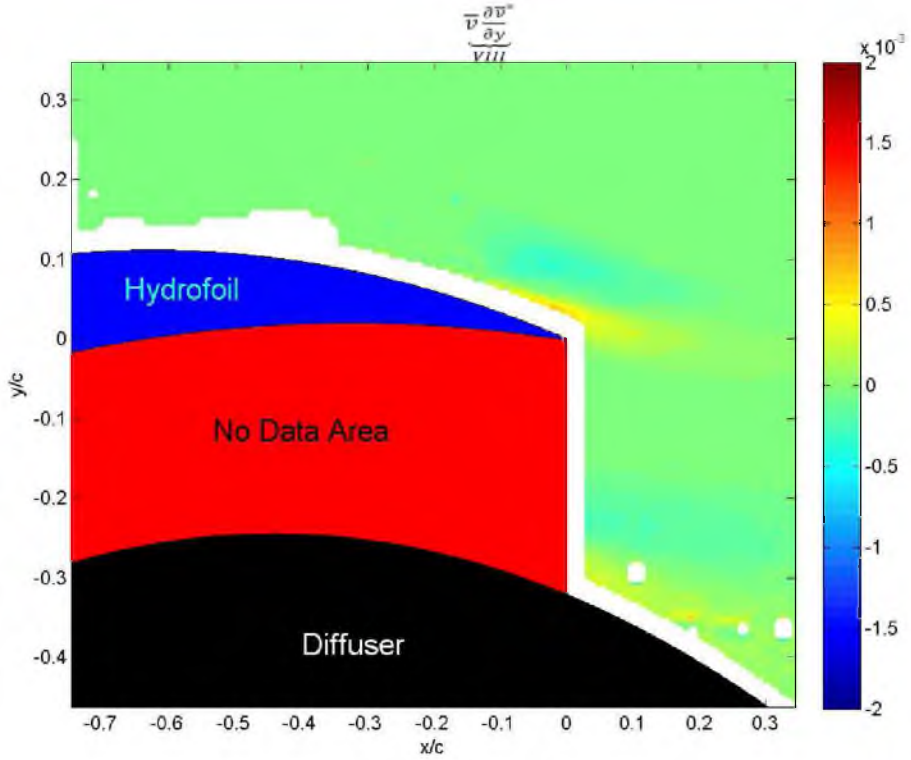

Figure A-85. 'Term VIII' for medium roughness at 0°.

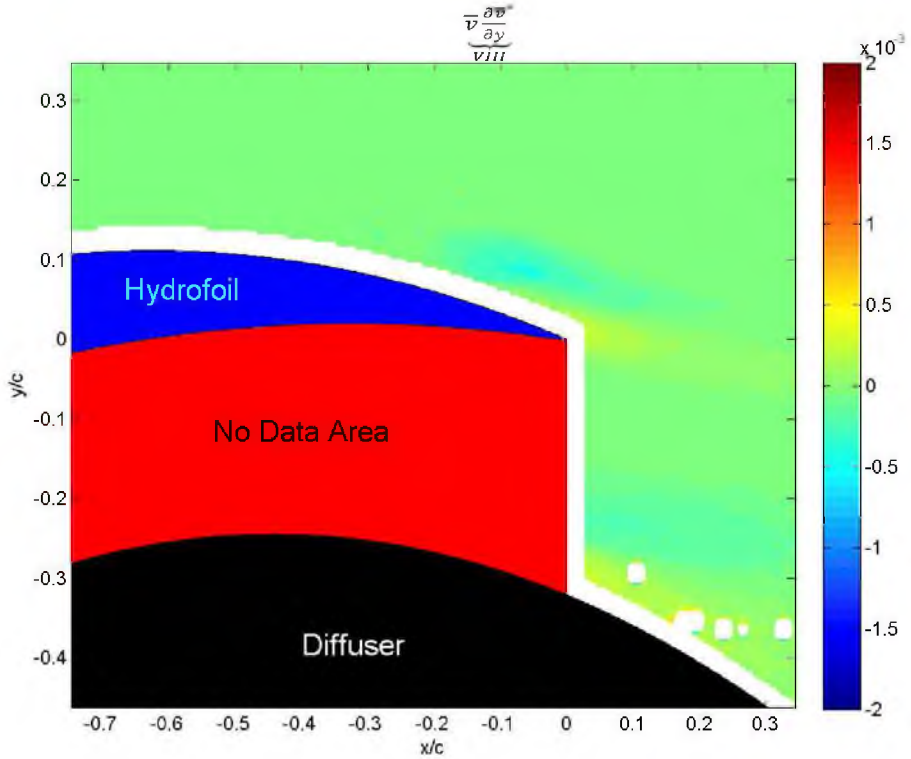

Figure A-86. 'Term VIII' for high roughness at 0°.

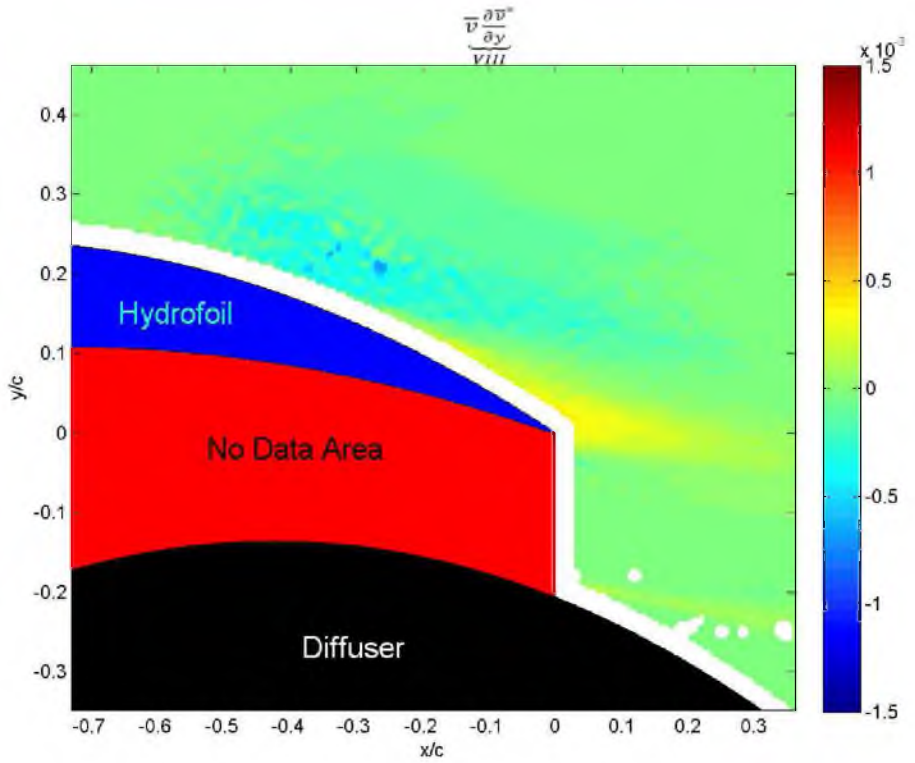

Figure A-87. 'Term VIII' for low roughness at 10°.

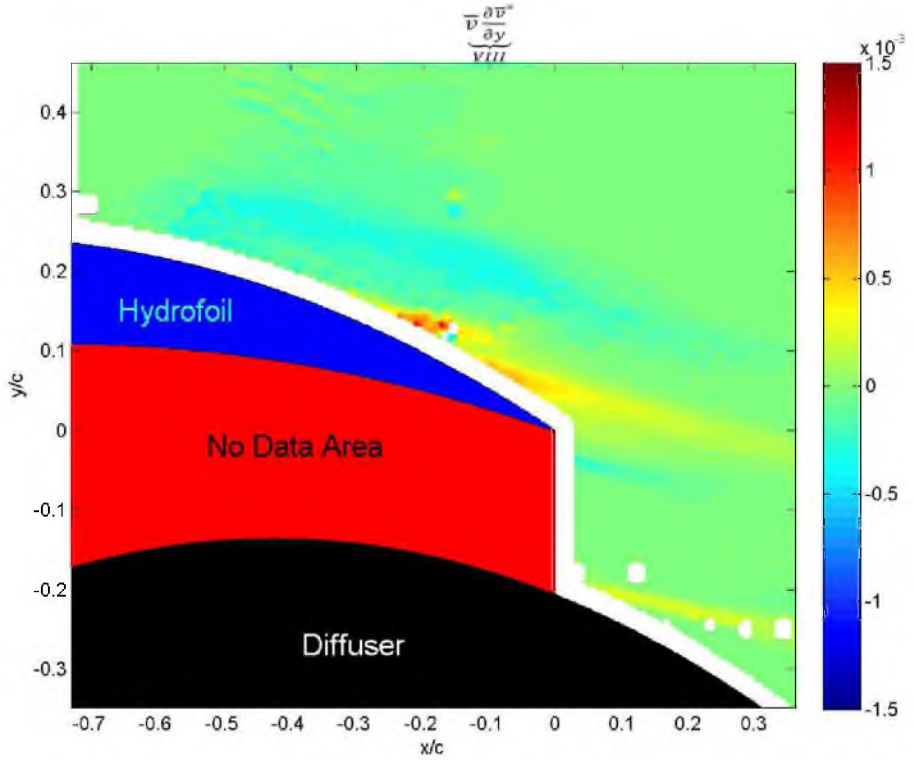

Figure A-88. 'Term VIII' for medium roughness at 10°.

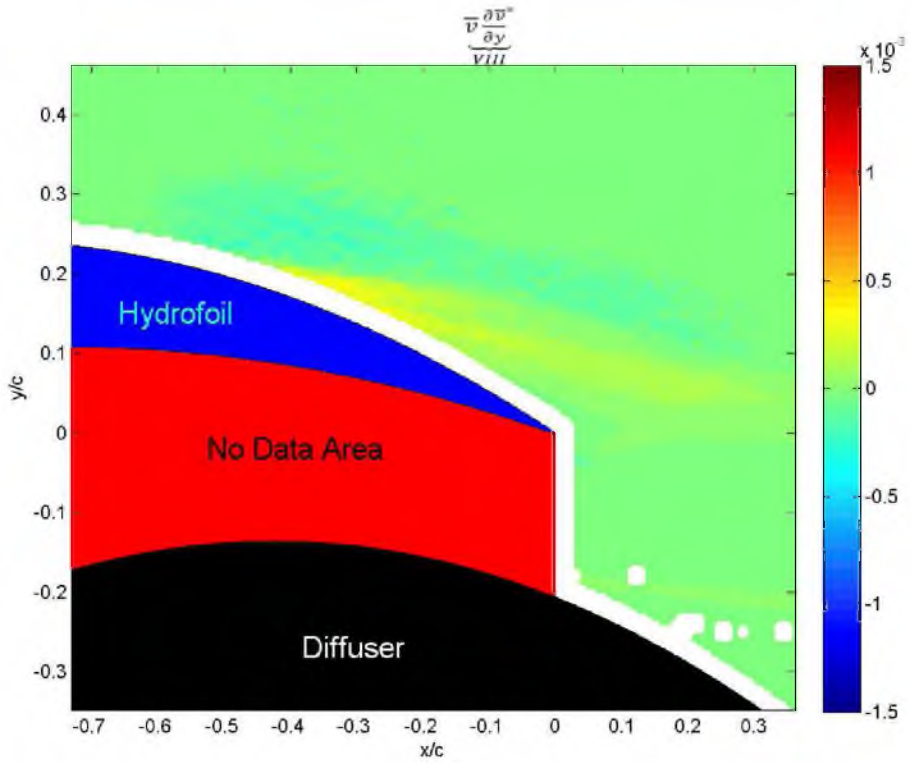

Figure A-89. 'Term VIII' for high roughness at 10°.

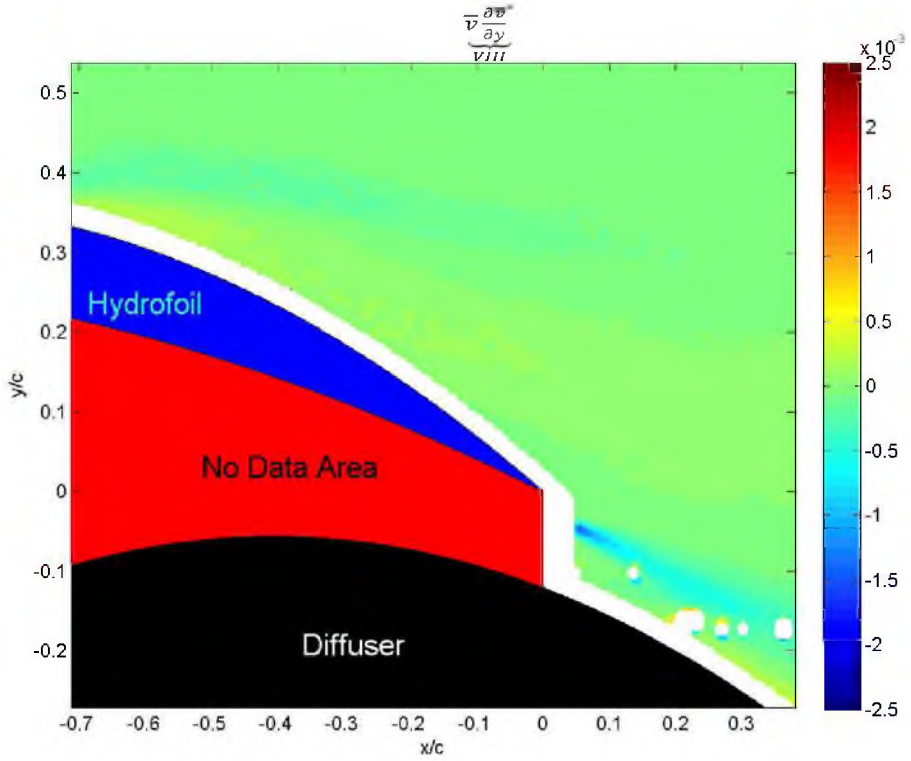

Figure A-90. 'Term VIII' for low roughness at 17°.

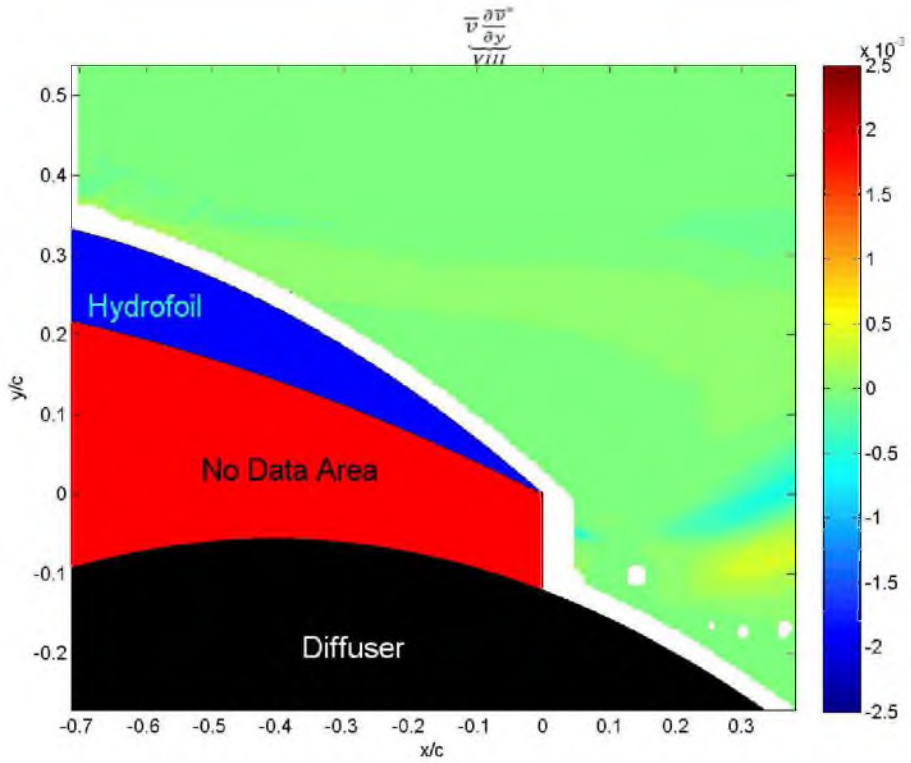

Figure A-91. 'Term VIII' for medium roughness at 17°.

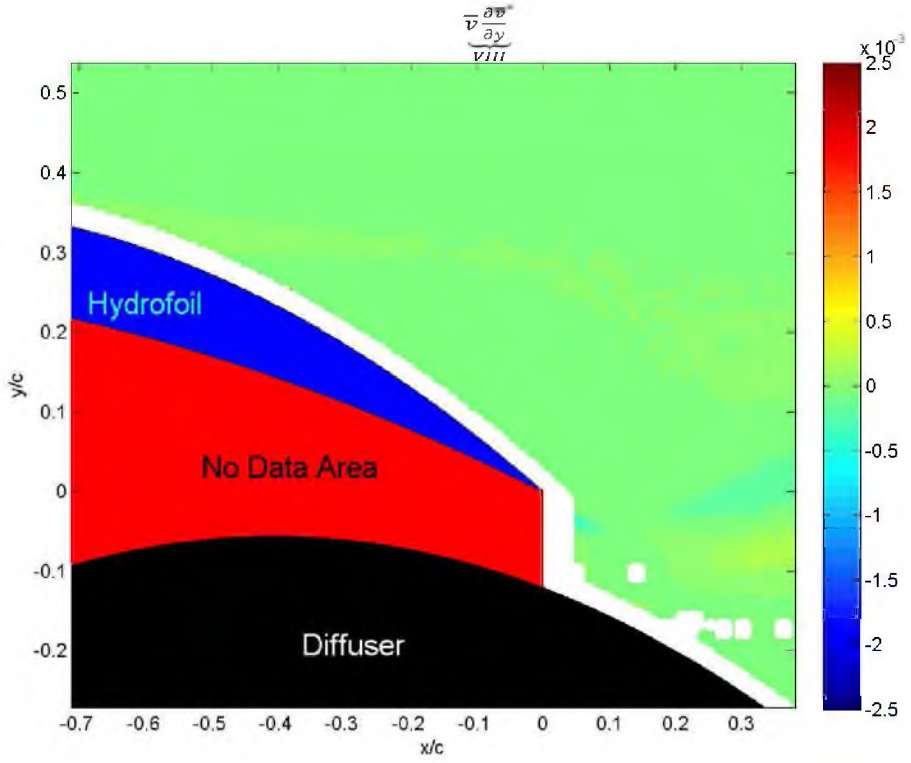

Figure A-92. 'Term VIII' for high roughness at 17°.

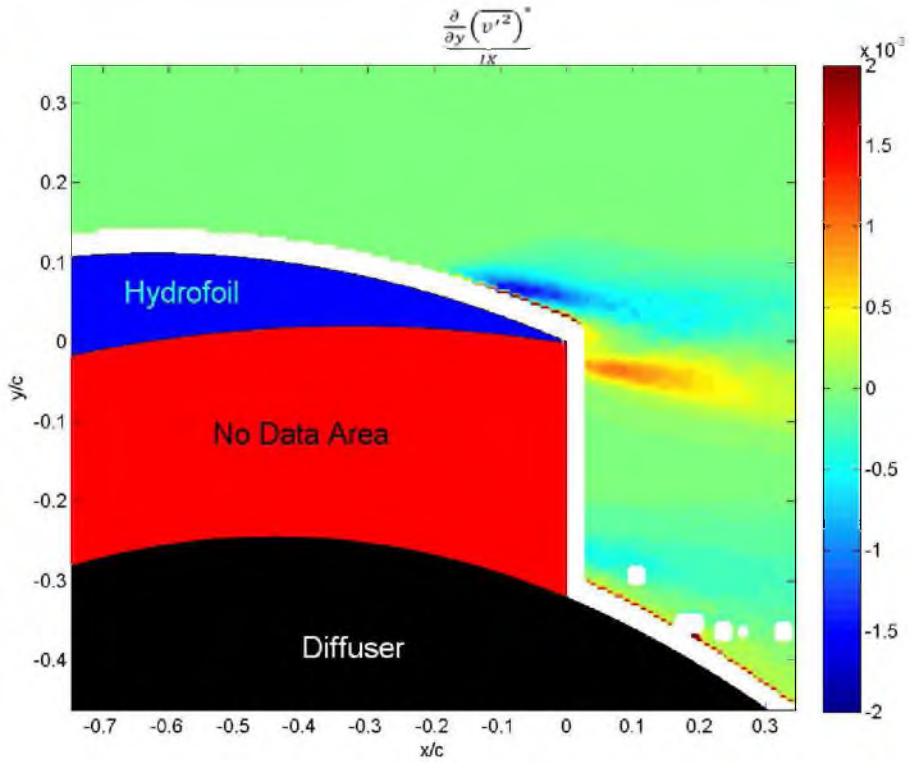

Figure A-93. 'Term IX' for low roughness at 0°.

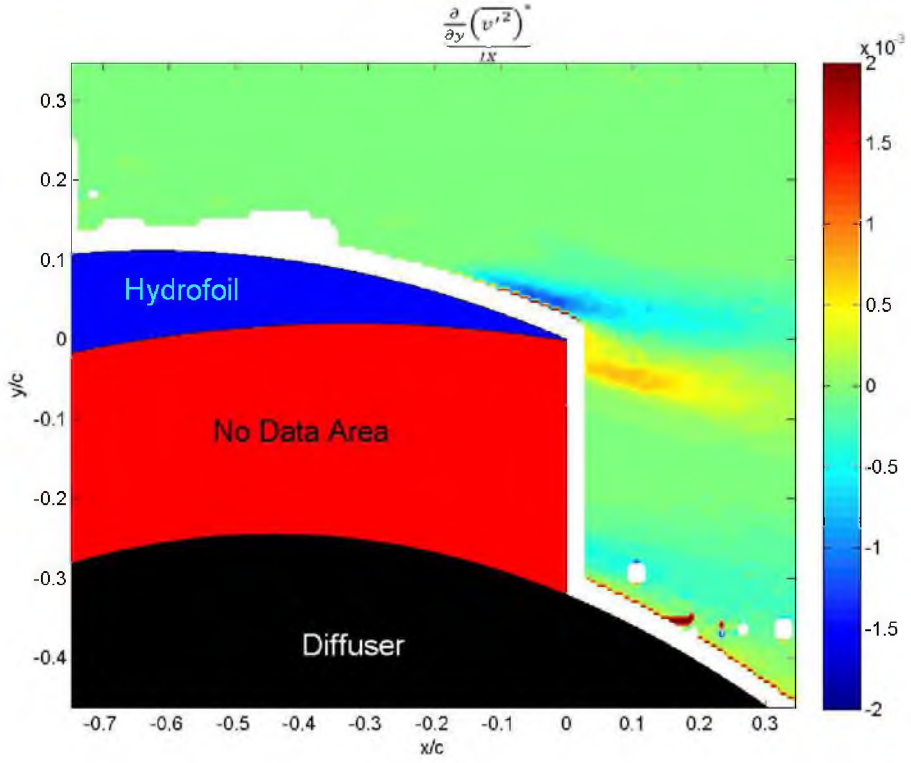

Figure A-94. 'Term IX' for medium roughness at 0°.

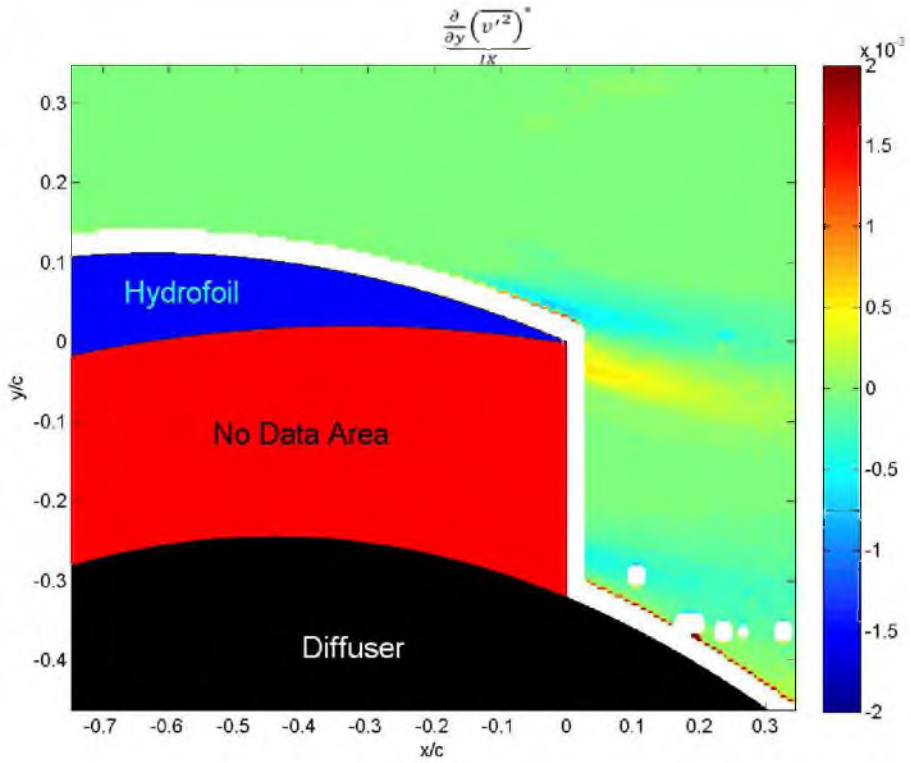

Figure A-95. 'Term IX' for high roughness at 0°.

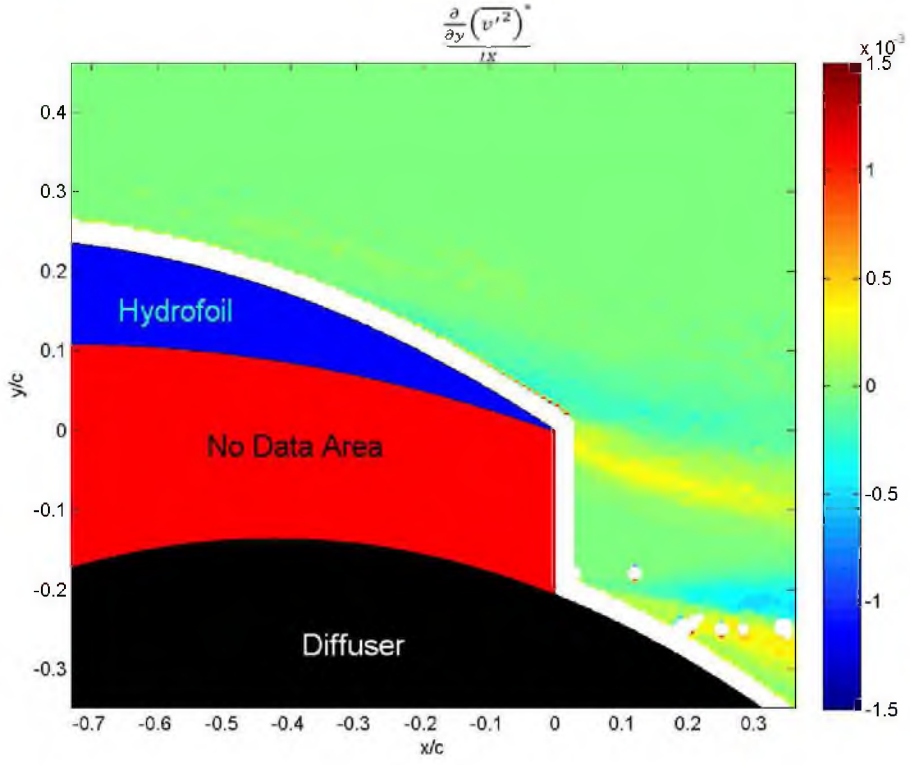

Figure A-96. 'Term IX' for low roughness at 10°.

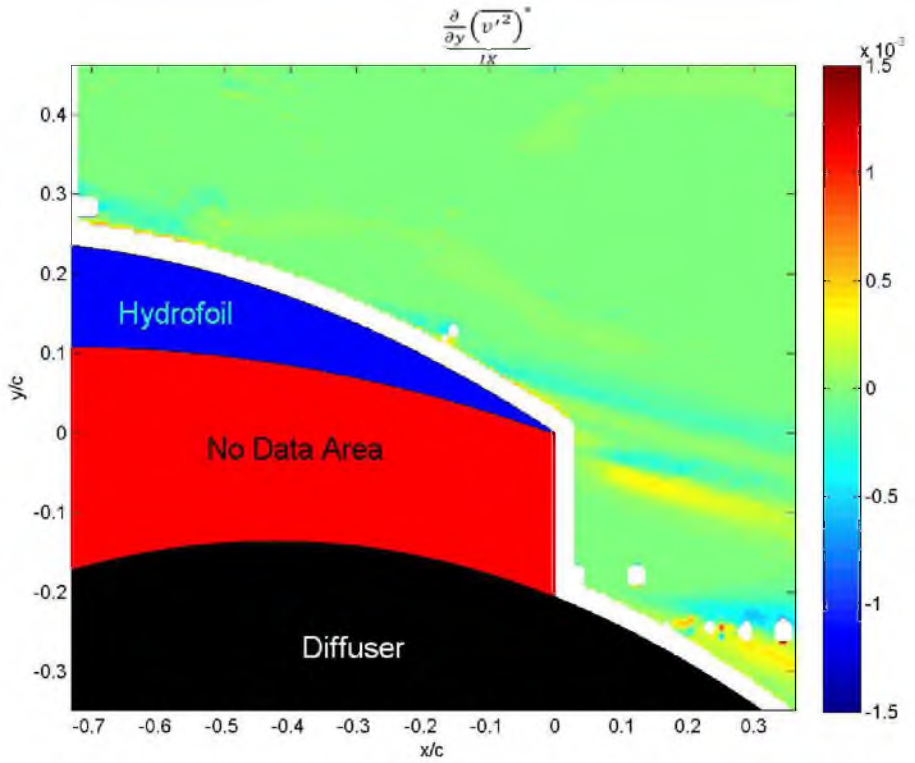

Figure A-97. 'Term IX' for medium roughness at 10°.

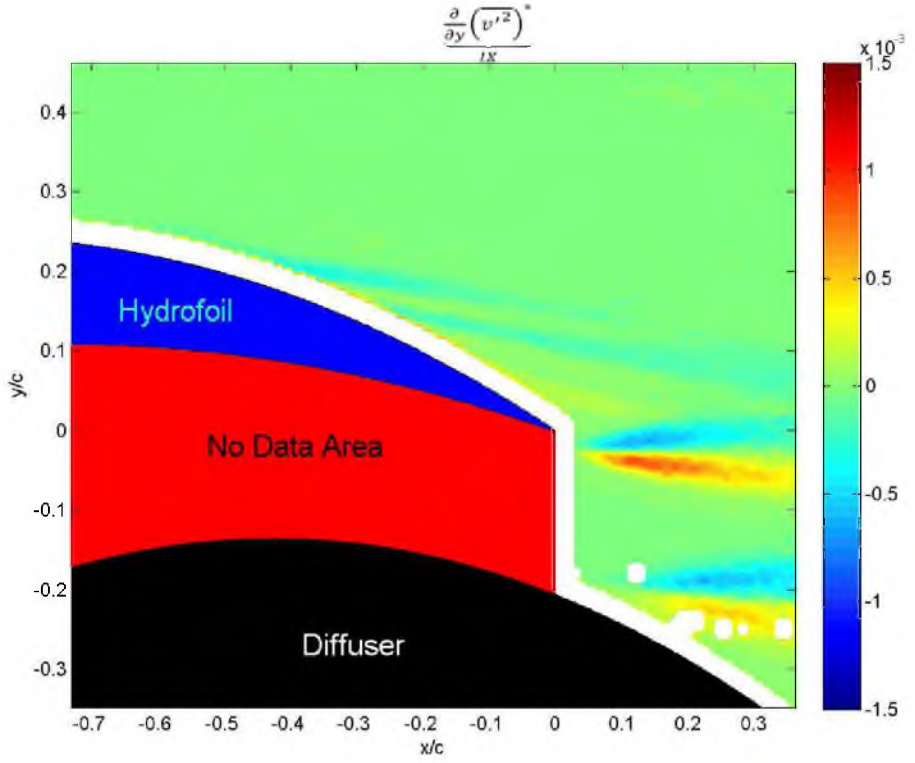

Figure A-98. 'Term IX' for high roughness at 10°.

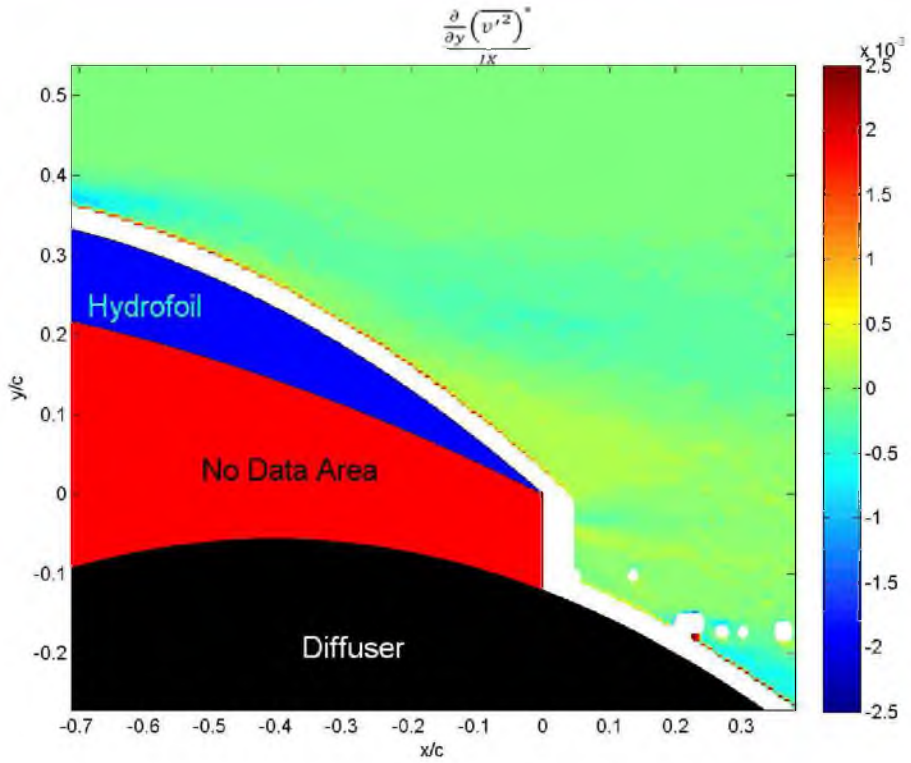

Figure A-99. 'Term IX' for low roughness at 17°.

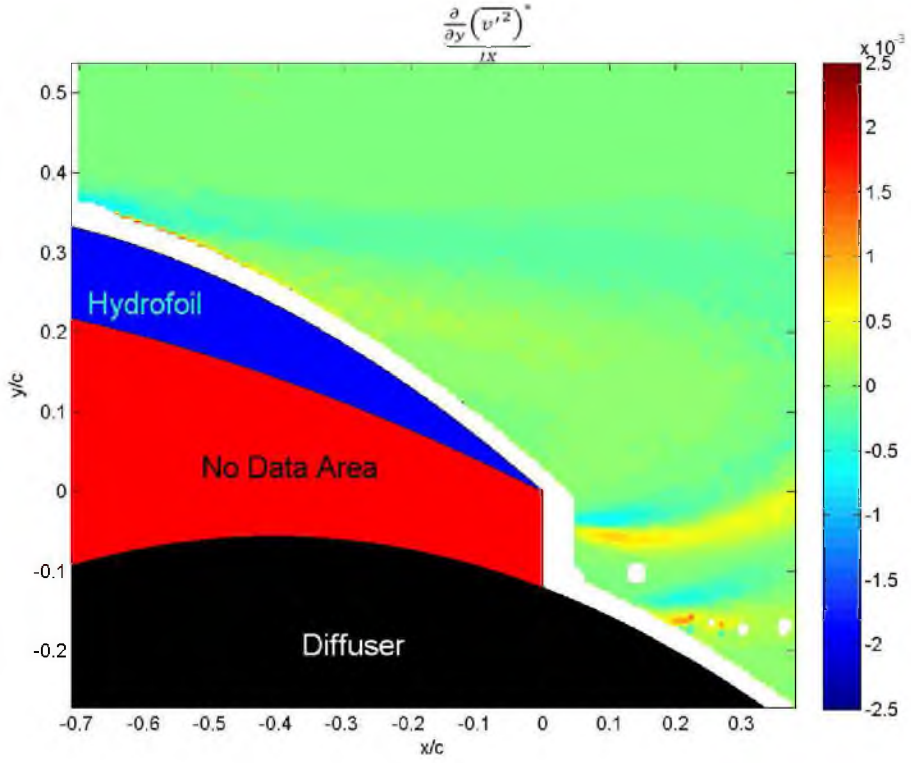

Figure A-100. 'Term IX' for medium roughness at 17°.

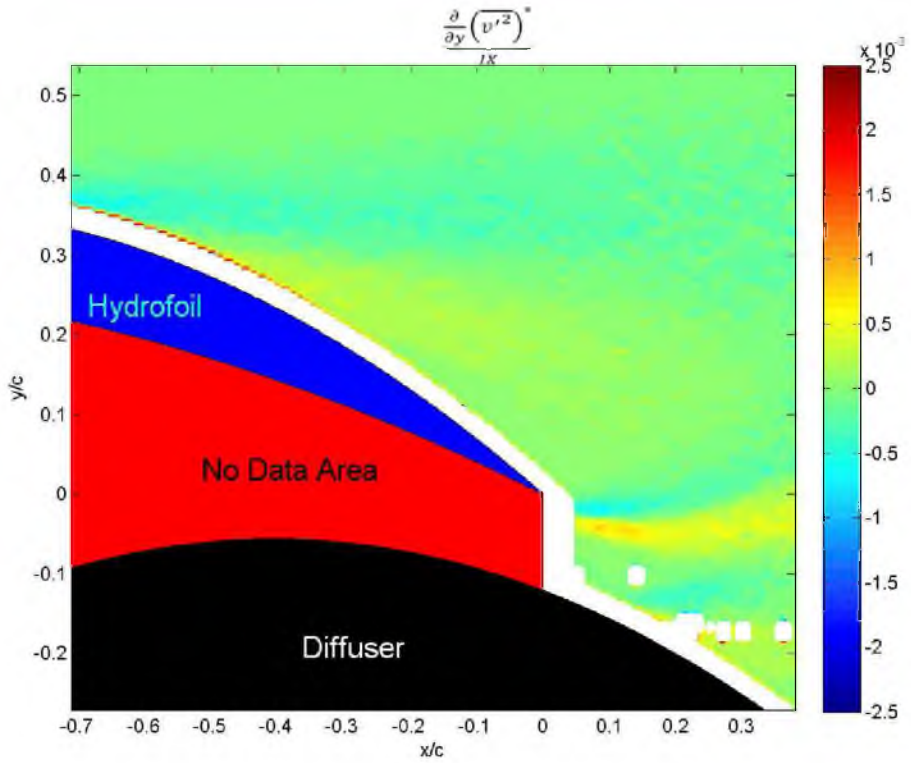

Figure A-101. 'Term IX' for high roughness at 17°.

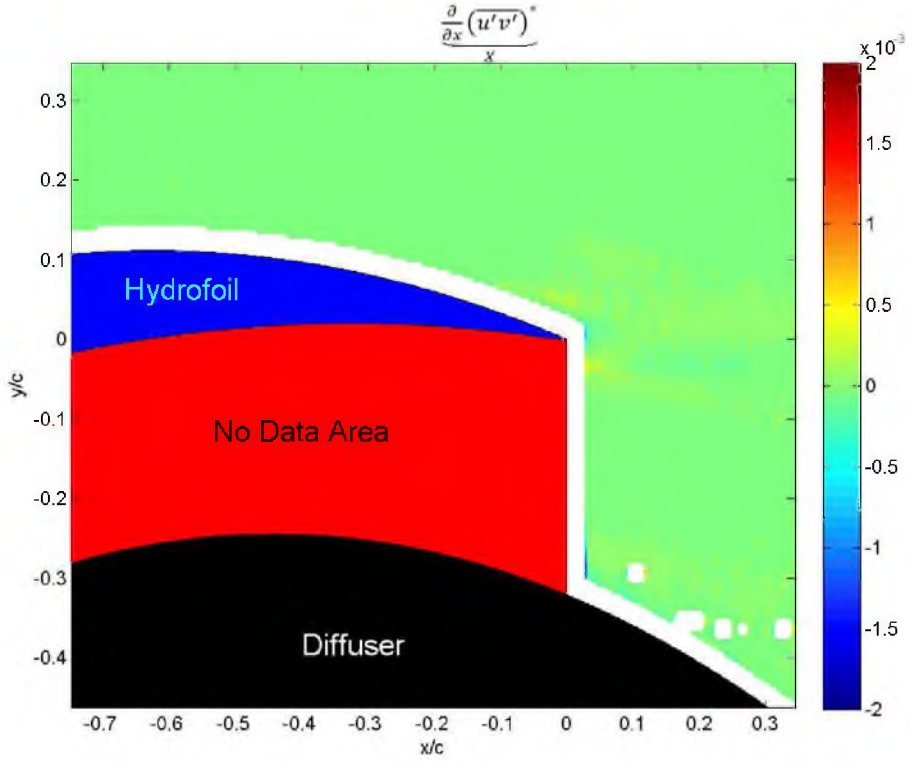

Figure A-102. 'Term X' for low roughness at 0°.

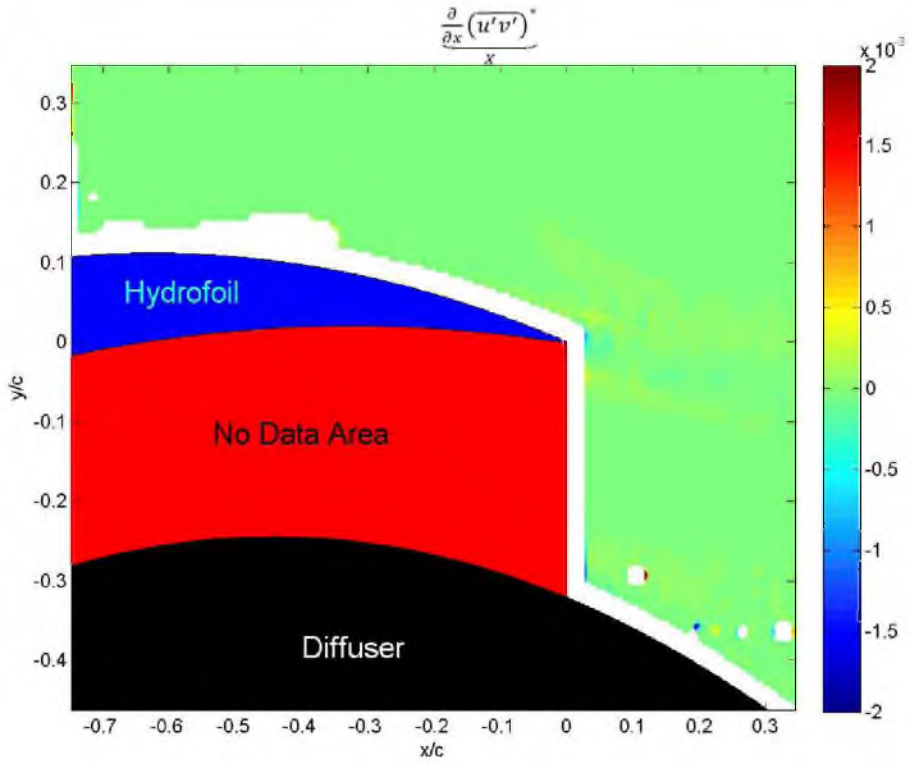

Figure A-103. 'Term X' for medium roughness at 0°.

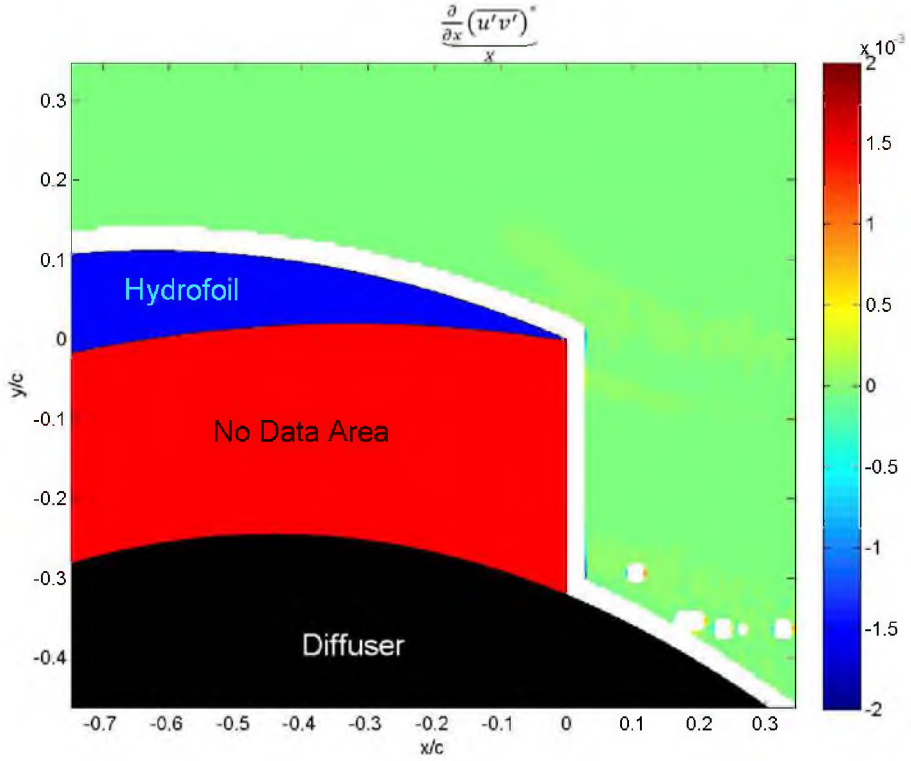

Figure A-104. 'Term X' for high roughness at 0°.

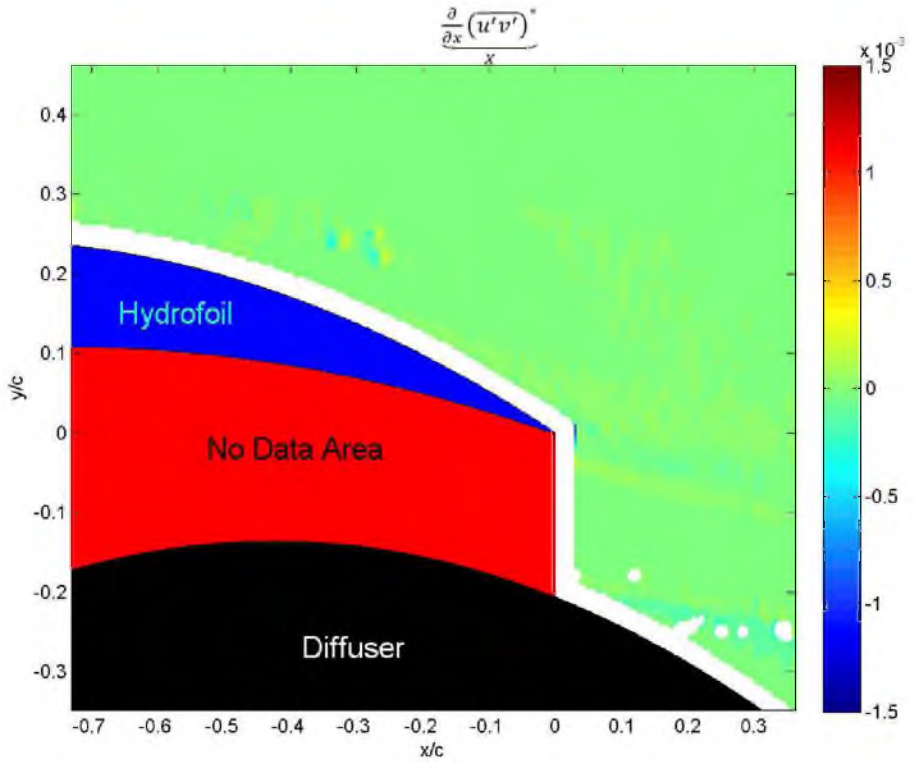

Figure A-105. 'Term X' for low roughness at 10°.

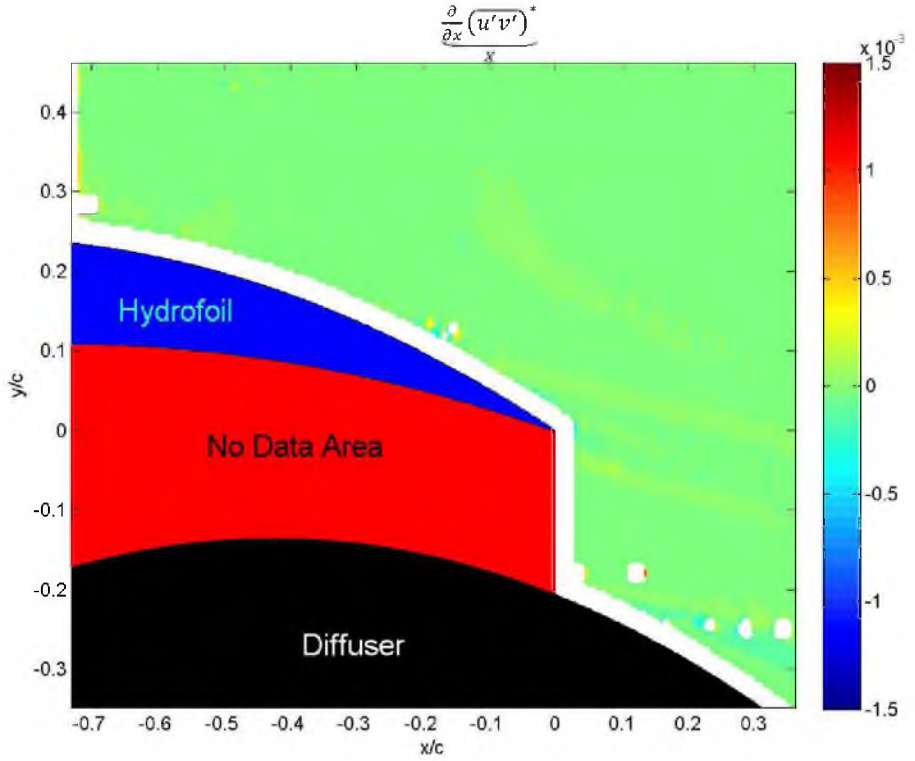

Figure A-106. 'Term X' for medium roughness at 10°.

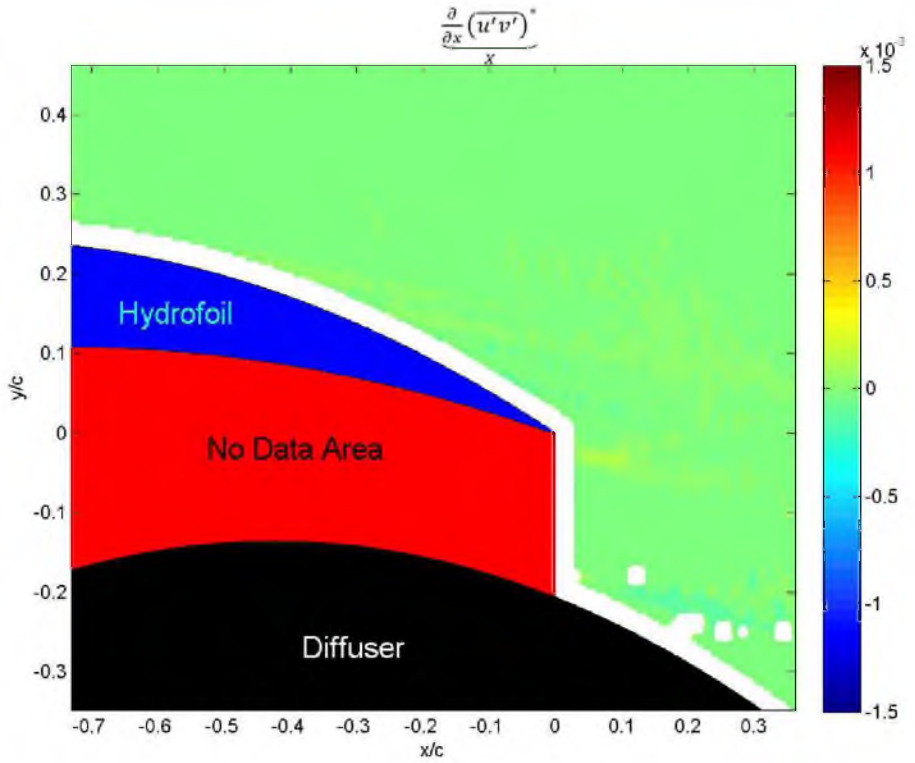

Figure A-107. 'Term X' for high roughness at 10°.

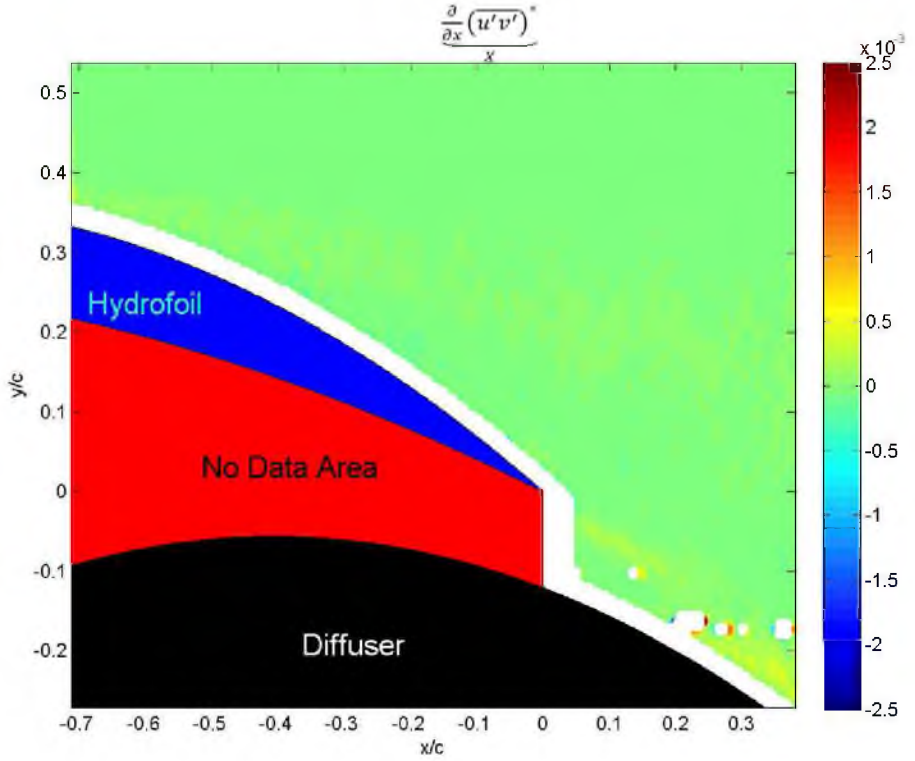

Figure A-108. 'Term X' for low roughness at 17°.

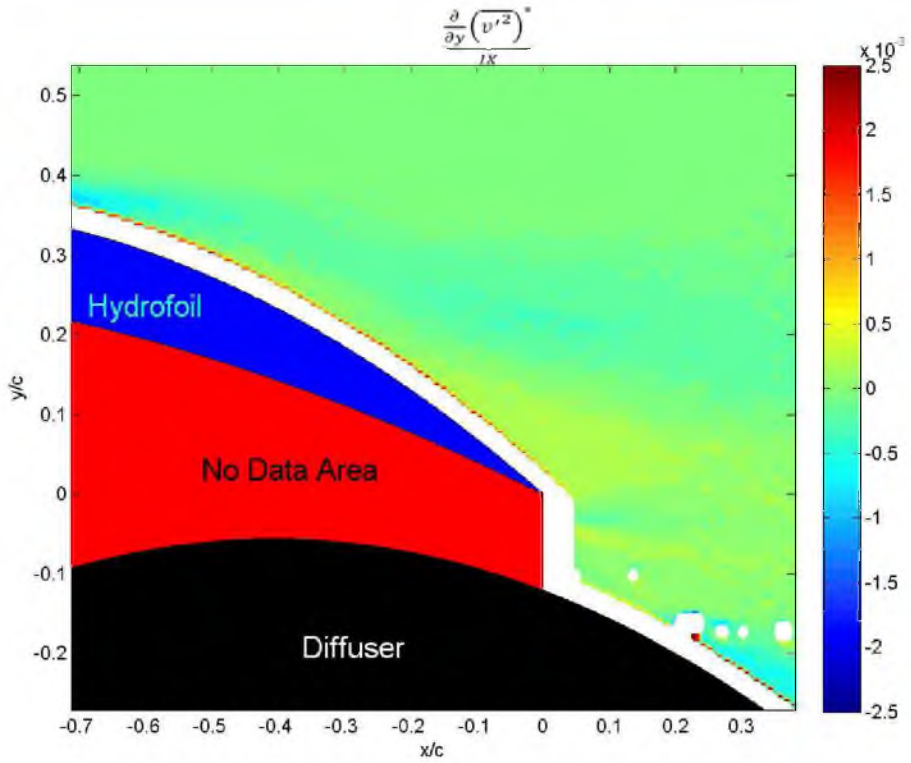

Figure A-109. 'Term X' for medium roughness at 17°.

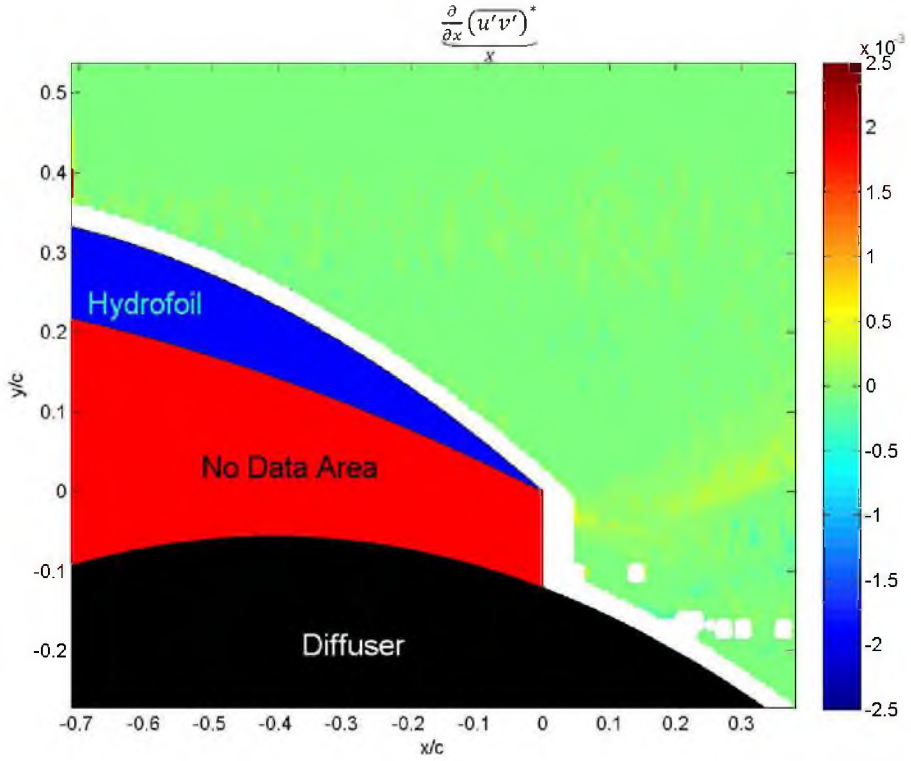

Figure A-110. 'Term X' for high roughness at 17°.

BIBLIOGRAPHY

1999: *6 Inch Flow Visualization Water Tunnel-Installation, Operation, and Maintenance Instructions.* ETL.

2011: *Insight 3G/4G User's Guide.* TSI Inc.

Anderson, J. D., 2007: *Fundamentals of Aerodynamics.* McGraw Hill, 4th edition.

Arndt, R. E., 1981: Cavitation in fluid machinery and hydraulic structures. *Annual Review of Fluid Mechanics*, **13**, 273-326.

Barnes, F., and Corlett, A., 1993: A comparison of flow visualisation and particle-image velcoimetry measurements in the wake of a bluff body at low Reynolds number. *Laser Anemometry Advances and Applications*, 501-508, 5th annual conference.

Bourgoyne, D. A., Ceccop, S. L., and Dowling, D. R., 2005: Vortex shedding from a hydrofoil at high Reynolds number. *J. Fluid Mech*, **531**, 293-324.

Chen, T., and Chwang, A. T., 2002: Trailing vortices in a free-surface flow. *Physics of Fluids*, **14**, 827-838.

Coleman, H. W., Hodge, B., and Taylor, R., 1984: A re-evaluation of Schlichting's surface roughness experiment. *Journal of Fluids Engineering,* **106**, 60-65.

Fox, R., McDonald, A., and Pritchard, P., 2004: *Introduction to Fluid Mechanics.* Wiley, 6th edition.

Hopkins, A. M., 2010: *Fluid Dynamics and Surface Pressure Fluctuations of Two-Dimensional Turbulent Boundary Layers Over Densely Distributed Surface Roughness.* Ph.D. dissertation, Virginia Polytechnic Institute and State University.

Ida, T., 1965: The effects of impeller vane roughness and thickness on the characteristics of the mixed-flow propeller pump. *Bulletin of JSME*, **8**, 634-643.

Keirsbulck, L., Labraga, L., Mazouz, A., and Tournier, C., 2002: Surface roughness effects on turbulent boundary layer structures. *Journal of Fluids Engineering*, **124**, 127-235.

Kundu, P., and Cohen, I., 2004: *Fluid Mechanics.* Elsevier Academic Press, 3rd edition.

Nikuradse, J., 1933: Laws of flow in rough pipes. *NACA TM 1292 - National Advisory Committee for Aeronautics* .

Oldroyd, H. J., 2010: *Scalar Flux Measurements in Turbulent Pipe Flow Employing Combined Particle Image Velocimetry and Planar Laser Induced Fluorescence.* Thesis for Master of Science, University of Utah.

Park, J., Yoon, C.-H., and Kang, J. S., 2009: Numerical prediction of a lifting pump for deep-sea mining. *The Eighth (2009) ISOPE Ocean Mining Symposium.* Chennai, India.

Raffel, M., Willert, C., and Kompenhans, J. (1998). *Particle Image Velocimetry: A Practical Guide.* Springer.

Schlichting, H., 1936: Experimental investigation of the problem. *NACA TM 823 - National Advisory Committee for Aeronautics* .

Sigal, A., and Danberg, J. E., 1988: *Analysis of Turbulent Boundary-Layer over Rough Surfaces with Application to Projectile Aerodynamics.* Army Ballistic Research Lab, Aberdeen Proving Grounds MD.

Sigal, A., and Danberg, J. E., 1990: New correlation of roughness density effect on the turbulent boundary layer. *AIAA Journal* , **28**, 554-556.

Tennekes, H., and Lumley, J. L., 1972: *A First Course in Turbulence.* MIT Press.

Tropea, Yarin, and Foss., 2007: *Springer Handbook of Experimental Fluid Mechanics.* Springer.

Van Rij, J., Belnap, B. J., and Ligrani, P. M., 2002: Analysis and experiments on three-dimensional, irregular surface roughness. *Journal of Fluids Engineering,* **124**, 671-677.

Varghese, G., Kumar, T. M., and Rao, Y., 1978: Influence of volute surface roughness on the performance of a centrifugal pump. *Journal of Fluids Engineering*, **100**, 473-476.

Walsh, M. J., 1990: Riblets. *American Institue of Aeronautics and Astronautics, Inc.* , 203-261.

Yun, Y. I., Park, I. Y., and Song, S. J., 2005: Performance degradation due to blade surface roughness in a single-stage axial turbine. *Journal of Turbomachinery*, **127**, 137-143.

Zhang, Q., Goodro, M., and Ligrani, P. M., 2006: Influence of surface roughness on the aerodynamica losses of a turbine vane. *Journal of Fluids Engineering* , **128,** 568-578.

Zobeiri, A., Avellan, F., Ausoni, P., and Farhat, M., 2010: Experimental investigation of the vortex shedding in the wake of oblique and blunt trailing edge hydrofoils using PIV-POD. *Proceedings of the ASME 2010 3rd Joint US-European Fluids Engineering Summer Meeting and 8th International Conference on Nanochannels, Microchannels, and Minichannels.* 149-154.